

Numerical Calculation of Transient Field Effects in Quenching Superconducting Magnets

vorgelegt von
Diplom-Ingenieur
Juljan Nikolai Schwerg

Von der Fakultät IV - Elektrotechnik und Informatik
der Technischen Universität Berlin
zur Erlangung des akademischen Grades

Doktor der Ingenieurwissenschaften
– Dr.-Ing. –

genehmigte Dissertation

Vorsitz der wissenschaftlichen Aussprache:

- **Prof. Dr.-Ing. habil. Gerhard Mönich**
Fachgebiet für Hochfrequenztechnik / Antennen und EMVt, Institut für
Hochfrequenz- und Halbleiter-Systemtechnologien, Fakultät
Elektrotechnik und Informatik, Technische Universität Berlin

Berichter:

- **Prof. Dr.-Ing. Heino Henke**
Fachgebiet für Theoretische Elektrotechnik, Institut für Technische
Informatik und Mikroelektronik, Fakultät Elektrotechnik und
Informatik, Technische Universität Berlin
- **Dr.-Ing. habil. Stephan Russenschuck**
TE-MS-CMDA-group, CERN Europäische Organisation für
Kernforschung, Genf, Schweiz

Tag der wissenschaftlichen Aussprache : 18.11.2009

Berlin 2010

D83

Numerical Calculation of Transient Field Effects in Quenching Superconducting Magnets

submitted by
Diplom-Ingenieur
Juljan Nikolai Schwerg

At the Faculty IV - Electrical Engineering and Computer Science
of the Technical University of Berlin
in order to receive the academic grade

Doktor der Ingenieurwissenschaften
– **Dr.-Ing.** –

approved dissertation

Chairperson of the Scientific Rehearsal:

- **Prof. Dr.-Ing. habil. Gerhard Mönich**
Chair of Antennas and EMC, Department of Computer Engineering and
Microelectronics, School of Electrical Engineering and Computer
Science, Technische Universität Berlin, Berlin, Germany

Scientific Board:

- **Prof. Dr.-Ing. Heino Henke**
Chair of Theoretical Electrical Engineering, Department of Computer
Engineering and Microelectronics, School of Electrical Engineering and
Computer Science, Technische Universität Berlin, Berlin, Germany
- **Dr.-Ing. habil. Stephan Russenschuck**
TE-MS-CMDA-group, CERN
European Organization for Nuclear Research, Geneva, Switzerland

Date of the Scientific Rehearsal : 18.11.2009

Berlin 2010

D83

Abstract

The maximum obtainable magnetic induction of accelerator magnets, relying on normal conducting cables and iron poles, is limited to around 2 T because of ohmic losses and iron saturation. Using superconducting cables, and employing permeable materials merely to reduce the fringe field, this limit can be exceeded and fields of more than 10 T can be obtained.

A quench denotes the sudden transition from the superconducting to the normal conducting state. The drastic increase in electrical resistivity causes ohmic heating. The dissipated heat yields a temperature rise in the coil and causes the quench to propagate. The resulting high voltages and excessive temperatures can result in an irreversible damage of the magnet - to the extend of a cable melt-down. The quench behavior of a magnet depends on numerous factors, *e.g.* the magnet design, the applied magnet protection measures, the external electrical network, electrical and thermal material properties, and induced eddy current losses. The analysis and optimization of the quench behavior is an integral part of the construction of any superconducting magnet.

The dissertation is divided in three complementary parts, *i.e.* the thesis, the detailed treatment and the appendix.

In the thesis the quench process in superconducting accelerator magnets is studied. At first, we give an overview over features of accelerator magnets and physical phenomena occurring during a quench. For all relevant effects numerical models are introduced and adapted. The different models are weakly coupled in the quench algorithm and solved by means of an adaptive time-stepping method. This allows to resolve the variation of material properties as well as time constants. The quench model is validated by means of measurement data from magnets of the Large Hadron Collider. In a second step, we show results of protection studies for future accelerator magnets. The thesis ends with a summary of the results and a critical outlook on aspects which could be subjected to further studies.

Common definitions and concepts in the design of superconducting magnets, derivations of electromagnetic models, and explanations of typical effects are collected in the detailed treatment. We introduce, *e.g.*, the temperature margin to quench and the MIITs, and define the magnetic energy and inductance in case of materials exhibiting hysteresis and diffusive behavior. The momentarily dissipated hysteresis losses are derived for the critical state model of hard superconductors. Furthermore, we review magnet protection methods and the voltages occurring during a quench.

The appendix contains all information required for the reproduction of the presented results. It comprises material properties such as the electrical resis-

tivity or the heat capacity for a temperature range spanning from cryogenic temperatures to some hundred kelvins. The model and simulation parameters for the magnets used for this work are collected at the end.

Zusammenfassung

in deutscher Sprache

Die maximale magnetische Induktion in Magneten für Teilchenbeschleuniger ist, aufgrund von Leitungsverlusten in den Kupferkabeln und Eisensaturierung, auf *ca.* 2 T beschränkt. Durch den Einsatz von supraleitenden Kabeln können jedoch Feldstärken von mehr als 10 T erreicht werden.

Als Quench wird der plötzliche Übergang vom supraleitenden zum normalleitenden Zustand bezeichnet. An dem sprunghaft vergrößerten elektrischen Widerstand wird Wärme erzeugt, die die supraleitende Spule aufheizt und zur Ausbreitung des Quenches führt. Die auftretenden elektrischen Spannungen und hohen Temperaturen können zu irreversiblen Schäden am Magneten führen - im Extremfall zum Schmelzen des Kabels. Das Verhalten eines Magneten während eines Quenches hängt von einer Vielzahl an Faktoren ab, wie z.B. von der Konstruktionsweise des Magneten, den verwendeten Schutzmaßnahmen, der externen elektrischen Beschaltung, den elektrischen und thermischen Materialeigenschaften und den induzierten Wirbelstromverlusten. Eine Analyse und Optimierung des Quenchverhaltens ist ein wichtiger Bestandteil der Konstruktionsphase supraleitender Magnete.

Die Doktorarbeit gliedert sich in drei Teile: den Hauptteil, eine Sammlung detaillierter Herleitungen und den Anhang.

Im Hauptteil der Arbeit wird der Quenchprozess in supraleitenden Beschleunigermagneten untersucht. Nach einem Überblick über die Bauweise von Beschleunigermagneten werden die unterschiedlichen physikalischen Effekte, die im Verlauf eines Quenches auftreten, eingeführt. Für alle relevanten Phänomene werden numerische Modelle vorgestellt und angepasst. Die einzelnen Modelle werden im Quenchalgorithmus zusammengefasst und schwach miteinander gekoppelt gelöst. Um die Variation von Materialeigenschaften und Zeitkonstanten auflösen zu können, wird der Algorithmus mit einer adaptiven Zeitschrittweitensteuerung ausgestattet. Das Quenchmodell wird anhand von Messungen von Magneten des Large Hadron Collider validiert. Im Anschluss werden Ergebnisse von Studien für zukünftige Beschleunigermagnete gezeigt. Der Hauptteil endet mit einer Zusammenfassung der Ergebnisse und einem kritischen Ausblick auf Aspekte, die im Rahmen weiterer Arbeiten untersucht werden könnten.

In den detaillierten Betrachtungen werden Konzepte aus dem Bereich supraleitender Magnete, z.B. Temperaturtoleranzen und die Quenchlast, eingeführt. Die Definitionen der elektromagnetischen Energie und der Induktivität werden im Zusammenhang von feldabhängigen und Hysterese behafteten Materialien untersucht. Es wird ein Ausdruck für die Augenblicksleistung bei Supraleiterhystereseverlusten hergeleitet. Weiterhin erfolgt eine ausführliche Darstellung aller Spannungen, die während eines Quenches auftreten und eine

Beschreibung gängiger Magnetschutzkonzepte.

Der Anhang enthält alle Daten, die zur Reproduktion der vorgestellten Ergebnisse nötig sind. Er umfasst Materialeigenschaften wie z.B. den elektrischen Widerstand oder die Wärmekapazität für Temperaturbereiche von kryogenischen Temperaturen bis hin zu mehreren hundert Kelvin. Die Modell- und Simulationsparameter der einzelnen Magnete sind ebenfalls im Anhang aufgeführt.

Acknowledgement

The work presented in this thesis has been carried out in the framework of the Doctoral Student Program at CERN in cooperation with the chair for electromagnetism at the Technische Universität Berlin.

I am very thankful to my supervisor at CERN, Dr.-Ing. habil. Russenschuck, for assigning me to this rich and diverse subject. I got many inspirations from our discussions, broadened my understanding on the design and computation of superconducting accelerator magnets, and learned about the high standards of scientific writing and notation.

I want to thank Dr. Auchmann who co-supervised my work for our discussions and his support.

I am most grateful to Prof. Dr.-Ing. Henke from the Technische Universität Berlin for supervising this external thesis. I am very glad for his support during the last years, *i.e.* our discussions about field theory and the world of science, his fast and profound feed-back and especially his positive spirit.

I want to thank Dr.-Ing. Bruns, Dr. Rodriguez-Mateos, and Dr. Verveij for discussions on numerical methods, quench simulation at CERN, and cable related aspects of quench.

I am very glad for all the support and advice I got from my first supervisor at CERN, Dr.-Ing. Völlinger, since my time as a technical student.

During the start of his Ph.D.-project Mr. Bielert helped me conducting the simulations for the inner triplet upgrade (used in Sec. 5.1). I very much enjoyed our lunch and coffee breaks.

Over the course of the Ph.D.-project I was assigned to three groups, *i.e.* AT-MEL, AT-MTM and TE-MS. I want to thank the group leaders Dr. Mess, Dr. Walckiers, and Prof. Rossi, as well as all my colleagues for the pleasant work atmosphere.

Furthermore, I want to thank those people who helped me keeping my personal balance by providing diversion and company: Thank you Deepali, Ruxandra and Fabio for the years we spent together in Geneva and for adding to my life.

Thanks to the people of the legendary Rue de Lyon 2: Thank you Diana, Tamara, Ahmed and Emilia for the time we shared and things we have experienced. Thanks to Fiona for proofreading parts of the thesis and being awesome!

My thanks to Steffen for our discussions on “gefangene Energie” and “Leis-

tungsübertragung". It was very comforting and helpful being able to share with someone what doctoral students eventually have to go through...

"What is the area covered by one bushel of corn in a field?" - this question led to numerous Sundays spent discussing with Swati in cafes and bars around the city - instead of working on my thesis. We have never reached a conclusion, but it was totally worth it!¹

I was always lucky to enjoy the support of my family. Therefore I am very grateful.

¹A bushel is a unit of dry volume, usually subdivided into eight local gallons in the systems of Imperial units and U.S. customary units. It is used for volumes of dry commodities, not liquids, most often in agriculture. It is abbreviated as bsh. or bu. The name derives from the 14th century buschel or busschel, a box.

- Wheat at 13.5% moisture by weight: 60 lb = 27.2155422 kg

(Wikipedia - <http://en.wikipedia.org/wiki/Bushel> - 01.08.2009)

*Nullus est liber tam malus, ut non aliqua parte
prosit!*

GAIUS PLINIUS CAECILIUS SECUNDUS
(AD 61/63 - ca. 113)

to my father
and our friends

Contents

1	Introduction	1
1.1	Superconductivity and Quench	1
1.2	Quench Simulation	3
1.3	Literature Overview	3
1.4	Objectives of the Thesis	5
1.5	Structure of the Dissertation	5
2	Magnet Features and Physical Phenomena	7
2.1	Superconducting Magnets	7
2.1.1	The LHC Main Bending Magnet	8
2.1.2	Other Magnet Types and Design Features	12
2.2	Quench Process	14
2.3	Relevant Effects	19
3	Numerical Modeling	21
3.1	Coil Discretization and Numbering Scheme	22
3.2	Superconductor Model	23
3.3	Magnetic Field Model	25
3.4	Induced Losses	28
3.5	Electrical Network	29
3.5.1	Lumped Network Elements	31
3.5.2	Magnet Representation and Introspection	33
3.6	Thermal Model	36
3.6.1	Temperature Change	38
3.6.2	Heat Transfer	38
3.6.3	Thermal Properties of Helium	40
3.6.4	Quench Heaters	41
3.6.5	Total Dissipated Power	42
3.7	Quench Algorithm	43
4	Introspection	47
4.1	LHC Main Dipole	47
4.1.1	Reproduction of Quench Measurements	48
4.1.2	Introspection - Simulation of a Quench in the LHC Tunnel	52
4.2	3-D Thermal propagation	54
4.3	Quench recovery	58
5	Extrapolation	61
5.1	Quench Protection Study Inner Triplet Upgrade Quadrupole	61

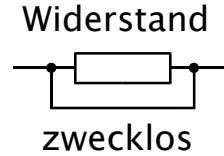
5.1.1	Unprotected Quench	62
5.1.2	Quench Heater Protection	63
5.1.3	Dump Resistor Studies	66
5.1.4	Power Supply Inversion	70
5.1.5	Full Protection	70
5.2	Fast-Ramping Dipole	71
5.2.1	Cooling Schemes	72
5.2.2	Quench Limits at Different Ramp Rates	73
5.2.3	Quench Detection During the Up- and Down Ramp	74
5.2.4	Robust Magnet Design	76
6	Conclusion and Outlook	77
7	Detailed Treatment	81
7.1	Margins to Quench	81
7.1.1	Current Density Margin	81
7.1.2	Temperature Margin	81
7.1.3	Margin on the Load-line	83
7.1.4	Enthalpy Margin/Energy Reserve	83
7.1.5	Minimum Quench Energy	86
7.2	MIITs	87
7.3	Magnetic Energy	89
7.4	Inductance	93
7.4.1	Self Inductance	93
7.4.2	Mutual inductance	95
7.4.3	Application of the Differential Inductance to Quench Computation	96
7.5	Non-linear Voltage-Current-Characteristic of Superconductors	100
7.5.1	Current-Sharing	101
7.5.2	Voltages Induced over a Superconductor	104
7.5.3	Graphical Solution	108
7.6	Cable Magnetization Losses	109
7.7	Superconductor Hysteresis Losses	114
7.8	Modeling Rutherford-Type Cables	122
7.9	Magnet Protection	126
7.9.1	Quench Detection	128
7.9.2	Dump Resistor	130
7.9.3	Isolating the Magnet	132
7.9.4	Subdivision and Coupled Secondary	132
7.9.5	Quench Heaters	133
7.9.6	Quench Protection Sequence of Events	137
7.10	Voltages Occurring During a Quench	138
7.10.1	Terminal Voltages	138
7.10.2	Coil Voltages	142
7.10.3	Voltages in the Coil Cross-Section	148
7.11	Runge-Kutta Method	151

A	Material Properties	153
A.1	Solids in Normal Conducting State	154
A.1.1	Temperature Levels	154
A.1.2	Mass Density	155
A.1.3	Electrical Resistivity	156
A.1.3.1	Copper	159
A.1.3.2	Niobium-Titanium	161
A.1.3.3	Niobium-3-Tin	161
A.1.3.4	Insulators (Kapton, PVA, Epoxy)	161
A.1.3.5	Other Materials	162
A.1.4	Thermal Conductivity	162
A.1.4.1	Copper	163
A.1.4.2	Niobium-Titanium	165
A.1.4.3	Niobium-3-Tin	165
A.1.4.4	Polyimide (Kapton)	165
A.1.4.5	Other Materials	165
A.1.5	Heat Capacity	167
A.1.5.1	Copper	169
A.1.5.2	Niobium-Titanium	169
A.1.5.3	Niobium-3-Tin	169
A.1.5.4	Polyimide (Kapton)	171
A.1.5.5	Other Materials	171
A.1.6	Permeability	171
A.1.6.1	Magnetic Iron	174
A.1.6.2	Other Materials	175
A.1.7	Dielectric Strength	175
A.1.8	Electrical Permittivity	175
A.1.8.1	Insulators	177
A.2	Solids in Superconducting State	177
A.2.1	Transition Temperature / Critical Field	178
A.2.2	Critical Current	179
A.2.3	The n-Index	181
A.2.4	Critical Current Density	182
A.2.5	Critical Surface Parameterization	183
A.2.5.1	Niobium-Titanium	183
A.2.5.2	Niobium-3-Tin	184
A.2.6	Electrical Resistivity	186
A.2.7	Thermal Conductivity	186
A.2.8	Heat Capacity	186
A.2.8.1	Niobium-Titanium	187
A.2.8.2	Niobium-3-Tin	187
A.2.9	Permeability	188
A.3	Fluid/Gaseous Matter - Helium Properties	188
A.3.1	Temperature Levels / Phases	189
A.3.2	Density	189
A.3.3	Latent Heat	190

A.3.4	Heat Conductivity	191
A.3.5	Volumetric Specific Heat	191
A.3.6	Dielectric Strength	191
B	Parameters	193
B.1	Geometrical Quantities	193
B.1.1	Filament	193
B.1.2	Strand	193
B.1.3	Cable	194
B.1.4	Cable Twist-pitch in a 2D Approach	197
B.1.5	Coil Cross-Section	197
B.1.6	Magnet	199
B.2	Filling Factors	200
B.2.1	Length, Area and Volume Ratios	200
B.2.2	Material Fractions	201
B.2.3	Effective Electrical Resistivity, Thermal Conductivity and Specific Heat	201
C	Cases	203
C.1	LHC Main Bending Magnet	203
C.1.1	Strand	203
C.1.2	Cable	203
C.1.3	Magnet Data	205
C.1.4	External Electrical Circuit	205
C.1.5	Magnet Protection	205
C.1.6	Operating Conditions / Critical Values	209
C.2	LHC Inner Triplet Nested Dipole - MCBX	212
C.2.1	Strand and Cable	212
C.2.2	Magnet Data	212
C.3	LHC Inner Triplet Upgrade Quadrupole - MQXC	215
C.3.1	Strand and Cable	215
C.3.2	Magnet Data	215
C.3.3	Electrical Circuit	215
C.3.4	Magnet Protection	215
C.3.5	Operating Conditions / Critical Values	215
C.4	Fast Ramping Dipole Magnet	218
C.4.1	Strand and Cable	218
C.4.2	Magnet Data	218
C.4.3	Electrical Circuit	218
C.4.4	Magnet Protection	218
C.4.5	Operating Conditions / Critical Values	218
D	Digressions	223
D.1	Surface-Charge of a Discontinuity of Resistivity	223
D.2	An Arbitrarily Cut Cylinder	224

D.3	Critical Current Density Relies on the Model of the Superconductor	225
E	Formulary and Constants	229
E.1	Formulary	229
E.1.1	Inductance of a Ring Conductor	229
E.1.2	Field of a Long Solenoid	229
E.2	Constants	229
	Bibliography	I
	List of Figures	XVII
	List of Tables	XXIII
	Notation and List of Symbols	XXV
	Curriculum Vitae	XXXV

1 Introduction



The maximum obtainable magnetic induction of accelerator magnets, relying on normal conducting cables and iron poles, is limited to around 2 T because of ohmic losses and iron saturation [Will 00, p. 55]. Using superconducting cables, and employing permeable materials merely to reduce the fringe field, this limit can be exceeded and fields of more than 10 T can be obtained.

For the new particle accelerator LHC [Lefe 95, Evan 09, Hein 07], currently under commissioning at CERN [CERN 91], more than 8000 superconducting magnets are used; some of them with a maximum field strength of more than 8 T. The coils of these magnets are mainly made of Nb-Ti strands where the technological challenges are well mastered and a variety of tools for design and calculation are available. With new materials available on an industrial scale, *e.g.* Nb₃Sn is able to carry much higher current densities [Devr 04, p. 7], or with new applications like fast-ramped accelerators, new problems occur and established design assumption do not hold any longer. Hence, the methods for the simulation of quench in superconducting magnets have to be revised.

1.1 Superconductivity and Quench

Superconducting accelerator magnets are made from hard, low-temperature superconductors. The materials used for the superconducting cables exhibit superconductivity if the temperature, the applied magnetic induction and the current density are below critical values which are interdependent and form the critical surface. The maximum current density in these superconductors is in the order of some 10^{10} Am^{-2} (Sec. A.2.5.1). This is a factor 1000 higher than in standard copper wires (rated at about 10^7 Am^{-2} [Wils 83, p. 3]).

Exceeding locally the limits of the critical surface, the affected fraction of the strand transits from superconducting to normal conducting state - denoted as *quench* [Appl 69]. Following IEC [Supe 07a],

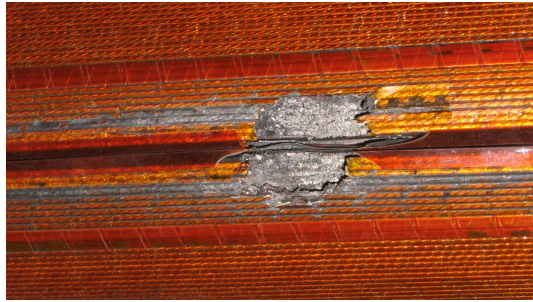


Figure 1.1: Coil windings of the LHC main bending magnet MB3004 after a quench at nominal current. The magnet developed an inter-turn short circuit which caused a meltdown of the cable and the cold bore (the tube separating the coil from the beam)[Walc 04, Siem 03].

[a] Quench [denotes] the uncontrollable and irreversible transition of a superconductor or a superconducting device from the superconducting state to the normal conducting state.

With the development of a quench, several physically different but mutually dependent processes start: Due to the ohmic heating, the temperature increases and the normal conducting zone expands over the superconductor. If the device is short-circuited, the growing resistivity causes the current to decrease. The changing current results in a change of magnetic flux and thus induces eddy and magnetization currents in the metallic parts and cables, respectively. These induced currents create losses and additional heating, which distribute the normal zone even further.

A quench poses two different threats to a superconducting device: high temperatures due to an unlimited ohmic heating, and excessive voltages due to a steadily growing resistance at high currents [Iwas 05]. High temperatures impair the electrical integrity of the insulation material or even cause a meltdown of the cable. Excessive voltages can result in an electric arc between adjacent coil windings punching holes into the insulation. In addition, the high current density and temperature gradients during a quench can cause an irreversible degradation of the current carrying capability of the superconductor.

The violence of an uncontrolled electromagnetic discharge shall be illustrated by an incident which happened to the LHC main bending magnet MB3004 during cold testing on the test bench. During a quench at nominal current the insulation of the magnet failed [Walc 04] and the magnet developed an inter-turn short circuit. The excessive heat deposition in the short circuited turn caused a meltdown of the cable and the cold bore tube (the tube between coil and beam) [Siem 03]. The integrity of the cryogenic system was lost. Figure 1.1 shows the burnt-out coil windings after the incident.

Superconducting devices, where the occurrence of a quench cannot be ex-

cluded by the choice of operating conditions, need to be equipped with a protection system. The protection either relies on an intrinsically safe design or on active measures taken upon quench detection. In the former case, the device is designed such that it can withstand a quench without overheating and the quench is eventually able to recover. In the latter case, the current is extracted actively - as soon as possible - from the device by either increasing the internal resistance or switching in an external resistor.

The design of the protection system is an essential part of the construction of any superconducting device. Therefore, quench simulation programs are needed in order to study the intrinsic quench behavior and define the necessary protection, to test protection schemes and to analyze measurement data.

1.2 Quench Simulation

The simulation of quenches in superconducting magnets constitutes both, a multi-physics and a multi-scale problem. The accurate modeling consists of a thermal, a magnetic and an electrical network problem coupled by means of energy exchange and non-linear material properties.

The required spacial resolution spans from less than a millimeter for the description of eddy currents in strands to several meters for an entire magnet. The involved time constants reach from some microseconds for the resolution of quench initialization to several minutes for the computation of full magnet ramp-cycles. The minimum energy required to quench part of a strand may be in the order of some micro joules while the total stored energy in a magnet ranges at several mega joules.

Furthermore, quench computation constitutes a strongly non-linear problem. The relevant material properties, *e.g.* the thermal capacity and electrical resistivity, vary over many orders of magnitudes during a quench. In addition, superconducting materials exhibit hysteresis behavior.

On this account, the simulation of quench on accelerator type magnets relies on the simplification of complex structures, homogenization of material properties, and analytical sub models. Consequently, any quench model is limited to a specific set of applications. This approach requires the coupling of several computation methods, *e.g.* finite-differences, finite elements, boundary-elements, Biot-Savart's law, and network-models. The variation of material properties can be encountered by using an adaptive time-stepping approach or iteration methods.

Quench models published in the literature mainly differ in their choice of simplification and their set of applied sub-models.

1.3 Literature Overview

Quench codes Many calculation methods for quench in superconducting magnets have been published. Except for the very recent publication of AIRD

[Aird 06], none actually aimed at the modeling of the entire multi-physics problem.

WILSON published the computer program QUENCH [Wils 68] modeling the quench propagation due to ohmic heating in superconducting solenoids. A concept of field and temperature dependent, anisotropic quench propagation velocities is used to span the normal conducting zone over the coil. This approach was further developed by ROSSI, first in DYNQUE [Cana 93] and later in QLASA [Ross 04]. A similar approach for accelerator type magnets can be found in [Laty 97] by LATYPOV.

KRAINZ modeled and studied the protection of the LHC test string using an electrical network model [Krai 97]. The simulation of the current decay in a quenching magnet considering the external network, and a string of magnets based on the commercial software SABER was done by RODRIGUEZ-MATEOS [Rodr 97, Rodr 96].

SONNEMANN and CALVI developed a finite difference model for the simulation of the quench propagation velocity based on thermal material properties and the local magnetic field called SPQR [Sonn 01b, Calv 00]. In [Sonn 01a] SONNEMANN presented a quench model and quench measurements for magnets of the LHC. KIM published a finite difference model for the simulation of quench in [Kim 01]. The quench behavior of a superconducting undulator was simulated with a finite difference model [Bett 06] by BETTONI.

CASPI and MASSON presented thermal models for the quench simulation using commercial finite elements packages ANSYS [Casp 03] and COMSOL [Mass 07], respectively.

The only program following an approach of hard-coupling of the different physical effects is the program of VECTORFIELDS [Aird 06]. Due to their focus on superconducting solenoids, with a huge number of fine windings, an individual winding scheme is not defined and turn-to-turn voltages can not be calculated.

Sources on superconducting magnets and quench phenomenon In addition to the publications on quench simulation models, the following studies of the quench process have to be mentioned. IWASA, MESS and WILSON address quench, relevant effects and quench protection in their books [Iwas 94], [Mess 96] and [Wils 83], respectively. Especially the book [Brec 73] of BRECHNA provides extensive material for the understanding of superconducting magnets and quench.

DEVRED performed analytical quench studies for the SSC [Devr 89]. The thesis of VERWEIJ provides valuable information on the stability of superconductors and on induced losses in superconducting cables [Verw 95].

Background for the presented work The work presented in this thesis builds on the CERN field calculation program ROXIE by RUSSENSCHUCK [Russ 98]. The program provides all necessary functionality for the electromagnetic design of superconducting accelerator magnets including the numerical computation of the magnetic field produced by superconducting cables

and parts made from non-linear iron. In the past years, ROXIE has been extended to simulate field disturbances and losses stemming from inter-filament coupling currents (IFCC) [Wils 83], inter-strand coupling currents (ISCC) [Mari 04] and persistent superconductor magnetization currents [Voll 02].

Equipping ROXIE with an electrical network and thermal model allows for a coupled computation of all physical phenomena occurring during a quench.

1.4 Objectives of the Thesis

The challenge of quench simulation is to model all relevant physical phenomena and effects with adequate accuracy, so that internal states of a quenching magnet can be reproduced and analyzed in order to understand the quench behavior. This leads to the following objectives:

- Analysis of the quench process in superconducting magnets focussing on all physical effects and their relevance for the quench model.
- Study and test of (existing) models describing relevant effects. Implementation and adaptation of the numerical models into a global computation environment.
- Development of a quench algorithm: Study of the interdependence of the different sub-models. Implementation of a computational scheme reflecting computational cost as well as the necessary coupling between the sub-models. Finding a numerical method to resolve changes in material properties and time constants.

The quench model has to be verified by reproducing measurement data with all material- and model-parameters chosen within the range of uncertainty. In a second step, the model can be used to extrapolate the magnet quench behavior to different initial conditions and slight design changes.

1.5 Structure of the Dissertation

The dissertation is divided in three complementary parts, *i.e.* the thesis, the detailed treatment and the appendix. The thesis is structured in 4 main chapters:

- Overview over features of accelerator magnets and physical phenomena occurring during a quench. We follow a typical quench process through a magnet and discuss the physical phenomena in respect to the magnet application. Definition of the scope for the quench model.
- Introduction of numerical models for all relevant effects occurring during a quench. We give detailed explanations on the implementation and/or adaptation of the used sub-models and their internal states. The different models are weakly coupled in the quench algorithm and solved

by means of an adaptive time-stepping method. The such developed algorithm allows to study quench propagation, magnetic quench back, and voltages building up within the magnet winding.

- Simulation results reproducing quench measurements from the LHC. The quench model provides a detailed view on the internal states of quenching magnets. The presented reproduction of the coil voltage signal including characteristic spikes clearly indicates the advantages of the coupled approach.
- Extrapolation of the simulation results on new magnet designs and protection concepts. We show a detailed protection study for the LHC inner triplet upgrade. For the case of fast-ramping magnets we are exploring new protection possibilities.

Moreover, we summarize the presented approach and obtained results. We give a critical analysis on aspects which could be subjected to further studies. In order to reduce the complexity of the main part, detailed treatments, *e.g.* common definitions and concepts of superconducting magnet design, derivations of electromagnetic models, and explanations of typical effects are collected in the last chapter. Notice that the different subjects are put down such that they can be read independently from the main parts.

- Analytical hot-spot calculation by means of the MIITs-concept indicating the need for numerical methods.
- Definition of the magnetic energy and the inductance in case of materials exhibiting hysteresis and diffusive behavior.
- Derivation of the instantaneously dissipated hysteresis losses for the critical state model of hard superconductors.
- Modeling Rutherford-type cables including induced losses.
- Overview over magnet protection methods and voltages occurring during a quench.

In order to provide the reader with all necessary information to reproduce the presented results the appendix contains the following sections:

- Researched values are provided for all materials commonly used in superconducting accelerator magnets. We briefly review the physical background to all relevant material properties.
- The definitions and formulae of model parameters describing the coil geometry.
- Description of all magnets presented in this work. We describe all parameters of the superconducting strand and cable, the coil cross-section and iron yoke, the winding scheme and electrical network, as well as magnet protection.

2 Magnet Features and Physical Phenomena

*Dicebat Bernardus Carnotensis nos esse quasi
nanos, gigantium humeris insidentes, ut possimus
plura eis et remotiora videre, non utique proprii
visus acumine, aut eminentia corporis, sed quia in
altum subvenimur et extollimur magnitudine
gigantea.*

JOHN OF SALISBURY
(1120 - 1180)

In this chapter we introduce relevant features of superconducting magnets and physical phenomena occurring during a quench. Due to the excessive requirements for the modeling of all physical effects, we have to reduce our approach and disregard a number of effects. The reduction is motivated by our application and briefly compared to other approaches.

2.1 Superconducting Magnets

We distinguish between superconducting accelerator-type magnets and other superconducting magnets. The first are used to guide the beam of a particle accelerator on their orbit, *i.e.* bending them on a circular trajectory or focussing the beam. The latter kind comprises superconducting magnets for MRI, the LHC experiments ATLAS and CMS, as well as fusion projects like ITER.

The typical design features of superconducting accelerator type magnets are introduced by means of the LHC main bending magnet. Major differences to other accelerator type magnets, *e.g.* superconducting correctors or superferric magnets, are discussed in the following. The section ends with a brief overview on the features of other commonly used superconducting magnets, *e.g.* solenoids, toroids, and undulators.

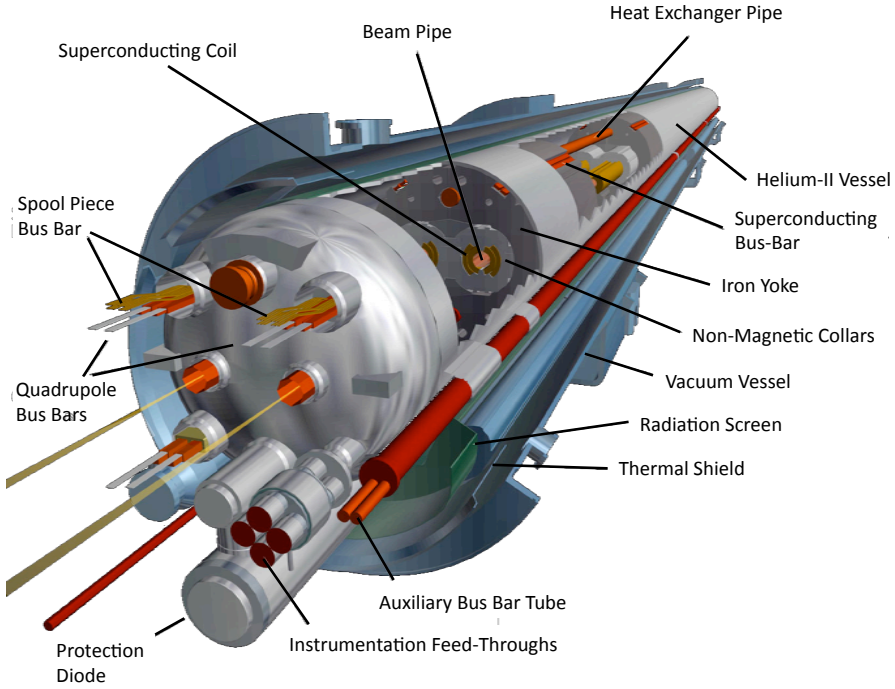


Figure 2.1: CAD image of the superconducting LHC main bending magnet showing all relevant features: Superconducting coil, iron yoke, helium-II vessel, bus bars and the protection diode. Courtesy of CERN©.

2.1.1 The LHC Main Bending Magnet

A typical superconducting accelerator magnet consists of a superconducting coil formed around the aperture, a non-magnetic collar to hold the coil in place, quench-heater strips, an iron yoke, and a helium vessel for the operation at cryogenic temperature. Figure 2.1 shows a CAD image of the 15 m-long LHC main dipole displaying all relevant features.

Aperture, beam pipe and beam screen The LHC operates with two beams of identical electrical charges circulating in opposite directions. Therefore, magnetic fields of opposite orientation are required to keep the particles on their circular trajectory. The LHC MB is a double aperture magnet with two dipolar coils in a common iron yoke and cryostat. The size of the aperture denotes the inner diameter of the coil (56 mm).

The particle beams circulate in two beam pipes providing an ultra-high vacuum in the inside and the inner wall of the helium-II-vessel. Inside the beam-pipe a perforated tube (beam screen) protects the magnets from synchrotron radiation and part of the beam losses.

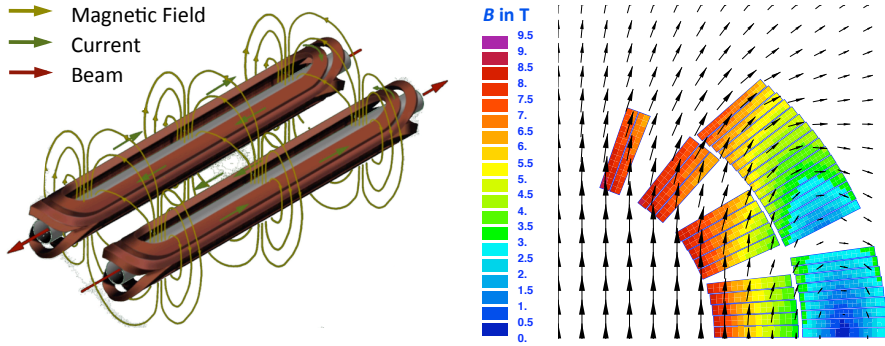


Figure 2.2: (left) CAD image of a double aperture coil configuration in $\cos\theta$ -design with a schematic representation of the magnetic field. Notice how the coil windings are bent upwards/downwards in order to leave room for the beam pipe. Courtesy of CERN©. (right) Quadrant of one aperture of the coil cross-section of the LHC MB showing the magnetic induction at nominal current level.

Superconducting coil Contrary to normal conducting magnets, where the magnetic field in the air gap strongly depends on the contribution of the ferromagnetic poles, the field inside the aperture of a superconducting magnet is basically created by the current in the coil.

The superconducting coil consists of an upper and a lower pole, which are typically race-track-type coils mounted below and above the beam pipe. By reducing the distance of the windings to the aperture, the efficiency and the magnetic main field can be increased. The windings are therefore pressed on a winding mandrel resulting in a coil shape as shown in Fig. 2.2 (left).

The dipole field configuration is obtained by approximating an ideal $\cos\theta$ current distribution, *e.g.* [Schw 05a, pp. 36]. Therefore, the coil windings (also denoted as conductors) are combined to blocks of different size and distributed around the aperture. The space between two adjacent blocks is filled with non-magnetic material in order to hold the conductors in their positions and to improve the circular shape approximation. Due to their shape the spacers are denoted as wedges.

The field of the magnet is further increased by nesting two or more coil layers. The coil cross-section of the LHC MB is shown in Fig. 2.2 (right). The figure indicates the field in the aperture and over the conductors. Due to the higher magnetic induction close to the aperture, the two layers use different cable types allowing to reduce the current density in the inner layer.

In the coil ends, the conductors are bent up/down in order to leave room for the beam pipe. This yields additional bending strain to the windings and results in a reduced mechanical support. The coil field in the ends is higher than in the straight part of the coil. This is compensated by means of the iron-yoke end design.

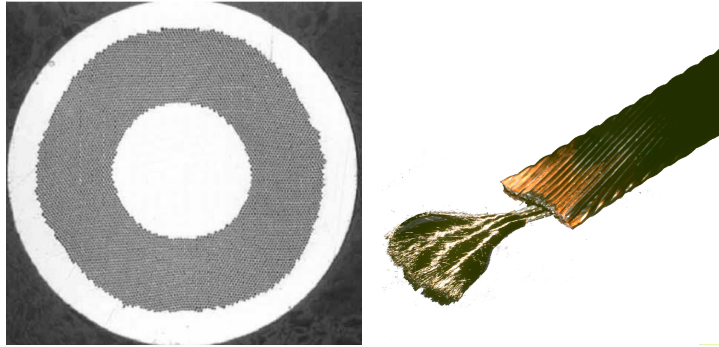


Figure 2.3: LHC Main Bending Magnet (MB) strand and cable. (left) strand cross-section featuring a copper core, Nb-Ti filaments (dark spots) embedded in the copper matrix and a copper coat. (right) Rutherford-type cable. The filaments of one strand are separated from the copper matrix by etching. Courtesy of CERN ©.

Superconducting cable The superconducting cables are made from several superconducting strands in parallel, twisted along the cable axis and pressed into a trapezoidal cross-section. The cable current of nearly 13 kA is distributed over the 28 or 36 strands (inner and outer layer cable). The strands are in resistive contact. This cable type is denoted as Rutherford-type cable.

The superconducting strands consist of several thousands of superconducting Nb-Ti filaments dispersed in a copper matrix, which provides mechanical stability and a parallel path for the current in case of a quench.

The cable is surrounded by three wraps of polyimide insulation tape providing the necessary electrical turn-to-turn insulation in case of a quench while being sufficiently porous to allow the liquid helium to percolate.

Figure 2.3 shows the photos of the strand and Rutherford-type cable used for the LHC MB.

Ground Insulation and quench heaters The outer layer of the coil is equipped with two sets of quench-heater strips. In case of a quench a capacitor is discharged over these resistive strips generating enough heat to quench the covered conductors.

The coil is covered with several polyimide layers as an insulation between the upper and lower pole, and to ground. Operating a string of magnets, the potential to ground of each coil is defined by the other magnets of the string. The collar, iron yoke, and helium-II-vessel are connected to ground.

In order to protect the coil from damage resulting from mechanical stress applied by the collars, metallic coil protection sheets are mounted in the outside of the coil.

The convection of liquid helium from the coil through the collars to the heat exchanger is hampered by the coil protection sheet in radial direction, and azimuthally around the beam pipe by the flaps of the ground insulation.

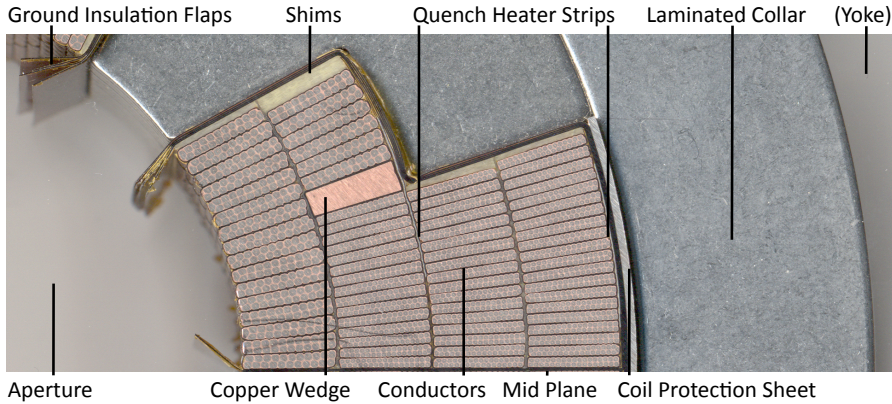


Figure 2.4: Photo of the coil cross-section of the LHC MQY featuring the aperture, the insulation to ground including flaps, the coil protection sheet, the conductors, and the collar. Courtesy of G. Kirby CERN TE MSC.

Figure 2.4 shows a photograph of the typical cross-section of a superconducting accelerator magnet featuring the aperture, insulation to ground including flaps, the coil protection sheet, the conductors, wedges, and the collar. (Notice that lacking a photograph of LHC MB with comparable quality the LHC MQY is shown).

Collars and iron yoke Consider the coil cross-section, the opposing currents of the two sides of the coil yield enormous electromagnetic forces pressing the coil apart. Therefore, the LORENTZ forces are carried by a stiff collar made from non-magnetic material. Furthermore, the collar provides prestress to the coil preventing conductor movements. In the case of the LHC MB the two coils are accommodated in a common collar made of stainless steel.

The iron yoke of a superconducting accelerator magnet serves two purposes:

- Enhancing the field in the aperture without increasing the excitation current or the number of superconducting cables. Hence, increasing the efficiency of the design.
- Reducing the magnetic field outside the magnet, *i.e.* the fringe field, in order to provide safe operating conditions for electronic equipment in close vicinity.

In the case of the LHC MB, the iron yoke accounts only for 3% of the magnetic induction compared to an iron free design [Evan 09, p. 75]. However, the iron yoke reduces the stray field outside the iron yoke to less than 50 mT [Russ 07, p. 391].

Both, collar and iron yoke, are stacked in order to reduce induced eddy current losses. In the case of the permeable iron this results in an anisotropy.

Helium-II vessel and heat exchanger The coil, the collar and the iron yoke are immersed in liquid helium II at 1.9 K. Helium II features an extremely low viscosity and percolates every cavity inside the coil windings and the stacked collar and iron yoke. The heat exchanger pipe provides a heat sink.

The helium-II vessel is made of the shrinking cylinder on the outside, the beam pipe on the inside and the end caps. The liquid helium is filled in to the vessel via the bus-bar pipes. The helium-II vessel is wrapped in super-insulation blocking heat radiation and placed in a vacuum cylinder preventing convective heating.

Magnet protection and external network In case of a quench the magnet needs to be protected from excessive voltages and temperatures. A quench needs to be detected as soon and reliably as possible and the current has to be extracted as fast as possible.

During operation the differential voltage over the two apertures is measured and compared to a given threshold voltage. When the voltage exceeds the threshold and the reading has been verified after a predefined delay, a quench is detected.

The LHC MB is operated in strings of 154 dipoles all connected in series. A current controlled power supply is setting the current in the string. In case of a quench, the power supply is switched off and by passed by a free-wheeling diode. A dump resistor is switched into the circuit in order to extract the current.

A bypass diode is mounted inside the cryostat of every magnet. After quench detection the quench heaters of the quenched magnet are fired. The resistive voltage switches the by-pass diode and the magnet current begins to commutate into the diode. Hence, the magnet disconnects from the rest of the string allowing for a faster current decay.

Bus bars The connection terminals of the dipoles are on one side of the magnet. For the series connection of the string of magnets the bus bar is placed within the cryostat on the outside of the iron yoke. The cryostat of the dipoles further more hosts small superconducting corrector magnets and their powering, as well as the current leads for the main quadrupoles.

2.1.2 Other Magnet Types and Design Features

Design features less pronounced or relevant for the LHC main dipoles are introduced by means of other magnet types. Due to the wide variety of applications and technical solutions, this list is in now way complete, nevertheless, will give the necessary overview.

Corrector magnets In order to compensate for field errors of the main bending and quadrupole magnets, and for the correction of particle offsets, corrector magnets are incorporated into the accelerator ring. The design of corrector magnets ranges from spool-pieces, small superconducting multipole magnets

wound from a single wire and placed on the beam pipe, to double aperture magnets of a few meters.

In the most basic design, the corrector is operated well below the critical surface, leaving enough margin to withstand probable disturbances [Evan 09, p. 76]. For the case of a quench, the magnets are provided with a parallel resistor taking over the current as soon as the quench has grown wide enough. Winding the coil with a single wire results in a significantly higher inductance.

Super ferric magnets The design of super ferric magnets is based on the same principles as for normal conducting magnets. The magnetic field is concentrated and formed by a ferromagnetic iron yoke in the center of the coil. Instead of water-cooled copper cables the coil is wound from superconducting cables. Owing to the high available current densities in superconductors and the domination of the field quality by the iron yoke, super-ferric magnets can be made with a small number of winding turns.

It is possible to use cable-in-conduit conductors; superconducting filaments inside a metal tube cooled by a constant flow of liquid helium. The superconducting coil is hosted in a cryostat mounted inside the iron yoke. With additional cooling, the magnet can withstand higher losses and be subjected to faster current ramps.

Block-coil and double pancake Alternatively to coils designed following a $\cos \theta$ -approximation, in the block-coil or double pancake design, the coil cross section consists of rectangular blocks arranged around the aperture.

Figure 2.5 shows a sketch of three non-accelerator type magnets: a toroidal coil, a solenoid, and an undulator. Notice that all three magnet types are based on completely different topologies and frames of reference. Hence, they require a different description and calculation method.

Solenoid Superconducting solenoids can be wound from a single strand (MRI) or a Rutherford-type cable (CMS).

In the first case, the coil features large number of windings and consequently a high inductance. Such systems may be subdivided to steer the field quality or for quench protection. All sub-coils are provided with a bypass diode or shunt resistor constituting a inductively coupled system. Winding the solenoid on a conductive central cylinder yields a coupled secondary coil providing resistance and heating during a current ramp or quench.

In the case of CMS, the cable used for the solenoid is surrounded by high-quality aluminum (many times the cross-sectional area of the cable) in order to provide mechanical stability as well as a parallel path in case of quench.

Superconducting Undulator Equipping an undulator with superconducting coils allows to operate with much higher current densities compared to copper

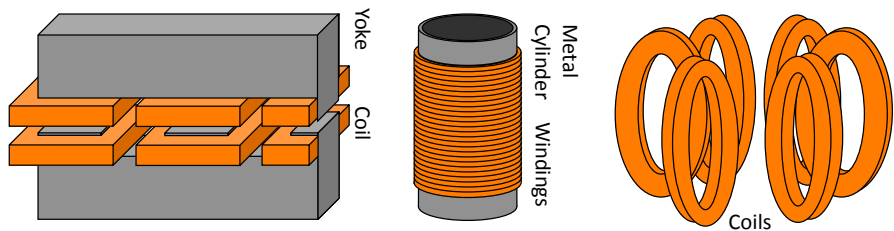


Figure 2.5: Sketch of other superconducting magnet configurations: part of a superconducting undulator featuring an iron yoke and two and a half poles, solenoidal coil wound on a metallic cylinder, and a toroidal coil configuration.

coils. Nevertheless, the poles of the iron yoke saturate completely and the field is mainly created by the coils [Hila 03].

The coils of the different poles may be connected in series and by-passed by diodes, or powered individually. In both cases, the current profile in all coils are coupled by the non-linear mutual inductance of the iron yoke.

Toroids In toroidal systems as for ATLAS or ITER, every coil is hosted in its own cryostat. The cable-in-conduits can be used for the windings allowing to cool efficiently. The coils are magnetically coupled.

2.2 Quench Process

The various physical effects occurring during a quench in a superconducting magnet are introduced following a typical quench in one of the LHC main bending magnets. Subsequently, we refer to other relevant phenomena.

Critical
Surface:
Sec. A.2

Quench cause A superconductor quenches when the working point defined by the local magnetic induction, the current density, and the temperature exceeds the critical surface. The temperature difference between the working temperature and the maximum temperature for the given field and current density is denoted temperature margin; the conductor quenches for zero margin.

Temperature
margin:
Sec. 7.1

A temperature increase in the magnet can be caused by conductor movements and the associated friction, induced eddy current losses in the superconducting cables, radiation and beam particles entering the coil, quench heaters and heat transfer from adjacent conductors. The current density in the superconducting cables consists of the current provided by the power supply and the current driven by the induced voltages. Both can result in a quench in case of an over-current. Figure 2.6 summarizes the different phenomena leading to a quench.

For accelerator magnets we can distinguish the following types of quench [Mess 96, p. 119]:

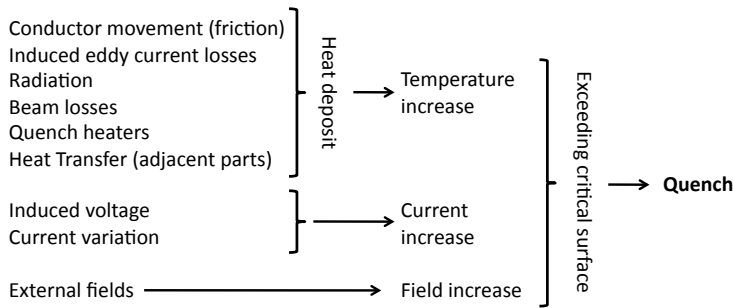


Figure 2.6: Different phenomena in superconducting magnets which may cause a quench.

- We talk of a *natural* quench, when the working point on the load line is moved across the critical surface by raising the excitation current and thus, synchronously, the magnetic flux density.
- Quenches can also be initiated due to local heating or beam losses in the accelerator. These *disturbance* quenches may happen with the working point well below the critical surface.
- Often coil windings move slightly under the influence of the electromagnetic forces and due to pressure changes during quenches. This may result in a successively higher field at subsequent quenches. The magnet thus shows a training characteristic and the quenches are consequently referred to as *training* quenches.

For the following explanations we consider a disturbance quench at a current level close to the nominal current of the magnet. The initial normal conducting zone extends only over some centimeters of a strand in the high-field region.

Current-sharing, current re-distribution In the superconducting state the resistivity of Nb-Ti is many orders of magnitude smaller than the resistivity of other commonly used conductors, *e.g.* copper or aluminum. In the normal conducting state the electrical conductivity of Nb-Ti is comparatively small. Figure 2.7 shows the resistivity of most materials commonly used in superconducting cables.

Electrical resistivity:
Sec. A.1.3
& A.2.6

During the transition from the superconducting to the normal conducting state the current commutates from the quenched filaments into the surrounding matrix material. The commutation is governed by the voltage-current-characteristic of the superconductor and OHM's law in the resistive matrix. This phenomenon is called current-sharing.

Current-sharing:
Sec. 7.5

The strands of the Rutherford-type cable are in resistive contact. With growing resistivity of the quenched strand, the current starts to by-pass the quench: The current flows over the cross-over and adjacent resistance to

Current re-distribution:
Sec. 7.8

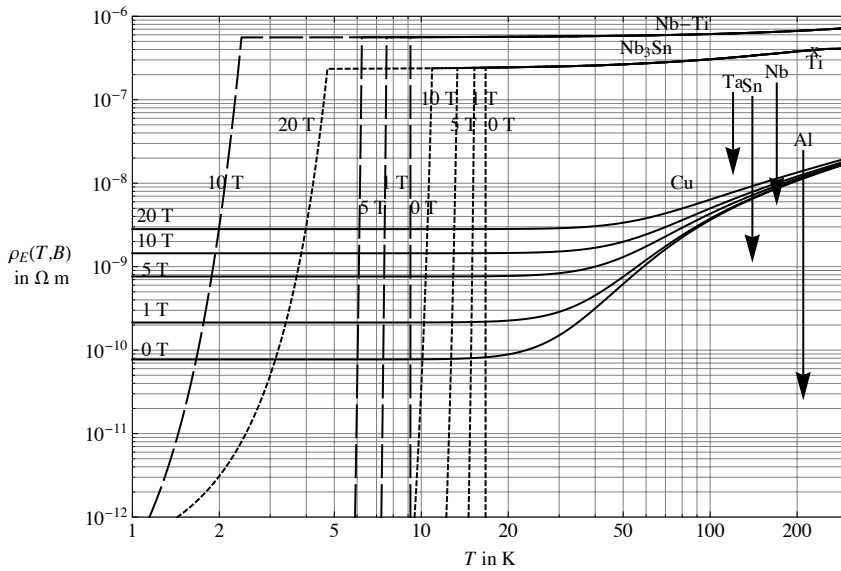


Figure 2.7: Electrical resistivity of the different materials used in superconducting cables. For the superconducting materials a design current density is assumed of $J_c(8.4 \text{ T}, 1.9 \text{ K}) = 2.6 \cdot 10^9 \text{ Am}^{-2}$ for Nb-Ti and $J_c(15 \text{ T}, 4.2 \text{ K}) = 1.4 \cdot 10^9 \text{ Am}^{-2}$ for Nb₃Sn. The resistivity of tantalum, niobium, tin and aluminum are displayed by means of an arrow pointing from the resistivity at room temperature to cryogenic temperatures. For titanium only a room temperature value could be given. See also material properties in Sec. A.1.3 and Sec. A.2.6

neighboring strands. This is denoted as current re-distribution and happens within some twist pitch lengths.

Ohmic heating, heat transfer, quench propagation, and quench recovery

The current flowing through the resistive part of the strand and cable causes ohmic heating. The temperature starts to rise. The temperature gradient causes a heat transfer along the strands, to the confined helium and over the insulation to adjacent conductors as well as to heat reservoirs outside the cable.

Properties
of liquid
helium:
Sec. A.3

Below the λ -point helium II features a very high heat conductivity, allowing to efficiently extract heat from the coil to the heat exchanger pipe. Furthermore, the heat capacity of liquid helium is many orders larger than of the materials used for the cable. Nevertheless, the heat transfer between the quenched strand and the percolating helium features phase transitions, altering the thermal contact on the surface [Gran 08]. Therefore, the influence of the helium strongly depends on the amount of heat and the time-span of its release.

With the heat transfer the quench propagates along the cable and to adjacent conductors. The propagation velocity and turn-to-turn propagation

delay depend on the temperature margin to quench as well as on the available cooling power and heat conductivity.

A superconductor recovers from a quench if the working point drops below the critical surface. This can happen, *e.g.* due to the reduction of the current density as a consequence of current-sharing/re-distribution or if the ohmic heating in the surrounding matrix/strands is smaller than the available cooling. Therefore, superconductors are provided with a maximum amount of parallel copper for stabilization without increasing the strand cross-section too much.

Quench load and MIITs Assuming adiabatic conditions disregarding any heat transfer, the temperature increase can be estimated based on the current profile and effective material properties. The integral over the profile of the current squared represents the quench load or MIITs. For the given electrical resistivity and heat capacity of the cable the quench load gives a conservative temperature estimate.

MIITs:
Sec. 7.2

Magnet protection With increasing temperature and quench propagation a resistive voltage builds up over the magnet. When the voltage passes the threshold of the quench detection system, the power supply is switched off and the current extraction is initiated by increasing the resistivity of the circuit.

Magnet
protection:
Sec. 7.9

Quench heater delay Upon quench detection, the quench-heater power-supplies discharge capacitors over the resistivity of the heater strips in the coil. The heat diffuses through several layers of insulation into the conductors increasing the temperature above the quench limit. The time between firing and quench in one of the covered conductors is denoted as the quench heater delay. The quench heater delay depends on the amount of energy released, the thermal properties of the contact between the heater strip and the coil, and the margin to quench in the covered conductors.

Internal voltages and iron saturation The resistance of the conductors quenched by the quench heaters increases the voltage beyond the forward threshold of the protection diode. The current of the string of magnets bypasses the quenched magnet over the diode. The magnet is isolated from the string and the terminal voltage is clamped to the diode forward voltage.

Voltages
during
quench:
Sec. 7.10

Consequently, the growing resistive voltage is matched by an inductive voltage driving down the current in the magnet. The resistive voltage is concentrated over the normal conducting parts of the coil. This voltage concentration can yield high electrical fields between adjacent turns and may results in a dielectric break-down of the insulation.

Parasitic capacitances in the coil, *i.e.* between the windings and from the windings to ground, influence the voltage distribution over the magnet. Directly after the occurrence of a resistive voltage, the voltage is concentrated

around the disturbance thus yielding higher electric fields and even small equilibration currents.

Differential
inductance:
Sec. 7.4

The distribution of the inductive voltage over the coil depends on the linked flux over the different turns and is not homogeneous. In addition, the magnetic induction in the magnet cross-section is subjected to saturation effects in the iron yoke and induced eddy currents in the coil. Therefore, any induced voltages or the differential inductance are in non-linear, diffusive and hysteretic dependence of the magnet current.

SC
hysteresis
losses: Sec.
7.7

Induced losses The Rutherford-type cables are subjected to three different types of losses: Superconductor hysteresis losses in the filaments, inter-filament coupling current (IFCC) losses in the strands, and inter-strand coupling current (ISCC) losses in the twisted cable. The hysteresis losses result from the persistent screening currents typically screening the inner of superconductors. The coupling currents are driven by the voltages induced over superconducting loops closing over the resistive matrix of the strand or the contact resistance between adjacent strands. The induced eddy current losses increase quadratically with the time derivative of the magnetic induction.

ISCC and
IFCC: Sec.
7.6

Furthermore, losses are induced in the copper wedges between coil blocks and in the laminated collar. The iron yoke shows small hysteresis losses.

Quench back GREEN distinguishes two different kinds of quench back in superconducting magnets [Gree 84a]: thermal quench back and magnetic quench back. In the first case, normal conducting regions are induced by heat transfer from other parts of the magnet, *e.g.* from an aluminum cylinder in the center of a solenoid or copper wedges in a $\cos\theta$ magnet. In the second case, normal regions are caused by induced eddy current losses in the superconductors due to changing magnetic fields.

Under normal operating conditions the amount of induced losses in a superconducting magnet has to be minimized and removed by cooling. However, in the case of quench the magnetic quench back aids the built-up of resistivity and fast current decrease. In the LHC MB wide parts of coil-cross section are quenched by magnetic quench back due to the fast current decrease.

Quench of adjacent magnets, helium heat wave In the case of a string of magnets, the temperature increase in one magnets can compromise the cooling of the adjacent magnets. Furthermore, neighboring magnets can be quenched by a front of warm helium traveling along the bus bars.

The following phenomena occur in other magnet configuration:

Convective cooling The heat stemming from induced losses or a quench can be removed by heat conduction or the convection of liquid helium. In the later case, the magnet design needs to be permeable for the helium flow or have tubes where the helium can be pumped through. Superferric magnets

as well as the toroids for the ITER tokamak are cooled by a forced helium flow.

Inductive coupling Consider an inductively coupled systems consisting of two coils connected in series. Each of the coils is bypassed with a diode. After a quench in one of the coils occurs, the resistive voltage growing due to quench propagation and temperature increase, switches the diode and disconnects the quenched coil from the rest of the circuit.

With the decreasing current in the quenched coil, a rising current is induced over the other coil. When the current exceeds the critical current limit in the second coil, the coil quenches instantaneously. Now the current decrease of the second coil drives up the current in the first coil. This concept is used for the protection of superconducting solenoids where a great number of coils is coupled causing multiple current commutations, or of superconducting undulators where the different coils are additionally coupled by non-linear iron material.

In solenoids a central aluminium cylinder can be considered a coupled secondary, providing additional resistance and heating in case of a quench.

Mechanical stress and coil deformations The fast temperature increase and the consequent thermal expansion of the different coil materials exposes the conductors to mechanical stress. This can yield to reduction of the critical current density (degradation) or even conductor movement. Both may influence the development of the quench and result in irreversible damage to the magnet.

2.3 Relevant Effects

Accelerator type magnets can be distinguished by means of the following five categories: Length of the magnet, margin to quench, magnetic induction level, ramp-rate, and powering.

Length of the magnet: A magnet is considered short if the magnetic field over the coil is dominated by 3D effects such as longitudinal iron saturation or peak field increase in the coil end. Furthermore, a magnet is considered short if quench propagation contributes significantly to the resistance built-up compared to dump resistors or quench heaters.

In the case of long magnets the problem can be merely treated in a 2D approach.

Margin to quench: The margin to quench is considered small if a quench of one strand in a cable triggers a quench in all parallel strands. The quench is immediate.

For magnets with a large margin, the effects of current-sharing, current re-distribution and quench recovery have to be taken into account. This

allows to study the stability of the cables/magnet against disturbances such as beam losses. A model of the cooling of the conductors is crucial.

Level of magnetic induction: The magnetic field level is high if iron saturation effects have to be considered. This requires to apply the concept of the differential inductance.

Ramp-rate: In magnets built for high ramp-rates design efforts are made in order to reduce induced losses in the cables and to remove the additional heat. Due to high induced voltages quench detection becomes more difficult.

In magnets designed for slow ramping, quench back is more pronounced.

Powering: We distinguish between single powering and magnet systems. The first kind can be protected individually. For the second kind, protection and operation has to extended to coupled coils.

In the following we develop a model for the description of long magnets operating at high magnetic induction and small margin to quench. The magnets are designed for a small ramp-rate and are individually powered. The model can be extended to study effects in fast ramping magnets as well as to analyze quenches in strings of magnets.

For the simulation of magnets requiring other features such as undulators or solenoids, more specialized codes, *e.g.* as by AIRD or BETTONI have to be used.

3 Numerical Modeling

"Consider a spherical cow... ."

JOHN HARTE
(1988)

A quench is the resistive transition of a superconductor that occurs if the current density, the magnetic field in the cable, or the cable temperature exceeds a critical value. From this description it is evident that quench simulation requires a multi-physics modeling approach. Figure 3.1 shows the different physical models interacting during the quench simulation:

- a)** A geometrical model describing the magnet and coil and providing distances and the size of all elements.
- b)** A model of the superconducting state and the transition to the normal conducting state.
- c)** Magnetic field computation consisting of analytical field computation of line currents by means of the Biot-Savart law and a BEM-FEM model for the numerical field computation of the magnetic induction in non-linear iron parts.
- d)** Analytical models for the cable magnetization, *i.e.* induced cable eddy current losses like inter-strand coupling currents and inter-filament coupling currents.
- e)** An electrical network model describing the external electrical circuit by means of lumped elements and determining the magnet current. Protection measures, *e.g.* bypass diodes and energy extraction resistors, are included in this model.
- f)** A thermal model for the calculation of the temperature increase and quench propagation. The model includes the quench protection heaters.

The solution of the individual sub-models is combined in the quench algorithm. Depending on the computational effort and the grade of coupling, the models are solved in two nested computation loops sharing their parameters and results. The strong variation of model parameters is resolved by an adaptive time-integration method.

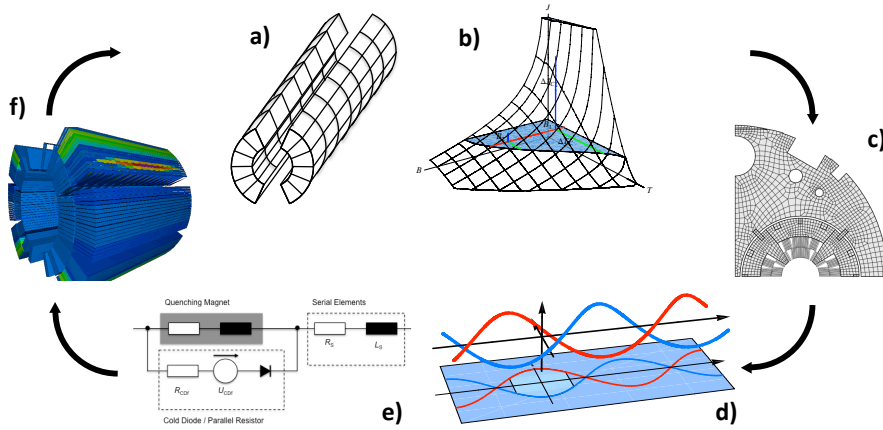


Figure 3.1: Different models interacting in a quench simulation. Clockwise starting at 11h00: a) geometrical model and discretization of the coil, b) superconductor model and quench decision, c) magnetic field computation with analytical field calculation and BEM-FEM model of the nonlinear iron yoke, d) induced losses by means of inter-filament and inter-strand coupling currents, e) electrical network of powering and protection elements, f) thermal network model of heat conduction and quench heaters.

3.1 Coil Discretization and Numbering Scheme

A superconducting magnet basically consists of the coil, the iron yoke, and the electrical circuit for powering and protection. While the electrical circuit can be described by means of lumped elements, the description of thermal and electromagnetic processes in the coil require a discretization.

We assume that a magnet is long, compared to the diameter of the magnet aperture (generally true for dipole- and quadrupole magnets in accelerators) and thus the numerical field computation can be carried out in two dimensions (2D). Coil end effects are neglected. Where necessary, global quantities, such as the inductance, are matched to measurements by geometric scaling factors.

Thermal computations are carried out in three dimensions (3D). The coil cross-section is longitudinally extruded to the average winding length ℓ_w . The connection of the conductors in the coil ends is seamless and modifications to the local properties are not considered. We denote the approach as 2+1D in comparison to a full 3D model also including the coil end region. The approach yields the following discretization and numbering scheme:

- Transversally, the coil can be sub-divided by means of the different conductors introducing the numbering $i = 1, \dots, N_c$.
- Longitudinally, every winding length ℓ_w is discretized in N_z elements of length $\ell_z = \ell_w / N_z$ with the numbering scheme $j = 1, \dots, N_z$.

The coil thus consists in total of $N_c N_z = N_e$ elements; identified by the tuples

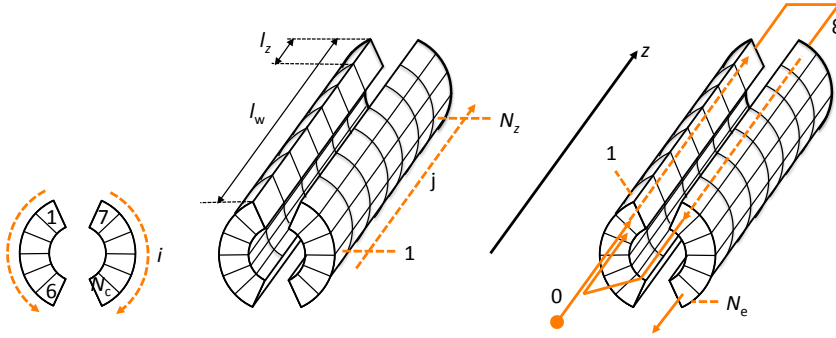


Figure 3.2: Discretization and numbering of a coil: (left) Transversal or 2D discretization by means of the conductors i . (center) Longitudinal or 2+1D discretization j over N_z cuts. (right) Topological numbering ξ along the winding of the coil. The magnet terminals are denoted $\xi = 0$ and $\xi = N_e$ (Number of elements).

ij . The numbering scheme is illustrated by means of a schematic coil in Fig. 3.2 (left) and (center).

Topologically one index is enough to identify a specific element in the coil. In order to represent the winding scheme of the coil, *i.e.* the connection of the different conductors in the coil ends, a complementary numbering scheme is introduced. The greek letter ξ follows the winding through the coil from one terminal to the other, $\xi = 1, \dots, N_e$. The mapping Ξ links the two numbering schemes:

$$\Xi : \xi \rightarrow ij \quad (3.1)$$

The numbering scheme Ξ defines a sense of orientation for the elements. If ξ increases with the z -coordinate it is considered positive:

$$\delta_{\Xi}^i = \begin{cases} 1 & \xi \text{ increases with } z \\ -1 & \xi \text{ decreases with } z \end{cases} \quad (3.2)$$

The magnet terminals are assigned to $\xi = 0$ and N_e . The current I enters the magnet at $\xi = 0$ in z -direction. Figure 3.2 (right) shows the topological numbering scheme for a schematic coil.

In case of Ribbon-type conductors the magnet is discretized on the strand level. The grouping of the strands in cables is thus ignored.

Notice that the numbering schemes ij and ξ are used through out this chapter.

Ribbon-type conductor: Sec. B.1.3

3.2 Superconductor Model

For the model of twisted Rutherford-type cables it is assumed that the current I is evenly distributed over all strands of the cable. Ribbon-type cables are modeled as cables consisting of one strand only.

Rutherford-type cables: Sec. 7.8

Electrical
resistivity:
Sec. A.1.3
and A.2.6

A strand consists of superconducting filaments embedded in a normal conducting matrix. Comparing the electrical resistivity of superconductors, *e.g.* Nb-Ti and Nb₃Sn, and common matrix materials, *e.g.* copper or aluminum, in Fig. 2.7, it can be concluded: In the superconducting state, the current is carried only by the superconducting part of the strand. In the quenched state, the current is only carried by the normal conducting part of the strand. During the transition from the superconducting to the normal conducting state, the current is shared between both fractions.

Quench
margins:
Sec. 7.1.1

Resistive transition An element of the coil is considered to be in the normal conducting state when the current density margin (Sec. 7.1.1) equals zero:

$$\Delta J_c^{ij} = \begin{cases} J_c(B_{\text{peak}}^i, T^{ij}) - J_{\text{SCm}}^i & J_{\text{SCm}}^i < J_c(B_{\text{peak}}^i, T^{ij}) \\ 0 & \text{else} \end{cases}, \quad (3.3)$$

J_c parameterization:
Sec. A.2.4

where J_c is the critical surface parameterization, B_{peak}^i the peak field on the conductor i and T^{ij} the temperature of the element ij . Here, J_{SCm}^i denotes the current density in the superconducting filaments, if the applied current I is only distributed over the superconducting fraction of the cable $A_{\text{cab,SC}}^i$ (defined in Sec. B.1.3):

$$J_{\text{SCm}}^i = \frac{I}{A_{\text{cab,SC}}^i}. \quad (3.4)$$

For the visualization of the quench process in time and over the coil cross-section, the current density and the temperature margin to quench can be used.

Non-linear
behavior of
SC: 7.5

Current-sharing When the critical current density is exceeded, *i.e.* the element is in the quenched state, the voltage across the superconductor starts to rise rapidly. With the increasing voltage, part of the current through the strand is drawn into the normal conducting material in parallel. The ohmic losses and the consequent heating of the strand further decrease the critical current density until the entire current is carried by the normal conducting matrix. The commutation process is determined by the strongly non-linear voltage rise over the superconductor.

Following STEKLY [Stek 65], a linear approach is used to model current-sharing: Exceeding the critical current density the excess current commutates from the superconducting fraction of the strand into the normal conducting matrix. The excess current is given by

Current
sharing:
Sec. 7.5.1

$$I_{\text{NC}}^{ij} = \begin{cases} 0 & \Delta J_c^{ij} > 0 \\ I_{\text{M}} - I_c^{ij} & (\Delta J_c^{ij} = 0) \text{ \& } (I_c^{ij} > 0), \\ I_{\text{M}} & \text{else} \end{cases}, \quad (3.5)$$

where I_{M} denotes the current through the conductor and I_c^{ij} the critical current in the element for a the local magnetic induction and temperature:

$$I_c^{ij} = J_c(B_{\text{peak}}^i, T^{ij}) A_{\text{cab,SC}}^i. \quad (3.6)$$

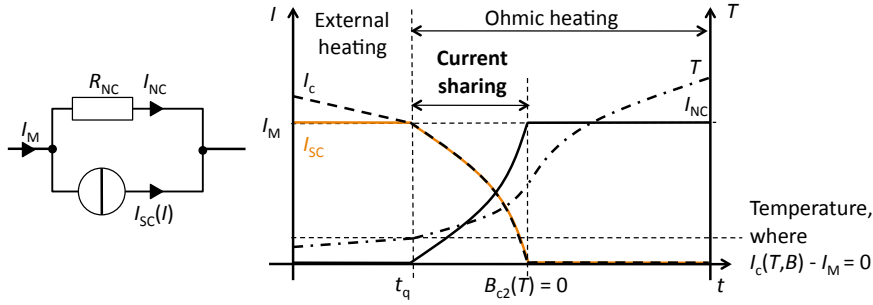


Figure 3.3: Current sharing: The transition from superconducting to normal conducting state can be subdivided into three phases. During the first phase, the conductor current is carried by the superconductor ($I_{SC} = I_M$). The temperature in the conductor increases only due to external heating or induced losses. The critical current in the conductor decreases due to the increase of temperature. The second phase begins, when the critical current drops below the conductor current and the excess current spills over into the normal conducting part ($I_{SC} + I_{NC} = I_M$). The conductor is considered in the quenched state. Ohmic heating in the normal conductor amplifies the temperature increase. The last phase is reached, when the critical current has decreased to zero and the entire current is carried by the normal conductor ($I_{NC} = I_M$).

Only the current I_{NC}^{ij} flows through the resistance of the element ij and therefore causes ohmic heating. The conductor current I_M flows entirely in the normal conducting matrix as soon as the critical current is zero, *i.e.* the critical field is zero. Figure 3.3 shows a schematic of the current transition including current sharing.

3.3 Magnetic Field Model

Assuming that the magnet is long compared to the diameter of the magnet cross-section, which is generally true for dipole- and quadrupole magnets in accelerators, a 2D approach is used for the magnetic field calculation.

The magnetic field problem can be divided in 3 sub-domains, *i.e.* the superconducting coil, magnetic materials as for the iron yoke, and empty space, *e.g.* the beam pipe. The coil consists of superconducting cables which are subjected to eddy currents and magnetization effects.

The quench model relies on the peak and average magnetic induction as well as on the average magnetic vector potential on all conductors. Assuming that induced eddy currents are small compared to the transport currents their contribution to the magnetic induction is not taken into account. Therefore, the field computation consists of the following two steps:

1. Calculation of the field created by the currents in the coils.
2. Computation of the secondary field of the magnetic materials as repercussion on the coil field.

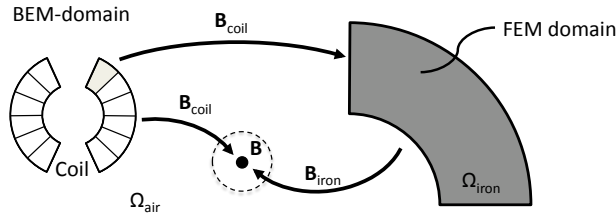


Figure 3.4: Magnetic field computation: The problem is subdivided into the coil, an iron and an air domain. The magnetic induction \mathbf{B} is composed from the field of the coil and the field of the iron domain.

The solution of both steps are iterated due to the field-dependent permeability. Figure 3.4 shows the subdivision of the magnet and the field calculation at an arbitrary position relying on coil and iron field. The total field is used for the computation of the cable eddy currents and magnetization, and the consequent losses.

Coil fields The magnetic field of the superconducting coils is calculated from the field of ideal line currents. The cross-section of any conductor is evenly subdivided into N_{Dis} patches, shown in Fig. 3.5 (left). Outside the cable, more precisely outside any strand, the magnetic field is given by the sum over the fields of the line currents placed in the center of the patches, \mathbf{r}_k^i . If evaluating the field inside a strand, *e.g.* for the calculation of peak fields on a conductor, the respective line current is replaced by a homogeneous, cylindrical current distribution and singular expressions are avoided, see Fig. 3.5 (right).

Rutherford-type cable:
Sec. 7.8

The transposition of the strands along the axis of Rutherford-type cables is not taken into account.

Magnetic Materials The influence of magnetic materials on the magnetic field in the coils is calculated by means of the BEM-FEM-coupling method.

According to this method only domains containing magnetic materials are meshed and described by means of finite elements (FEM). Empty space and more relevant the coils are not modeled in finite elements but considered by expressing the magnetic field on the boundary to the iron/FEM domain. The field repercussion of the magnetic materials on the coil fields is calculated using a boundary element approach (BEM). For field-dependent magnetic permeability (iron saturation) the coupling between the two domains is solved iteratively.

The BEM-FEM approach reduces the necessary number of finite elements significantly. Furthermore, coil fields can be modeled more precisely and independently of the used mesh.

Differences of the magnetic permeability, as shown in Sec. A.1.6.1 between

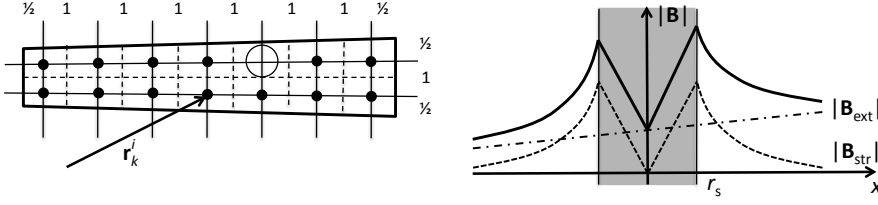


Figure 3.5: Calculation of the field of a conductor. (left) Discretization of the conductor i . The index k denotes the patch number. (right) Peak field calculation. The field inside a strand (shaded) is given by the field of all line currents, \mathbf{B}_{ext} , plus the field of the homogeneous cylindrical current distribution inside the strand, \mathbf{B}_{str} .

various operation conditions and manufacturers, are negligible for the calculation of quench relevant quantities, *i.e.* for coil fields and the inductance.

Total magnetic induction - Superposition The magnetic induction as well as the magnetic vector potential at any of the positions \mathbf{r}_k^i is given by the sum of all field sources. In the present work only the coil field and the iron repercussion are considered, thus

$$\mathbf{B}_k^i = \sum_{\text{model}} \mathbf{B}_{\text{model}}(\mathbf{r}_k^i) = \mathbf{B}_{\text{coil}}(\mathbf{r}_k^i) + \mathbf{B}_{\text{iron}}(\mathbf{r}_k^i) \quad (3.7)$$

$$A_{z,k}^i = \sum_{\text{model}} \mathbf{A}_{\text{model}}(\mathbf{r}_k^i) = A_{z,\text{coil}}(\mathbf{r}_k^i) + A_{z,\text{iron}}(\mathbf{r}_k^i) \quad (3.8)$$

Discrete field quantities For the present work two different cable types are considered: Ribbon-type and Rutherford-type cables. The strands of a Rutherford-type cable are twisted along the cable axis, *i.e.*, every strand of the cable takes every position within the cable cross-section over the twist-pitch length. With a twist-pitch much shorter than the magnet length, the magnetic field varies only over the cross section but not along the conductor. Therefore each strand is exposed to the full variation of the field. For the calculation of material properties the average field is used as discussed in Sec. 7.8.

Cable
types: Sec.
B.1.3

For the calculation of field dependent material properties, *e.g.* magneto-resistivity and specific heat of superconductors, the average modulus of the field on the conductor is required. The quench decision depends on the peak

field on the conductor:

$$\mathbf{B}_{\text{av}}^i = \frac{\sum_{k=1}^{N_{\text{Dis}}^i} \mathbf{B}_k^i}{N_{\text{Dis}}^i}, \quad (3.9)$$

$$B_{\text{av}}^i = \frac{\sum_{k=1}^{N_{\text{Dis}}^i} |\mathbf{B}_k^i|}{N_{\text{Dis}}^i}, \quad (3.10)$$

$$B_{\text{peak}}^i = \max\{|\mathbf{B}_k^i|\}_{k=1, \dots, N_{\text{Dis}}^i}, \quad (3.11)$$

The average magnetic vector potential in conductor i is used for the calculation of linked fluxes and induced voltages,

$$A_{z,\text{av}}^i = \frac{\sum_{k=1}^{N_{\text{Dis}}^i} A_{z,k}^i}{N_{\text{Dis}}^i}. \quad (3.12)$$

We can assign a local frame to every conductor cross-section by defining a vector parallel, \mathbf{e}_{\parallel} , and orthogonal, \mathbf{e}_{\perp} , to the broad face. For keystoneed cables the parallel vector is approximated by the cable center as indicated in Fig. 7.20. We define the average magnetic induction parallel and orthogonal to the broad face as:

$$B_{\parallel}^i = \mathbf{B}_{\text{av}}^i \cdot \mathbf{e}_{\parallel}, \quad B_{\perp}^i = \mathbf{B}_{\text{av}}^i \cdot \mathbf{e}_{\perp}. \quad (3.13)$$

Magnetic
length

Although the variation of the magnetic field in the coil ends is not directly taken into account for the computation of losses or material properties, it has to be considered for the computation of induced voltages and the differential inductance. In Sec. B.1.6, three different coil lengths are introduced, the winding length ℓ_{w} , the magnetic length ℓ_{mag} and the inductance length ℓ_{ind} . Comparing the inductance per length as well as the inductance of a magnet measured or calculated in 3D gives the inductance length. For the calculation of induced voltages over elements the factor

$$k_{\text{mag}} = \frac{\ell_{\text{ind}}}{\ell_{\text{w}}} \quad (3.14)$$

is used to scale the longitudinal extensions.

3.4 Induced Losses

Cable eddy
currents:
Sec. 7.6

Eddy-current losses in the cable are calculated from the local field sweep. We distinguish inter-filament (IFCC) and inter-strand coupling currents (ISCC). Interfilament coupling currents are induced in the twisted superconductor-copper matrix of a strand. Inter-strand coupling currents are induced in a Rutherford-type cable in loops of superconducting strands and contact resistances between strands. The two phenomena are summarized as cable magnetization, see Sec. 7.6.

Hysteresis
losses: Sec
7.7

Superconductor magnetization hysteresis losses are disregarded as discussed in Sec. 7.7. Eddy currents in copper wedges between coil blocks and in coil collars are not taken into account.

Analytical magnetization losses Consider a Rutherford-type cable consisting of N_s strands. The loss density for a time-variant magnetic induction are given by Eq. (7.63). Since every strand is fully exposed, the average loss per strand can be calculated from the average magnetic induction over the cable cross-section. The inter-filament coupling losses dissipated in the cable are then given by

$$P_{\text{IFCC}}^i = V_{\text{e, str}}^i p_{\text{IFCC, av}}^i, \quad (3.15)$$

where $V_{\text{e, str}}^i$ denotes the volume occupied by the strands in any element of the conductor i .

The inter-strand coupling loss density calculated from the average magnetic induction as given in Eq. (7.68). We get:

$$P_{\text{ISCC}}^i = V_{\text{e, str}}^i p_{\text{ISCC}}^i \quad (3.16)$$

In case of a quench the ohmic heating over the resistive zone, exceeds the induced losses. Furthermore, the loss models are based on the assumption of superconducting filaments and strands. Therefore, induced losses are only taken into account while an element is in the superconducting state. The total losses in one element are calculated from the sum of different loss models

$$P_{0, \text{losses}}^{ij} = \begin{cases} P_{\text{IFCC}}^i + P_{\text{ISCC}}^i & \Delta J_c^{ij} > 0 \\ 0 & \text{else} \end{cases} \quad (3.17)$$

Time dependence The analytic loss models are lacking the diffusive process, *i.e.* the losses are an immediate response to any field change. In order to avoid an over estimation, the coupling-current time-constants τ_{losses} is a user supplied parameter. The total losses are given to

$$P_{\text{losses}}^{ij} = P_{0, \text{losses}}^{ij} \left(1 - \exp \left(-\frac{t - t_{\text{fc}}}{\tau_{\text{losses}}} \right) \right), \quad (3.18)$$

where t_{fc} denotes the instance of the last field change.

Notice, for the quench algorithm it can be required to split the time interval τ_{losses} over several calculation steps. The steady continuation of exponential decays is shown in Sec. 7.5.2.

3.5 Electrical Network

The magnet is connected to an external network represented by an generic network model as shown in Fig. 3.6. It consists of a power supply, an energy extraction system with switch and dump resistor, and a serial resistance and inductance. The power supply is bridged by a free-wheeling diode in order to conduct the current after it is switched off. The serial elements can represent resistive current leads and the inductance of magnets connected in series to the magnet. The magnet itself is represented by its electrical resistance and

the differential inductance. It can be bridged with a parallel resistor or a by-pass diode.

Magnet
protection:
Sec. 7.9

This generic electrical network allows to simulate quenching magnets in single operation, *e.g.* on a test bench, or in a string, *e.g.* as for the main dipoles in the LHC tunnel. Both configurations are explained in Sec. 7.10.1 and in Sec. 7.9 in respect of quench protection. The by-passing of the quenching magnet is explained in Sec. 7.9.3. The generic approach allows only to simulate one current in the magnetic system. Therefore it does not permit to simulate quench protection by magnet subdivision or a coupled secondary winding (see 7.9.4).

Sequence
of events:
Sec. 7.9.6

Quench detection and validation A quench is detected as soon as the resistive voltage over the magnet U_{res} exceeds the detection threshold voltage U_{det} . The quench is validated, if the resistive voltage remains above the threshold level after a discrimination time Δt_{Dis} . Quench protection measures are triggered after quench validation, $t = t_{\text{val}}$.

The numerical simulation automatically distinguishes the induced and resistive voltage over the magnet. Therefore, compensation methods as described in Sec. 7.9.1 are not required. Nevertheless, it is possible to monitor and use any voltage within the magnet windings for quench detection.

Current change The generic electrical network model can be described by means of three currents: the current through the quenching magnet I_{M} , the current through the by-pass diode I_{D} and the current in the main circuit I_{E} . The current through the power-supply commutates instantaneously into the free-wheeling diode after switch-off and therefore does not require the definition of a fourth independent current. The three currents are related by

$$I_{\text{E}} = I_{\text{M}} + I_{\text{D}}. \quad (3.19)$$

The underlying mechanism of current decrease in the three branches, changes with the switching of the two diodes. While the power supply is connected to the network, the current function $I_{\text{PS}}(t)$ is imposed, *i.e.* $I_{\text{PS}} = I_{\text{M}} = I_{\text{E}}$. Quenching of the magnet or switching of the dump resistor show no effect. The current change is given by,

$$\frac{dI_{\text{E}}}{dt} = \frac{dI_{\text{M}}}{dt} = \frac{dI_{\text{PS}}}{dt}, \quad \frac{dI_{\text{D}}}{dt} = 0. \quad (3.20)$$

After the power supply is disconnected, the current decrease is defined by the main circuit ($I_{\text{E}} = I_{\text{M}}$) and yields

$$\frac{dI_{\text{E}}}{dt} = \frac{dI_{\text{M}}}{dt} = -\frac{(R_{\text{Q}} + R_{\text{s}})I_{\text{M}} + U_{\text{DR}} + U_{\text{fDf}}}{L_{\text{d}} + L_{\text{s}}}, \quad \frac{dI_{\text{D}}}{dt} = 0. \quad (3.21)$$

When the terminal voltage U_{Terminal} reaches the threshold voltage of the by-pass diode, the magnet current starts to commutate into the parallel path.

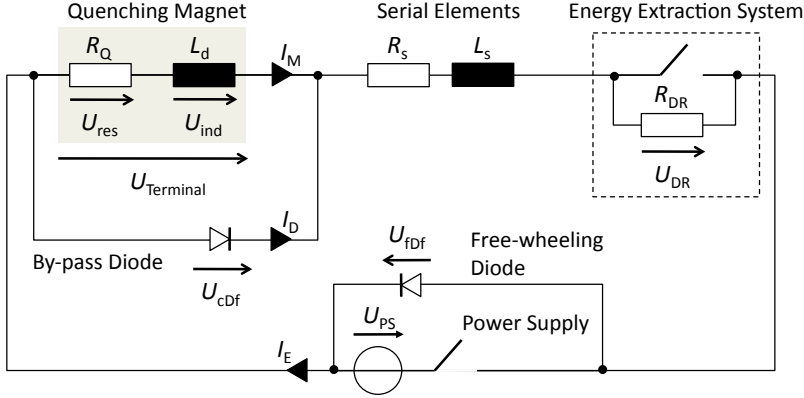


Figure 3.6: Generic electrical network model: Quenching magnet, energy extraction system with dump resistor and switch, power-supply with free-wheeling diode, and serial elements. The magnet is represented by the resistivity of the quenched conductors and its differential inductance. It can be bridged with a parallel resistor or a diode.

The current decrease in the main circuit thus depends only on the serial inductance.

$$\frac{dI_E}{dt} = -\frac{U_{fDf} + U_{cDf} + U_{DR} + R_s I_E}{L_s}, \quad (3.22)$$

$$\frac{dI_M}{dt} = -\frac{R_Q I_M - U_{cDf}}{L_d}, \quad (3.23)$$

$$\frac{dI_D}{dt} = -\frac{dI_M}{dt}. \quad (3.24)$$

If no serial inductance is present, the current in the main loop I_E drops to zero instantaneously.

For a string of magnets, where the total inductance is orders of magnitude larger than the inductance of the quenching magnet, protected by means of quench heaters, the main current I_E can be considered as constant (see Sec. 7.10.1).

3.5.1 Lumped Network Elements

Power supply In the absence of a quench, the magnet current is imposed by the power supply. The current ramping $I_{PS}(t)$ is determined by the magnet operating conditions. The voltage over the power supply is controlled such that the current change follows the specifications. This compensates for the non-linear inductance and the resistive components in the circuit, *i.e.* resistive joints or a quenching magnet.

After quench validation, the power supply switch-off is delayed by Δt_{QT} . The current commutates instantaneously into the free-wheeling diode.

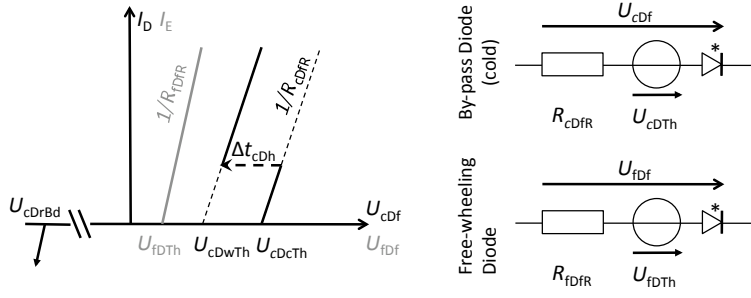


Figure 3.7: (left) Current-voltage characteristic of the cold and warm diode. (right) Diode model with lumped electrical elements.

Diodes The current flowing through a semiconductor diode is an exponential function of the applied voltage [Elsc 92, p. 46]. The non-linear voltage current characteristic can be simplified assuming zero conductance for an applied voltage smaller than the diode threshold voltage and a differential resistance for voltages above the threshold [Elsc 92, p. 86]. This linearization can be represented by means of three lumped electrical network elements: A voltage source providing the constant threshold voltage, the differential resistance limiting the current for voltages above the threshold voltage and an ideal diode. The ideal diode switches on for a voltage greater zero and switches off when the current through the diode equals zero. Any current in reverse direction is thus blocked. Note that in off-state the constant voltage drops over the ideal diode.

Figure 3.7 (left) shows the voltage current characteristic for the two different diodes used in the model. The free-wheeling diode is described by the forward threshold voltage U_{fDTh} and its differential forward resistance $R_{fDfR} = dU/dI$.

Isolating
the
magnet:
Sec. 7.9.3

The diode parallel to the magnet can be mounted in the magnet cryostat and is then denoted cold diode. The threshold voltage of a cold diode is significantly higher (around 6 – 8 V compared to ≈ 0.7 V) due to the cryogenic temperatures. After switching, the dissipated ohmic losses increase the junction temperature and the forward voltage threshold drops to some volts (see *e.g.* [Krai 97, pp. 136]). Therefore, the cold diode is modeled by the forward threshold voltage U_{cDcTh} in cold state, its differential forward resistance R_{cDfR} , the forward threshold voltage U_{cDwTh} in warm state and the time it takes to heat up the junction Δt_{cDh} . If the parallel diode is mounted outside the cryostat under warm operating conditions, the parameters have to be chosen as above.

Figure 3.7 (right) shows the lumped electrical element model of the free-wheeling and by-pass diode. The ideal diode is marked with an asterisk. The forward voltage is denoted by U_{wDf} and U_{cDf} , respectively.

With the simplified diode model, the terminal voltage of a magnet in a

string as well as in single operation can be reproduced. Setting the forward threshold voltage in the model to zero, the diode can be used to simulate a parallel resistor.

Energy extraction system In order to extract energy from the magnetic system and to reduce the time constant of the current decay, a dump resistor can be switched in. The current commutation from the switch into the resistor R_{DR} is assumed to be instantaneous. Current flows through the resistor after a time interval Δt_{DR} after quench validation.

Dump
resistor:
Sec. 7.9.2

3.5.2 Magnet Representation and Introspection

In respect to the external electrical network the magnet is defined by the lumped elements differential inductance L_{d} and the resistivity of the quenched windings R_{Q} . Internally, the resistance and the induced voltage is further assigned to the individual elements. This allows for the computation of turn-to-turn voltages as well as peak electrical fields.

Element Resistance The electrical resistance R_{E}^{ij} of an element depends on the effective resistivity, the element cross-section and the element length ℓ_z . The superconducting filaments are in parallel to the normal conducting matrix material. In the superconducting state, the electrical resistance of the element can be considered to be zero. After a quench, the electrical resistivity of the superconducting filaments shows to be orders of magnitude greater than of the matrix material (compare Fig. 2.7). Therefore, the resistance is determined only by the matrix material and the normal conducting cross-section area $A_{\text{cab,NC}}^i$. Different materials, used for stabilizing and coating superconducting strand, are in parallel along the strand.

Strand
parts: Sec.
B.1.3

The effective parallel electrical resistivity is defined in Sec. B.2.3. In general, the electrical resistivity depends on the applied magnetic induction, temperature and purity of the material. The element resistance is thus given by

Electrical
resistivity:
Sec. A.1.3

$$R_{\text{E}}^{ij} = \frac{\ell_z}{A_{\text{cab,NC}}^i} \rho_{\text{E}}^{\text{eff}}(T^{ij}, B_{\text{av}}^i, RRR^i) \begin{cases} 0 & \Delta J_c^{ij} > 0 \\ 1 & \text{else} \end{cases}, \quad (3.25)$$

where RRR^i is the residual resistivity ratio of the conductor as defined in Sec. A.1.3.

Resistive Voltages The resistive voltage over an element U_{res}^{ij} is given by the local resistance and the current in the normal conducting fraction of the conductor I_{NC}^{ij} . In the present model the current in the superconducting filaments does not yield a voltage drop over the element. The distribution of the current over both parts is determined by means of current-sharing, see Sec. 3.2. The voltage drop over the element ij reads:

Current-
sharing:
Sec. 7.5.1

$$U_{\text{res}}^{ij} = R_{\text{E}}^{ij} I_{\text{NC}}^{ij}. \quad (3.26)$$

Summing over all elements yields the total resistive voltage of the magnet used for quench detection,

$$U_{\text{res}} = \sum_{\xi=1}^{N_e} U_{\text{res}}^{\xi}. \quad (3.27)$$

Consequently, the total voltage U_{res} differs from the voltage $I \sum_{\xi=1}^{N_e} R_{\text{E}}^{\xi}$, which ignores current-sharing.

Dissipated power The current flowing through the normal conducting fraction of the conductor causes ohmic losses and thus heating. The power dissipated in each element is calculated from

$$P_{\text{ohm}}^{ij} = U_{\text{res}}^{ij} I_{\text{NC}}^{ij} = R_{\text{E}}^{ij} \left(I_{\text{NC}}^{ij} \right)^2 \quad (3.28)$$

Induced voltages: The induced voltage over an element is calculated from the line integral of the magnetic vector potential. As shown in Sec. 7.4.3, in a bulk conductor the vector potential can be split into an average part yielding the induced voltage and a differential part causing eddy currents. In case of Rutherford-type cables these eddy currents are accounted for by the inter-strand coupling currents. The induced voltage U_{ind}^{ij} over an element reads

$$U_{\text{ind}}^{ij} = \ell_z k_{\text{mag}} \delta_{\Xi}^i \frac{\partial}{\partial t} A_{z,\text{av}}^i, \quad (3.29)$$

where $\ell_z k_{\text{mag}}$ represents the magnetic length of the element and $A_{z,\text{av}}^i$ is the average magnetic vector potential over the element i as explained in Sec. 3.3. The induced voltage is defined positive along the winding for increasing vector potential respectively current. δ_{Ξ}^i takes into account the orientation of the line segment in respect to the integration direction.

The total induced voltage U_{ind} is thus given by the sum over all elements:

$$U_{\text{ind}} = \sum_{\xi=1}^{N_e} U_{\text{ind}}^{\Xi(\xi)} \quad (3.30)$$

Scaling
factor k_{mag}
defined in
(3.14)

Inductance:
Sec. 7.4

Inductance As introduced in Sec. 7.4, the differential inductance is calculated from the flux change in the coil divided by the current change. With the flux change expressed by the induced voltage U_{ind} this results in

$$L_{\text{d}} = \frac{U_{\text{ind}}}{\frac{\text{d}}{\text{d}t} I_{\text{M}}}. \quad (3.31)$$

The fact that the differential inductance is calculated from the current change as well as the current change is computed for the differential inductance has to be resolved by either determining L_{d} in advance, an iteration scheme, or an explicit scheme with small time steps. For zero current change

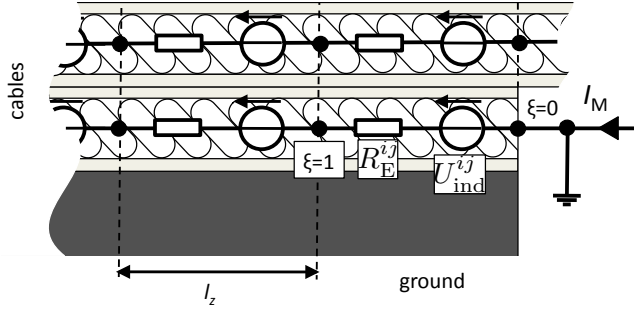


Figure 3.8: Longitudinal cut through the discretized coil winding with lumped electrical elements.

Eq. (3.31) is undefined and replaced by the apparent inductance. The apparent inductance L_Ψ is given by

$$L_\Psi = \frac{\sum_{i=1}^{N_c} \delta_{\Xi}^i A_{z,av}^i}{I_M} \ell_{\text{mag}}, \quad (3.32)$$

where ℓ_{mag} is the magnetic length of the magnet (defined in Sec. B.1.6). For the present model no mutual inductances need to be considered.

Internal Voltage Calculation Without limitations we connect the magnet terminal $\xi = 0$ to the ground. The electrical potential along the magnet windings can be calculated by summing the inductive and resistive voltages following ξ :

$$\phi^\xi = \sum_{\zeta=1}^{\xi} \left(U_{\text{ind}}^\zeta + U_{\text{res}}^\zeta \right) \quad (3.33)$$

The induced voltage is calculated in all turns of the coil from the time-derivative of the linked flux. To evaluate resistive voltages we interpolate the resistivities before- and after each time-step. This allows to define the voltage between any two elements, as well as the electrical field between two elements of identical longitudinal position j :

$$U^{ij,nk} = \phi^{ij} - \phi^{nk}, \quad |\mathbf{E}|^{ij,nj} = \frac{|\phi^{ij} - \phi^{nj}|}{d_E^{i,n}}, \quad (3.34)$$

with the distance of two parallel elements $d_E^{i,n}$ derived in Sec. B.1.5. Figure 3.8 shows the discretized coil winding with the lumped electrical elements U_{ind}^{ij} and R_E^{ij} .

During the quench simulation the peak electrical field and its location are constantly recorded.

Parasitic
capaci-
tances:
Sec. 7.10.3

Parasitic capacitances Following the approach by BRECHNA [Brec 73, pp. 332], the voltage distribution over the coil of a superconducting magnet is influenced by parasitic capacitances. If the capacitance to ground is much larger than the winding capacitance of the coil, a sudden voltage rise over the magnet is concentrated around the terminals instead of decreasing linearly along the winding. This results in a significant increase of voltages and electric fields between adjacent conductors.

Dielectric
strength:
Sec. A.1.7

For accelerator type magnets comparable to the SSC dipole, the voltage increase can be estimated to a factor of two. As peak electrical fields are at least an order of magnitude below critical limits, *i.e.* below the dielectric strength of the insulation material, the effect of parasitic capacitances can be neglected. Note that the electrical topology of the coil changes if capacitances are considered.

3.6 Thermal Model

The thermal problem is described by the heat conduction equation for non-stationary systems [Lewi 96, p. 4]:

$$\rho_D(T)c'_V(T,B)\frac{dT}{dt} = P + \nabla \cdot (\kappa_T(T,B)\nabla T), \quad (3.35)$$

Material
Properties:
Sec. A

where T is the temperature and B the applied magnetic flux density. The external heating power is denoted by P . The material parameters are the volumetric specific heat c'_V , the thermal conductivity κ_T , and the mass density ρ_D . Equation (3.35) does not consider convection, therefore cooling by helium mass flow can not be taken into account.

Finite volumes and linear approximations Introducing finite volumes, Eq. (3.35) can be transformed into a network equation with lumped elements. In the coil cross-section, each conductor constitutes one node in the network, whereas the longitudinal subdivision is a user supplied parameter N_z (Sec. 3.1).

Rutherford-
type cable:
Sec. 7.8

The temperature of each element is assigned to its center. The temperature over the conductor cross-section is assumed homogeneous as shown in Sec. 7.8. For the calculation of the temperature change, the element volume spans the metal parts of the conductor, its voids and the surrounding insulation (see Fig. 3.9 (upper row)). The thermal capacitance of the element is calculated based on the node temperature (constant temperature approach) and the conductor average magnetic induction.

For the calculation of heat fluxes, we assume a linear temperature variation along the conductor and over the insulation. Two adjacent nodes are connected by means of a thermal resistor with the conductor cross-section or the conductor surface (both without the insulation layer) as end planes. The thermal conductivity between two adjacent elements is calculated based on their average temperature and local average magnetic induction (see Fig. 3.9 (lower row)).

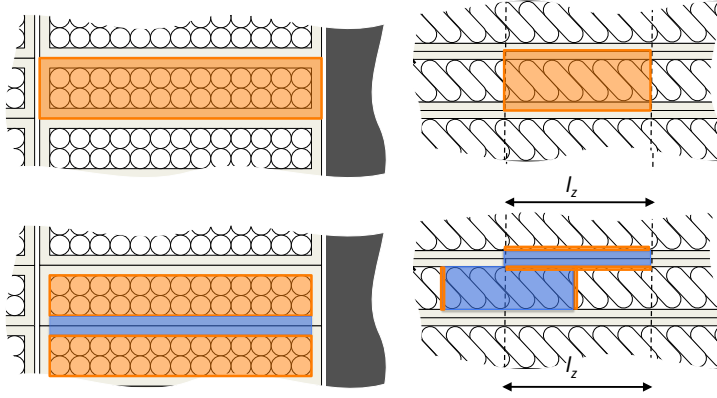


Figure 3.9: Finite volumes and linear/constant approximations for the thermal network model. The left-hand side shows the cable cross-section and the right-hand side its longitudinal extension.

Heat capacity (upper row): For the calculation of the heat capacity the volume spans over the conductor cross-section including the insulation. The temperature is assumed to be constant over the volume. The network node is situated in the center of the element.

Thermal conductance (lower row): For the calculation of longitudinal thermal conductances and heat fluxes, the conductor cross-section without the insulation is used as end planes (orange) of a thermal resistor (blue). For transversal heat fluxes the conductor surface planes (orange) are used. In between two planes a linear temperature distribution is assumed (blue). Material properties use the average temperature of the two adjacent elements.

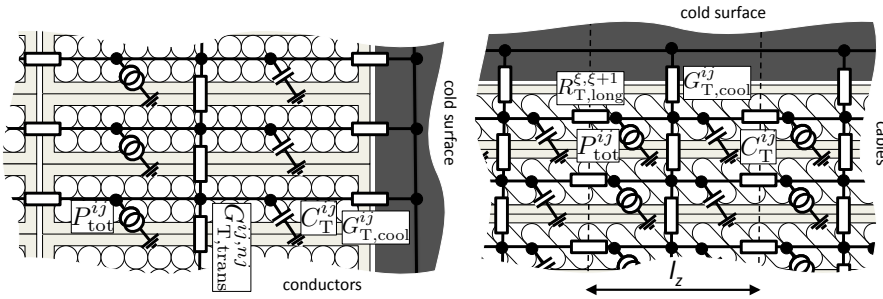


Figure 3.10: Lumped thermal network model in comparison to the the coil/conductor geometry.

Figure 3.10 shows the resulting thermal network model with lumped elements. The network elements are defined below.

Since in the transverse plane the temperature across each conductor is assumed to be constant, current redistribution between the strands [Verw 06] cannot be considered.

3.6.1 Temperature Change

The temperature change in an element is given by

$$\frac{dT^{ij}}{dt} = \frac{1}{C_T^{ij}} \left[P_{\text{tot}}^{ij} - \left(S_{\text{trans}}^{ij} + S_{\text{long}}^{\Xi^{-1}(ij)} + S_{\text{cool}}^{ij} \right) \right], \quad (3.36)$$

where S^{ij} denotes the heat transfer from/to adjacent elements or to a coolant (Sec. 3.6.2), and P_{tot}^{ij} denotes the total dissipated power (Sec. 3.6.5). The heat capacity of the element is given by

$$C_T^{ij} = V_e^i c_T^{\text{eff}}(T^{i,j}, B_{\text{av}}^i) \quad (3.37)$$

Volumetric
specific
heat: Sec.
A.1.5

with the effective specific heat $c_T^{\text{eff}}(T, B)$ defined in Sec. B.2.3. Figure 3.11 (left) shows the specific heat of materials for superconducting cables. Large differences between copper and the superconductors as well as between the superconductors and helium can be noticed at low temperatures. At room temperature the differences are smaller. Liquid helium is dominant below approximately 10 K and can be neglected beyond. The element volume is given by

$$V_e^i = A_{\text{cab,eff}}^i \ell_z \quad (3.38)$$

with the cross-section of the insulated conductor $A_{\text{cab,eff}}^i$ defined in Sec B.1.3.

3.6.2 Heat Transfer

Longitudinal Heat transfer The longitudinal heat transfer in the coil is given by

$$S_{\text{long}}^\xi = (T^\xi - T^{\xi-1}) \frac{k_{\text{T,long}}^{\xi,\xi-1}}{R_{\text{T,long}}^{\xi-1,\xi}} + (T^\xi - T^{\xi+1}) \frac{k_{\text{T,long}}^{\xi,\xi+1}}{R_{\text{T,long}}^{\xi,\xi+1}}. \quad (3.39)$$

The heat flow between two elements can be modified by the parameter $k_{\text{T,long}}^{\xi,\xi+1}$. This allows to steer the quench propagation velocity, to take into account regions of lower or higher thermal conductivity within the coil, and to model quench stoppers, *i.e.* barriers for the heat flux along the conductor. By means of the numbering scheme Ξ the conductors are connected seamlessly over the coil ends. The terminals of the magnet are perfectly insulated, *i.e.* $k_{\text{T,long}}^{0,1} = k_{\text{T,long}}^{N_e, N_e+1} = 0$.

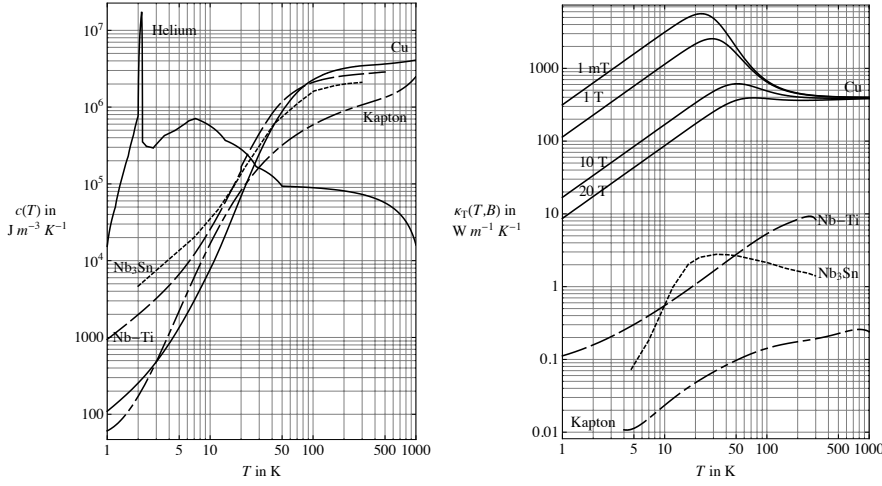


Figure 3.11: (left) Volumetric specific heat of all relevant materials versus temperature. (right) Thermal conductivity of all relevant materials versus temperature.

The longitudinal thermal resistance $R_{T,\text{long}}^{\xi,\xi+1}$ is given by

$$R_{T,\text{long}}^{\xi,\xi+1} = \frac{\ell_z}{A_{\text{cab,xs}}^i \kappa_T^{\text{eff},[=]} \left(\frac{T^\xi + T^{\xi+1}}{2}, B_{\text{av}}^i \right)}. \quad (3.40)$$

For the heat transfer all parts of the cable, *i.e.* superconductor, copper matrix and insulation, are in parallel. Comparing the thermal conductivity of the different materials in Fig. 3.11 (right), only the conductivity of copper needs to be considered. The thermal conductivity of the two available superconductors and of the insulation material kapton are 2-4 orders of magnitude smaller. The effective parallel thermal conductivity $\kappa_T^{\text{eff},[=]}(T, B)$ is defined in Sec. B.2.3. The conductor cross-section without insulation, $A_{\text{cab,xs}}$, is derived in Sec. B.1.3.

Thermal conductivity: Sec. A.1.4

Transversal Heat transfer Transversally, each element is subjected to the heat transfer of all elements in the vicinity:

$$S_{\text{trans}}^{ij} = \sum_{n=1, n \neq i}^{N_c} (T^{ij} - T^{nj}) G_{T,\text{trans}}^{ij,nj}. \quad (3.41)$$

The thermal conductance,

$$G_{T,\text{trans}}^{ij,nj} = K_{\text{trans}}^{i,n} \kappa_T^{\text{eff},[||]} \left(\frac{T^{ij} + T^{nj}}{2} \right), \quad (3.42)$$

consists of a geometrical contact factor $K_{\text{trans}}^{i,n}$ and the effective thermal conductivity $\kappa_{\text{T}}^{\text{eff},[||]}(T)$ (Sec. B.2.3). The geometrical contact factor is introduced in Sec B.1.5. It represents the distance and area of the conducting surface between two elements. Furthermore, it includes a parameter $k_{\text{T,trans}}^i$ to adjust the heat flow and the turn-to-turn quench propagation velocity, respectively.

Conductive Cooling In the presented model, cooling is included by an additional, global node of fixed temperature T_{b} . Therefore, the cooled face of the cable and the distance to the cold surface have to be specified. The thermal conductance to this heat sink is calculated in the same way as between two conductors. This allows to simulate the heat extraction without considering an increase of the bath temperature or the limitation of the heat exchangers to extract more than a certain amount of heat.

$$S_{\text{cool}}^{ij} = (T^{ij} - T_{\text{b}}) G_{\text{T,cool}}^{ij} \quad (3.43)$$

The thermal conductance to the cold surface is given by

$$G_{\text{T,cool}}^{ij} = \sum_{\alpha} K_{\text{cool},\alpha}^i \kappa_{\text{T}}^{\text{eff}} \left(\frac{T^{ij} + T_{\text{b}}}{2} \right), \quad (3.44)$$

where $\alpha \in \{a, b, c, d\}$ is any of the four faces of the conductor as introduced in Sec. B.1.5.

3.6.3 Thermal Properties of Helium

Properties
of liquid
helium:
Sec. A.3

The thermal model and its coefficients have to be modified in the presence of liquid helium in the voids of the cable, subsequently referred to as the confined helium.

Superfluid helium features two phases. Phase I for temperatures above the lambda-point (approx. 2.17 K at saturated vapor pressure) and phase II below. The heat conductivity of phase II helium exceeds the conductivity of copper by orders of magnitudes. Phase I liquid helium and super-critical helium have negligible thermal conductivity. The specific heat of both, Phase I and II helium exceeds that of copper or niobium-titanium by orders of magnitudes. Super-critical helium, however features a relatively small specific heat compared to copper. Thus, for temperatures below the phase transition and below the lambda-point, the confined helium needs to be considered.

We make the following assumptions on mass- and volume balance inside the conductors: Below the lambda-point the mass density and total mass of helium remains constant. At temperatures above this point the helium is adiabatically compressed until the local pressure in the conductor rises up to a limit p_0 . Then, the helium is heated at constant pressure, *i.e.*, mass flows out of the conductor (see Sec. A.3.5). The helium content and thus the heat capacity of elements adjacent to a quench is reduced. Therefore, in direct neighborhood of a quench helium properties are evaluated at a higher

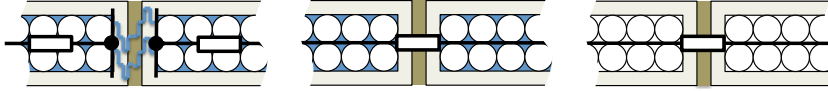


Figure 3.12: Influence of liquid helium in the coil windings on the thermal model. (left) Helium II: perfect heat conduction through the micro channels. Heat flow is limited by the copper inside the cable and by the maximum permitted heat flux through the channels. (center) Helium I: heat flow between conductors is dominated by the insulation material. The huge heat capacity of the helium inside the cable limits the temperature increase. (right) No confined helium.

temperature, *e.g.* 30 K above the element temperature. Figure 3.11 shows the specific heat of helium for constant volume inside a conductor as derived from measurements in [Van 86]. The helium content under nominal operation conditions is a user-supplied parameter in the simulation and depends on the compaction of the cable (see Sec. B.1.3).

Below the lambda-point, heat conduction between adjacent conductors is determined by the helium percolating across the insulation and by the conductivity of the conductors. The thermal conductivity of superfluid helium being infinite at first approximation, the conductivity is determined by the conductor material, *i.e.*, mostly by the copper in the strands. The size and availability of these helium channels depend on the used insulation material and the applied pressure. If a maximum heat flux is exceeded the superfluid helium “quenches” [Iwas 94, p. 117] and loses its perfect heat transfer properties. The maximum flux is user supplied and set to zero if no channels are considered. Above the lambda-point or in the “quenched” state, the heat conductivity of helium is neglected in our model.

Figure 3.12 shows how helium inside the cables influences the thermal model of the coil.

The model does not consider the energy absorbed by the helium phase-transitions. The confined helium is assumed to be in close contact with the strands. Variations in the thermal contact due to nucleate and especially film boiling are not considered.

3.6.4 Quench Heaters

Quench protection heaters are thin resistive strips colaminated with insulation material mounted on the superconducting coil. In case of a quench, the quench heaters are fired heating up the covered conductors. The heating causes further quench and thus significantly increases the coil resistivity.

In the present work, quench heaters are modeled as effective heat sources inside the covered conductors, *i.e.* without constituting a node in the thermal network model.

Each quench heater is described by three parameters, the effective initial heating power P_{QH0} , an internal delay Δt_{QH0} , and the discharge time constant τ_{QH} . These properties may vary between quench-heater circuits and are

Quench
heaters:
Sec. 7.9.5

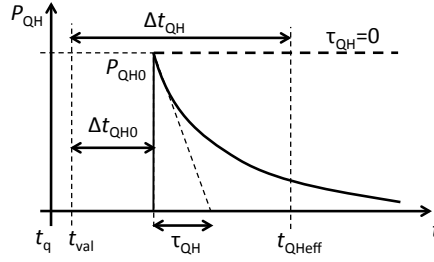


Figure 3.13: Quench heater model depicting the relevant parameters as initial power P_{QH0} , decay constant τ_{QH} , and internal delay Δt_{QH0} . Setting the decay constant to zero yields a constant power output.

therefore directly assigned to the covered conductor i :

$$P_{QH}^i = P_{QH0}^i \begin{cases} 0 & t < t_{\text{val}} + \Delta t_{QH0}^i \\ \exp\left(-\frac{t - t_{\text{val}} - \Delta t_{QH0}^i}{\tau_{QH}^i}\right) & \text{else} \end{cases}, \quad (3.45)$$

where t_{val} is the time of quench validation, *i.e.* the instance when the quench is detected and validated after a discrimination time. The power is dissipated homogeneously along the covered conductor i .

The time constant τ_{QH} is determined by the electrical heater circuit and the strip resistivity. As derived in Sec. 7.9.5, the dissipated power decays with half the time constant of the discharge current or voltage. A time constant set to zero allows to study steady heating of parts of the coil. Figure 3.13 shows the three parameters in the context of the events during a quench.

The parameters P_{QH0} and Δt_{QH0} are chosen such that the observed/expected quench heater delay Δt_{QH} , *i.e.*, the time between firing a heater and the occurrence of a quench, can be reproduced. The quench heater delay depends on the working point of the covered conductor and varies nonlinearly over the full current range (see Sec. 7.9.5). Note, that both parameters are model specific and have no direct meaning or measurable representation.

The quench heater model does not permit to compute the quench heater temperature. Furthermore, it is not possible to calculate the effect of the longitudinal variation of the heater strip resistivity, *i.e.* heater cladding [Rodr 00] and [Sonn 01a].

3.6.5 Total Dissipated Power

The following heat sources are considered in the thermal model: Ohmic heating P_{ohm}^{ij} in the quenched parts of the superconductor, in the superconducting parts induced losses P_{losses}^{ij} and heating by quench heaters P_{QH}^i . Furthermore, external heat sources, *e.g.* beam losses or other external heating mechanisms,

Quench
detection:
Sec. 7.9.1

Sequence
of Events:
Sec. 7.9.6

can be applied by means of P_{ext}^{ij} . The total dissipated power per element yields:

$$P_{\text{tot}}^{ij} = P_{\text{ohm}}^{ij} + P_{\text{losses}}^{ij} + P_{\text{QH}}^i + P_{\text{ext}}^{ij}. \quad (3.46)$$

Book-keeping of the individual heat sources and of the total heat transfer permits to determine the cause of quench for each element in the thermal model. It can be distinguished between local quench due to quench-back, quench propagation, or quench heaters.

Combining the sequence of quench events with their cause, allows to determine the quench heater efficiency, *i.e.* does the quench heater cause a quench, the quench heater delays Δt_{QH} , and the first time when quench back occurs t_{QB} .

3.7 Quench Algorithm

The description of the quench process is based on the afore introduced five sub-models, *i.e.* the description of the superconducting state and its transition, the magnetic field computation, analytical models of induced losses, the electrical network model, and the thermal model; and their coupled solution.

Start of Simulation We distinguish two different starting conditions for the quench simulation. Dynamic conditions where a quench is triggered during a pre-defined ramp-cycle or a quench starting from a specified steady-state working point. In the latter case, the quench has to be actively triggered by means of a heat pulse or by increasing the conductor temperature beyond the critical temperature. In order to prevent an instant quench recovery the temperature is raised at least 10% above the quench limit. The local extend of the quench can be set to one element or an entire conductor.

In the former case, a quench can be caused by induced losses, by exceeding the critical current limit or by using the active trigger after a pre-defined delay.

Static computation The magnetic field model, *i.e.* the analytical calculation of the coil fields and the numerical calculation of magnetic materials by means of the BEM-FEM-coupling method, can be performed under static conditions. The time derivative of all field quantities is derived from the change between two successive computational steps.

The analytical models of the induced cable eddy currents are also static. As explained above, the results are interpolated in order to obtain the diffusive characteristics of the losses. However, the loss models are evaluated together with the magnetic field computation.

Time integration scheme The thermal-network-equations and the electrical-network equation constitute coupled, non-linear, inhomogeneous differential equations of first order. Both are solved with a classical Runge-Kutta method of 4th order in an explicit time-integration scheme (Sec. 7.11). Within each

computational step, we update all parameters by the most recently computed values, *i.e.* in the case of the induced losses with the current value of interpolation.

The material properties vary significantly with temperature, *e.g.* the heat capacity of copper increases by several orders of magnitude from cryogenic to room temperature. Therefore, typical time constants of the differential equation system are subjected to drastic variations. This can be taken into account using adaptive time-stepping.

The Runge-Kutta method of 4th order can be equipped with a quality factor [Coll 55, p. 68]. The quality factor gives indication whether to accept or discard the result of the last integration step. If discarded, the step is repeated with a shorter time-step width. In the case the step was accepted, the time-step width can eventually be increased. The adaptive time-stepping allows to cope with the highly-nonlinear material parameters, and to resolve the growth of the resistive zone inside the magnet as well as the switching-in of the protection resistor. The time step-width is limited by a minimum value in order to ensure a finite computation duration.

Nested computation loops The update of the magnetic field is computationally more expensive than a time-step in the thermal model. Time-constants in the thermal model, however, are much shorter than those of the eddy currents in the magnetic model. It is therefore reasonable to foresee a weak coupling between thermal and magnetic computations, updating magnetic values only when the excitation current has changed significantly.

Figure 3.14 shows the quench algorithm featuring two nested computation loops. The outer loop contains the magnetic field and analytic loss computation. The inner loops consists of the Runge-Kutta algorithm for the thermal and electrical model. The critical state of the superconductors is evaluated in the inner loop - denoted quench decision.

Loop Termination Ohmic losses and coupling-current losses are driven by the stored magnetic energy in the magnet. We use this to calculate the energy decrease in the magnetic field. When it has decreased by a user-supplied factor, the field is updated, *i.e.*, the inner simulation loop is interrupted and a magnetic field model computation is carried out. The quench simulation then proceeds with updated values for the field- and coupling-current-loss distribution.

End of Simulation The quench simulation ends, when the current or its derivative have dropped below a predefined level, or the hot-spot temperature exceeds a maximum value of 1000 K.

In general, calculations have to be repeated with twice the minimum step-size to check for numerical stability.

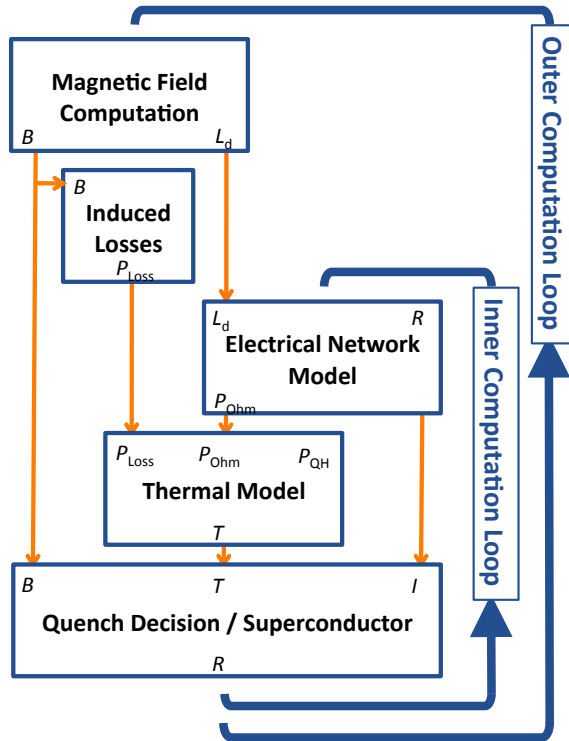


Figure 3.14: Block diagram of the quench simulation algorithm. We distinguish an inner and outer computation loop. In the outer loop we perform the magnetic field and loss computation. In the inner loop we evaluate the thermal model, the electrical field model and the quench status of all superconductors.

4 Introspection

The purpose of computing is insight, not numbers.

RICHARD W. HAMMING
(1915-1998)

The quench model includes a number of parameters which need to be determined in order to reproduce the measurements. Most parameters can be derived from specifications given to the manufacturers or measurements of magnet components. Other parameters evade direct measurement and are determined indirectly, *e.g.* the thermal properties of the coil are adapted to reproduce the measured quench propagation velocity, and quench-heater parameters are validated on quench-heater delay studies.

Reproducing quench measurements, the simulation allows to review the internal state of the magnets which is not accessible to measurements, *e.g.* the temperature margin or the reason for a quench over all conductors. This way, we can analyze quench propagation, heater efficiency, and quench protection methods.

4.1 LHC Main Dipole

The quench routine is demonstrated and validated by means of measurements for the LHC main bending magnet (MB) [Brun 04]. We review relevant properties of the magnet, and specify the used parameters.

The LHC main bending magnets guide particles with a nominal energy of 7 TeV on an orbit of 27 km circumference [Brun 04, p. 164]. With the maximum magnetic induction of 9 T they bend the trajectory by 0.29° over the magnetic length of 14.3 m [Evan 09, p. 75].

The dipole features two apertures in a common collar and iron yoke. The coils in each aperture are composed of an upper and a lower pole. Each pole consists of 6 conductor-blocks per quadrant, arranged in two layers. Figure 4.1 shows the magnet

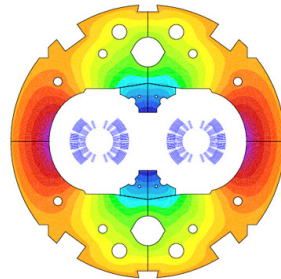


Figure 4.1: LHC MB. Schematic coil cross-section and iron yoke. Outer iron diameter 570 mm.

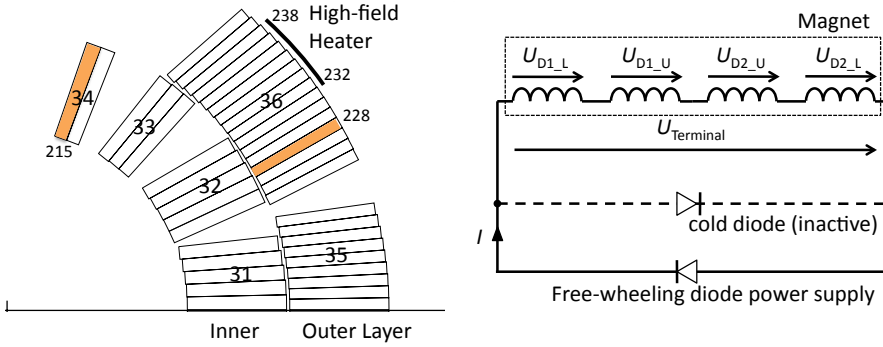


Figure 4.2: (left) Coil blocks and quench-heater positions in one aperture of the LHC main bending magnet. (right) Electrical circuit of the magnet measurement test station after the current source is switched off. D1_L denotes the lower pole in aperture 1. D2_U denotes the upper pole in aperture 2.

Saturation
influence
on L_d Sec.
7.4.3

cross-section including the iron yoke. Saturation has a relatively small impact on the differential inductance, which varies only by 5% with excitation. For the thermal and resistivity calculations we use an average conductor length between the two coil ends of 14.57 m.

The coil is wound from two different kinds of Rutherford-type Nb-Ti cable. The critical current density in the strands is given by a fit to measurement [Bott 00]. The magnet operates at a temperature of 1.9 K. The residual resistivity ratio (RRR) of the copper matrix in the strands is in the range of 150 to 250 [Char 06].

Magnet
protection
Sec. 7.9

The quench protection consists of a detection system, a cold bypass diode and quench heaters placed on the outer layer of the coil as indicated in Fig. 4.2. The threshold voltage of the detection system is 0.1 V [Denz 06]. Quench heaters are fired after a delay of 10 ms for signal validation [Denz 06]. The timing of the different heaters may vary by up to 10 ms [Sonn 01a]. A capacitor is discharged over the resistance of the heater strip, resulting in an exponential voltage decay [Rodr 01]. The time constant for the dissipated power is about 37.5 ms [Sonn 01a].

An exhaustive list of all parameters and properties used for the simulation of the LHC main bending magnet can be found in Sec. C.1.

4.1.1 Reproduction of Quench Measurements

The quench model is gauged in order to reproduce the measured induced losses and quench-heater delays. Finally, the the current decay measured at the LHC test stand is reproduced and the voltages over the different coils are analyzed.

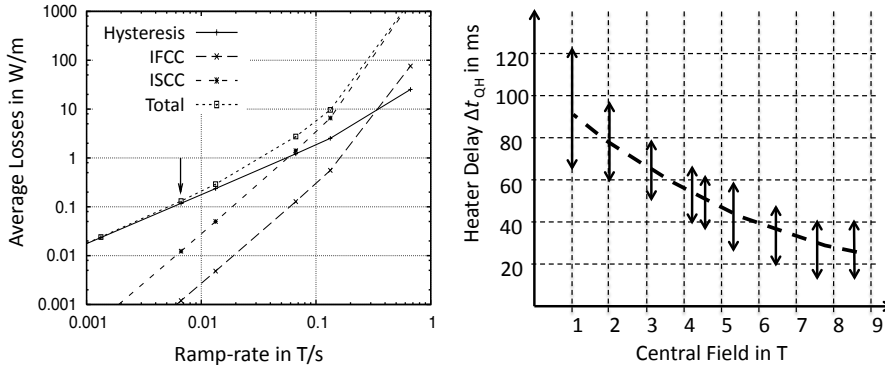


Figure 4.3: (left) Average cable losses for different ramp-rates. The vertical arrow highlights the nominal ramp-rate of the LHC. (right) Quench heater delays for the main bending magnet. The arrows signify the range of measured values. Reprint of the quench heater measurements by P. Pugnat [Pugn 07].

Induced Losses The cross-over contact resistances, R_c , of the inner and outer layer cables are about $30 \mu\Omega$ and $60 \mu\Omega$, respectively [Lero 06]. The adjacent resistance R_a is set to $100 \mu\Omega$ for both cables [Verw 07b]. Figure 4.3 (left) shows the simulated dissipated cable losses for different ramp-rates. For the graph, the losses are averaged over the coil cross-section and given per unit length. In the case of the superconductor hysteresis losses the losses are averaged over the complete ramp-cycle (as discussed in Sec. 7.7). The losses for the nominal ramp-rate of 0.0066 T s^{-1} (up-ramp in 1200 s) are highlighted by a vertical arrow. The results are in good agreement with the values published in [Verw 95, p. 153] (inter-strand and inter-filament losses) and [Voll 02, p. 135] (hysteresis losses).

Cable magnetization losses Sec. 7.6

As expected, in the double logarithmic plot the graphs for the induced inter-filament and inter-strand coupling current losses show a slope of 2, and the hysteresis of 1, respectively. The hysteresis losses are dominant up to a ramp-rate of approximately 0.07 T/s and are disregarded during a quench. From Eq. (7.69) we can calculate a maximum ramp-rate of approximately 1.5 T s^{-1} .

Quench heaters The quench heater delay, *i.e.* the time between firing the quench heaters and causing a quench in the coil, depends on the working point of the magnet. For a lower current and thus greater temperature margin, the delay is longer. Figure 4.3 (right) shows a reprint of the measured quench heaters delays for the LHC MB [Pugn 07].

Temperature margin Sec. 7.1.2

The quench heaters are described by the effective power injected into the covered conductors. The number of conductors under the heater strips as well as the time constant of the discharge are defined by the heater geometry and powering circuit.

Quench heater model Sec. 3.6.4

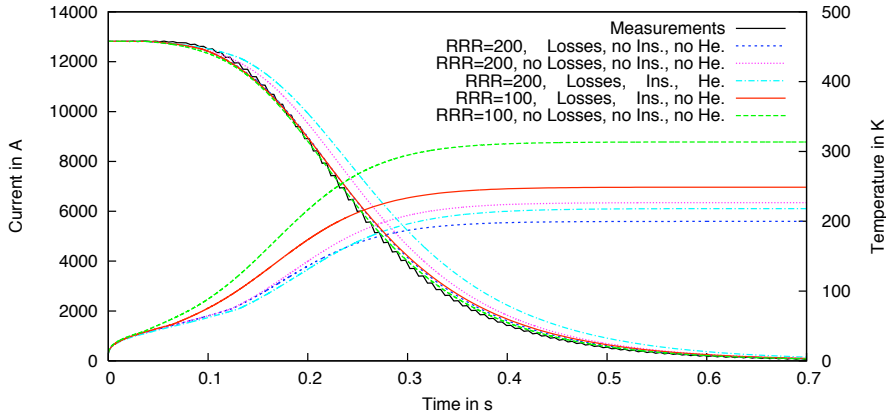


Figure 4.4: Measured and simulated current decrease for varying simulation parameters. Simulated peak temperature. Losses refer to cable eddy current losses such as inter-strand and inter-filament coupling currents.

The simulation is gauged to the measurements by means of the initial power P_{QH0} and the firing-delay Δt_{QH0} . Both are determined by a parametric study simulating quench heater firing for various values of power and initial magnet current. After reproducing the characteristic shape of the function, the result can be adjusted to the measured values by means of the additional delay. For the following simulations we use an initial power of 20 W/m per covered conductor and a delay of 23 ms.

Current We compare the simulations to the measured current and voltage signals during a training quench of magnet MB2381 [Choh 07]. For this measurement, the magnet was mounted on the LHC test stand and directly connected to the power supply with a free-wheeling diode in parallel. After quench detection, the power supply is switched off and the current commutates into the diode. The protection diode inside the magnet cryostat is consequently clamped to the forward voltage of the free-wheeling diode and prevented from switching, see Fig. 4.2 (right). From the measured terminal voltage we derive the diode properties, *i.e.*, a diode threshold voltage of 0.7 V and a forward resistance of about $390 \mu\Omega$. The quench starts at a current level of 12.82 kA in conductor number 215 of pole D1_U.

Figure 4.4 shows the simulated current decays for different RRR values, with and without induced losses in the conductors. Furthermore, the effective heat capacity of the cable is varied by means of considering the influence of the insulation and the confined helium. The results are compared to the measured current decay.

It is possible to reproduce the measured current decrease for three different sets of parameters grouped in two families:

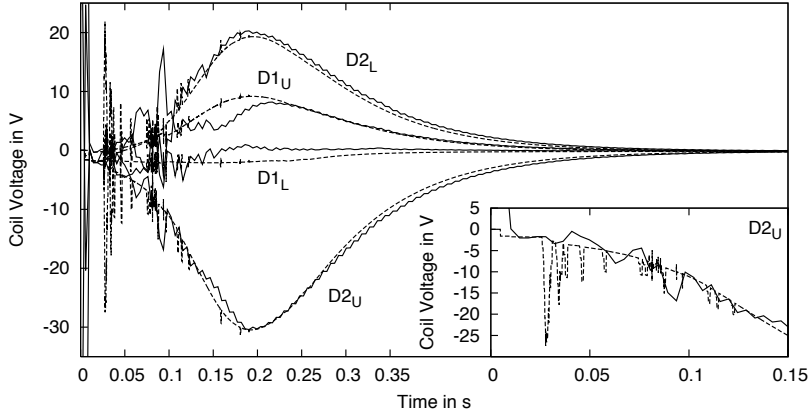


Figure 4.5: Measured (solid) and simulated (dashed) voltage over the 2 poles of the 2 apertures of LHC 2381 during a training quench. (inset) The measured voltage, as well as the simulation, show ripples during the first 150 ms.

1. Cable measurements indicate for the cables of the LHC MB a residual resistivity ratio (RRR) of 200 [Char 06]. We can reproduce the current decrease if we disregard the influence of the insulation material and the confined helium.
2. Older specifications, *e.g.* [Lefe 95, p. 86], suggested a RRR value of less than 100. In this case the measurements can be reproduced in two ways; either including the heat capacity of the insulation or neglecting all sorts of induced losses.

For the resulting hot-spot temperature we observe a temperature difference of more than 100 K. We obtain the highest temperature in the second case where no quench back takes place and the necessary resistance is built up only by the quench heaters and temperature dependence of the resistivity. We chose the first set of parameters for the following simulations.

In addition, we show the influence of the insulation material and content of 1% confined helium. The current decrease is slower compared to the previous cases. The peak temperature, however, increases only by 20 K. The measurement data cannot be reproduced for a RRR value of 200 if losses are neglected.

Voltages The measured and simulated voltages across the four poles of the two-in-one magnet are shown in Fig. 4.5. Small differences in the timing of the quench heaters over the four poles cause asymmetric voltage distributions. To reproduce the asymmetry, the quench heaters in our model were de-tuned by less than 2 ms.

The measured voltage, as well as the simulation, show ripples during the first 150 ms. We explain this by the fact that every conductor turning resistive

causes a sudden increase in ohmic voltage. The magnet's terminal voltage, however, is clamped to the forward voltage of the diode. Disregarding parasitic internal capacitances, the increase in ohmic voltage must be distributed evenly over the four pole inductances, resulting in a sudden change of all voltages. Once all conductors are quenched, the ohmic voltage changes smoothly with temperature which is reflected by the measured and simulated curves. In order to distinguish from also existing numerical effects the voltage spikes are studied analytically in Sec. 7.10.2.

The presented result underlines the advantage of a coupled approach for the quench simulation: The thermal model as well as the models for cable magnetization losses determine the growth of the resistive voltage. Owing to the simultaneous calculation of the electrical network and magnetic field problem, the voltage re-distribution can be resolved.

Interpretation The large number of different parameters, *e.g.* thermal properties, residual resistivity ratio, quench heater timings, and loss model parameters, offer a wide range of possibilities to reproduce a limited set of observables such as the measured current decrease and coil voltages. Nevertheless, we are confident that if the parameters are chosen within a justifiable range, we can gain deeper insight into the quench process and the interdependent effects.

4.1.2 Introspection - Simulation of a Quench in the LHC Tunnel

The validated model can be used to simulate a quench in the LHC tunnel where no measurements are available.

We consider a quench at the nominal current of 11.85 kA. The quench origin is located in the outer layer in conductor number 228, compare Fig. 4.2 (left). It is centered longitudinally. The forward voltage of the diode in the magnet cryostat is assumed to be constant at 6 V [Verw 08a].

Figure 4.6 shows the temperature margin to quench in each conductor at the magnet's center as a function of time. Three different phenomena can be distinguished: Quench propagation, quench-heater delay, and quench-back. After the quench has been initiated, it propagates transversally and longitudinally. The detection voltage is reached at 28 ms (marked with 'a' in Fig. 4.6); 10 ms later the quench is validated and the heaters are fired (b). After the pre-defined 23 ms, the dissipated heat starts to decrease the quench margin in the conductors covered by heaters and cause a quench at 65 ms. With the additional quenched conductors, the diode threshold voltage is reached and the current in the magnet starts to decrease (c). Eddy-current losses create additional heating. The inner layer is quenched by quench-back at approximately 132 ms (d). The quench propagation in the outer layer is also accelerated by the induced losses. After about 300 ms the magnet is fully quenched (f).

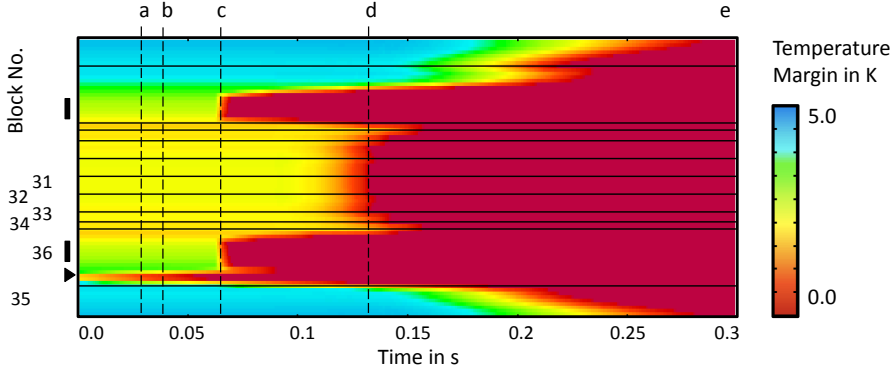


Figure 4.6: Temperature margin to quench over the conductors versus time for the pole of quench origin. The numbers correspond to the block numbers in Fig. 4.2. From the evolution of the temperature margin we can distinguish quench propagation, quench heater delay, and quench-back. The position of the quench heaters is indicated by the vertical, black bars. The quench origin is high-lighted by a black triangle.

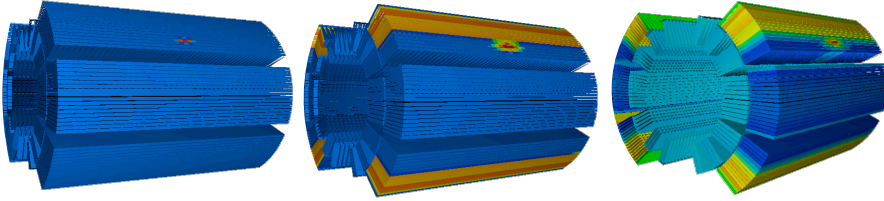


Figure 4.7: Illustrated temperature distribution over one aperture of the magnet. We distinguish quench propagation, quench-heater firing, and quench-back. The coil is scaled 1:100 in axial direction. The pictures is taken after 40 ms (left), 100 ms (center) and 300 ms (right).

Figure 4.7 shows the coil temperature at three different stages of the quench. On the left, the initial quench zone propagates transversally and longitudinally due to thermal conduction. In the middle, the quench heaters have been fired and the covered conductors are resistive. The figure on the right shows the magnet after quench-back. The coil is almost completely resistive.

4.2 3-D Thermal propagation

The 3-D thermal propagation of a quench is studied for the LHC MCBX corrector magnet [Brun 04]. The MCBX consists of two nested, independently powered dipoles, see Fig. 4.8. We consider the outer dipole only. The magnet is wound from a 7-strand ribbon-type conductor using a strand of the LHC MB inner layer cable rolled into a rectangular form. The strands are connected in one coil end, such that each radial layer of strands is connected in series. This connection allows for radial and azimuthal quench propagation within a coil block as well as for longitudinal propagation within each radial layer of strands. The coil is fully impregnated so that no cooling needs to be considered. The magnet is operated at 1.9 K and the quench occurs at 734 A. Figure 4.9 (left) shows the series connection of the strands in the magnet end. The soldering is covered by copper plates and immersed in liquid helium; therefore, functioning as a quench stopper. Figure 4.9 (right) shows the outer layer coil before mounting into the iron yoke. For the present simulations, the magnet is neither protected by quench heaters nor a dump resistor. The voltage across the power supply is neglected.

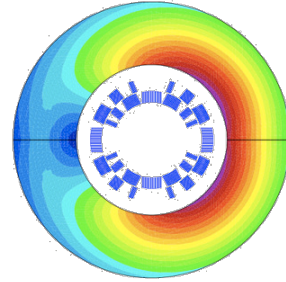


Figure 4.8: LHC MCBX. Schematic coil cross-section and iron yoke. Outer iron diameter 330 mm.

Plotting the temperature margin to quench over each conductor versus time illustrates the quench process and allows to determine the turn-to-turn quench propagation delay. Figure 4.10 shows how a quench originating on the upper pole propagates through the coil. Both, measured and simulated turn-to-turn quench propagation delay, yield 4 ms. The longitudinal quench propagation velocity is calculated to be 18 m/s which is in good agreement with measurements [Karp 08c].

Please notice: The quench propagation velocity increases with decreasing margin to quench. Close to the critical surface the quench would propagate

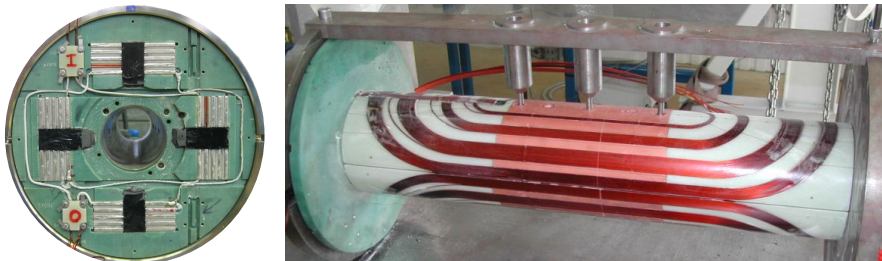


Figure 4.9: MCBX Magnet. (left) Series connection of the strands in the magnet end. The soldering is covered by a copper block and functions as a quench stopper. (right) Outer layer coil before mounting into the iron yoke. Courtesy of M. Karppinen CERN TE MCS.

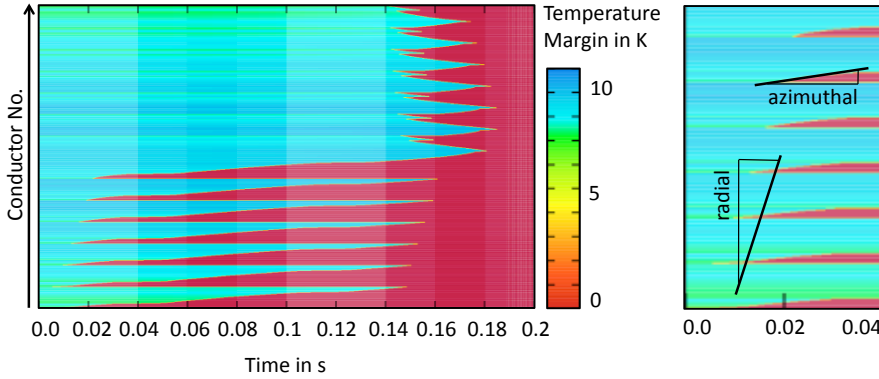


Figure 4.10: MCBX temperature margin over conductors versus time. (left) The quench originated in the first conductor and spreads azimuthally and radially to neighboring strands. The lower half of the plot covers the conductors in the upper pole of the magnet and the upper half the lower pole. The conductors in the lower pole start quenching 130 ms later. (right) The detailed view of the temperature margin plot gives one way to determine the turn-to-turn propagation delay.

with infinite velocity. Induced losses cause an additional temperature increase in the conductors and the margin to quench is reduced. The quench propagation is accelerated by means of the smaller margin. Thus, in presence of losses the quench propagation velocity depends also on the current decrease rate. This process re-inforces itself since a faster growth of resistivity causes a faster current decay which causes greater losses. At magnetic quench-back the induced losses cause fractions of the magnet to quench which are disconnected from the initial quench zone. Here and for conductors covered by quench heaters the quench propagation velocity becomes meaningless.

Figure 4.11 (left) shows the measured [Gilo 08] and simulated current decrease which match nicely up to 0.3 s. Then the measured current decreases slower than the simulation. Due to the short overall length of the magnet, the 3-D saturation of the iron yoke is likely to influence the inductance and thus the current decays in a different way than predicted from 2-D calculations. This problem will have to be addressed in future simulations. The final temperature distribution over the coil cross section is shown in Fig. 4.11 (right). Figure 4.12 shows the temperature in the whole coil for different times.

A good match between simulation and measurements could be obtained without gauging the material properties, since neither cooling nor helium need to be considered.

The quench model allows to investigate critical voltages and electrical fields in the magnet cross-section. Figure 4.13 shows the potential to ground over all conductors versus time. The maximum potential stays below 180 V, which corresponds to maximum electrical field of 3000 Vm^{-1} . The voltage distribution over the coil cross-section is smooth and does not show high gradients. In Fig. 4.14 (left) the voltage along the conductor winding is plotted for

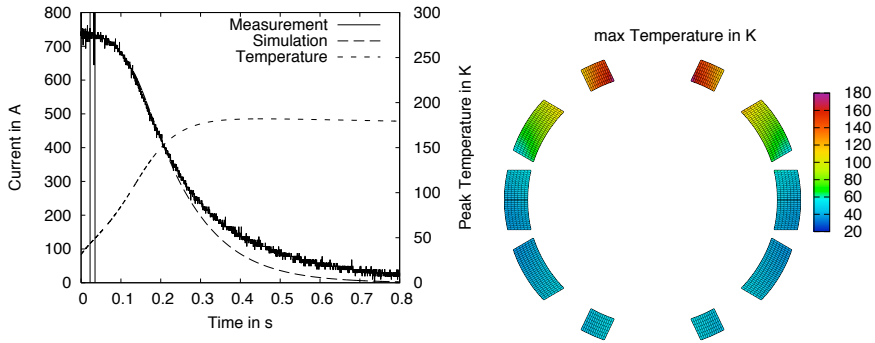


Figure 4.11: (left) Current decrease during quench in the MCBX: Simulation and measurement match well up to 0.3 s. (right) Maximum temperature over the coil cross-section.

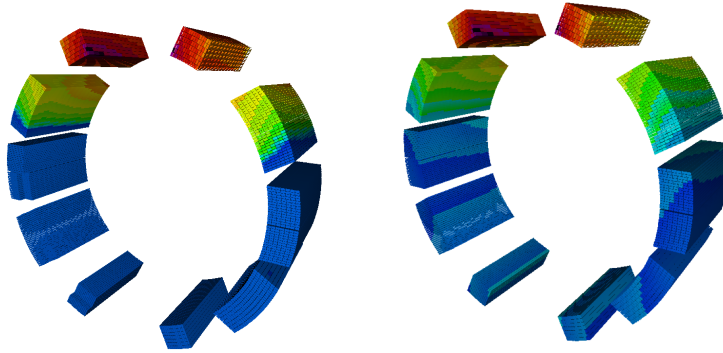


Figure 4.12: Quench propagation in the MCBX outer coil: The 3D model is displayed from the non-connection side of the coil and longitudinally compressed by a factor of 10. The quench started in upper pole, inner most turn, close to the coil end. (left) Temperature distribution after 0.1 s. The quench propagated longitudinally and transversally in the upper most block. It spread to the block below over the connection-side. (right) Temperature distribution at the end of the quench. The lower pole shows an elevated temperature due to induced losses. The maximum temperature is 180 K.

the instance where the highest potential to ground could be observed (at $t = 200$ ms). The left-hand side of the plot (conductor no. smaller than 800) corresponds to the upper pole of the magnet. In the upper pole the ripple on the voltage is caused by sequences of normal conducting (quenched) and superconducting strands. Therefore, the voltage to ground is reduced by approximately 45 V by the winding scheme (Sec. 7.10.3). In the lower pole, the variation in the potential is caused by changes of the confined flux over the coil cross-section and therefore by the variation of the induced voltage.

By comparing the cumulated heat transfer from neighboring elements, induced losses, and quench heaters, the reason for a conductor to quench can

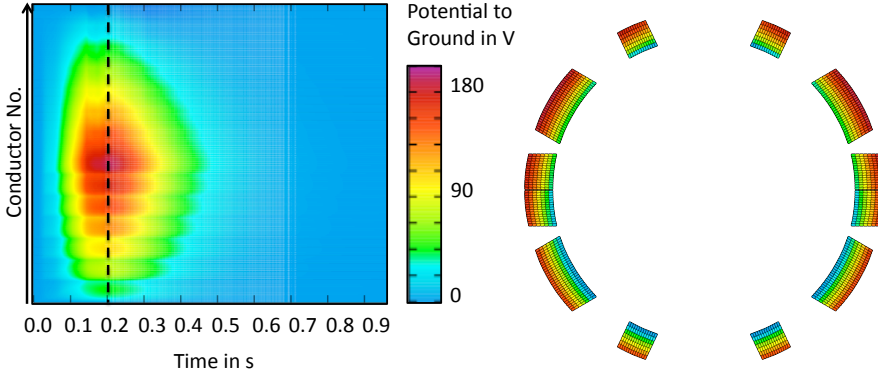


Figure 4.13: Potential to ground during a quench in the MCBX. (left) Variation in time. (right) Potential to ground over the coil cross-section at $t = 200$ ms. The potential varies smoothly over adjacent conductors.

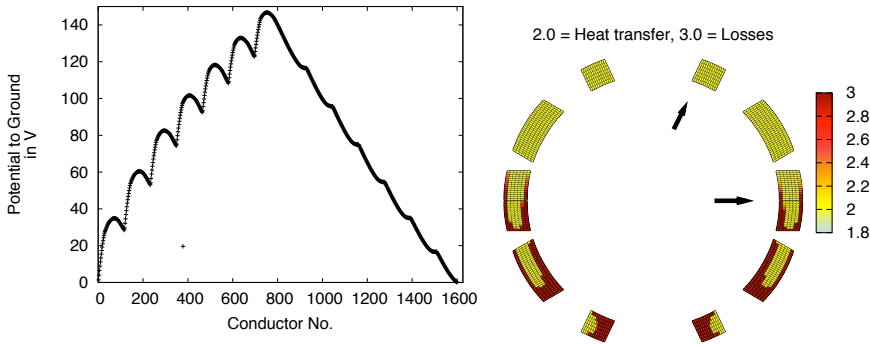


Figure 4.14: (left) Voltage along the coil winding of the MCBX when the voltage to ground is at its maximum ($t = 200$ ms). The left-hand side of the plot corresponds to the upper pole of the magnet and the right-hand side to the lower pole. The voltage ripple in the upper pole is caused by the alternating connection of normal conducting and superconducting strands. (right) Cause of quench in the MCBX: The light colored conductors quenched due to heat transfer from other quenched conductors, the dark colored conductors quenched due to induced losses.

be derived. Figure 4.14 (right) shows that only a few turns are quenched by induced losses. Especially the conductors in the low field region (see arrow), where inter-filament losses are small, are quenched by heat transfer.

4.3 Quench recovery

During a test of the LHC MQY quadrupole magnets [Brun 04], quench heaters were fired at a magnet current level of only 80 A (compared to a nominal current of 3610 A). The current measurement [Denz 08b] show clearly two different slopes indicating a quench in the magnet and a later recovery. The quench model is used to reproduce this effect.

The MQY is a double aperture magnet (see Fig. 4.15) with quench heaters on the outer radius of the coils as well as between the second and the third coil layer. The coils of both apertures are powered independently. Figure 4.16 shows the electrical circuit. At low currents, the two apertures are magnetically decoupled. This allows to reduce the simulation effort by calculating only one aperture and halving the values of the external electrical network elements.

For the simulation, the effective power of the quench heaters has been varied until a quench is triggered at 80 A and the slope of the current decrease is consistent with the measurements. Furthermore, the cooling is set such that a recovery from quench is within reach after few seconds. Figure 4.17 (left) shows both, measured and simulated current decay. Notice: In the measurement the current of both apertures are shown. Figure 4.17 (right) shows the change of temperature margin to quench over the conductors of one pole of the magnet during the heater discharge. The quench occurs 0.1 s after firing the heaters and the conductors recover 1 – 3 s later.

By means of this simulation details of the quench recovery which evade direct measurements can be studied. The results have been obtained by gauging model parameters within their reasonable range.

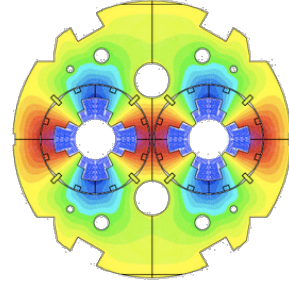


Figure 4.15: LHC MQY. Schematic coil cross-section and iron yoke. Outer iron diameter around 495 mm.

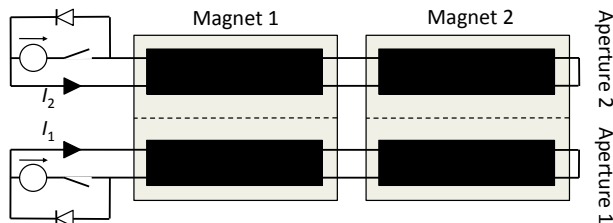


Figure 4.16: The two apertures of the LHC MQY are powered independently. Nevertheless, the apertures of two adjacent MQY magnets are connected in series.

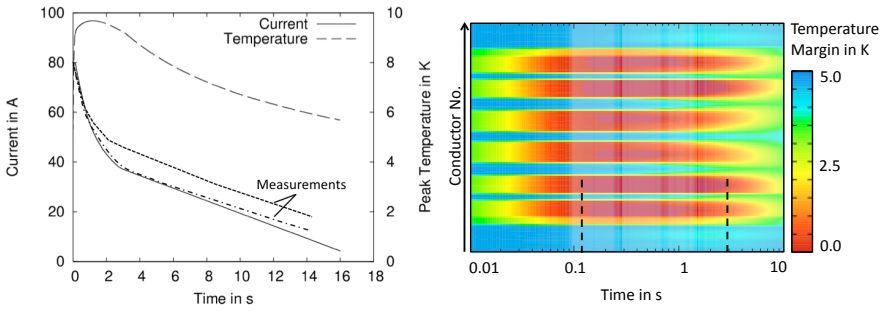


Figure 4.17: (left) Current decrease in the MQY after triggering the quench heaters at a current level of 80 A. The two dashed lines correspond to the measurement of the currents of the two apertures. The full line represents the simulation. (right) Temperature margin to quench for one coil of the MQY. Note the logarithmic time scale.

5 Extrapolation

*When you have a hammer,
all problems start to look like nails.*

ROBERT KAGAN
(Of Paradise and Power)

In the previous chapter the quench model was used to reproduce quench measurements of different LHC magnets. Model parameters were thoroughly determined and the inner state of the magnet could be analyzed.

In this chapter we show the quench analysis of two future accelerator magnets. We study different conventional quench protection concepts, *e.g.* quench heaters or dump resistor, for the inner triplet upgrade quadrupole. For a fast-ramping dipole we investigate the influence of different quench detection thresholds as well as a magnet design protected only by the copper stabilizer.

By nature, the design of future magnets lacks measurement data. Therefore, we extrapolate from the results of existing magnets. The simulation is based on the parameters determined above and adopted to values expected from other simulations or experience.

5.1 Quench Protection Study for the Inner Triplet Upgrade Quadrupole

In the framework of the LHC luminosity upgrade a series of magnets in the interaction region near the experiments ATLAS and CMS will be replaced [Bagl 08]. The protection of one of the inner triplet magnets, the MQXC superconducting quadrupole magnet, is studied. The study has been carried out in an early state of the project in order to demonstrate feasibility and to explore the necessary protection efforts.

Specific attention is given to the evaluation of the different quench protection methods, *i.e.* quench heaters, dump resistor or both. The study consists of the following five parts:

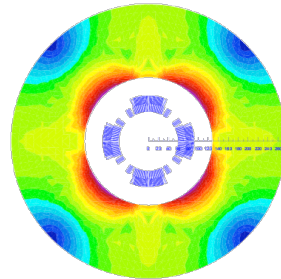


Figure 5.1: MQXC schematic coil cross-section and iron yoke. Outer iron diameter 550 mm.

- Simulation of an unprotected quench, where the magnet is short-circuited upon quench detection and discharged over the normal conducting zone. This motivates the need for quench protection and allows to study the intrinsic quench behavior of the magnet, *e.g.* quench propagation within the coil cross-section.
- Simulation of different quench-heater layouts. The chosen heater setup is checked for reliability in case of a partial heater failure.
- Parametric study of the protection with a dump resistor. The study allows to determine minimum and maximum values in order to guarantee safe operation and to avoid quenching by quench back in case of a regular discharge.
- Discharging the magnet over the power supply and feeding the energy back to the grid.
- Comparison of the two different protection methods and their combination.

The MQXC quadrupole magnet is wound from the same two cables as the LHC main bending magnet (MB), see Sec. C.1. A thorough selection of the strands is expected to result in a 10% higher critical current density [Osto 08]. The magnet features one aperture in a circular iron yoke, see Fig. 5.1. For the time being, no holes for heat exchangers or notches are considered in the iron yoke. The coil consists of four poles in two layers wound from two different cables. The magnet is 10.3 m long with a magnetic length of $\ell_{\text{mag}} = 10$ m [Fess 08]. Neither Helium nor cooling are considered. All parameters were chosen based on the simulation and measurement results of the LHC MB. The full list of parameters can be found in Sec. C.3.

5.1.1 Unprotected Quench

The quench behavior of a magnet depends on intrinsic features of the magnet design, *e.g.* the inductance, quench propagation and induced losses, as well as on the external electrical network. In order to study the intrinsic quench behavior, a quench is simulated at three different locations assuming the magnet to be short-circuited and unprotected. The quench either originates in block 2 conductor 18, in block 1 conductor 14 or in conductor 6 of the same block, see Fig. 5.2 (left).

Figure 5.3 shows the temperature margin to quench versus time for each conductor of the first quadrant. Due to the isolated location of block 2 the quench in conductor 18 can only propagate over the block of quench origin. In the other two cases, the quench propagates also from the inner to the outer layer. Nevertheless, the turn-to-turn quench propagation delay is smallest for the quench in conductor 18. This is due to the higher magnetic induction and the hence smaller temperature margin to quench.

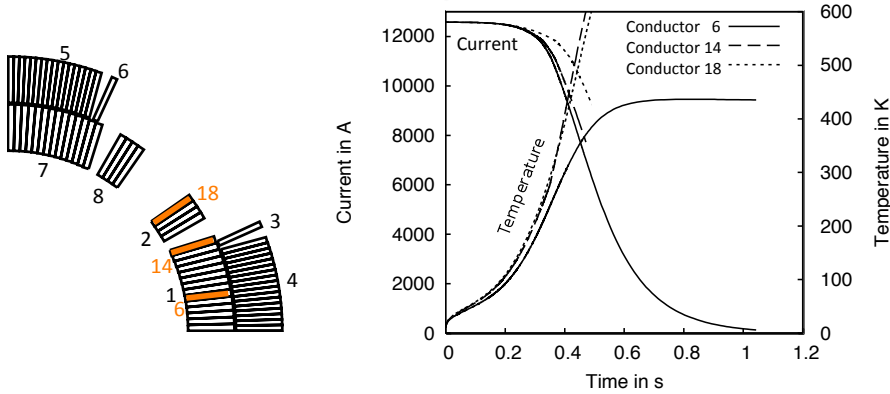


Figure 5.2: (left) LHC MQXC Conductor and coil block numbering scheme for the first quadrant. (right) Temperature and current change versus time for an unprotected quench originating either in conductor 6, 14 or 18. The simulation of the quench starting in conductors 14 and 18 was stopped when the hot-spot temperature exceeded the temperature limit of 600 K.

The faster and further the quench propagates within the coil cross-section, the faster the resistance of the magnet grows. Since the magnet is short-circuited, the internal resistance is the only cause for the current decrease. Figure 5.2 (right) shows the current and hot-spot temperature versus time. The current decrease in case of the quench in conductor 18 begins much later than in the two other cases. This is due to the fact, that the quench could not propagate as far and therefore quench back sets in later (compare Fig. 5.3).

Although the current change is similar for the two quenches in block 1, the hot spot temperature differs significantly. In case of the quench in conductor 14, the quench propagates radially to block 3. Due to its isolated position the single conductor of block 3 cannot transfer any heat. Furthermore, the conductor is located in a region of peak magnetic induction and is made from a different cable than the inner layer. Both result in a higher resistivity and therefore in larger ohmic losses for an identical current. The hot-spot moved from the quench origin to block 3, see Fig. 5.4 (center). The effect of hot-spot movement poses another limitation to the MIITs-concept (Sec. 7.2). Although, the outer layer conductor receives a smaller number of MIITs, it yields the higher temperature due to a different function Υ .

5.1.2 Quench Heater Protection

For magnets where the current discharge merely depends on its internal resistance, *i.e.* a magnet connected to a power supply which is switched off upon quench detection or a magnet which is by-passed in case of a quench, quench heaters can be used for magnet protection (Sec. 7.9.5). For the MQXC two

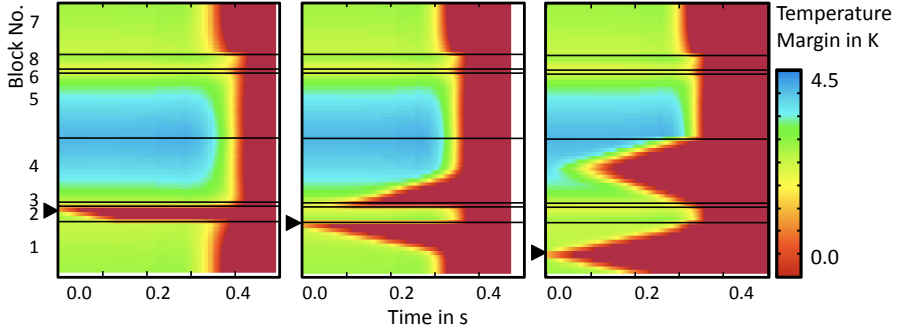


Figure 5.3: LHC MQXC Temperature margin over the conductors of the first quadrant versus time in case of an unprotected quench. (left) The quench originated in conductor 18 (highlighted by a triangle) and spread azimuthally over block 2 only. The turn-to-turn quench propagation delay is approx. 30 ms. (center) The quench originated in conductor 14 and spread radially from block 1 to block 3 and 4. Due to the block boundaries the quench can only propagate azimuthally to one side. (right) The quench originated in conductor 6 and spread to both sides over block 1 as well as over block 4. For the last two cases the turn-to-turn quench propagation delay is approx. 50 ms. Both show quench back in the outer layer at around 0.35 s, compared to 0.4 s in case of a quench in conductor 18. Quench back in the inner layer appears 0.025 s before.

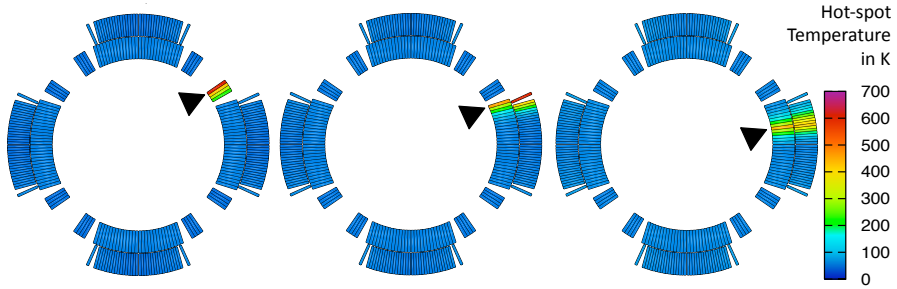


Figure 5.4: LHC MQXC hot-spot temperature over the coil cross-section at the end of an unprotected quench. (left) The quench originated in conductor 18 (highlighted by a triangle) and spread over the entire block 2. (center) The quench originated in conductor 14 and spread from block 1 to block 3 and 4. Note that the hot-spot is located in block 3 and not where the quench originated. (right) The quench originated in conductor 6 and spread to both sides over block 1 as well as over block 4. This case shows the lowest hot-spot temperature.

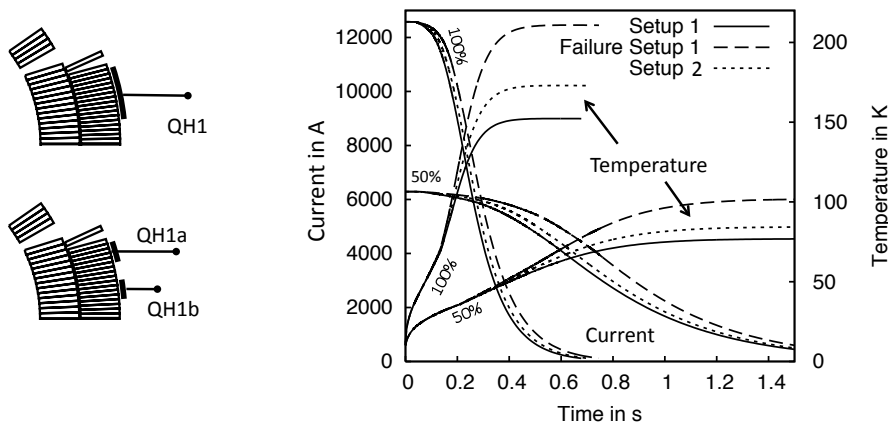


Figure 5.5: (left) LHC MQCX Quench heater layouts. (top) Setup 1: The quench heater strip covers 11 conductors. It is connected in series to the strip below the horizontal plane as well as to two strips on the other side of the aperture. The connection scheme is shown in Fig. C.8. (bottom) Setup 2: Each strip covers 4 conductors. Both belong to different heater circuits consisting of 4 strips at similar locations. (right) Temperature and current change versus time for 3 different heater setups and for two different initial current levels. In addition to the heater setups 1 and 2 a heater failure in setup 1 is simulated. The initial current levels are the nominal current and half the nominal current.

different heater designs were suggested as shown in Fig. 5.5 (left). The first layout covers 11 conductors per heater strip and features two independent electrical circuits; the second layout covers 4 conductors per strip and constitutes 4 circuits [Fess 08].

The quench heater delays, *i.e.* the time between firing the heater circuits and detecting a quench in one of the covered conductors, is expected to be identical to values measured for the LHC main bending magnet (MB) [MQXC 08a], since the same cable and heater technology is used. The quench heater model parameters (quench heater delay time and quench heater power) have been determined as for the LHC main bending magnets (Sec. 4.1.1).

The quench heater performance is compared at nominal and half the nominal current. Setup 1 yields a faster current decrease and therefore a lower hot spot temperature, see Fig. 5.5 (right). This is due to the larger resistivity built up by in total 88 compared to 64 conductors covered by quench heaters. Furthermore, quench back sets in approximately 0.02 s earlier in setup 1.

For setup 1, a quench heater failure is simulated. We assume that four heater strips are connected in series to one quench heater power supply covering half of each pole, see Fig. C.8. The magnet is supposed to be protected even if one power supply fails to fire. Figure 5.6 (center) shows the hot-spot temperature at the end of the quench in comparison to the setup 1 (left) and 2 (right). For the heater failure the highest temperatures are obtained, but considering a temperature limit of 300 K the magnet can still be regarded as protected.

In all three cases hot-spot movement can be observed - most pronounced in case of the heater failure. The temperature plot in Fig. 5.5 shows a kink at around 0.15 s for a quench at nominal current. The two slopes result from the different thermal properties of inner and outer layer cable. For a quench at half the nominal current the kink is harder to observe, but hot-spot movement persists.

The temperature margin of a conductor increases with decreasing current. Hence, more energy is required to quench a conductor. The efficiency of quench heaters is reduced at lower currents what results in longer quench heater delays. Figure 5.7 (bottom) shows the variation of the temperature margin over all conductors of the first quadrant versus time for a quench at half the nominal current and protection by setup 1. Compared to the cases at nominal current (top) the quench process is much slower, *e.g.* quench back sets in only after 0.55 s. Regarding the conductors covered by quench heaters, the conductors with the smallest margin on the outside of the block quench first. The hot-spot temperature of all three different cases is around half the value of the quench at nominal, see Fig. 5.5 (right).

In the following, setup 1 will be used since it gives the lowest hot-spot temperature, is reliable also in case of a heater failure and at half the nominal current, and consists of a smaller number of electrical circuits which might malfunction.

5.1.3 Dump Resistor Studies

Alternatively or complementary to quench heaters, the magnet can be protected by means of a dump resistor. Upon quench detection, the dump resistor is switched into the electrical circuit causing the current to decrease. If the current decreases fast enough, induced losses cause quench back, spreading the normal zone over the entire magnet and therefore accelerating the current decrease. If a dump resistor is used to discharge the magnet without a pre-existing quench, the current change rate needs to be limited in order to prevent quench back. For more details see Sec. 7.9.2.

For an analysis of the magnet quench behavior an energy extraction study is performed. The magnet is discharged over a dump resistor of variable resistance and the extracted energy, *i.e.* the energy dissipated in the dump resistor, is compared to the total energy initially stored in the magnet. The study is performed once with a quench initialized in conductor 18 and once without pre-existing quench. The dump resistor is switched in after detection without additional delay.

Figure 5.8 shows exemplarily the current decrease and temperature rise in the magnet for two different dump resistors, 2 m Ω and 20 m Ω , respectively. In case of the pre-existing quench, the dump resistor of 2 m Ω shows to be too small to provide sufficient protection (the computation was stopped when the temperature limit of 600 K was reached). The larger resistor reduces the hot-spot temperature to 130 K. In absence of a quench, the magnet is quenched after 3.9 s and 0.05 s, respectively. The induced losses and the absence of

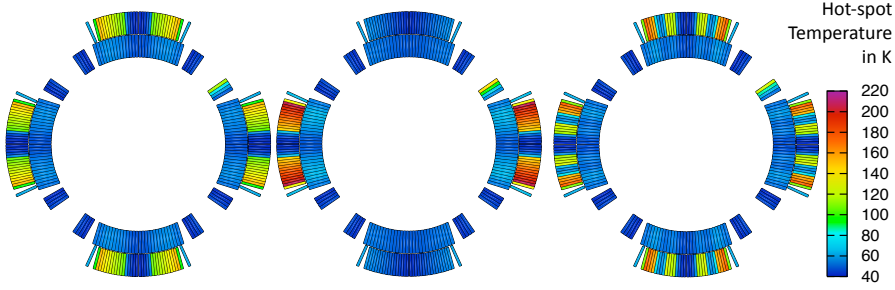


Figure 5.6: LHC MQXC hot-spot temperature in the coil cross-section at the end of the quench for different heater setups and a simulated heater failure. (left) Setup 1 (center) Setup 1, where one heater circuit fails, *i.e.* half the strips are not fired. (right) Setup 2.

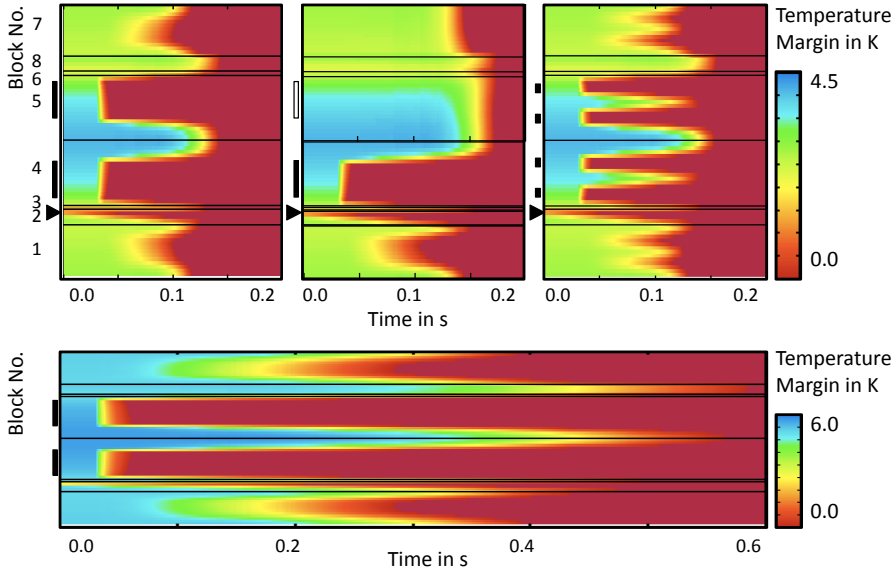


Figure 5.7: LHC MQXC Temperature margin over the conductor of the first quadrant versus time for different heater setups and a simulated heater failure. The quench heater positions are indicated by a black bar on the side. The failing heater is indicated by a white bar. The quench origin is highlighted by a triangle. (top) Quench at nominal current level. (left) Setup 1 (center) Setup 1, where one heater circuit fails, *i.e.* half the strips are not fired. (right) Setup 2. (bottom) Quench at half the nominal current level for setup 1. The quench propagation and heater induced quench take much more time than in the cases above.

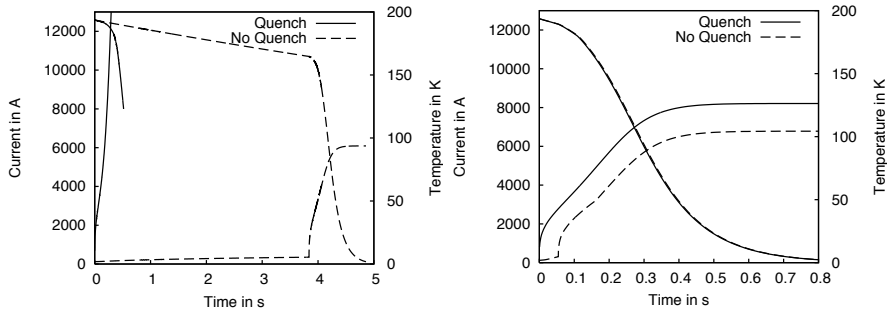


Figure 5.8: LHC MQXC Dump resistor study. The magnet is discharged over a dump resistor. Different resistances were studied in case of a quench and in case of no pre-existing quench. (left) Dump resistor of $2\text{ m}\Omega$. For a pre-existing quench the resistor shows to be too small to significantly reduce the hot-spot temperature. In absence of a quench, the magnet starts to heat up while discharging and quenches due to losses at around 3.9 s. The internal resistance of the magnet accelerates the discharge. (right) Dump resistor of $20\text{ m}\Omega$. The dump resistor shows to be large enough to protect the magnet in case of a quench. The discharge in case of no pre-existing quench causes a stronger temperature rise due to losses compared to the $2\text{ m}\Omega$ case. The magnet quenches after ca. 0.05 s. The hot-spot temperature is lower due to the shorter heating duration and lower current at quench start.

cooling cause the coil temperature to rise above the quench limit.

Figure 5.9 (left) shows the current decrease for all simulated dump resistor values in case of a pre-existing quench. For a dump resistor smaller than $5\text{ m}\Omega$ the simulation was stopped when the temperature limit of 600 K was reached. For a dump resistor larger $10\text{ m}\Omega$ the hot-spot temperature remains well below 300 K. In Fig. 5.9 (right) the same simulation was repeated without initial quench. Only for a dump resistor of $1\text{ m}\Omega$ and below, the magnet does not quench while discharging. In both cases, initially quenched or not, the onset of the current decrease becomes steeper and the current decay curve approaches an exponential decay for an increasing resistor size.

Figure 5.10 shows the extracted energy normalized to the total stored energy for all simulated cases versus terminal voltage. Plotting over the terminal voltage, *i.e.* in this case the voltage across the dump resistor, allows to compare measurement/simulation results for different initial currents. If the magnet is simply discharged over the dump resistor, the extracted energy ratio drops from 1, where no quench occurs, to 0.1 at around $5\text{ m}\Omega$, and then increases again to nearly 0.5. In case of a pre-existing quench, the ratio increases with dump resistor size.

Figure 5.10 also shows the hot-spot temperature for all simulated cases. For a terminal voltage below approximately 100 V, the peak temperature is significantly higher in case of a pre-existing quench (left) although a similar amount of energy is extracted (see above). Compared to the confined pre-existing quench, the quench caused by the induced losses is spread over large fractions of the coil cross-section and thus results in a faster current decay. In the right-hand plot, a significant dip can be observed at around 100 V. Here,

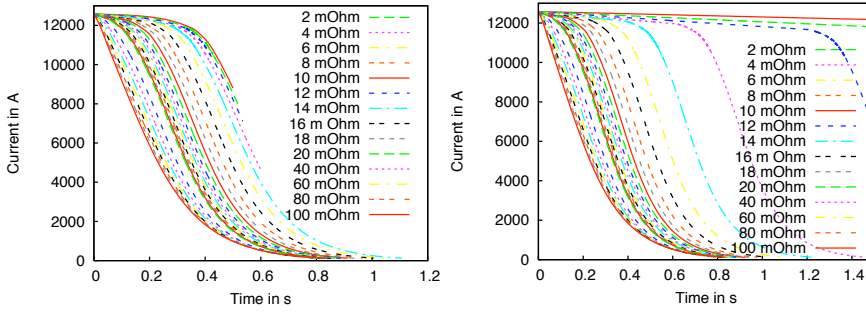


Figure 5.9: LHC MQXC dump resistor study for various dump resistors in the range from 1 to 100 m Ω . Current decrease versus time. (left) In the case of a preexisting quench: The simulations were stopped when the temperature limit of 600 K was reached (1 to 5 m Ω). Aiming at a maximum hot-spot temperature of less than 300 K a resistor greater than 10 m Ω has to be chosen. (right) For the case of no initial quench.

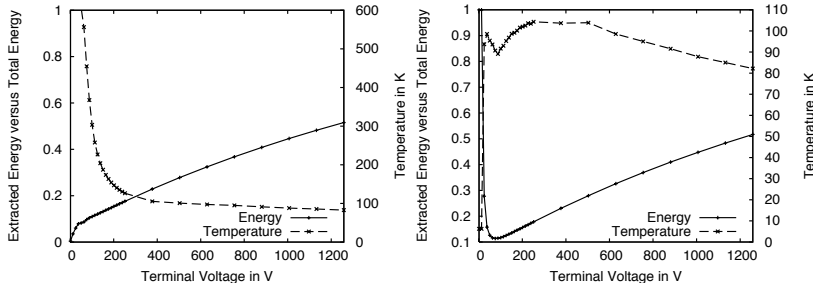


Figure 5.10: Extracted energy versus voltage over the dump resistor. (left) Temperature and extracted energy as function of terminal voltage with initial quench. (right) Temperature and extracted energy as function of terminal voltage without pre-existing quench. The terminal voltage corresponds to the dump resistor size via $U_{\text{Terminal}} = R_{\text{DR}} I_{\text{nom}}$.

the hot-spot moves within the coil cross-section from the inner to the outer layer. Beyond 500 V or 40 m Ω , respectively, the results of both experiments are similar. Notice the different scales on the temperature axis.

The maximum terminal voltage as well as the voltage over the dump resistor was set to 500 V. Therefore, for the magnet protection a dump resistor of 40 m Ω is chosen since it yields the smallest hot-spot temperature with a terminal voltage of 503 V for a quench at nominal current. The current decrease and temperature rise are shown in Fig. 5.11 (left). For a dump resistor of 1 m Ω (corresponding to a terminal voltage of 12 V), the magnet can be safely discharged without causing a quench. All stored energy can be extracted, see Fig. 5.10 (right).

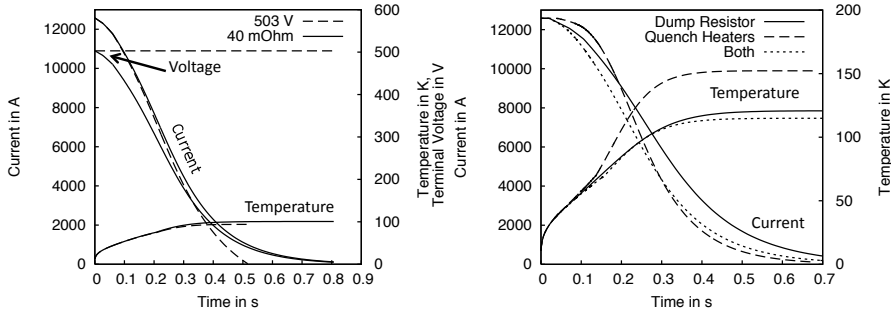


Figure 5.11: (left) Current extraction by inverting the power supply (dashed line). The full line shows the protection by means of a dump resistor. The initial and maximum voltage are identical 503 V. While for a dump resistor the voltage over the magnet decreases with the current, it remains constant for the power supply and causes a faster current decay at the end of the quench. (right) Comparison of the three different protection methods. When quench heaters and dump resistor are used, the peak temperature is about the same as before

5.1.4 Power Supply Inversion

A power supply which can be operated in two quadrants, *i.e.* which can provide a positive and negative output voltage for a positive current, can be used to actively drive down the magnet current in case of quench. This has three advantages to a dump resistor. The stored magnetic energy is not dissipated in heat, but fed back to the power grid; no-cool down time for the dump resistor has to be observed; and for a given maximum voltage, the current decrease is faster.

As part of the study, the protection of the magnet with the dump resistor chosen above is compared to the protection with a power supply. The power supply provides constant -503 V over the magnet which is identical to the initial voltage over the dump resistor. Figure 5.11 (left) shows the current decrease and temperature rise in comparison. The discharge into the grid results in a slightly smaller temperature due to the faster current decrease at the end of the quench.

5.1.5 Full Protection

Figure 5.11 shows the current and temperature change for quench protection by means of quench heaters, a dump resistor or the combination of both. The quench is detected and validated after 10 ms. The dump resistor of $40\text{ m}\Omega$ is switched into the circuit after an additional delay of 10 ms.

All three temperature graphs show the distinct kink which indicates hot-spot movement - most pronounced for the protection with quench heaters only. It is therefore not surprising that the hot-spot temperature in case of the combined protection is only slightly lower than for the dump resistor only.

The quench heaters provoke a quench in the outer layer before quench back does without heaters and therefore these conductors are subjected to ohmic heating for a longer period.

Nevertheless, the combination of both methods has the advantage of a higher redundancy since both methods separately prove to be sufficient.

5.2 Fast-Ramping Dipole

The quench protection of superconducting accelerators is usually based on a reliable detection of a quench, the decoupling of the quenching magnet from the non-quenching magnets by means of diodes or thyristors, an energy extraction system, and the shut-down of the power converters. In recent projects, *e.g.*, the SIS300 dipole magnet for the FAIR project [Henn 04], ramp-rates of 1 T/s, *i.e.* about 1100 A/s, are proposed. The flat-top is considered to last from 10 to 100 seconds. Considering an inductance of about 25 mH for a magnet length of 2.9 m, the ramp-induced voltage across a magnet is 27.5 V. The ring will be powered by several power converters in order to deal with the total voltage of *e.g.*, 3000 V for an installation of 110 magnets.

Calculations below show that a quench detection threshold of 1 V will be desirable during the ramp in order to protect the magnets. The precision of the electronics must be at least a factor 10 better in order to cover unexpected behavior such as parasitic transient effects. This is no technological challenge at the flat-top. However, during the ramp the induced voltage across a magnet rises in a short time to 27.5 V, while the common mode voltage rises to ± 1500 V (or 300 V if five independent powering sub-sectors are chosen). In particular during the acceleration and deceleration of the ramps, the required 50 dB signal to noise ratio (detection precision of 0.1 V over a signal of 27.5 V) "riding" on a rapidly changing 84 dB common mode background (Ratio of precision over common mode voltage) is a challenge in a large installation where reliability is the most important requirement.

Based on the fact that a magnet designed for fast-ramping operation can be ramped down much faster than existing superconducting magnets, an alternative possibility can be considered. It would be sufficient to detect a quench on the flat-top or at the injection plateau, if the magnets can survive an undetected quench during the ramp. Bypass diodes would not be needed in this case, which themselves represent a technological challenge. If state-of-the-art power converters with capacitive storage are used, even the dump resistors and switches would not be required.

In the subsequent sections we discuss four aspects of quench simulation for fast-ramping magnets:

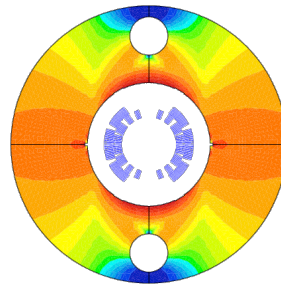


Figure 5.12: Fast-Ramping Dipole. Schematic coil cross-section and iron yoke. Outer iron diameter 504.6 mm.

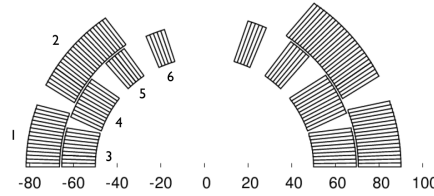


Figure 5.13: The standard coil cross-section of the SIS300 two-layer dipole is shown on the left-hand side of the figure ($x < 0$).

The modified coil cross-section with a wider cable and additional strands for a 50% increase in copper content is shown on the right-hand side. In order to keep the main field, the field quality and the quench margin unchanged, two conductors had to be added to the outer layer. The axis shows the x -position in mm.

- We show the influence of different thermal models (Sec. 3.6) on the simulated coil temperature during the powering cycle.
- We study the ramp-rate dependence of the quench current.
- We investigate the peak temperature in a magnet for undetected quenches during the ramp phases. We compare the cases of quench detection during ramp for a threshold of 1 V and the 100 mV threshold that is standard in slowly-ramping magnets.
- We discuss whether additional copper-content in the coil could protect a fast-ramping magnet for an undetected quench during the ramps, or even during an entire cycle.

For the purpose of this study we simulate the 2-layer design of a SIS300 dipole magnet as defined in [Kozu 06], see Fig. 5.12. The relevant data for the quench calculation is summarized in Sec. C.4. The cross-section of the magnet is illustrated in Fig. 5.13.

We consider conductive cooling via the Kapton insulation to the helium bath across the inner and outer radial surfaces of the coil. The ramp cycle is given in [Kozu 06] as an up-ramp from 1.6 T to 6 T in 4.4 s, followed by a plateau at 6 T of 11 s, and a down ramp to 1.6 T in 4.4 s.

5.2.1 Cooling Schemes

The temperature variation during a ramp-cycle can be calculated with three different thermal diffusion models:

1. Adiabatic conditions, *i.e.*, no cooling and no helium as it is appropriate for potted coils.
2. Heat transfer across the inner and outer radial surfaces without considering confined helium inside the cable.

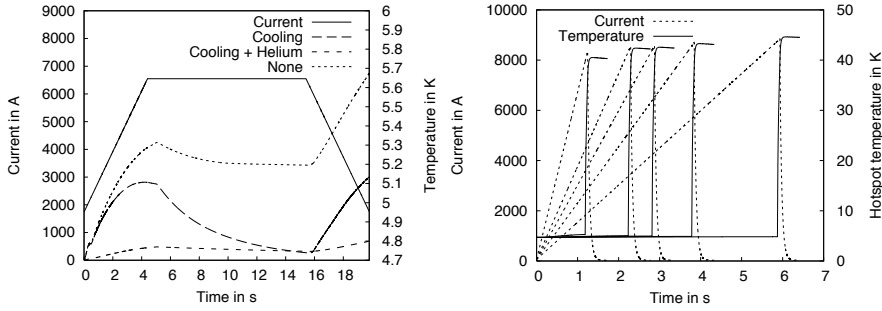


Figure 5.14: (left) Temperature variation during ramp-cycle of the SIS300 dipole magnet. (right) Current and peak temperature in a magnet during an up-ramp to the quench limit and quench detection. The graphs correspond to ramp rates (from right to left) of 1.0 T/s, 1.5 T/s, 2.0 T/s, 2.5 T/s, and 4.5 T/s.

3. Modeling of conductive cooling (see above) and of the thermal capacity of the confined helium (about 10%) inside the cable.

Figure 5.14 (left) shows the temperature variation during one ramp-cycle for the three cases. The temperature variation per cycle is an order of magnitude smaller for the wetted coil, as the heat capacity of helium is dominant at low temperatures. In all cases the temperature decreases at the flat-top. In case of the adiabatic model 1) this is due to the transversal thermal conduction, which is, however, not sufficient to prevent a quench already in the second cycle. In the following model 3 is used, which reproduces data published in [Kozu 06].

5.2.2 Quench Limits at Different Ramp Rates

In Fig. 5.14 (right) we see the evolution of current and peak-temperature inside the magnet for quenches near the flat-top. The magnet is ramped until the quench limit is reached; and the quench protection system detects a resistive voltage of 100 mV. The magnet is protected with quench heaters and a dump resistor, see Sec. C.4. The ramp rate varies between 1.0 T/s and 4.5 T/s.

The temperature in the magnet rises due to ramp-induced losses [Verw 95] that reduce the temperature margin to quench. The quench current thus decreases for higher ramp rates. The peak temperature after quench is also reduced as a consequence of the lower quench current.

In Fig. 5.15 (left) the temperature margin to quench is shown for each conductor in the cross-section as a function of time. The plot corresponds to the fastest ramp-rate in Fig. 5.14 (left), *i.e.* a ramp-rate of 4.5 T/s. The margin reduces steadily as a consequence of increasing current and field, and due to induced losses. At $t = 1.18$ s the magnet quenches in block number 5. The quench is detected at $t = 1.19$ s and the quench heaters are fired at

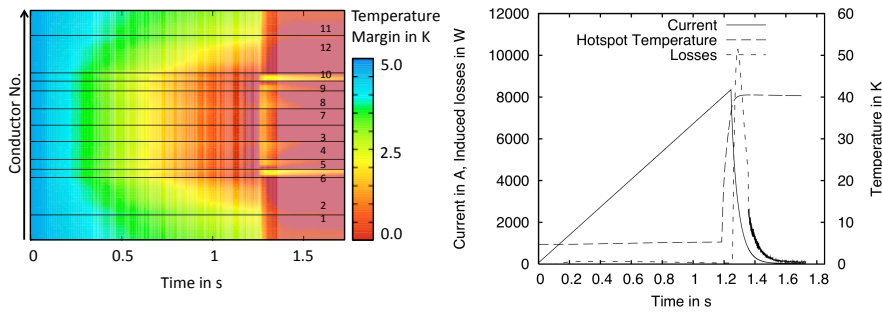


Figure 5.15: (left) Temperature margin to quench versus time for an up-ramp with 4.5 T/s. Block 1, 2, 11 and 12 belong to the outer layer and are partially covered by quench heaters. (right) Current and losses versus time during quench.

$t = 1.24$ s. At the same time the dump resistor is switched into the circuit and the current drops sharply. The quench heaters are effective about 40 ms later.

The temperature margin in the inner layer coil increases after the quench. As a matter of fact, a number of conductors recover from quench. This is explained by the fact that the current density and field in the superconductor drops quickly. The time constant of the induced eddy-current losses in the cable, however, is of about 50 ms, compare Fig. 5.15 (right). Moreover, the heat capacity of the confined helium in the cable results in a long thermal time constant. This explains why the temperature rise due to induced losses is slow and the margin grows immediately after the dump resistor is switched in. Eventually the inner layer is quenched by induced losses. The block number 6, see Fig. 5.13, does not get an equal share of induced losses. The reason is that it is placed in parallel to the electromagnetic field. The Rutherford cable used for the SIS300 magnet has a stainless steel core, which reduces the cross-over resistance. Consequently, very little eddy-currents are induced in a cable that is positioned in parallel to the field lines.

5.2.3 Quench Detection During the Up- and Down Ramp

We study the current decay and peak-temperature after a quench during the up-ramp. Different detection scenarios are investigated. Quenches are assumed to occur at either 50% or 75% of the plateau level. Quenches are detected either only at the plateau, or when the resistive voltage has reached a threshold of 100 mV or 1 V. Figure 5.16 (left) shows the current and peak-temperature evolution for the six different cases.

An undetected quench during the up-ramp leads to a fatal temperature rise in the magnet. The earlier the quench occurs during the up-ramp phase, the higher is the peak-temperature. A detection threshold of 1 V during the ramp is sufficient to protect the magnet against quenches occurring at 50%

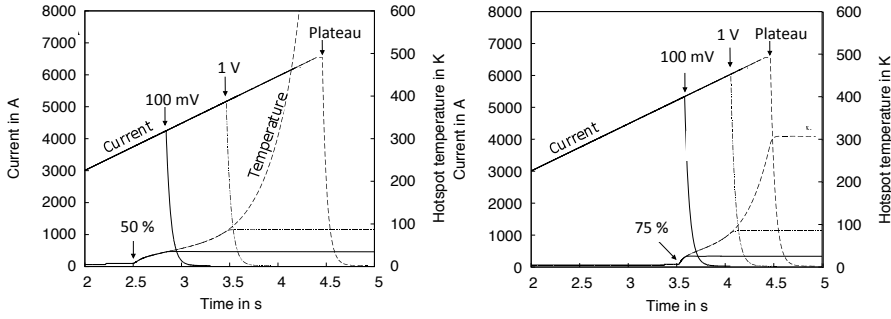


Figure 5.16: Current decay and peak-temperature for quenches during the up-ramp phase. A Quench is initiated at 50% (left) or 75% (right) of the nominal current level. It is assumed that quenches can only be detected at the plateau (dashed line), at a resistive voltage threshold of 1 V (dash-dotted line), or 100 mV (continuous line).

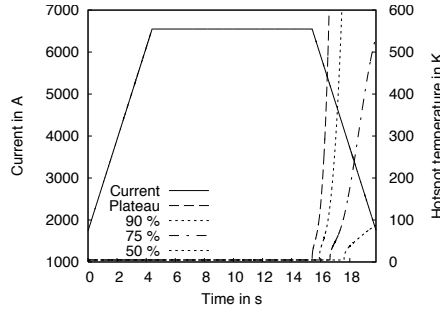


Figure 5.17: Current- and peak-temperature evolution for quenches during the down-ramp. Quenches start at the end of the plateau, at 90%, 75%, and 50% of the nominal current level. It is assumed that quenches can only be detected at the injection level.

of the plateau level. The delays of the protection system can be deduced from Fig. 5.16 by taking the time laps between the first rise in temperature and the point where the current decays (and the energy is extracted by the dump resistor). The detection delays are longer at lower excitation, since the resistive voltage rises more slowly.

In Fig. 5.17 the same exercise is carried out for quenches occurring on the down-ramp. It is assumed that quenches can only be detected at the injection level. Comparison with Fig. 5.16 shows that quenches occurring near the upper plateau are more critical during the down-ramp than during the up-ramp. This was expected, since a current is forced to flow through the quenched magnet during a longer period of time.

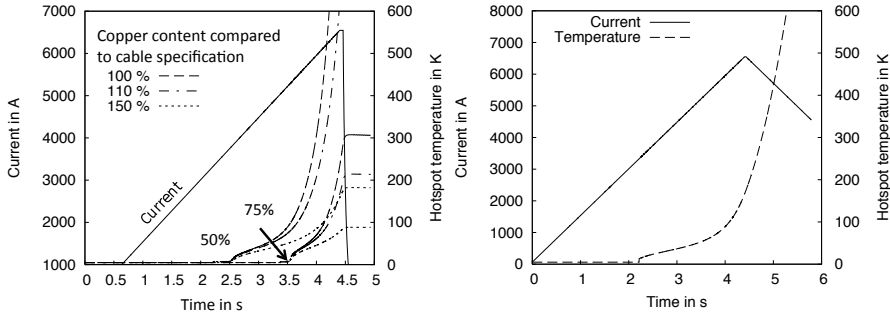


Figure 5.18: (left) Peak-temperature and current evolution during quenches at 50% and 75% of the plateau level. It is assumed that the quench cannot be detected until the plateau is reached. The simulation is carried out for the SIS300 conductor, as well as for conductors that have a 10% to 50% higher copper content. (right) Peak temperature and current evolution during a quench. The quench starts at 50% of the up-ramp. It is detected at the plateau. Then the magnet is immediately driven down with the standard slope.

5.2.4 Robust Magnet Design

We can also investigate how much copper would need to be added to the Rutherford-type cable so that the magnet survives an undetected quench during a ramp. Figure 5.18 (left) shows quenches occurring at 50% and at 75% of the plateau for different copper content. The baseline of 100% is given by the cable described in Sec. C.4.1. In case of 150% copper we added strands and increased the copper-to-superconductor ratio for all strands, to result in 50% more copper and the same amount of Nb-Ti superconductor. As the cables become wider, the coil cross-section is re-designed with two more conductors in the outer layer, in order to maintain the field quality, see Fig. 5.13 (right-hand side). The inductance of this coil increases by about 10%. It can be seen in Fig. 5.18 (left) that this magnet could survive a quench that occurs half-way on the up-ramp and that is detected only at the plateau.

Active protection may be reduced to a strict minimum, if a magnet contains enough copper to survive a full powering cycle with an undetected quench. We assume that a quench occurs at 50% of the up-ramp, that it is detected at the plateau, and that the magnet is then ramped-down immediately with the regular ramp rate. For the cable with 50% extra copper, Fig. 5.18 (right) shows the temperature evolution. This cable had survived an undetected quench during an up ramp, see Fig. 5.18 (left). We can see that the magnet is not sufficiently protected for the shortened cycle. It follows that for a magnet with only 50% additional copper a method of fast current shut-down is indispensable.

6 Conclusion and Outlook

Rerum cognoscere causas

VIRGIL
(70 BCE - 19 BCE)

Most quench models published in the literature either focus on a single aspect of the quench process, such as *e.g.* the propagation of the quench, or cover parts of the quench process with constant parameters, *e.g.* a constant inductance of pre-calculated field maps. An exception is the coupled approach of AIRD, which on the other hand does not permit to calculate internal voltages.

The quench algorithm presented in this thesis, solves the numerical models of all relevant physical effects in a coupled approach. This allows to model the interdependence of various physical phenomena, *e.g.* quench propagation, induced losses, and quench back. Adaptive time-stepping is implemented to resolve the highly nonlinear behaviour of materials such as the heat capacity or the electrical resistivity.

The user is required to supply data for the characterization of the magnet protection system, electrical and thermal properties of cable and insulator materials, as well as geometrical description of the magnet. The data must be available at a wide temperature range reaching down to cryogenic temperatures, and for a range of magnetic fields and pressures.

Given the large number of empirical parameters in the models, it must be noticed that an important part of the simulation work consists of the determination of parameters such that the simulation matches the measurement. It is important to realise that only when all relevant phenomena have been taken into account and modelled accurately, the choice of material parameters is physically reasonable and within the range of measured values, the simulation result matches the measured data within the uncertainty of the measurement. Then we are able to reproduce the internal states of a quenching magnet, *i.e.*, observe quantities that evade measurement.

With this approach we could observe the movement of the hot-spot within the coil cross-section and find an explanation for the voltage ripples during the first phase of a quench. Under the aforementioned premise, the model can be used for extrapolation; for the comparison of different protection methods and for a study of design options for future magnets.

The special properties of the materials used in superconducting accelerator

magnets, *i.e.* field dependent, diffusive, and exhibiting hysteresis, required a review on the formulae for the electromagnetic energy and the concept of the inductance. Furthermore, an expression for the instantaneously dissipated power (in contrast to the dissipated energy) was derived for the superconductor hysteresis losses.

Critical conclusion Regarding the large number of parameters in comparison to the limited number of observables, the famous quote on fitting an elephant comes to mind¹. However, the range and hence the impact of every parameter is limited by the underlying physical models. Therefore, fitting means to adjust the influence of all physical phenomena involved in the quench process, and the interpretation of the necessary set of parameters offers additional understanding of the process. Parameters which would need to be chosen outside the physically reasonable domain in order to fit measurements indicate an incomplete model² and give rise to further refinement.

Critical Outlook Not all aspects of the modeling of superconducting magnets and quench simulations could be treated in this dissertation. Some had to be disregarded because they exceed the scope of a thesis in electromagnetic theory, some due to the limitation of computing power and some because adequate models were not yet available. Therefore, future work should address the following aspects:

- The magnetic field and cable magnetization model are static and calculated in 2D. The calculation of cable eddy currents relies on the assumption of superconducting strands and is therefore only weakly coupled to the magnetic field computation. This approach allows to describe the magnetic field in long accelerator magnets operated close to the critical surface.

With increasing computing power the following approach could be implemented: Improving the magnetic field model to full, time-transient 3D. This allows to consider the variation of the magnetic field over the coil ends, the change of magnetic length with iron saturation and induced eddy current losses in copper wedges. Including the current and temperature dependence of the superconducting strands into the models for cable eddy currents requires a cable model down to the level

¹ “Fitting an elephant” was attributed to C. F. Gauss, N. Bohr, Lord Kelvin, and E. Fermi, and R. Feynman [Brow 03]:

Give me four parameters and I can fit an elephant. Give me five and I can wag its tail.

² Consider an electromagnetic wave in an arbitrary medium. In a first approach we describe the problem by means of the wave equation. If measurements can only be reproduced applying complex values for the electrical permittivity, we conclude that the wave exhibits losses in the medium, and that the problem was ill-posed: it is correctly described by an electromagnetic wave equation with an additional term carrying the first time derivative (comparable to the telegrapher’s equation on transmission lines).

of individual strands resulting in longitudinal variations of the induced magnetic fields. The magnetic field and eddy current models have to be strongly coupled. This way, one could take into account the current redistribution between adjacent strands, simulate the signal for quench antennas and consider the voltages induced by eddy currents.

- The presented thermal model is designed for the calculation of quench in magnets operating close to the critical surface and protected by quench heaters. Heat transfer, cooling and the physics of liquid helium are only implemented in a rudimentary fashion.

The thermal network should be extended using a Finite-Element Approach (with a higher resolution), modeling the cooling channels through the coil and the iron yoke, and including a helium mass flow, *i.e.* convective cooling. Furthermore, the strand/cable helium interface should be studied for possible homogenization, *i.e.* how to include the limitation of the heat transfer without resolving below the dimensions of a strand.

This would allow to simulate magnets cooled by forced-flow helium, to study magnets with big thermal margin and to analyze the impact of heat depositions within the coil cross-section.

- The quench algorithm is based on the assumption that the time constants of the magnetic field and cable magnetization model are much longer than the ones of the thermal model. The electrical network model works as a synchronization agent between the two time scales.

The coupling between the different sub-models should be made more flexible allowing for changes of the individual time scales. This requires a detailed analysis of the coupling between systems by means of input values and variation of parameters.

- The presented model disregards all mechanical aspects of a quench, *i.e.* the triggering of a quench by a sudden conductor movement and heat of friction, or the mechanical tension in the coil cross-section due to thermal expansion of the different components during a quench.
- The presented approach for the computation of the instantaneously dissipated hysteresis losses in superconductors should be generalized. It should include the field and temperature dependence of the critical current density and be applied to circular geometries in order to describe superconducting strands.

7 Detailed Treatment

*I didn't have time to write a short letter, so I wrote
a long one instead.*

MARK TWAIN
(1835-1910)

7.1 Margins to Quench

In order to secure safe and stable operating conditions of superconducting accelerator magnets, margins to quench, *i.e.* intervals between working and critical conditions, are defined and monitored during design and operation.

All margins to quench are derived from the critical current density. The quenched state is reached when the applied current density exceeds the critical current density, or the critical current is zero. This approach is conservative since the transition from superconducting to normal conducting state is not abrupt. Note that safe, but probably unstable, operation conditions can be realized beyond the critical current density limit (Sec. 7.5.1).

It should be noticed that the definition (Sec. A.2.4) and derivation of the critical current density (Sec. D.3) contain some uncertainty.

7.1.1 Current Density Margin

The current density margin $\Delta J_c(B, J, T)$ denotes the difference between transport current density J and critical current density J_c ,

$$\Delta J_c(B, J, T) = \begin{cases} J_c(B, T) - J & J < J_c(B, T) \\ 0 & \text{else} \end{cases}. \quad (7.1)$$

The current density margin is highlighted in Fig. 7.1 by means of a blue vertical line for two different working points (B_1 and B_2).

7.1.2 Temperature Margin

The transition temperature, or critical temperature of a superconductor, $T_c(B, J)$, is a function of the applied magnetic induction and current density. It can be calculated from the critical surface parameterization J_c by

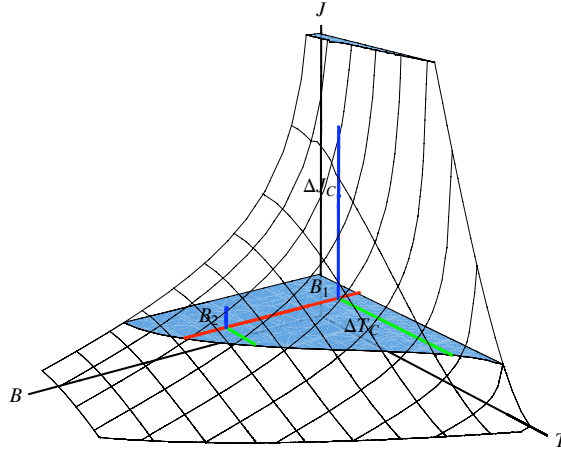


Figure 7.1: Margins to quench: Given are a constant operating current density (horizontal plane) and temperature (red line). The temperature margin to quench for different fields are highlighted by horizontal lines in the plane (green). The current margin is highlighted by vertical lines (blue).

solving the equation

$$T_c(B, J) = \min\{T | \Delta J_c(B, J, T) = 0\}. \quad (7.2)$$

Equation (7.2) poses an implicit root-finding problem depending on 3 quantities. The solution relies on numerical algorithms as, *e.g.*, NEWTON's method [Stoe 05, pp. 301]. Figure 7.3 (left) shows the critical temperature as a function of local magnetic induction for different values of applied current density. The temperature margin to quench is then given by [Siem 05]:

$$\Delta T_c(B, T, J) = \begin{cases} T_c(B, J) - T & T < T_c(B, J) \\ 0 & \text{else} \end{cases}. \quad (7.3)$$

The temperature margin to quench is highlighted in Fig. 7.1 by a horizontal green line for two different working points. Figure 7.2 shows the temperature margin to quench for the LHC main dipole, for injection and nominal current level. At low excitation the temperature margin is 7 K and nearly no differences can be noticed over the cross-section. At high excitation the margin reduces to 1 K where the magnetic field is highest, while the margin of 6 K remains in the low field region.

Autobahn
plot

Plotting the temperature margin to quench for each conductor versus time gives a very good tool to analyze the sequence of events during a quench. Due to the non-linear root-finding process this is computationally costly. Similar results can be achieved plotting the current density margin.

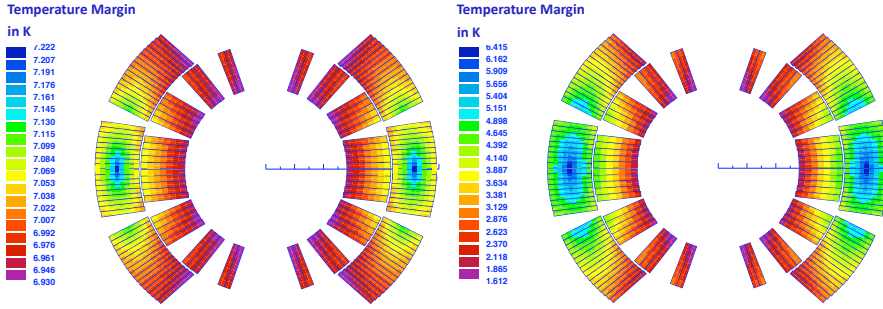


Figure 7.2: Temperature margin to quench, ΔT_c for the LHC MB at injection current level (left) and at nominal current level (right).

7.1.3 Margin on the Load-line

The margin on the load-line is a global criterium for a constant operation temperature, $T_{op} = \text{const.}$. It has little implication on quench computation in accelerator magnets. It is mentioned here for the sake of completeness and because of its common use in magnet design.

The performance of a magnet is limited by the peak magnetic induction in the coil. The function of peak field versus excitation current density is called load-line. For safe operation the working point P_W , *i.e.* the pair of applied current density J and peak field B_{peak} on the conductor, must not exceed the limit given by the critical current density $J_c(B)$. Extrapolating the working point onto the function of the critical current density yields the "quench point", P_Q , an estimate for the quench field respectively quench current density (see Fig. 7.3 (right)). The distance from the working point to the quench point, divided by the distance of the quench point to the origin, yields the margin on the load-line (usually expressed in per cent).

$$\text{Margin-on-the-Load-line} = \frac{\overline{OP_Q} - \overline{OP_W}}{\overline{OP_Q}} \quad (7.4)$$

7.1.4 Enthalpy Margin/Energy Reserve

Consider a volume V of homogeneous volumetric specific heat c_{eff} and temperature T_s . The volume is thermally isolated and the work done by the system can be neglected, *i.e.* the pressure p does not change. An external heat flux causes the temperature of the system to rise. Without heat transfer, the amount of external energy and the change of the temperature in the volume V are related by

Definition

$$\Delta H(T) = V \int_{T_s}^T c_{\text{eff}}(\tau) d\tau, \quad (7.5)$$

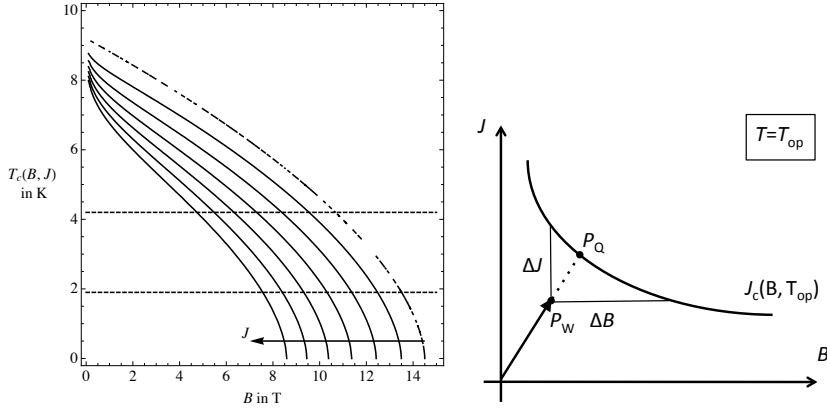


Figure 7.3: (left) Critical temperature T_c as a function of applied current density J and local magnetic induction B . The discontinuous (due to bad conversion of the root-finding) line represents zero applied current density. The current density is increased between two successive lines by 20% of the current density used to obtain a field of 8.4 T at 1.9 K. The dotted lines represent the two common operating temperatures 1.9 K and 4.2 K. The temperature margin to quench, ΔT_c is the vertical distance between the dotted line and the line of T_c . (right) Margin on the load-line.

as can be easily derived from the continuous heat equation (3.35). The energy reserve ΔH is also called the change of the enthalpy of the system. For an effective specific heat greater than zero, the change of enthalpy yields a monotonous function and is invertible. The inverted function allows to calculate the temperature change for a given external energy.

The change of energy density from the operating temperature T_s to the critical temperature T_c is called the energy density reserve, or enthalpy density margin,

$$\Delta h_c = \frac{\Delta H(T_c)}{V}, \quad [\Delta h_c] = \text{mJ cm}^{-3}. \quad (7.6)$$

Approach

The stability of the operation of superconducting magnets against beam losses can be estimated by means of the energy density reserve [Jean 96]. Depending on the time and spatial distribution of the beam losses, different parts of the superconducting cables are considered [Boci 06] and represented in the applied effective specific heat (see Sec. B.2.3).

strand, very fast - Δh_c^{str} The beam interacts with part of one strand. The pulse is too short to allow significant heat transfer along the strand or transversally. The temperature increase is calculated from the strand properties only. Exceeding the enthalpy margin causes the strand to quench and the current to re-distribute into the neighboring strands.

cable, very fast - Δh_c^{cab1} The beam losses interact with the cable homogeneously over the full cross-section and length. The beam particles interact only with the metal part of the cable. The loss pulse is too short

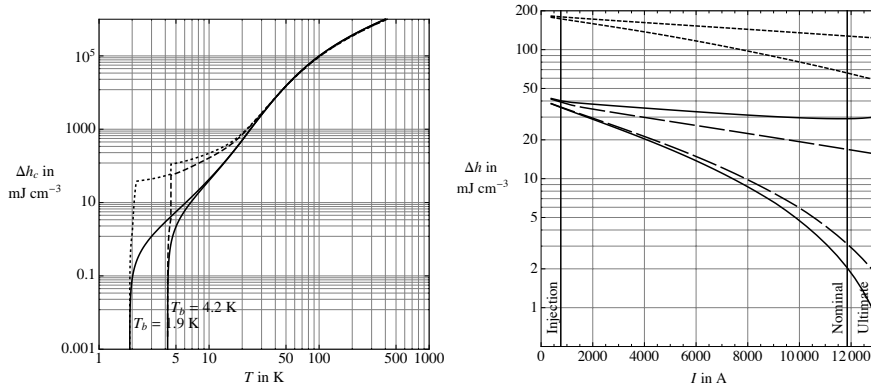


Figure 7.4: (left) Energy reserve density Δh_c between the bath temperature T_b and the elevated temperature T . The continuous line represents the energy change of a strand. The dashed line represents the energy change for a cable with %10 insulation and 2% liquid helium. (right) Minimum and maximum energy reserve density within the LHC main dipole coil cross section for a strand (full), a cable with (dotted) and without (dashed) helium and insulation.

for a significant energy transfer to the helium in the cable. The temperature increase is calculated from the average properties of the strands of the cable.

cable, fast - Δh_c^{cab2} As for Δh_c^{cab1} but with a longer duration so that the heat can be transferred to helium and the insulation, but it is too short for significant heat transfer along the cable or to neighboring cables. All materials of the cable are considered for the effective specific heat. If the cable temperature is below the vaporization temperature of helium, the latent heat of vaporization has to be considered with approximately 2.6 J cm^{-3} for helium (see Sec. A.3.3).

Note, in case of Δh_c^{cab2} it is incorrect to speak about enthalpy density margin [Jean 96] since the enthalpy is defined for constant pressure. For helium the pressure changes significantly when the temperature increases over the point of evaporation (see Sec. A.3.2).

Example : Energy reserve of the LHC main dipole (MB) Considering a strand and a cable of the LHC MB outer layer and assuming a confined helium content of approximately 2%, Fig. 7.4 (left) shows the energy reserve Δh_c^{str} and Δh_c^{cab2} between the bath temperature T_b and the elevated temperature T . The helium creates a thermal buffer and increases the reserve by a factor 100. The temperature of the cable does not change up to an external energy of 40 mJ cm^{-3} . The influence of the helium is much less pronounced if the operation temperature is 4.2 K. Beyond 15 – 30 K the influence of the helium fully vanishes due to evaporation and the strong increase of specific

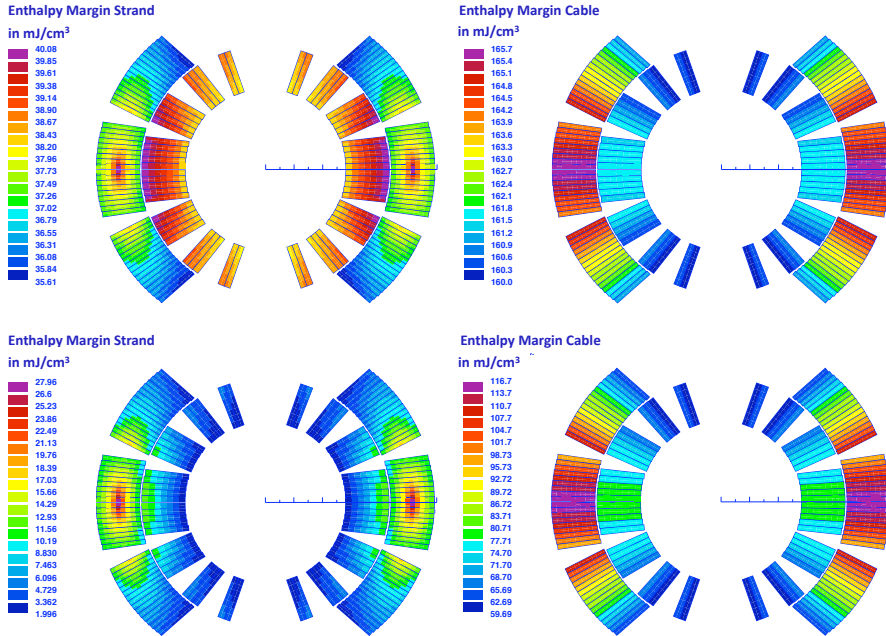


Figure 7.5: Energy margin to quench Δh_c for the LHC MB (see Sec. C.1) with 2% helium in the cable. The upper row shows the margins at injection current level and the lower row at nominal current level. The left column shows the enthalpy margin in the strands for fast losses and the right column the energy reserve of the cable for slow losses.

heat of the other solids.

Figure 7.5 shows the energy reserve of a strand (top) and cable with helium (bottom) over the coil cross-section for injection (left) and nominal (right) current. Due to the minimum of the magnetic field at the mid-plane of the coil, strands in that region show only very little change of margin between both current levels. Figure 7.4 (right) shows the minimum and maximum energy reserves within the coil cross section over excitation.

7.1.5 Minimum Quench Energy

The energy reserve in Sec. 7.1.4 neglects all heat transfer, cooling and current redistribution and is therefore a conservative estimated for most disturbances. The minimum quench energy (MQE) takes into account the full thermal system of the superconducting cables, including recovery from quench. It expresses the minimum amount of energy and its distribution within the cable in order to irreversibly drive a conductor into the normal conducting state. The MQE can not be expressed analytically and requires measurements or simulations as in [Will 08a, Will 08b].

7.2 MIITs

Following the approach of MADDOCK and JAMES the hot spot-temperature in a superconducting magnet after a quench can be calculated from the recorded current decrease [Wils 83, pp. 201]:

A time dependent current $I(t)$ flows through a volume $V = A\ell$. The volume consists of a conducting fraction $\eta_A^{\text{Cond.}}$ with electrical resistivity ρ_E and a fraction of negligible conduction (see Fig. 2.7 for a comparison of the resistivity of the different cable materials). The effective volumetric specific heat of the total volume is c_V^{eff} . Neglecting any kind of cooling or heat transfer out of the considered volume, the dissipated ohmic power $P = I^2 \rho_E \ell / (\eta_A^{\text{Cond.}} A)$ results in a temperature rise:

Area ratio:
Sec. B.2.1

Effective
specific
heat: Sec.
B.2.3

$$\underbrace{\rho_E(B, T, RRR) \frac{\ell}{\eta_A^{\text{Cond.}} A}}_P I(t)^2 = A \ell c_V^{\text{eff}}(T) \frac{dT}{dt} \quad (7.7)$$

For constant magnetic induction $B = B_0$, Eq. (7.7) can be re-arranged and separated. Integrating the left-hand side over time from quench start t_q to $t \rightarrow \infty$, *i.e.* until the current decreased to zero, and the right-hand side over temperature from operation or bath temperature T_b to the final temperature T yields:

$$\begin{aligned} \text{MIITs} &= I_0^2 (t_{\text{val}} - t_q) + \int_{t=t_{\text{det}}}^{\infty} I(t)^2 dt \\ &= A^2 \eta_A^{\text{Cond.}} \underbrace{\int_{T_b}^T \frac{c_V^{\text{eff}}(\tilde{T})}{\rho_E(B_0, \tilde{T}, RRR)} d\tilde{T}}_{\Upsilon(T)|_{B_0}} \end{aligned} \quad (7.8)$$

The integral on the left-hand side is denoted mega current-square time integral (short: MIIT-integral)¹ and its value MIITs ($[\text{MIITs}] = \text{MA}^2\text{s}$). The integral on the right-hand side constitutes a function Υ depending on the material mix in the volume and the applied magnetic induction B_0 . For $c_V^{\text{eff}}/\rho_E > 0$ for all T , the function Υ is monotonous and can be inverted giving the hot-spot temperature $T_{\text{hot-spot}}$:

Introduction
of Υ

$$T_{\text{hot-spot}} = \Upsilon^{-1} \left(\frac{\text{MIITs}}{A^2} \right) \Big|_{B_0}. \quad (7.9)$$

Figure 7.6 (left) shows the function Υ for different materials. The large differences in resulting hot spot temperatures mainly stem from the differences in electrical resistivity. Adding about 2% of helium to cable significantly changes the function Υ for temperatures above 50 K.

¹ In the field of power electronics, the so-called ‘‘Grenzlastintegral’’ $\int i^2 dt$ is used to estimate the overload protection of semi-conductors for short over current pulses [Lapp 91, p. 101].

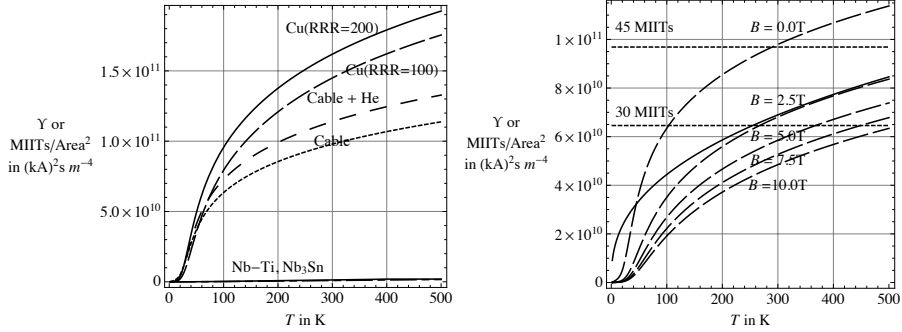


Figure 7.6: MIITs or Υ computation. (left) MIITs versus temperature for different materials. In case of the cable, only the resistivity of copper is considered. In all other cases the resistivity of the respective materials is taken into account. (right) LHC MB outer layer cable with 2% helium, 10% kapton insulation and $RRR = 200$ for different applied magnetic induction (dashed). The horizontal lines (dotted) correspond to 30 and 45 MIITs related to the square of the cross-sectional area of the LHC MB outer layer cable. The full line represents the analytic approximation $\tilde{\Upsilon}$.

Example : LHC MB outer layer cable MIITs Figure 7.6 (right) shows the function Υ for varying applied magnetic induction for the LHC MB outer layer cable taking into account 2% helium and 10% kapton insulation (dashed lines). The horizontal lines signify 30 and 45 MIITs, respectively. In the first case the expected hot-spot temperature yields approximately 100 K for zero field and 375 K for 5 T. In the second case the differences are even more profound, *i.e.* 280 K and more than 500 K, respectively.

Following [Brun 04, p. 159] the function Υ can be analytically approximated for the LHC. Applying the above terminology the approximation $\tilde{\Upsilon}$ reads,

$$\tilde{\Upsilon}(T) = 0.13 \text{ MA}^2 \text{ s m}^{-4} \cdot \eta_A^{\text{Cond.}} \left(\frac{T}{375 \text{ K}} \right)^{0.4}. \quad (7.10)$$

The approximation is represented by a full line in 7.6 (right).

Discussion: The MIITs concept is expected to be conservative, yielding higher temperatures than in reality as cooling and heat transfer are neglected. This is only correct if the hot-spot location in the magnet coincides with the quench origin and when additional heat sources do not contribute significantly to the temperature rise. In a case where the hot-spot moves during quench within the coil cross-section from the quench origin to a conductor with much less favorable properties (see Sec. 5.1.1), *e.g.* higher resistivity, the hot-spot temperature will be underestimated.

The strong field dependence of the electrical resistivity of copper at cryogenic temperatures (Sec. A.1.3.1), and the field variation during current switch off, cause a significant uncertainty in the application of Eq. (7.9) and thus in the final hot-spot temperature. The uncertainties in determining the helium content in the cable cross-section map directly on the uncertainties of the hotspot-temperature.

A quench occurs at $t = t_q$ at a constant current I_0 . After quench detection and validation at $t = t_{\text{val}}$ (see Sec. 7.9.1) the current is switched off as fast as possible. The value of the MIIT-integral, and therefore the hot-spot temperature, thus depend on the time it takes to detect the quench ($t_{\text{det}} - t_q$) [Brun 04, p. 159] as well as the time constant of the magnet current decay [Schm 00]. Quench protection mainly addresses the minimization of these two time constants (see Sec. 7.9).

7.3 Magnetic Energy

For the calculation of problem sets including materials with field dependent material properties or materials exhibiting hysteresis, the formulae for the magnetic energy have to be reviewed.

Poynting's theorem: Starting from the general formulation of MAXWELL's equations, POYNTING's theorem is derived. By multiplying the induction law in differential form,

$$\nabla \times \mathbf{E} = -\frac{\partial \mathbf{B}}{\partial t}, \quad (7.11)$$

by \mathbf{H} and using the vector identity $\nabla \cdot (\mathbf{a} \times \mathbf{b}) = \mathbf{b} \cdot (\nabla \times \mathbf{a}) - \mathbf{a} \cdot (\nabla \times \mathbf{b})$ we can write $-\mathbf{H} \cdot \frac{\partial \mathbf{B}}{\partial t} = \mathbf{H} \cdot (\nabla \times \mathbf{E}) = \nabla \cdot (\mathbf{E} \times \mathbf{H}) + \mathbf{E} \cdot (\nabla \times \mathbf{H})$. Substituting with AMPERE's circuit law,

$$\nabla \times \mathbf{H} = \mathbf{J} + \frac{\partial \mathbf{D}}{\partial t}, \quad (7.12)$$

this yields POYNTING's theorem in differential form:

$$\mathbf{E} \cdot \mathbf{J} = -\nabla \cdot (\mathbf{E} \times \mathbf{H}) - \mathbf{H} \cdot \frac{\partial \mathbf{B}}{\partial t} - \mathbf{E} \cdot \frac{\partial \mathbf{D}}{\partial t}. \quad (7.13)$$

Integrating Eq. (7.13) over a volume V and using GAUSS' law, yields POYNTING's theorem in integral form,

$$\boxed{\int_V \mathbf{E} \cdot \mathbf{J} dV + \int_{\partial V} (\mathbf{E} \times \mathbf{H}) \cdot d\mathbf{a} = - \int_V \mathbf{H} \cdot \frac{\partial \mathbf{B}}{\partial t} dV - \int_V \mathbf{E} \cdot \frac{\partial \mathbf{D}}{\partial t} dV,} \quad (7.14)$$

where $d\mathbf{a}$ denotes the differential surface element on the volume boundary ∂V .

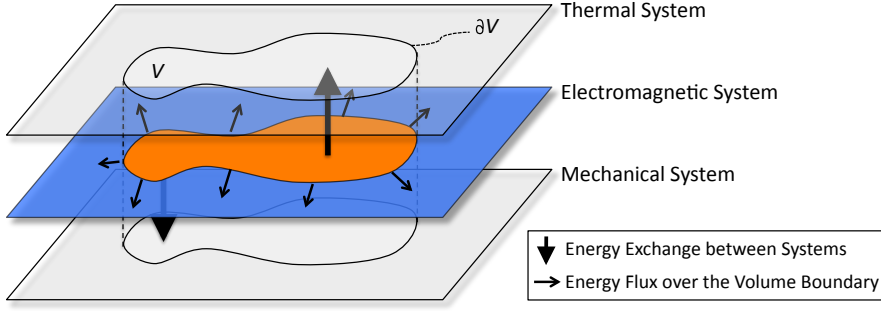


Figure 7.7: Energy exchange between different physical systems and different volumes. We distinguish between energy flux over the volume boundary ∂V and energy exchange to the thermal and mechanical system within the volume V .

Interpretation of the different terms We assume general electromagnetic fields. We interpret:

$\int_V \mathbf{E} \cdot \mathbf{J} dV$ as an energy exchange to other physical systems, *e.g.* the mechanical or thermal system (see Fig. 7.7). For $\mathbf{E} \cdot \mathbf{J} > 0$, it describes the work per time done on electric charges, *e.g.* ohmic losses. An inner product smaller than zero means imposed current densities delivering energy to the field.

It is important to notice that hysteresis and polarization losses are not covered by this expression. The additional energy exchange to the thermal system is introduced below.

$\oint_{\partial V} (\mathbf{E} \times \mathbf{H}) \cdot d\mathbf{a}$ as the flux of electromagnetic energy over the volume boundary ∂V . The term $\mathbf{E} \times \mathbf{H} = \mathbf{S}$ is denoted poynting vector and represents the energy flux density (see Fig. 7.7); $[\mathbf{S}] = \text{J s}^{-1} \text{m}^{-2}$.

Notice that in the presence of electromagnetic waves, the energy flux over the infinite far-field boundary remains finite [Henk 01, pp. 283].

$\int_V \mathbf{H} \cdot \frac{\partial \mathbf{B}}{\partial t} dV$ as the change of magnetic energy stored in the volume V and the energy loss in hysteretic materials:

We integrate $\int_V \mathbf{H} \cdot \frac{\partial \mathbf{B}}{\partial t} dV$ over time and assume that the order of integration can be changed, *i.e.* the integral over the volume does not depend on time.

$$\int_{t_0}^{t_1} \int_V \mathbf{H} \cdot \frac{\partial \mathbf{B}}{\partial t} dV dt = \int_V \int_{t_0}^{t_1} \mathbf{H} \cdot \frac{\partial \mathbf{B}}{\partial t} dt dV. \quad (7.15)$$

Note that if $\mathbf{H} \cdot \frac{\partial \mathbf{B}}{\partial t}$ is a continuous function over the interval $[t_0, t_1]$, the integral can be solved by means of the fundamental theorem of calculus and the antiderivative represents the magnetic energy W_{mag} .

For piece-wise continuous functions the integral is given by the sum over the continuous sub-intervals.

For general materials we assume the magnetic field is a continuous function of the magnetic induction $\mathbf{H}(\mathbf{B})$ and the magnetic induction $\mathbf{B}(t)$ is piece-wise continuous differentiable over time. For a “path” $\mathbf{B}(t_0) \rightarrow \mathbf{B}(t_1)$ we apply the rule for line integrals,

$$\int_V \int_{t_0}^{t_1} \mathbf{H} \cdot \frac{\partial \mathbf{B}}{\partial t} dt dV = \int_V \int_{\mathbf{B}(t_0) \rightarrow \mathbf{B}(t_1)} \mathbf{H} \cdot d\mathbf{B} dV. \quad (7.16)$$

The integral is generally not independent of the path $\mathbf{B}(t)$ and \mathbf{H} does not represent a conservative field over \mathbf{B} . Therefore it consists of both, the magnetic energy and dissipated hysteresis losses. Due to the difficulties to calculate hysteresis losses for anything else than a closed cycle, it is not possible to extract the conservative part from integral (7.16). The hysteresis losses over a closed cycle, $\gamma_{\mathbf{B}} : \mathbf{B}_0 \rightarrow \mathbf{B}_1 \rightarrow \mathbf{B}_0$ are given by:

$$\boxed{W_{\text{hyst}}^V \Big|_{\gamma_{\mathbf{B}}} = \int_V \oint_{\gamma_{\mathbf{B}}} \mathbf{H} \cdot d\mathbf{B} dV.} \quad (7.17)$$

Assuming $\oint \mathbf{H} \cdot d\mathbf{B} = \oint \mathbf{B} \cdot d\mathbf{H}$, and substituting $\mathbf{B} = \mu_0(\mathbf{H} + \mathbf{M})$ as well as $\gamma_{\mathbf{B}} \rightarrow \gamma_{\mathbf{H}}$, the integral can be reduced to the volume $V_{\mathbf{M}}$ where the magnetization \mathbf{M} is defined.

$$\begin{aligned} \int_V \oint_{\gamma_{\mathbf{B}}} \mathbf{B} \cdot d\mathbf{H} dV &= \int_V \underbrace{\oint_{\gamma_{\mathbf{H}}} \mu_0 \mathbf{H} \cdot d\mathbf{H}}_{=0, \text{ for closed cycle}} dV + \int_V \oint_{\gamma_{\mathbf{H}}} \mu_0 \mathbf{M} \cdot d\mathbf{H} dV \\ &= \int_{V_{\mathbf{M}}} \oint_{\gamma_{\mathbf{H}}} \mu_0 \mathbf{M} \cdot d\mathbf{H} dV \end{aligned}$$

If \mathbf{H} can be expressed as the gradient of a potential W_{mag} , with $H = \frac{\partial W_{\text{mag}}}{\partial B}$, then the integral is path independent and the potential constitutes the magnetic energy.

$$W_{\text{mag}} \Big|_{B_0}^{B_1} = \int_V \int_{\mathbf{B}_0}^{\mathbf{B}_1} \mathbf{H} \cdot d\mathbf{B} dV. \quad (7.18)$$

For materials with constant properties, *i.e.* $\mathbf{H} = (\mu)^{-1} \mathbf{B}$, this further simplifies to:

$$W_{\text{mag}} \Big|_{B_0}^{B_1} = \int_V \frac{1}{2} (\mu)^{-1} \mathbf{B}^2 \Big|_{\mathbf{B}_0}^{\mathbf{B}_1} dV. \quad (7.19)$$

$\int_V \mathbf{E} \cdot \frac{\partial \mathbf{D}}{\partial t} dV$ as the change of electrical energy stored in the volume V as well as the energy loss in hysteretic materials analog to above.

Conclusion: POYNTING's theorem then reads: *Consider a volume V , the energy exchange from the electromagnetic system to other physical systems and the flux of electromagnetic energy through the volume boundary equal the increase of electromagnetic energy inside the volume plus all losses in electric/magnetic hysteresis and polarization.*

An expression for the magnetic energy inside the volume V can be defined only for materials without hysteresis:

$$W_{\text{mag}}^V \Big|_{B_0}^{B_1} = \int_V \int_{\mathbf{B}_0}^{\mathbf{B}_1} \mathbf{H} \cdot d\mathbf{B} dV. \quad (7.20)$$

Application to slowly varying fields In case of slowly varying electromagnetic fields, the term $\frac{\partial \mathbf{D}}{\partial t}$ can be neglected. Introducing the magnetic vector potential \mathbf{A} with $\nabla \times \mathbf{A} = \mathbf{B}$, the electric field in Eq. (7.11) can be expressed by $\mathbf{E} = -\frac{\partial \mathbf{A}}{\partial t}$. Equation (7.14) changes to:

$$-\int_V \frac{\partial \mathbf{A}}{\partial t} \cdot \mathbf{J} dV - \int_{\partial V} \left(\frac{\partial \mathbf{A}}{\partial t} \times \mathbf{H} \right) \cdot d\mathbf{a} = -\int_V \mathbf{H} \cdot \frac{\partial \mathbf{B}}{\partial t} dV \quad (7.21)$$

At this point, we refrain from giving a physical interpretation of the surface integral. For quasi-static problems variations of the magnetic field are instantaneously distributed over the entire domain and an energy flux density is not defined.

Extending the volume to infinity $V \rightarrow \infty$, the integral over the far field boundary can be dropped: The magnetic vector potential decays with $1/r$ and the magnetic field with $1/r^2$ while the surface increases with r^2 only. For the integral containing the current density \mathbf{J} the integration domain can be reduced to the volumes where the current density is different from zero $V_\infty \rightarrow V_{\mathbf{J}}$:

$$\int_{V_\infty} \mathbf{H} \cdot \frac{\partial \mathbf{B}}{\partial t} dV = \int_{V_\infty} \frac{\partial \mathbf{A}}{\partial t} \cdot \mathbf{J} dV = \int_{V_{\mathbf{J}}} \frac{\partial \mathbf{A}}{\partial t} \cdot \mathbf{J} dV \quad (7.22)$$

We integrate over time and apply the rule for line integrals assuming that the same conditions hold for \mathbf{J} and \mathbf{A} as explained above for \mathbf{H} and \mathbf{B} :

$$\int_{V_\infty} \int_{\mathbf{B}_0 \rightarrow \mathbf{B}_1} \mathbf{H} \cdot d\mathbf{B} dV = \int_{V_{\mathbf{J}}} \int_{\mathbf{A}_0 \rightarrow \mathbf{A}_1} \mathbf{J} \cdot d\mathbf{A} dV \quad (7.23)$$

We obtain an alternative form for the hysteresis losses over a full cycle $\gamma_{\mathbf{A}}$: $\mathbf{A}_0 \rightarrow \mathbf{A}_1 \rightarrow \mathbf{A}_0$,

$$W_{\text{hyst}}^\infty \Big|_{\gamma_{\mathbf{A}}} = \int_{V_{\mathbf{J}}} \oint_{\gamma_{\mathbf{A}}} \mathbf{J} \cdot d\mathbf{A} dV \quad (7.24)$$

For materials without hysteretic behavior, the left-hand side of Eq. (7.23) represents the magnetic energy in the entire domain. In the case of lossy

materials, the volume V_J on the right-hand side requires further subdivision. We distinguish sub-domains with an imposed current density thus providing energy to the electromagnetic system, and domains where energy is dissipated in losses - to be identified by $\mathbf{E} \cdot \mathbf{J} > 0$. For loss and hysteresis free materials we obtain an alternative form for the stored magnetic energy:

$$W_{\text{mag}}^\infty \Big|_{A_0}^{A_1} = \int_{V_J} \int_{\mathbf{A}_0}^{\mathbf{A}_1} \mathbf{J} \cdot d\mathbf{A} dV \quad (7.25)$$

7.4 Inductance

The magnetic flux in a superconducting magnet is in non-linear, diffusive and hysteretic relationship with the applied current due to iron saturation, induced eddy currents and superconductor magnetization. For the simulation of quench, the electrical circuit is represented by lumped elements and the current change in the loop is calculated from the voltage over the inductance. Therefore, the inductance is derived for general materials and then applied to quench computation.

7.4.1 Self Inductance

Consider a simple current loop connected to a current source as shown in Fig. 7.8. The loop spans a surface A with differential surface element $d\mathbf{a}$ and boundary ∂A . The differential line segment $d\mathbf{s}$ follows the boundary in a right-hand orientation.

The total magnetic induction \mathbf{B} consists of the field created by the current I and the effect of any magnetic object with field-dependent, diffusive or hysteretic properties. The dependence of the magnetic induction \mathbf{B} on the current I , the current change ($\frac{dI}{dt}$) and the current history ($\int_{t_0}^t I d\tau$) is modeled by the relation Γ ,

$$\mathbf{B} = \mathbf{B} \left(\mathbf{r}, \Gamma \left(I, \frac{dI}{dt}, \int_{t_0}^t I d\tau \right) \right). \quad (7.26)$$

For the general case, the following, commonly used equations give rise to the definition of three different types of self inductance [Kurz 04].

$$\Psi_{\text{mag}} = L_\Psi I, \quad U_{\text{ind}} = L_d \frac{dI}{dt}, \quad W_{\text{mag}} = \frac{1}{2} L_W I^2. \quad (7.27)$$

In the stationary case, with constant material properties and no hysteresis, all three inductances are identical: $L_\Psi = L_d = L_W$.

Apparent inductance: For a given instance and current, the magnetic flux Ψ_{mag}^A through the surface A is given by

$$\Psi_{\text{mag}}^A = \int_A \mathbf{B} d\mathbf{a} = \int_{\partial A} \mathbf{A} \cdot d\mathbf{s}, \quad (7.28)$$

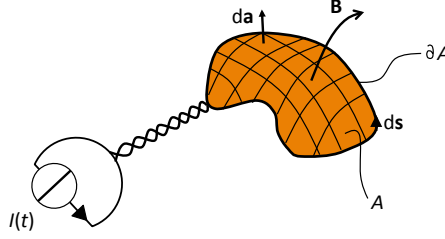


Figure 7.8: Self inductance geometry. The current loop with surface A and boundary ∂A . The differential line segment and surface element are denoted da and ds , respectively.

where \mathbf{A} denotes the magnetic vector potential with $\nabla \times \mathbf{A} = \mathbf{B}$. The *apparent inductance* [Deme 99] L_Ψ is defined by

$$L_\Psi = \frac{\Psi_{\text{mag}}^A}{I} = \frac{\int_{\partial A} \mathbf{A} \cdot d\mathbf{s}}{I}. \quad (7.29)$$

The magnetic flux shows the same dependence on the current as the magnetic induction. With the limitation to a constant current, *i.e.* a steady state situation, the apparent inductance may be non-linear and hysteretic.

Differential inductance: Assuming a current ramp-rate $\frac{dI}{dt}$, the voltage induced over the terminals of the current source, U_{ind} , is given by

$$U_{\text{ind}} = \frac{d\Psi_{\text{mag}}^A}{dt} = \frac{d}{dt} \oint_{\partial A} \mathbf{A} \cdot d\mathbf{s} = \oint_{\partial A} \frac{\partial \mathbf{A}}{\partial t} \cdot d\mathbf{s}, \quad (7.30)$$

and defines the *differential inductance* L_d [Naun 02, pp. 33] to:

$$L_d = \frac{U_{\text{ind}}}{\frac{dI}{dt}} = \frac{\frac{d\Psi_{\text{mag}}^A}{dt}}{\frac{dI}{dt}} = \frac{\frac{d}{dt} \oint_{\partial A} \mathbf{A} \cdot d\mathbf{s}}{\frac{dI}{dt}}. \quad (7.31)$$

The differential inductance inherits the behavior of the magnetic induction and may generally be non-linear, time-dependent and hysteretic.

Under the condition that $\frac{d\Psi_{\text{mag}}^A}{dt} = \frac{d\Psi_{\text{mag}}^A}{dI} \frac{dI}{dt}$, *i.e.* that the system is time-invariant, non-hysteretic and does not contain any secondary loops, the definition can be further simplified to:

$$L_d(I) = \frac{d\Psi_{\text{mag}}^A}{dI} = \frac{d(IL_\Psi)}{dI} = \frac{dL_\Psi}{dI} I + L_\Psi. \quad (7.32)$$

Notice that a second current loop, which is magnetically coupled to the primary loop, would influence the induced voltage, but has no effect on the apparent inductance.

Energy inductance: For a system in virgin state, *i.e.* current and all fields equal zero, the current is changed to $I(t)$. The amount of energy W_{source} supplied by the power supply can be calculated from

$$W_{\text{source}}(t) = \int_{\tau=0}^t U_{\text{ind}}(\tau) I(\tau) d\tau = \int_{t=0}^t \frac{d\Psi_{\text{mag}}^A(I(\tau))}{d\tau} I(\tau) d\tau. \quad (7.33)$$

Note that only for a loss and hysteresis free system, the energy supplied by the source and the magnetic energy stored in the system are identical. The *energy inductance* L_W is then defined as time-dependent function:

$$L_W(t) = \frac{W_{\text{source}}(t)}{1/2 I(t)^2} = \frac{2}{I(t)^2} \int_{t=0}^t \frac{d\Psi_{\text{mag}}^A(I(\tau))}{d\tau} I(\tau) d\tau. \quad (7.34)$$

Under the following two conditions the expression for the energy inductance can be further simplified. If again $\frac{d\Psi_{\text{mag}}^A(I)}{dt} = \frac{d\Psi_{\text{mag}}^A(I)}{dI} \frac{dI}{dt}$, then the time derivative can be split off. If the system is conservative, *i.e.* the energy change does not depend on the current history, but only on start and end current, then Eq. 7.34 reads:

$$L_W(t) = \frac{2}{I(t)^2} \int_{t=0}^t \frac{d\Psi_{\text{mag}}^A(I(\tau))}{dI} \frac{dI}{d\tau} I(\tau) d\tau \quad (7.35)$$

$$= \frac{2}{I(t)^2} \int_{I=0}^{I(t)} \frac{d\Psi_{\text{mag}}^A(I)}{dI} I dI \quad (7.36)$$

$$= \frac{2}{I(t)^2} \int_{I=0}^{I(t)} L_d(I) I dI \quad (7.37)$$

From the energy inductance the concept of inner and outer inductance can be derived. Using the formula for the magnetic energy inside a volume V , Eq. (7.20), the energy can be calculated separately inside and outside the cable. Both energy fractions define complementary parts of the total induction. For materials with constant properties where all three concepts of induction are identical, the two parts can be conveniently approximated: The outer induction is calculated from the geometrical induction of a loop along the conductor. The inner inductance is given by the inductance per unit length of a straight infinite long wire with the same cross-section multiplied by the length along the loop.

7.4.2 Mutual inductance

Consider a second current loop of surface B and boundary ∂B . Surface and boundary can be parameterized by $d\mathbf{a}$ and $d\mathbf{s}$, respectively. The two surfaces A and B do not intersect. Both loops are magnetically coupled, *i.e.* the flux of loop A penetrates loop B and vice-versa. The geometry may contain magnetic objects with field-dependent, diffusive or hysteretic properties.

The concept of the geometrical and differential inductances are adapted to the new situation:

Apparent mutual inductance : For a given current $I = I_A$ in loop A and I_B in loop B , the apparent mutual inductance of B on A , is given by relating the magnetic flux created by B in loop A to the current I_B :

$$M_{\Psi}^{AB} = \frac{\Psi_{\text{mag}}^A}{I_B} = \frac{\oint_{\partial A} \mathbf{A} \cdot d\mathbf{s}}{I_B}. \quad (7.38)$$

In general, the magnetic flux depends on both currents, *i.e.* on Γ^A and Γ^B and so does the apparent mutual inductance. If the material properties are constant, the flux can be separated into the contributions of either coil. The apparent mutual inductance is then constant and symmetric, $M_{\Psi}^{AB} = M_{\Psi}^{BA}$. Note that symmetry is not easy to define in case of varying material properties when the mutual induction is given by a function.

Differential mutual inductance: The current in loop A shall be constant I_A . The voltage induced over loop A due to loop B is now related to the current change in loop B :

$$M_d^{AB} = \frac{U_{\text{ind}}^A}{\frac{dI_B}{dt}} = \frac{\frac{d\Psi_{\text{mag}}^A}{dt}}{\frac{dI_B}{dt}} = \frac{\frac{d}{dt} \oint_{\partial A} \mathbf{A} \cdot d\mathbf{s}}{\frac{dI_B}{dt}} \quad (7.39)$$

7.4.3 Application of the Differential Inductance to Quench Computation

Since magnet components may be build from field-dependent, diffusive and hysteretic materials the general definition of the differential inductance given in Eq. (7.31) is applied.

Bulk or Rutherford-type conductors For a current loop made from a bulk conductor, the confined flux varies over the conductor cross section. Isolating the average linked flux, yields a differential flux over the cross section giving rise to eddy currents. The change of the average flux induces a voltage over the loop terminals (see Fig. 7.9 (left, center)).

For a Rutherford-type cable, all strands are connected in parallel and follow a zig-zag trajectory along the cable (see Sec. 7.8). The linked flux on all parallel paths is identical and the total induced voltage can be calculated from the average inductance. The variation of the differential electrical field along the strands also gives rise to induced eddy currents - inter-strand-coupling currents (see Fig. 7.9 (right)).

Field-dependent materials The permeability of the iron yoke is field dependent and decreases strongly as soon as the magnetic induction exceeds the saturation level. Therefore, the contribution of the iron yoke to the flux in the magnet decreases with increasing current. If no other dependence needs to be considered it can be shown that the differential inductance is smaller

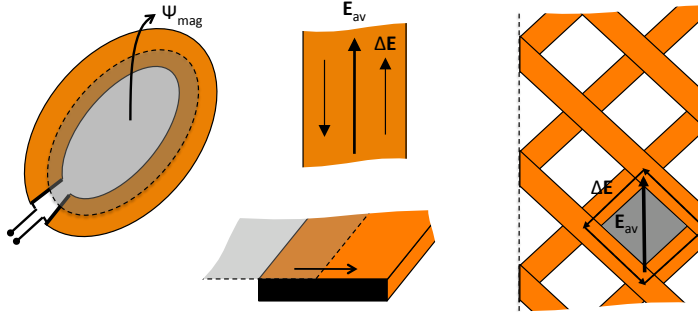


Figure 7.9: Inductance of a bulk or Rutherford-type conductor. (left) and (center, bottom) The confined flux varies over the conductor cross section. (center, top) The induced electric field can be split in an average and differential part. (right) The average induced electric field is identical for each strand. The differential electrical field gives rise to induced inter-strand eddy currents.

or equal to the geometrical inductance. Compare Eq. (7.32) where the flux change with current is negative.

Notice that the magnetic field computation is carried out entirely in 2D, *i.e.* over the magnet cross-section. The variation of the magnetic field in the coil ends and the magnetic length are taken into account by scaling parameters. For the induced voltages the magnetic length ℓ_{mag} is used (see discussion of magnetic length and inductance length in Sec. B.1.6). The iron saturation is different in the magnet ends. Hence, the magnetic length is a function of excitation current.

Figure 7.10 shows the differential inductance for the LHC main bending magnet considering saturation effects in the iron yoke.

The influence of induced eddy currents and superconductor magnetization on the differential inductance are not taken into account in the present quench model. Nevertheless, the general dependence is discussed allowing to analyze peculiarities of inductance measurements.

Diffusive materials Induced eddy-currents or inter-strand coupling currents show a diffusive characteristic. The influence on the differential inductance is estimated by means of a simple network representation [Smed 93]. The induced eddy-currents are considered as coupled secondary loops. The magnet is represented by the primary side of a transformer with inductance L_1 . The sum of all inter-strand and inter-filament coupling currents is taken into account by a secondary circuit with inductance L_2 and resistance R_2 . The two sides are coupled by the mutual inductance $M = k\sqrt{L_1 L_2}$, where k is denoted the coupling factor, $k \in [0, 1)$. The inductances L_1 , L_2 and M are constant. At $t = 0$ a constant voltage U_1 is switched over the magnet.

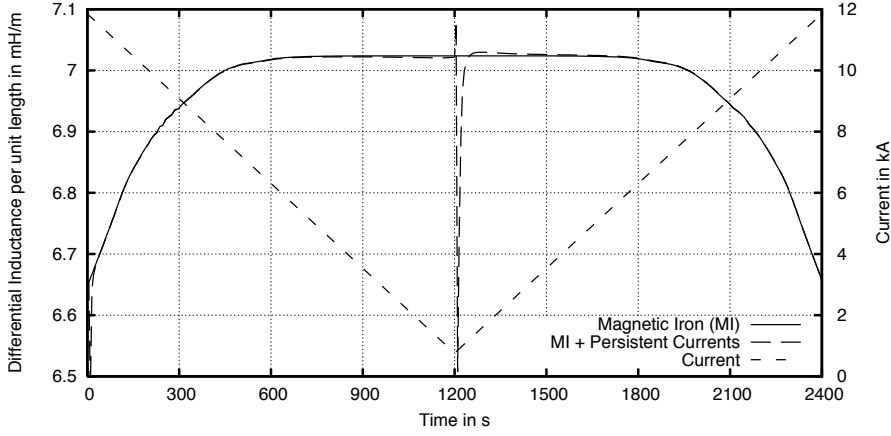


Figure 7.10: ROXIE simulation of the differential inductance of the LHC main bending magnet considering field dependent and hysteretic materials. The differential inductance only considering the field depending iron decreases by approximately 5% from injection to nominal current. Considering persistent currents (hysteresis), the differential inductance shows a significant dip after the current ramp-rate changed sign (at $t = 0$ and $t = 1200$ s, assuming a pre-cycle for $t < 0$).

For a symmetrically oriented transformer (see *e.g.* [Flei 99, p. 494]) the current in the secondary winding is given by

$$i_2(t) = -\frac{U_1}{R_2} \frac{M}{L_1} \left(1 - \exp\left(-\frac{t}{\tau}\right) \right), \quad \tau = \frac{L_2}{R_2} (1 - k^2). \quad (7.40)$$

Calculating the differential inductance from the induced current change on the primary side yields,

$$L_d(t) = \frac{U_1}{\frac{di_1}{dt}} = L_1 \frac{1}{1 + \frac{k^2}{1-k^2} \exp\left(-\frac{t}{\tau}\right)} \quad (7.41)$$

The time constant and the initial value of the inductance are both simple functions of the coupling factor k . Figure 7.11 shows the change of differential inductance for different values of the coupling factor. It can be seen how the differential inductance is reduced in the first instance after the voltage rise.

Hysteretic materials: In superconducting magnets the magnetic iron and the superconducting filaments show a magnetization behavior which features a hysteresis. The influence on the concept of the differential inductance is highlighted by means of a simplified model.

Figure 7.12 (top, left) shows the magnetic flux stemming from the hysteretic material in the magnet versus applied magnet current. The transition from the lower to the upper branch as well as the shape of the minor loop are typical for the superconductor magnetization. In case of ferromagnetic hysteresis, the

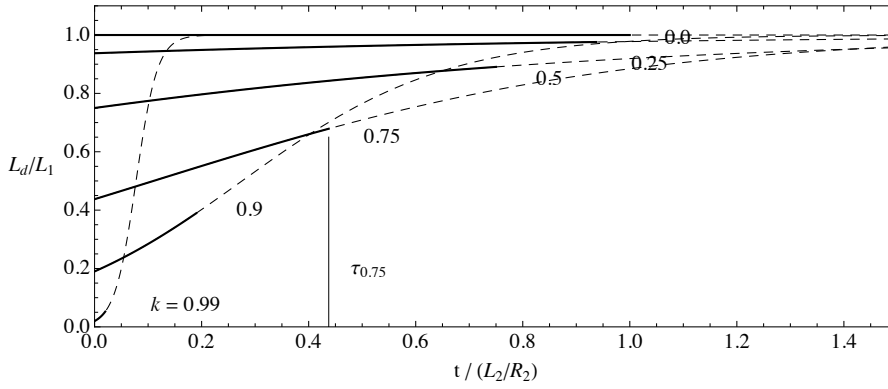


Figure 7.11: Differential inductance of a magnet with time-transient effects, *e.g.* inter-strand coupling currents. The plot shows the change of differential inductance over time for different values of k : On the left we can read off the initial value. The time constant τ corresponds to the ending of the full lines.

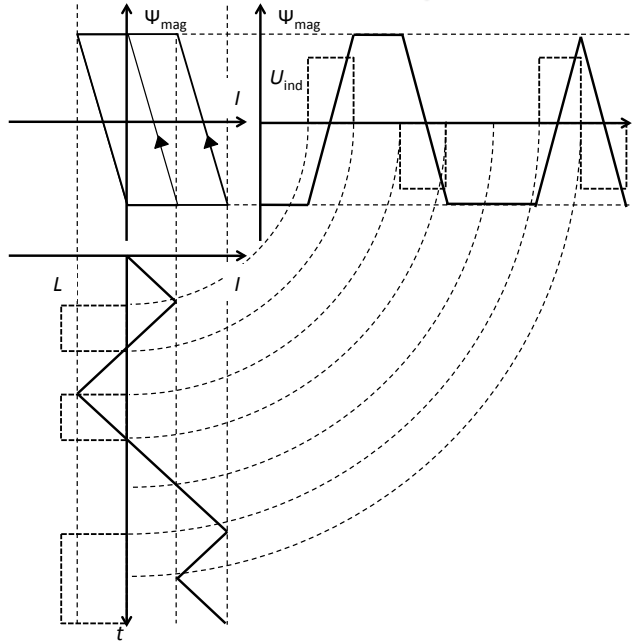


Figure 7.12: Differential inductance by means of hysteretic materials. The hysteresis loop represents a simplified superconductor magnetization loop including a minor loop. Starting from the current, the magnetic flux in the magnet can be constructed by a simple projection. The induced voltage is given by the flux change. Finally, the differential inductance is calculated from the ratio of induced voltage and current ramp rate.

transition occurs while increasing the current as compared to superconducting materials where the transition occurs on the on-set of the current decrease. Minor loops are followed horizontally instead of vertically.

Following the approach used in [Naun 02, pp. 36], the flux in the magnet can be constructed graphically from the applied current. The flux belonging to the geometry of the magnet winding is not considered here. The induced voltage is calculated from the flux change. Both are shown in Fig. 7.12 (top, right). For this simplified model, the differential inductance is constant and negative during the branch transition and zero everywhere else. In case of ferromagnetic materials, the differential inductance is of constant positive values during the transition (which occurs at different times). In first order, this effect can be superimposed on the geometrical inductance and thus yields lower/higher values during the transition.

Figure 7.10 shows the differential inductance for the LHC main bending magnet considering the effect of superconductor magnetization currents.

7.5 Non-linear Voltage-Current-Characteristic of Superconductors

Non-linear
VAC

The voltage-current-characteristic (VAC) of a superconductor is a strongly non-linear function of applied magnetic field, temperature and current (or current density), see Sec. A.2.2. Following WILSON [Walt 74, p. 30], the voltage over a superconductor, U_{SC} , can be expressed by a power of the applied current I_{SC} ,

$$U_{SC} = U_c \left(\frac{I_{SC}}{I_c} \right)^{N_{SC}}, \quad (7.42)$$

where N_{SC} serves as fit parameter and U_c as reference voltage (Sec. A.2.3). The critical current I_c depends on the applied magnetic field and temperature (see critical current density in Sec. A.2.4).

Current
controlled
voltage
source

In an electrical network, superconducting elements constitute current-controlled voltage sources, $U_{SC}(I_{SC})$. Therefore, branch currents and voltages cannot be determined by a simple inversion of the network matrix, but require a (numerically expansive) iterative approach to resolve the interdependence (non-linearity).

Consider the combination of a superconducting and a resistive element in one branch of a simplified electrical network as shown in Fig. 7.13. Depending on the type of connection, in parallel or in series, and the boundary condition, current or voltage driven, four different elementary problems can be derived:

- a) superconductor in parallel to a resistor driven by a current source: The current splits over the two branches, the current through the superconductor defines the voltage over the branch and thus the current through the resistor. This situation is called *current-sharing* and represents the situation of a quenching copper-stabilized wire, see Sec. 7.5.1.

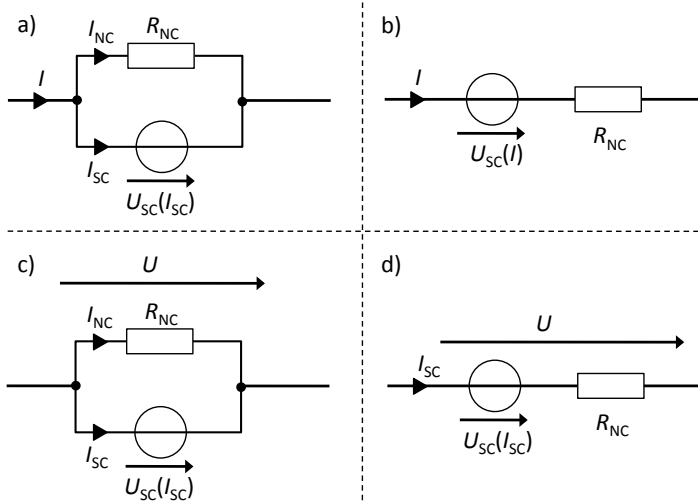


Figure 7.13: Simplified electrical networks containing superconducting and normal conducting elements. The following situations can be identified: a) Current-sharing or the voltage over a quenching copper stabilized wire. b) Voltage over a partly quenched magnet winding. d) Voltage over superconducting current loop with resistive joints. The subscripts “NC” and “SC” stand for normal conductor (ohmic resistive) and superconductor, respectively.

- b) superconductor in series with a resistor driven by a current source: The current through both elements defines the total branch voltage. This situation can be found in case of partly quenched magnet windings.
- c) superconductor in parallel to a resistor driven by a voltage source: The voltage over the branch defines the two branch currents.
- d) superconductor in series with a resistor driven by a voltage source: The voltage over the branch splits over the two elements. The voltage over the superconductor defines the branch current and therefore the voltage over the resistor. This situation can be found for induced voltages over superconducting loops with resistive joints, see Sec. 7.5.2.

While the situations b) and c) are easily solved and implemented, the circuits a) and d) require either further simplifications, iteration techniques or a graphical solution (Sec. 7.5.3).

7.5.1 Current-Sharing

Superconducting filaments are usually embedded in a normal conducting matrix for stabilization. The matrix gives mechanical support, heat transfer to the coolant and in longitudinal direction along the strands, and provides a parallel path for the current in case of a quench.

Such a superconducting strand can be described by the circuit shown in Fig. 7.13 a). While the current is much smaller than the critical current I_c , the voltage over the superconductor is negligible due to the usually large n -index (in the order of 20-50). For an increasing current I or a decreasing critical current I_c , *e.g.* due to a temperature or magnetic field increase, the voltage U_{SC} , given in Eq. (7.42), starts to grow. This voltage draws part of the current into the path through the resistor - the external current I is shared between the resistive and superconducting path.

Implicit
equation of
current-
sharing

Neglecting the inductive coupling of the two current paths, the current in the superconductor I_{SC} can be calculated from Eq. (7.42) with the implicit equation,

$$R_{Cu}(B, T, RRR)(I - I_{SC}) = U_c \left(\frac{I_{SC}}{I_c(B, T)} \right)^{N_{SC}}, \quad (7.43)$$

where R_{Cu} denotes the temperature and field dependent resistance of the copper matrix.

Figure 7.14 (right) shows the current commutation for different values of applied magnetic induction and transport current density. The current sharing temperature range, *i.e.* the temperature interval where the current is shared between the superconductor and normal conductor, decreases with decreasing applied field and current density. The maximum range is approximately 3 K. The current-sharing temperature range decreases with decreasing values for N_{SC} .

The voltage over the branch causes ohmic losses in the strand. In case of insufficient cooling, the ohmic heat results in a temperature increase and further reduction of the critical current. The fraction of the current through the resistive part grows.

Current-Sharing Temperature The implicit equation for the current in the superconductor, Eq. (7.43), causes a high computational effort, especially for large numbers of N_{SC} . Therefore, STEKLY proposed an approximation relying on the following assumptions [Stek 65]: 1.) While the current in the superconductor is smaller than the critical current, it is entirely carried by the superconducting fraction of the strand and no losses are dissipated. 2.) When the current exceeds the critical current, the excess current “spills over” into the surrounding copper matrix. The current in the normal conductor causes ohmic losses. 3.) When the critical current density reaches zero, the current is carried only by the normal conducting copper matrix.

This simplifies the solution of electrical networks containing superconducting elements significantly. The current controlled voltage source of Eq. (7.42) has been replaced by a current source controlled by the external current I , and both branches have been decoupled.

$$I_{SC}(I) = \begin{cases} I & I < I_c \\ I_c & \text{else} \end{cases} \quad (7.44)$$

STEKLY
current-
sharing

Figure 7.14 (left) shows the commutation calculated according to Eq. (7.43)

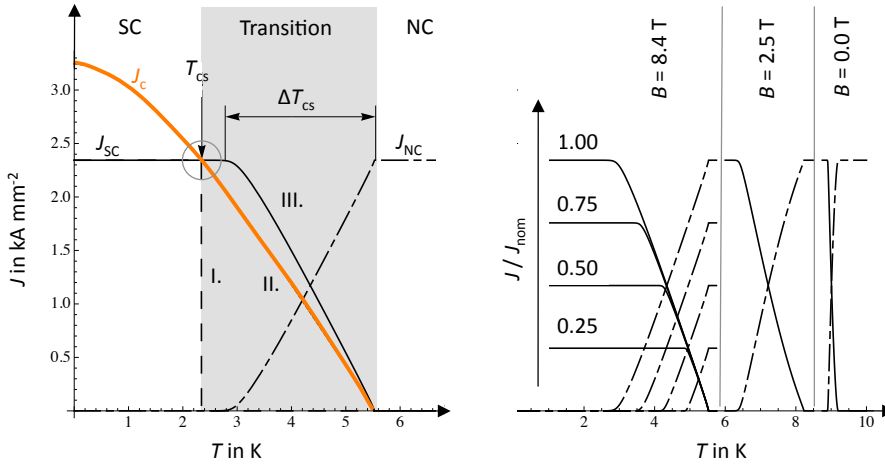


Figure 7.14: Current-sharing: Consider a Nb-Ti superconductor ($N_{SC} = 40$) embedded in a copper matrix of identical cross-sectional area ($\lambda = 1$) and RRR of 200. The current-sharing is shown for varying applied magnetic inductions and transport current densities. The nominal current density $J_{nom} = 2.34 \text{ kAmm}^{-1}$ is 10% below the critical current density at 8.4 T and 1.9 K.

(left) Different models for a quench and the consequent current commutation from the superconductor to the copper matrix. The thick orange line represents the critical current density J_c as a function of temperature for an applied magnetic induction of 8.4 T. The temperature where the applied current density in the superconductor equals the critical current density is highlighted by a circle. Beyond this temperature all three models show a different behavior:

I. Step-function: The current commutates instantaneously from the superconductor into the normal conductor (dashed line).

II. Current-sharing by STEKLY: When the current density in the superconductor exceeds the critical current density, the excess current “spills over” into the copper matrix. The current density in the superconductor equals the critical current density. The temperature, for which the transition sets in, is denoted current-sharing temperature T_{cs} . With increasing temperature the critical current density decreases and more and more current is carried by the normal conductor.

III. Current-sharing as defined by Eq. (7.43) and necessary iteration: The current commutation from the superconductor (full line) to the normal conductor sets in at higher temperatures compared to I and II. The temperature interval between the onset of current sharing and the complete commutation into the normal conductor is denoted current-sharing temperature range ΔT_{cs} . The current density in the normal conductor is given by the dash-dotted graph.

(right) Current sharing (after model III) for different applied current densities and magnetic inductions. The current sharing temperature range decreases with field and current density. The current density in the superconductor is given by the solid lines and in the normal conductor by the dash-dotted lines.

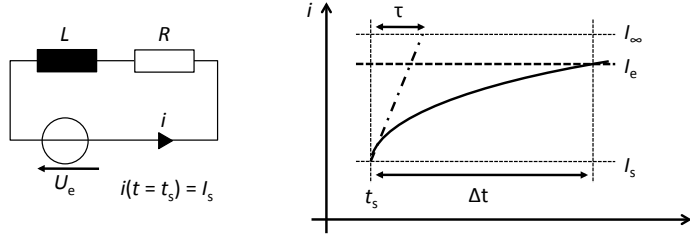


Figure 7.15: (left) Model problem circuit. (right) Solution of the initial value problem (if $R > 0$) depicting all relevant parameters.

in comparison to the critical current density. The approach after STEKLY features a longer current-sharing temperature range and smaller currents in the superconductor. Therefore, dissipated ohmic losses are over estimated. For small temperature rises and strong cooling, the stability of the superconductor can be under estimated. For the calculation of quench, where dissipated losses and heat transfer from quench heaters and neighboring conductors exceed the cooling capability by many orders of magnitude, the differences can be neglected.

Current-sharing
temperature

The temperature where current-sharing sets in is denoted current-sharing temperature T_{cs} . STEKLY furthermore linearizes the critical current over temperature for a fixed magnetic induction B_0 ,

$$I_c^{\text{lin}}(T) = I_c(B_0, T_b) \frac{T_c - T}{T_c - T_b}, \quad (7.45)$$

where T_b is the bath temperature and T_c denotes the critical temperature for the applied field B_0 . For $I = I_c^{\text{lin}}(T_{cs})$, this can be re-arranged and gives the current sharing temperature as function of the applied current I [Mess 96, p. 120]:

$$T_{cs} = T_b + (T_c - T_b) \left(1 - \frac{I}{I_c(T_b, B_0)} \right). \quad (7.46)$$

7.5.2 Voltages Induced over a Superconductor

The model problem Given is a circuit consisting of a resistance R , an inductance L and a constant voltage source U_e . The circuit is shown in Fig. 7.15 (left). At a starting time t_s the circuit carries an initial current I_s . The value of the resistivity may be zero or greater and the value of the voltage may be negative, zero or positive. The value of the inductance is always greater zero.

After solving the initial value problem, it is investigated whether an arbitrary current level I_e is met by the current i depending on the model parameters and initial values. The time Δt to reach I_e is calculated.

The circuit can be described by the following linear, inhomogeneous differential equation of first order with constant coefficients:

$$L \frac{di}{dt} + Ri = U_e \quad (7.47)$$

For a resistivity R greater than zero the solution of the initial value problem reads:

$$i(t) = I_\infty + (I_s - I_\infty) \exp\left(-\frac{t - t_s}{\tau}\right), \quad (7.48)$$

with $\tau = L/R$ and the current limit $I_\infty = U_e/R$. For $t \rightarrow \infty$ the current converges towards I_∞ . Figure 7.15 (right) shows the solution with all relevant parameters. For a resistivity of $R = 0$ the equation greatly simplifies and the solution of the initial value problem reads:

$$i(t) = I_s + (t - t_s) \dot{I}, \quad (7.49)$$

with the constant slope $\dot{I} = U_e/L$. In this case, the current change is not limited, thus $I_\infty = \pm\infty$ (depending on the sign of \dot{I}).

Equations (7.48) and (7.49) are rearranged in order to express $\Delta t = t - t_s$ as a function of the model parameters, starting values and the given current level I_e :

$$\Delta t = \begin{cases} \frac{I_e - I_s}{U_e/L} & R = 0 \\ \tau \log\left(\frac{I_\infty - I_s}{I_\infty - I_e}\right) & R > 0 \end{cases} \quad (7.50)$$

The current I_e can be reached, if the expression for Δt returns a positive, real value. For a positive voltage U_e the current level I_e needs to fulfill $I_s < I_e < I_\infty$, while for a negative voltage it has to meet $I_\infty < I_e < I_s$. In the special case of $R = 0$ and $U_e = 0$ the current is constant.

Notice that sometimes it is necessary to split the period of observation/calculation. Therefore, Eq. (7.48) or (7.49) can be joint repetitively using the final current of one interval as the starting current of the preceding interval.

Currents Induced in a Superconducting Current Loop with Resistive Joint

Considering a superconducting current loop with a resistive joint in a time-transient magnetic field. The joint has a resistivity R_{joint} and the loop an inductance L . The initial current is zero. The changing magnetic flux $d\Psi_m/dt$ induces a voltage U_{ind} over the loop. The geometry is shown in Fig. 7.16 (left).

Taking into account the non-linear resistivity of the superconducting material, the maximum induced current is calculated.

The voltage over a superconductor is a strongly non-linear function of the current through the superconductor (see Sec. A.2.2). In superconducting state the voltage can be considered as infinitely small, while in normal conducting state it is orders of magnitude greater than over comparable amounts of copper. As shown above (Sec. 7.5), this causes the current to rapidly commutate from the superconductor into a surrounding copper matrix. The

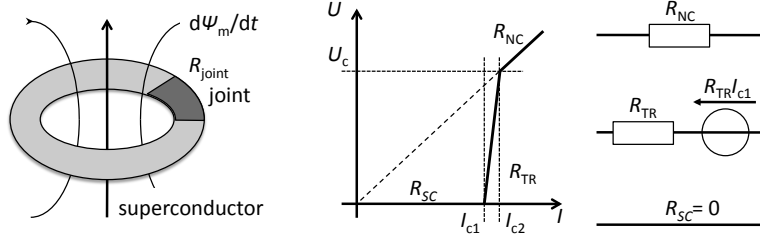


Figure 7.16: Currents induced in a superconducting current loop with resistive joint. (left) Geometry. (right) Model of the superconductor and the associated network elements.

voltage-current characteristic can be simplified as shown in Fig. 7.16 (right) [Verw 95, pp. 68]. While the current is below the onset current of the transition, I_{c1} , the resistivity is zero. In normal conducting state, *i.e.* above I_{c2} , the superconductor is replaced by the resistivity of the normal conducting matrix material R_{NC} (or if not available, by its normal resistivity). During the transition the superconductor is modeled by the differential transition resistivity $R_{TR} = U_c(I_{c2} - I_{c1})$ and a virtual voltage source $R_{TR}I_{c1}$. The three resistivities compare as $R_{joint} < R_{NC} \ll R_{TR}$.

The current rise can be expressed by the solution of the model problem (see Sec. 7.5.2). Without limitations, the induced voltage shall be greater than the critical voltage U_c ($U_{ind} > U_c$). While the current rises all three regimes of the simplified current-voltage-characteristic are passed, thus constituting three different sets of parameters for the model problem. For each phase the limiting current I_∞ and the time constant τ are given by:

Phase	Time	Current	I_∞	τ
1	$0 < t < t_1$	$0 < i < I_{c1}$	$\frac{U_{ind}}{R_{joint}}$	$\frac{L}{R_{joint}}$
2	$t_1 < t < t_2$	$I_{c1} < i < I_{c2}$	$\frac{U_{ind} + R_{TR}I_{c1}}{R_{joint} + R_{TR}}$ $\approx I_{c1} + \frac{U_{ind}}{R_{TR}}$	$\frac{L}{R_{joint} + R_{TR}}$
3	$t_2 < t < \infty$	$I_{c2} < i < I_\infty$	$\frac{U_{ind}}{R_{joint} + R_{NC}}$	$\frac{L}{R_{joint} + R_{NC}}$

Figure 7.17 (left) shows schematically the current rise over the three phases.

The current through the resistive joint and later through the transitioning superconductor causes ohmic losses. The maximum dissipated power is then given by $P_{max} = U_{ind}^2 / (R_{joint} + R_{NC})$. If this heat is not transferred away from the loop, it results in a temperature rise and a decrease in critical current. In the simplified model, the two limits, I_{c1} and I_{c2} shift towards lower currents. Therefore phase 1 and 2 are passed faster without changing the current rise itself. This is shown schematically in Fig. 7.17 (right).

The model works for both, negative and positive induced voltages, in the same way. For a negative voltage the orientation of the virtual voltage source has to be inverted. For an induced voltage $|U_{ind}|/R_{joint}$ smaller than I_{c1} or I_{c2} not all regimes are passed.

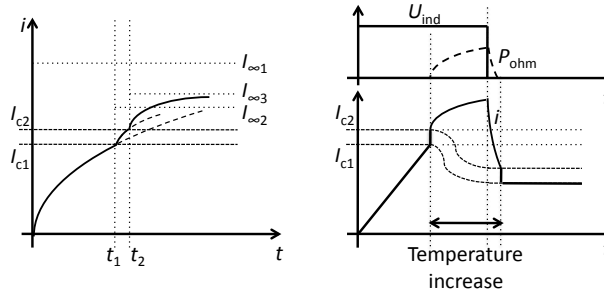


Figure 7.17: (left) Superconductor with resistive joint. The induced current passes the three regimes of the superconductor model. (right) Without a resistive joint the induced current increases linearly over time until the critical current I_{c1} is reached. The ohmic losses yield a temperature rise and therefore the critical current to decrease. After the induced voltage disappeared, the induced current reduces until it reaches the critical current I_{c1} and flows without resistance.

Quench model: The analytical models for the cable eddy currents, *i.e.* inter-filament and inter-strand coupling currents, are based on similar topologies. Hence, without taking into account the U - I -characteristic of the superconductor, induced cable eddy currents and losses are over estimated for very high ramp-rates.

Currents Induced in a Superconducting Loop without Resistive Joint Considering a seamless superconducting current loop, *i.e.* without resistive joint $R_{joint} = 0$, the approach has to be slightly modified. During the first phase the current rises linearly with a slope of U_{ind}/L and is not limited. As soon as the current reaches I_{c1} the differential resistivity R_{TR} switches in and phase 2 and 3 follow as above. The current is therefore limited to $I_{\infty} = U_{ind}/R_{NC}$.

If now, in a preloaded state $i > I_{c2}$, the magnetic flux stops changing, then the induced voltage drops to zero and the current starts decreasing. Phase 3 and 2 are followed in reverse direction. The current stops decreasing as soon as it reaches I_{c1} . In this simplified model the total resistivity of the circuit equals zero and the current is kept constant by the inductance.

Looking more accurately, the constant current actually decreases with a time constant in the order of years. This is due to the tiny residual voltage over the superconductor as can be calculated from the realistic voltage-current-characteristic (see Sec. A.2.2).

During this cycle ohmic losses are only dissipated during phases 2 and 3. If the temperature rise at the end of the cycle is small enough to maintain a finite critical current, the loop keeps a permanent current. If the superconductor is cooled, the temperature decreases again due to the lack of any heating and the critical current rises. Nevertheless, the permanent current does not change.

Considering the the finite inductance of the current loop and the special

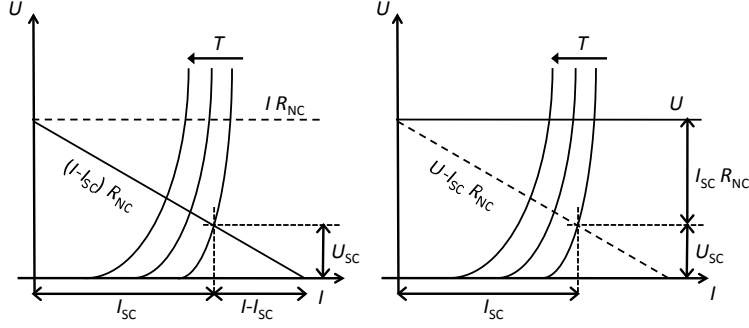


Figure 7.18: Graphical solution of the parallel and series circuit with a superconducting and a normal conducting element, Fig. 7.13 a) and d). (left) parallel case. (right) series case.

properties of the superconductor, we can give an explanation of the widely known experiments where superconducting samples float in permanent magnetic fields. The inductance limits the slope of the current rise while the superconductor limits the final current².

7.5.3 Graphical Solution

If a superconductor is either placed in parallel to a normal conductor driven by an external current source I (see Fig. 7.13 a)) or the superconductor is placed in series to a normal conductor driven by an external voltage source U (see Fig. 7.13 d)), the following non-linear equations have to be solved:

$$U_{SC}(I_{SC}) = R_{NC}(I - I_{SC}), \quad U_{SC}(I_{SC}) = U - R_{NC}I_{SC}. \quad (7.51)$$

The graphical solution is shown in Fig. 7.18. For the parallel case (left), the diagonal line represents the voltage over the resistance R_{NC} and the intersection with U_{SC} defines the partition of the current I into I_{SC} and I_{NC} . In case of the series connection (right), the voltage over the resistance R_{NC} is represented by the space in between the horizontal and the dashed line. The intersection therefore gives the partition of the voltage U and determines the current through the branch, I_{SC} .

The voltage-current-characteristic depends strongly on the applied magnetic induction and temperature. Therefore, the graphical solution, obtained above, has to be re-determined if any of these quantities changes.

²The explanation given is for type II superconductors. Most of the experiments are either performed with type I materials or so called high-temperature superconductors. The physics behind these kind of materials is different, but nevertheless the limitation of the current holds.

7.6 Cable Magnetization Losses

Time varying magnetic fields induce eddy currents over superconducting current loops and excite screening currents in superconducting filaments. In superconducting cables, the former two are denoted inter-filament and inter-strand coupling currents. The latter are denoted as persistent currents or superconductor magnetization. All three effects are summarized as cable magnetizations.

In the context of superconducting accelerator magnets, the three phenomena are associated with induced field errors [Auch 08] and losses in the cables [Kirb 07]. While we can ignore field quality for the quench simulation, the model requires to include all relevant heat sources.

Inter-filament coupling currents Strands for superconducting accelerator magnets consist of a large number of superconducting filaments embedded in a copper matrix. The filaments are twisted around the strand axis. Eddy currents induced over loops formed by superconducting filaments close over the resistive copper matrix and cause heating. These currents are denoted inter-filament coupling currents (IFCC).

The magnetization resulting from the eddy currents in these meshes can be calculated analytically [Wils 83, pp. 176]. The calculation is carried out in four steps: Calculation of the induced voltage over a segment along two twisted filaments, determination of the current density in the surrounding matrix material, calculation of the surface current density constituting the return path and determination of the equivalent magnetization density.

Induced voltage: Consider two filaments along helical paths around the z -axis, shown in Fig. 7.19. Without loss of generality they are exposed to an applied field parallel to the y -axis; $\mathbf{B} = B_y \mathbf{e}_y$.

The voltage induced over a segment of the two filaments is calculated by means of FARADAY's law,

$$\int_{\partial F} \mathbf{E} \cdot d\mathbf{r} = - \int_F \frac{d\mathbf{B}}{dt} \cdot d\mathbf{a}, \quad (7.52)$$

where F denotes the surface spanned by the double helix. The surface is longitudinally delimited by $\pm z$.

For the surface integral we can exploit that the integral is zero on faces tangential to \mathbf{B} and evaluate the integral in the xz -plane. The projection of F , denoted as \tilde{F} , is transversally bounded by $\pm r_0 \cos\left(\frac{2\pi}{p_s} z\right)$ with r_0 the radius of the helical paths and p_s the twist pitch length. The change in magnetic flux is given to

$$\begin{aligned} \int_{\tilde{F}} \frac{d\mathbf{B}}{dt} \cdot d\mathbf{a} &= \int_{-z}^z \int_{-r_0 \cos\left(\frac{2\pi}{p_s} z'\right)}^{r_0 \cos\left(\frac{2\pi}{p_s} z'\right)} \frac{dB_y}{dt} dx dz' \\ &= 4r_0 \sin\left(\frac{2\pi}{p_s} z\right) \frac{p_s}{2\pi} \frac{dB_y}{dt}. \end{aligned} \quad (7.53)$$

While the filaments are in the superconducting state, the voltage must drop entirely across the resistance matrix. Assuming symmetry, the contour integral simplifies to $\int_{\partial F} \mathbf{E} \cdot d\mathbf{r} = 4U(z)$ and it follows:

$$U(z) = -\frac{dB_y}{dt} \frac{p_s}{2\pi} r_0 \sin\left(\frac{2\pi}{p_s} z\right). \quad (7.54)$$

Current density in the matrix material: In the next step, we consider a rod covered by filaments twisted along the axis and approximate the ensemble by a thin superconducting layer at the radius r_0 . Disregarding any mutual dependence between filaments, the induced voltage constitutes a boundary condition for the potential inside the matrix material. The potential ϕ can be expressed as a function of the φ -coordinate. With $\varphi = 2\pi z/p_s$, Eq. (7.54) can be rewritten as

$$\phi(\varphi) = -\frac{dB_y}{dt} \frac{p_s}{2\pi} r_0 \sin \varphi = -\frac{dB_y}{dt} \frac{p_s}{2\pi} y, \quad (7.55)$$

and the gradient yields a uniform electric field. The current density in the matrix can be calculated from OHM's law:

$$J_y = \frac{1}{\rho_{\text{eff}}} E_y = \frac{1}{\rho_{\text{eff}}} \frac{dB_y}{dt} \frac{p_s}{2\pi}. \quad (7.56)$$

Surface current density: The y -directed current density closes on the cylindrical shell by means of a helical surface current density \mathbf{J}_F . Owing to the longitudinal invariance, the φ -component of the surface current density can be determined from the continuity equation,

$$\oint_{\partial V} \mathbf{J} \cdot d\mathbf{a} = \Delta z \left(\int_{\pi/2}^{\varphi} J_y \mathbf{e}_y \cdot (-\mathbf{e}_\rho) r_0 d\varphi' + J_{F,\varphi}(\varphi) \right) = 0 \quad (7.57)$$

where $d\mathbf{a}$ is a differential surface element on the closed surface ∂V (see Fig. 7.19) and Δz an arbitrary length in longitudinal direction. This results in

$$J_{F,\varphi}(\varphi) = \int_{\pi/2}^{\varphi} J_y \sin \varphi' r_0 d\varphi' = -\frac{1}{\rho_{\text{eff}}} \frac{dB_y}{dt} \frac{p_s}{2\pi} r_0 \cos \varphi. \quad (7.58)$$

As the filaments in the cylinder follow helical paths, the azimuthal and longitudinal current densities are coupled. With one full transposition over a twist pitch length p_s we have

$$J_{F,z} = -\frac{p_s}{2\pi r_0} J_{F,\varphi}. \quad (7.59)$$

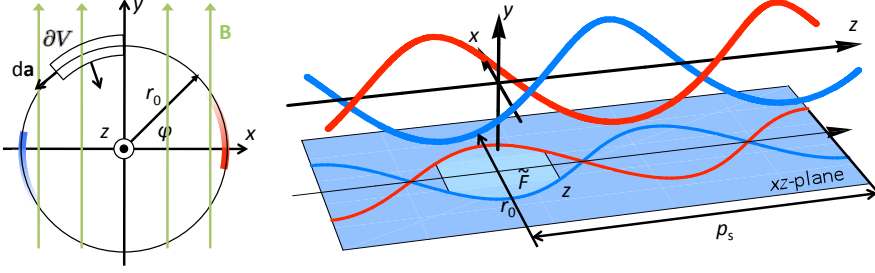


Figure 7.19: Inter-filament coupling currents. (left) Geometry in the xy -plane. The integral over the current density is evaluated over the closed surface ∂V . (right) two twisted filaments along the z -axis and the projection on the xz -plane.

Magnetization density: After [Henk 01, p. 156], we can express a homogeneous magnetization \mathbf{M} in a volume V by means of a magnetization surface current density $\mathbf{J}_{\text{F,mag}}$ flowing on ∂V ,

$$\mathbf{M} \times \mathbf{n} = \mathbf{J}_{\text{F,mag}}, \quad (7.60)$$

where \mathbf{n} denotes the normal vector on the boundary. Identifying $\mathbf{J}_{\text{F,mag}} = J_{\text{F,z}} \mathbf{e}_z$ and disregarding the azimuthal component, the inter-filament magnetization is given by

$$\mathbf{M}_{\text{IFCC}} = M_y \mathbf{e}_y = -\frac{1}{\rho_{\text{eff}}} \frac{dB_y}{dt} \left(\frac{p_s}{2\pi} \right)^2 \mathbf{e}_y. \quad (7.61)$$

Notice the negative sign. The magnetization opposes the change of magnetic induction.

For a homogenous distribution of filaments within the strand, the result can be scaled with the strand filling factor η_s . The field dependent resistivity of the matrix material can be taken into account by

$$\rho_{\text{eff}} = \rho_{\text{IFCC}} + \frac{d\rho_{\text{IFCC}}}{dB} |\mathbf{B}| \quad (7.62)$$

ρ_{IFCC} is the constant part of the effective resistivity and $\frac{d\rho_{\text{IFCC}}}{dB}$ the slope of the magneto-resistive effect; $[\frac{d\rho_{\text{IFCC}}}{dB}] = \Omega \text{mT}^{-1}$.

The eddy-current losses are only dissipated in the matrix material. The loss density can be calculated from the field components parallel to the applied magnetic induction:

$$p_{\text{IFCC}} = \mathbf{E} \cdot \mathbf{J} = \rho_{\text{eff}} J_y^2 = -\mathbf{M}_{\text{IFCC}} \cdot \frac{d\mathbf{B}}{dt} = \frac{1}{\rho_{\text{eff}}} \left(\frac{p_s}{2\pi} \right)^2 \left(\frac{dB_y}{dt} \right)^2. \quad (7.63)$$

The derivation is based on the assumption of filaments in superconducting state. For a strand in the quenched state, the model is not valid. Due

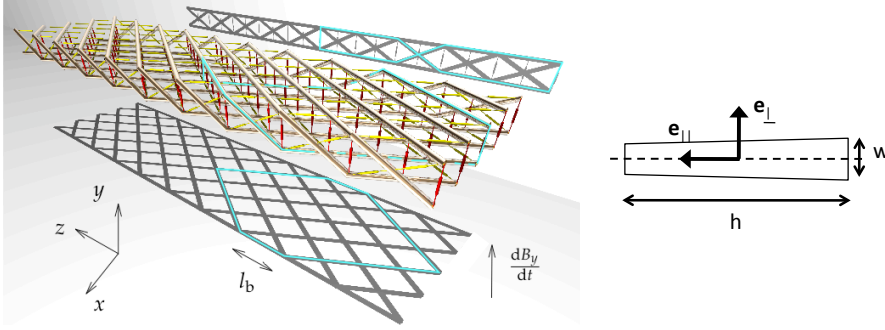


Figure 7.20: (left) Model for inter-strand coupling currents. Courtesy R. de Maria [Mari 04]. (right) Local frame and cable parameters for the derivation of the inter-strand coupling current magnetization.

to the comparably low critical temperature of common superconductors we do not need to consider the temperature dependence of the matrix material. Furthermore, the induced eddy currents are not treated as a diffusion process. Currents and losses appear instantaneously.

Inter-strand coupling currents Cables for superconducting accelerator magnets consist of a number of strands connected in parallel and sharing the transport current. The strands are twisted along the cable axis in order to reduce the size of superconducting loops and to obtain a homogeneous current distribution. Nevertheless, varying magnetic fields induce eddy currents over the twisted strands which close over the contact resistance between neighboring strands. The current flow through the contact resistance causes heating. These currents are denoted inter-strand coupling currents (IFCC).

A number of models for the calculation of inter-strand coupling currents can be found in the literature. Electrical network models describing the strands and their inter-connection by means of lumped elements [Devr 95], allow to calculate induced coupling currents for various ramp-rates and field patterns [Verw 95], see Fig. 7.20 (left). However, the numerical solution on the scale of a full length magnet is computationally too demanding.

Analytical models describing eddy currents by means of the magnetization \mathbf{M} [Mess 96, pp. 102] and [Wils 72], reduce the computational effort significantly at the expense of accuracy. These models do not allow to compute the time transient change of the magnetization after a field variation, or the change of the resistivity in the contact resistances or the superconducting strands with temperature and field.

The derivation of the analytical model by WILSON is lengthy and can be found in [Wils 72]. We solely quote the result for the magnetization and losses. Consider a Rutherford-type cable of mean width w , height h and twist pitch length ℓ_p . We assume all strands in the superconducting state.

The cable defines a local frame consisting of one vector parallel \mathbf{e}_{\parallel} and one vector normal \mathbf{e}_{\perp} to the broad face of the cable, see Fig. 7.20 (right). The magnetization can be calculated from the average magnetic induction over either cable face:

$$M_{\perp}^c = -\frac{1}{120R_c}\ell_p N_s(N_s - 1)\frac{h}{w}\frac{dB_{\perp}}{dt}, \quad (7.64)$$

$$M_{\perp}^a = -\frac{1}{3R_a}\ell_p\frac{h}{w}\frac{dB_{\perp}}{dt}, \quad (7.65)$$

$$M_{\parallel}^a = -\frac{1}{8R_a}\ell_p\frac{w}{h}\frac{dB_{\parallel}}{dt}, \quad (7.66)$$

where N_s is the number of strands and the indices c,a stand for the cross and adjacent resistances, respectively. Notice that the magnetization opposes the field change following LENZ's law. The total inter-strand coupling current magnetization is given by

$$\mathbf{M}_{\text{ISCC}} = (M_{\perp}^c + M_{\perp}^a)\mathbf{e}_{\perp} + M_{\parallel}^a\mathbf{e}_{\parallel} \quad (7.67)$$

In this simplified model, neglecting the time constant of the induced eddy currents, the loss power density can be calculated from the magnetization and field change [Mess 96, pp. 101], *i.e.* from $p = -\mathbf{M} \cdot \frac{d\mathbf{B}}{dt}$. This can be motivated remembering that $M \sim J$ and $\frac{d\mathbf{B}}{dt} \sim E$ and thus we get:

$$p_{\text{ISCC}} = -\mathbf{M}_{\text{ISCC}} \cdot \frac{d\mathbf{B}_{\text{av}}}{dt} \quad (7.68)$$

For the inter-filament coupling currents we could derive the same result analytically.

The analytical magnetization model assumes that the strands are in the superconducting state and that the induced currents are well below the critical current. The maximum current induced in the superconducting strands $I_{\text{SC,max}}$ can be estimated from the following equation [Verw 95, p. 75]:

$$I_{\text{SC,max}} = 0.0415\frac{\ell_p h N_s}{R_c}\frac{dB_{\perp}}{dt}, \quad [I_{\text{SC,max}}] = A. \quad (7.69)$$

Superconductor magnetization The superconductor magnetization is fundamentally different to the former two induced currents. It does not depend on the rate of field change and exhibits a hysteresis in a varying field.

The arising magnetic fields are accurately described by means of the intersecting-ellipses-model [Voll 02]. Although the model allows to calculate the hysteresis losses, the dissipated power remains undefined. In Sec. 7.7 the power is derived for a simplified analytical model. The results allow to conclude that losses stemming from persistent currents can be neglected for fast ramping magnets and during a fast discharge as for a quench.

7.7 Superconductor Hysteresis Losses

Cables in superconducting magnets are subjected to field dependent losses, *i.e.* induced inter-strand and inter-filament coupling losses, and superconductor hysteresis losses. For the two kinds of induced eddy currents, analytical and numerical models are available, allowing to calculate the dissipated power under various operating conditions (Sec. 7.6). For the losses stemming from the superconductor magnetization - as for hysteresis losses in general - the literature only gives formulae for the dissipated energy over closed excitation cycles.

The thermal stability of a cable to quench depends on the amount of dissipated losses compared to the available cooling power. Whenever losses and heating exceed the cooling capacity of the magnet, the cable temperature rises and the conductor eventually quenches. Hence, the computation of the cable stability against time transient losses, as well as the simulation of the quench propagation process in a magnet, depend on the exact description of all dissipated losses in time.

In the following, we derive an expression for the instantaneously dissipated hysteresis losses during an arbitrary ramp-cycle using a simplified geometry and hysteresis model.

Energy loss over a closed cycle We recall the approach for the calculation of the energy loss over a full cycle. Consider a magnetic system exhibiting hysteresis and subjected to a periodic input variation. In the steady state, we can assume that the system is in an identical state at the start and end of any closed cycle. Hence, all field quantities and especially the magnetic energy are identical. The hysteresis energy loss is then given by (see Sec. 7.3),

$$W_{\text{hyst}}^V = \mu_0 \int_V \oint \mathbf{M} \cdot d\mathbf{H} dV. \quad (7.70)$$

Based on the principle of energy conservation, the same result can be obtained by integrating the energy supplied by the source (disregarding all other losses). In the steady state, the net energy supply during a full period is dissipated in losses. (The energy associated with the working point of the system is not affected).

Approach For the calculation of the instantaneously dissipated losses, we combine the principle of energy conservation with a physical model describing the superconductor hysteresis.³ We make the following assumptions:

³ BERTOTTI and MAYERGOYZ [Bert 06, pp. 347] write:

It should not be surprising that the expression for hysteretic energy losses has been found only for the case of periodic input variations. The reason behind this fact is that the energy losses occurring for periodic input variations can be easily evaluated by using only energy conservation principle; no knowledge of actual mechanisms of hysteresis or its model is required. The situation is much more complicated when arbitrary input variations are considered. Here, the

- The dissipated energy constitutes a monotone function in time. We can therefore deduce the dissipated energy from the energy supplied by a source by successively subtracting the energy stored in all sub-systems.
- If a model adequately describes the hysteresis measurements, the model is exhaustive and no additional effects need to be considered. Therefore, all relevant energy storages are established and can be monitored.

In the case of superconductors, the hysteresis can be well described by means of mere electromagnetic models and the energy balance can be calculated by means of POYNTING's theorem.

Simplified Problem The approach is demonstrated by means of a simplified problem. Consider an infinite slab of superconducting material with thickness $2d$. The slab is aligned parallel to the yz -plane and the center is placed at $x = 0$, see Fig. 7.21 (left). A coil with N' windings per unit length is mounted on the surface of the superconductor. The coil constitutes a surface current density $\mathbf{J}_F = \mp N' I \mathbf{e}_z$ (at $x = \pm d$). The corresponding primary magnetic field inside the coil is homogeneous

$$\mathbf{H}_e = H_e \mathbf{e}_y = N' I \mathbf{e}_y, \quad (7.71)$$

and cancels for $|x| > d$. The excitation current I is shown in Fig. 7.21 (right), where I_0 and τ denote an arbitrary current level and time interval, respectively. The ramp-cycle contains two closed cycles, *i.e.* $2 \rightarrow 10\tau$ and $12 \rightarrow 14\tau$. The ramp-rate of the second cycle is twice the ramp-rate of the first cycle.

Applying the approach to an infinite slab, reduces the complexity of the analytical field calculation significantly. We merely deal with polynomials of, at maximum, second order. The superconductor can be described by means of the well established critical state model. With a given current ramp-cycle, we can calculate the superconductor magnetization analytically without relying on a numerical hysteresis model.

Critical state model The critical state model was developed by BEAN for a slab of hard superconducting material [Bean 62, Bean 64]. The model gives a macroscopical description of the superconductor magnetization. It is based on the following principles:

- The interior of a superconductor is shielded from an external magnetic field by a layer of screening currents.
- The maximum current density in the superconductor is limited. The limit is denoted critical current density J_c .

energy conservation principle alone is not sufficient, and an adequate model of hysteresis should be employed in order to arrive at the solution to the problem.

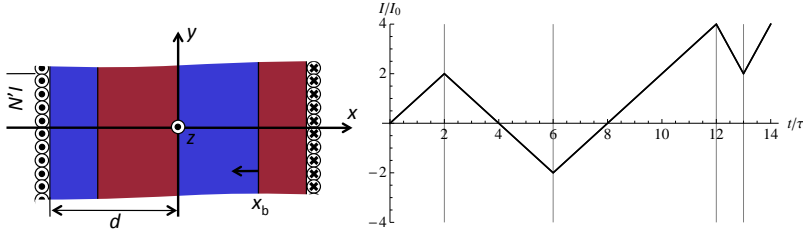


Figure 7.21: (left) Critical state model of a superconducting slab. The slab of thickness $2d$ is placed in a coil with current I and N' windings per unit length. The coil constitutes a surface current density $\mathbf{J}_F = \mp N'I\mathbf{e}_z$. The magnetic field of the excitation coil, \mathbf{H}_e , is y -directed. Two screening current layers are shown. The inner layer was to screen a positive external field. When the field starts decreasing the outer layer grows inwards. The boundary is denoted x_b . (right) Excitation current of the coil. We can distinguish two closed cycles, $2 \rightarrow 10\tau$ and $12 \rightarrow 14\tau$. The current ramp-rate of the second cycle is twice the ramp-rate of the first cycle.

- Any magnetic field, albeit small, always induces the critical current density independent of the ramp-rate. With increasing applied external field, the screening layer grows inwards. The width of the screening layer is called penetration depth.
- When reaching a certain field level, the screening currents cover the full sample. This state is denoted as fully penetrated.
- Whenever the change of external magnetic field inverts direction, a new screening layer of opposite polarity is created on the boundary of the superconductor. The new layer annihilates the previous layer while growing inwards, see Fig. 7.21 (left).

For the simplified model, the field and temperature dependence of the critical current density (Sec. A.2.4) are not taken into account. For the demonstration of our approach, we arbitrarily set

$$J_c = \frac{H_e(t=\tau)}{d} = \frac{N'I_0}{d}. \quad (7.72)$$

For the ramp-cycle given in Fig. 7.21 (right), this results in a fully penetrated state as soon as the current changes by more than $\Delta I = I_0$.

Screening currents In the following, we determine the screening current layers and their magnetic field for the given external field ramp. For the sake of simplification, we give functions only for $x > 0$ and note the kind of symmetry in x , *i.e.* odd or even function.

The current cycle shown in Fig. 7.21 (right) defines 5 intervals. During each interval a new current layer is created at $x = d$ and grows inwards.

Intervall i	1	2	3	4	5
lower boundary t_1^i	0τ	2τ	6τ	12τ	13τ
upper boundary t_u^i	2τ	6τ	12τ	13τ	14τ

The ramp-cycle was chosen such that we do not need to be concerned with merging current layers, *i.e.* layers of identical polarity growing into each other. We define \dot{H}_e^i as the derivative of the external magnetic field within the interval i . The inner boundary $x_b^i(t)$ of each current layer can be calculated by:

$$x_b^i(t) = \begin{cases} d & t - t_1^i < 0 \\ d - \frac{|\dot{H}_e^i|}{J_c}(t - t_1^i) & 0 < t - t_1^i < \frac{dJ_c}{|\dot{H}_e^i|} \\ 0 & \text{else} \end{cases} \quad (7.73)$$

The screening current density as a function of the position x and time t , is built from the individual current layers \mathbf{J}^i . The function \mathbf{J}^i is odd,

$$\mathbf{J}^i(x, t) = J_c \frac{\dot{H}_e^i}{|\dot{H}_e^i|} \mathbf{e}_z \begin{cases} 0 & x < x_b^i(t) \\ 1 & x \geq x_b^i(t) \end{cases}. \quad (7.74)$$

The superposition yields the total screening current density \mathbf{J} ,

$$\mathbf{J}(x, t) = \mathbf{J}^1(x, t) + 2 \sum_{i=2}^5 \mathbf{J}^i(x, t). \quad (7.75)$$

Notice that the screening current layers for $i > 1$ are added twice. This is in order to annihilate previous layers and does not violate the limitation of the maximum current density in a superconductor.

Figure 7.22 (left) shows the screening current density distribution within the slab cross-section over time. The slope of the “fish-bone” pattern depends on the rate of change of the applied magnetic field H_e . For $x > 0$ and $\tau < t < 2\tau$, the current density is $+z$ -directed. The center of the slab ($x = 0$) remains current free until $t = 1\tau$.

Electromagnetic Fields The screening field \mathbf{H}_i is calculated from the screening current density \mathbf{J} . Assuming symmetry we obtain

$$\mathbf{H}_i(x, t) = - \int_{x'=x}^d J(x', t) dx' \mathbf{e}_y. \quad (7.76)$$

The function is even and opposing the external field change, see Fig. 7.22 (right). The magnetic induction in the superconducting slab yields

$$\mathbf{B}(x, t) = \mu_0 (\mathbf{H}_e(t) + \mathbf{H}_i(x, t)). \quad (7.77)$$

Due to the screening currents, the center of the slab remains field free ($\mathbf{B} = \mathbf{0}$) until $t = 1\tau$. Thereafter, the magnetic induction in the center of the slab lacks

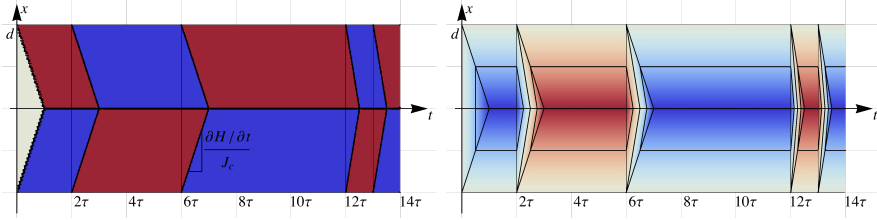


Figure 7.22: The system of the critical state model: (left) Screening current density over the x -axis versus time. For an external field with piece-wise constant ramp-rate the layers are of trapezoidal shape in the time-space contour plot. (right) Contour plot of the internal magnetic field H_i over the x -axis versus time. The field increases by $J_c d$ for every two contour lines. The function can be obtained by integrating the current density along the x -axis from the outside to the inside.

the applied magnetic field. Integrating over the cross-section of the slab yields the enclosed magnetic flux per unit length Ψ' .

$$\Psi'(x, t) = \int_{x'=0}^x B(x', t) dx'. \quad (7.78)$$

The magnetic induction and magnetic flux are shown in Fig. 7.23. The electrical field can be obtained either by integrating the change of magnetic induction along the x -axis or by differentiating the total magnetic flux over time:

$$\mathbf{E}(x, t) = \int_{x'=0}^x \frac{\partial B}{\partial t}(x', t) dx' \mathbf{e}_z = \frac{\partial \Psi'}{\partial t}(x, t) \mathbf{e}_z \quad (7.79)$$

The change of magnetic induction and the electrical field are shown in Fig. 7.24.

Hysteresis loop Integrating the magnetic screening field \mathbf{H}_i over the slab cross-section, yields the internal magnetic flux per unit length Ψ'_i . Figure 7.25 shows the internal flux plotted over the applied external magnetic field H_e . We can distinguish a “virgin curve” for $0 \rightarrow 1\tau$ and two closed hysteresis loops, $2 \rightarrow 10\tau$ and $12 \rightarrow 14\tau$, respectively.

Apart from the first layer of screening currents, every new layer annihilates the previous layer and creates a new layer of opposite polarity. This results in a steeper slope than on the virgin curve.

Energy Balance We calculate the energy balance for the given current cycle applying POYNTING’S theorem in integral form (derived in Sec. 7.3) and integrating the different terms over time. Due to the 1D-approach all quantities are given per unit area and denoted by calligraphic characters, *i.e.* \mathcal{S} , \mathcal{W} and \mathcal{P} , with $[\mathcal{S}] = [\mathcal{W}] = [\mathcal{P}] = \text{Jm}^{-2}$.

In the simplified model, the magnetic field is zero for $|x| > d$. We identify the surface integral over the superconductor boundary as the electromagnetic

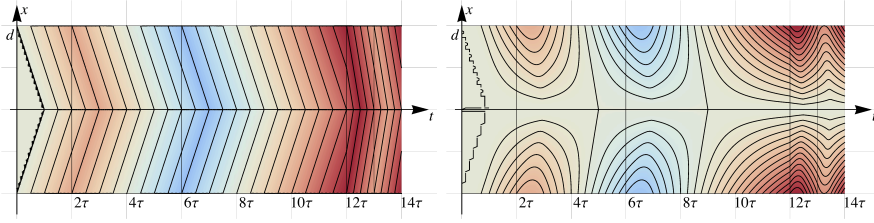


Figure 7.23: (left) Contour plot of the total magnetic induction over the x -axis versus time. The magnetic induction increases by $\mu_0 J_c d = \mu_0 N' I_0$ for every two contour lines. The magnetic induction is given by the sum of the external magnetic field H_e and the screening field H_i (or magnetization M). Note that the field in the center of the slab is completely shielded (equals zero) until $t = \tau$. Further more, the field in the center of the slab shows a time lack compared to the excitation, compare Fig. 7.21. (right) Contour plot of the magnetic flux per unit length over the x -axis versus time. The confined flux increases by $\mu_0 J_c d^2$ for every two contour lines. The flux is given by the integral over the magnetic induction from the center of the slab to the position x .

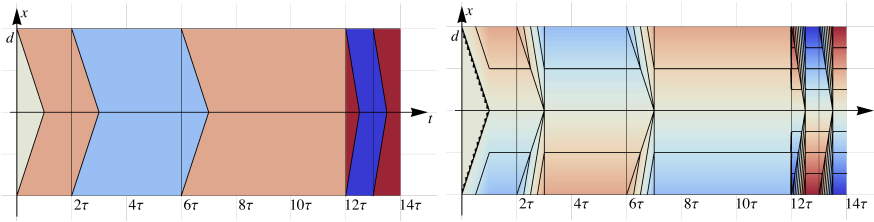


Figure 7.24: (left) Contour plot of the time derivative of the magnetic induction over the x -axis versus time. The inner magnetic field varies only within the triangular shapes. (right) Contour plot of the electrical field over the x -axis versus time. The electrical field increases by $\mu_0 J_c d^2 / T$ for every two contour lines. This function can be obtained by integrating over the time derivative of the magnetic induction from the center of the slab to the position x or by differentiating the magnetic flux in Fig. 7.23 (right) over time.

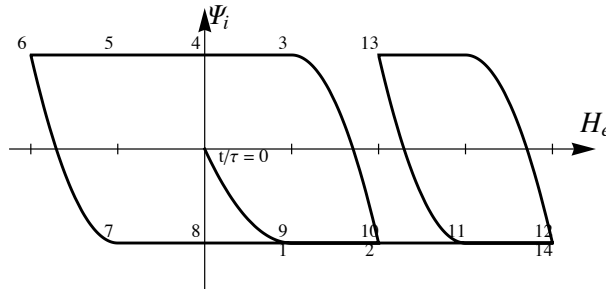


Figure 7.25: Hysteresis loop of the inner magnetic Ψ_i flux through the coil versus applied magnetic field H_e . We can identify two closed cycles: $2 \rightarrow 10\tau$ and $12 \rightarrow 14\tau$. The slope of the "virgin" curve $0 \rightarrow 1\tau$, is different to the slopes during all following magnetization changes.

energy exchange with the current source (factor 2 because of the two surfaces). This is denoted by \mathcal{S} ,

$$\begin{aligned}\mathcal{S}(t) &= 2 \int_{t'=0}^t [\mathbf{E}(x=d, t') \times \mathbf{H}(x=d, t')] \cdot \mathbf{e}_x dt' \\ &= 2 \int_{t'=0}^t [\mathbf{E}(x=d, t') \times \mathbf{H}_e(t')] \cdot \mathbf{e}_x dt'.\end{aligned}\quad (7.80)$$

The superconductor magnetization is expressed by means of the screening current density \mathbf{J} and therefore $\mathbf{B} = \mu_0 \mathbf{H}$. Integrating $\partial \mathbf{B} / \partial t \cdot \mathbf{H}$ over time and the cross-section of the slab, we obtain the magnetic energy stored in the slab \mathcal{W} at the time t :

$$\begin{aligned}\mathcal{W}(t) &= \int_{x=-d}^d \int_{t'=0}^t \frac{\partial \mathbf{B}}{\partial t}(x, t') \cdot \mathbf{H}(x, t') dt' dx \\ &= \frac{\mu_0}{2} \int_{x=-d}^d [\mathbf{H}_e(t) + \mathbf{H}_i(x, t)]^2 dx\end{aligned}\quad (7.81)$$

The energy loss per unit area of the slab is given by \mathcal{P} ,

$$\mathcal{P}(t) = \int_{x=-d}^d \int_{t'=0}^t \mathbf{E}(x, t') \cdot \mathbf{J}(x, t') dt' dx. \quad (7.82)$$

The three quantities fulfill the following equation at all time,

$$-\mathcal{S} = \mathcal{P} + \mathcal{W}. \quad (7.83)$$

We conclude that the electromagnetic model of the superconductor hysteresis is exhaustive, *i.e.* the critical state model comprises all energy storages and sinks, and no further effects need to be considered.

Figure 7.26 (left) shows all three quantities plotted over time. The graph for \mathcal{P} is monotonous, *i.e.* the accumulated energy is only growing and thus constitutes the dissipated losses. The energy loss over either of the two closed cycles can be read off from the graphs for \mathcal{P} or \mathcal{S} . It is given by the difference of the start and end value.

Figure 7.26 (right) shows the time derivative of the three quantities. We interpret the function $d\mathcal{P}/dt$ as the dissipated power P ,

$$P = \int_V \mathbf{E} \cdot \mathbf{J} dV \quad (7.84)$$

Regarding the dissipated power in Fig. 7.26 (right), we can distinguish two dependencies. During the built-up of a screening current layer the power reduces to zero following the shape of a parabola. After the screening layer is fully established, the dissipated power is constant. The magnitude of the dissipated power is in linear dependence of the applied ramp-rate.

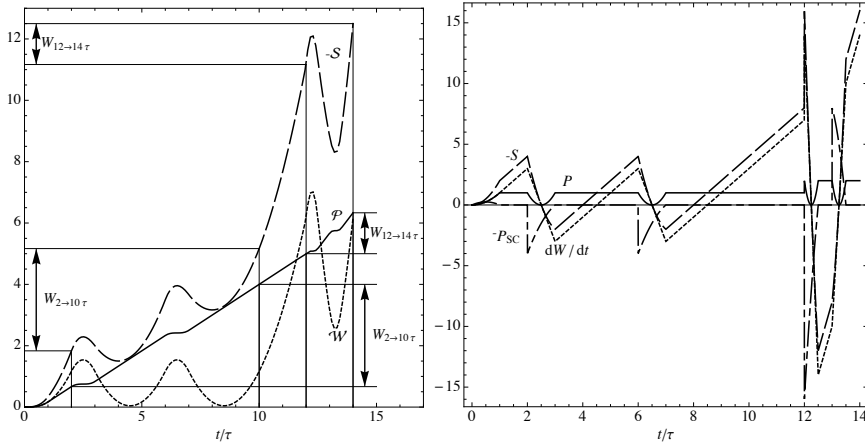


Figure 7.26: (left) Supplied, dissipated and stored magnetic energy over time: The dashed line shows the integrated energy flux from the poynting vector, the dotted line the magnetic energy and the solid line the integrated losses. The energy loss for the two closed loops, $2 \rightarrow 10\tau$ and $12 \rightarrow 14\tau$, is indicated. (right) Energy change and power versus time. The dotted line shows the change of stored magnetic energy and the solid line the dissipated power. For comparison, the dash-dotted line shows the negative power as seen from the current source. Note that the power at the source only differs from zero while the screening layers change. Furthermore, the maximum power depends on the applied field level and is both, positive and negative.

Circuit approach For the sake of completeness, we give a description by means of lumped circuit elements. In the 1D-approach, the voltage induced over the excitation coil can be calculated from the electric field,

$$U''_{\text{ind}} = N' E_z, \quad (7.85)$$

with $[U''_{\text{ind}}] = \text{Vm}^{-2}$. This can be split into a part induced over the self inductance of the coil and a part stemming from the superconductor U''_{SC} ,

$$U''_{\text{SC}} = \mu_0 N' \frac{\partial H_i}{\partial t}, \quad (7.86)$$

As shown in Fig. 7.26 (right), the dissipated power $P_{\text{SC}} = U''_{\text{SC}} I$ presents four distinct spikes during the time when the screening layers are changing. The magnitude and the sign of the spikes differ. Therefore, P_{SC} represents both stored and dissipated energy and cannot be used to derive the momentarily dissipated losses. An integration over the two closed cycles yields the energy loss as above.

Quench model For the calculation of the heat load in superconducting magnets, superconductor hysteresis losses can be considered by means of the average power, *i.e.* the total energy of a cycle divided by the cycle duration. In the case of the LHC main bending magnet, the total hysteresis losses for

a complete ramp-cycle, from injection to nominal and down to injection current, account for 280 J/m [Voll 02, p. 135]. Over a ramp-duration of 2×1200 s this constitutes an average heat load of 0.12 Wm^{-1} .

For slow ramping magnets, the hysteresis losses can be neglected. Compared to the quadratic ramp-rate dependence of induced eddy currents, hysteresis losses increase only linearly and are easily exceeded. In the case of the LHC MB the induced eddy current losses are in the same order of magnitude at a ramp-rate of approximately 0.1 T/s. The full discharge of the magnet takes less than half a second.

Comparison to the literature BRECHNA [Brec 73, pp. 241] and IWASA [Iwas 94, pp. 274] derive the superconductor hysteresis losses for periodic operation conditions also using POYNTING's theorem and the critical state model. The problem of the momentarily dissipated losses is not addressed.

In his work on the model of the critical state of superconductors [Camp 07], CAMPBELL uses $\mathbf{E} \cdot \mathbf{J}$ as an expression for the dissipated power density without giving a derivation. The problem of the calculation of hysteresis losses is not discussed.

KANBARA [Kanb 87] derives the hysteresis losses from the induced voltage over a pick up coil yielding the power provided by the current source. As shown above, the energy flux from the current source contributes to both, stored energy and hysteresis losses. Therefore, it is possible to calculate the energy loss for a complete cycle, but not to express the momentarily dissipated power.

The approach of energy separation was applied to deduce the dissipated losses from hysteresis measurements of ferromagnetic materials [Bozo 93, pp. 518], [Town 35] and [Okam 36]. Due to the number of different physical effects interacting in ferromagnetic materials, the modeling of the different energy storages is much more complicated. Furthermore, magnetostriction couples the electromagnetic system to the mechanical system and the magneto caloric effect requires to include the thermodynamic system.

7.8 Modeling Rutherford-Type Cables

Roebel bar Most superconducting accelerator magnets are wound from Rutherford-type cables, *i.e.* twisted multi strand cables resembling the Roebel bar [Roeb 15] used in electrical machines.

The variation of the magnetic flux over the cable cross-section causes a non-uniform current distribution in the different strands. By fully transposing all strands over a short length, the maximum loop size and thus the induced eddy currents are reduced. In the 1970s it was shown at Rutherford Appleton Laboratory (RAL) that a twisted hollow tube of superconducting strands could be rolled into a rectangular or trapezoidal shape without significantly reducing its current carrying capability (degrading). Cables with a trapezoidal cross-section are used to built $\cos \theta$ -type coils and are denoted as

Keystoneing

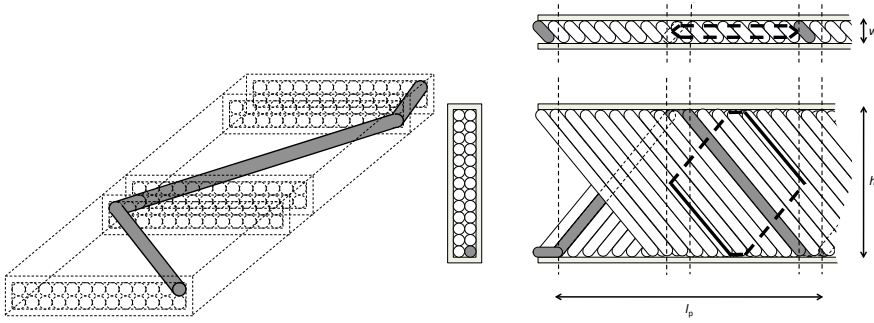


Figure 7.27: Rutherford-type cable. (left) Trajectory along one strand of a 26 strand cable over the twist pitch length ℓ_p . (right) Projections of the cable on each of the 3 coordinate planes. The strand from the figure left is highlighted in grey. Two loops for induced eddy currents are indicated by a thick black line.

keystoned. Figure 7.27 (left) shows the trajectory along one strand of a 26 strand cable over the twist pitch length ℓ_p .

The strands of a Rutherford-type cable are in resistive contact. We distinguish between adjacent resistances and cross-over resistances. The resistance depends on the strand coating material, the cable compaction, which may vary over the cable cross section, and eventually on the cable core material. Eddy currents induced in loops formed by superconducting strands close over the resistive contacts and cause heating (losses). These currents are denoted inter-strand coupling currents (ISCC). Figure 7.27 (right) shows the transposed strands and highlights two superconducting current-loops.

Resistive
contacts

In general two different types of coils have to be distinguished, potted coils, where the voids in between the strands of the cables are filled with glue/insulation, and wetted coils, where the voids are flooded with liquid helium. In the latter case, the heat capacity of the confined liquid helium contributes significantly to the thermal stability of the cable. In both cases, the resistive connection between adjacent and crossing strands allows heat transfer between strands and a quench can spread over the cable cross-section.

Thermal
properties

Model for Quench For the simulation of quench in accelerator magnets the numerical description of Rutherford-type cables on the level of strands is too demanding. Not only that for every cable one node per strand has to be considered, but also, due to the transposition of the strands, the cable has to be discretized longitudinally at least with the same number of steps per twist-pitch length.

In the present model, Rutherford-type cables are discretized with one node in the center of the conductor cross-section and a user supplied number of nodes along the length of the magnet. This reduces the number of elements significantly. For the LHC main bending magnet, where already 320 conductors have to be considered in the cross-section, the number of elements can

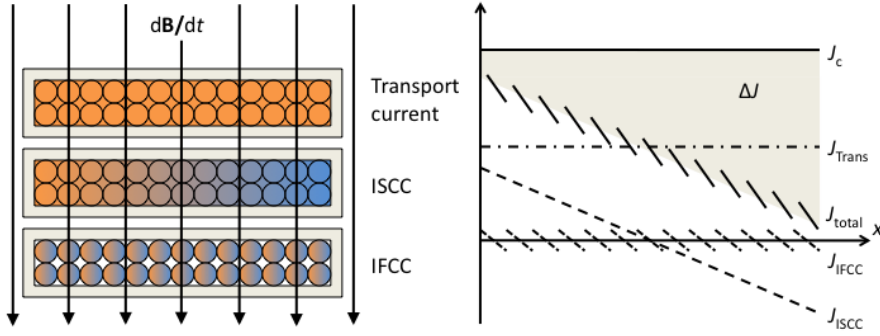


Figure 7.28: (left) Current distribution due to transport current, inter-strand coupling currents and inter-filament coupling currents. (right) Current density over the broad face of the cable. The difference between total current density and critical current density is available for superconductor screening currents as described by the critical state model. Note that the current density margin to quench ΔJ is much smaller on the left hand side of the cable. The values are not to scale.

be reduced by a factor of approximately $30^2/\ell_p$, *i.e.* by 5000 in total.

For the quench model relevant properties, *i.e.* current density, temperature, magnetic induction and loss power, we make the following assumptions:

Current density: The current density is constant over the conductor cross-section and over the length of the cable.

The transport current is evenly distributed over all strands of the cable. Between cables of different type the current density may vary due to differences in cross-sectional area or copper-to-superconductor ratio.

Figure 7.28 illustrates how the current distribution over the cable and strand cross-section is influenced by induced cable eddy currents, *i.e.* inter-strand and inter-filament eddy currents. Under the assumption that the induced current density is much smaller than the transport current density, this effect is disregarded.

Current redistribution, *i.e.* the by-passing of quenched strands over the cross-over and adjacent contact resistances, is not considered.

Temperature: The temperature is constant over the cable cross-section and varies linearly along the cable.

The thermal conductivity of the strand materials is many orders of magnitudes greater than of the surrounding insulation materials. Due to the transposition of the strands along the cable axis, the thermal gradient over the cable cross section is much smaller than between adjacent cables. Although, measurements show a gradient of up to 2.5 K over the cable cross-section, in a worst case scenario a homogeneous temperature distribution is assumed. In the case of confined helium II, the overall temperature gradient is small.

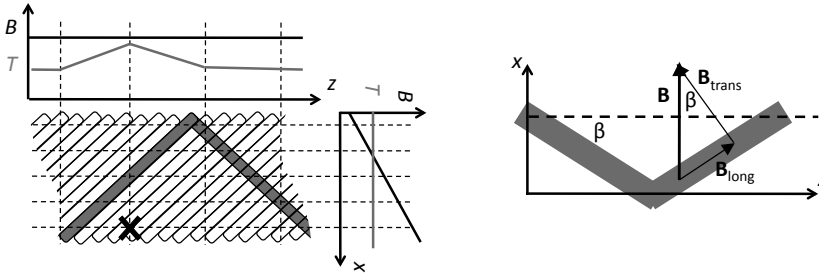


Figure 7.29: (left) Field and temperature over a twisted cable. Every strand is exposed to the full variation of magnetic field (grey). The quench is calculated from the peak field (thick cross). (right) Field decomposition.

Consequently, a quench always occurs immediately over the full conductor cross-section.

Magnetic induction: The model relies on the average and peak value of the magnetic induction and magnetic vector potential. These values are constant along the conductor.

Magnetic induction and magnetic vector potential vary over the conductor cross-section. Fully transposed, every strand is exposed to the total variation of the field.

Field-dependent material properties, *e.g.* the electrical resistivity of copper, are evaluated for the average of the magnetic induction yielding mean properties. Based on the assumptions for current density and temperature, a conductor quenches where the local field is maximum - conductor peak field. Note that in case of cables with large cabling angle β , we have to distinguish between longitudinal and transversal field components, see Fig. 7.29 (right).

The inductance of the magnet is calculated from the integral over the mean magnetic vector potential, see Sec. 7.4.

Induced losses: Induced losses are constant over the cable cross section. The losses are constant along superconducting parts of a conductor and zero where the conductor is quenched.

The loss models rely on the assumption of superconducting current loops over the cables and within the strands. Therefore, the model and losses change in case of a quench. The longitudinal temperature variation does not need to be considered.

Figure 7.29 (left) shows the distribution of current density, magnetic conduction, and temperature over the broad face of the cable and along the cable axis.

Note that a twisted cable produces, additionally to the azimuthal field, a longitudinal field on its axis. In a Rutherford-type cable, the transport current follows a helical trajectory along the cable axis. We decompose the current into a part flowing parallel to the cable axis and an orthogonal fraction, *i.e.* a solenoidal component. The parasitic field along the cable axis can be estimated by means of an ideal solenoid (Sec. E.1.2). For $N/h = 28/115$ mm and $IN = 11850$ A (data for the LHC MB inner layer cable), we obtain a central field of $B = 0.13$ T. This effect is small compared to the peak field of approximately 9 T and hence does not influence the simulation of quench. Nevertheless, in the low field region of the coil, this additional field can be of interest for the calculation of persistent currents.

7.9 Magnet Protection

Protection: high temperatures, excessive voltages	<p>In case of a quench, a superconducting magnet has to be protected from high temperatures and excessive voltages [Coul 96, Iwas 05]. High temperatures can destroy the insulation material or even result in a meltdown of the cable. Excessive voltages can result in arcs that could punch holes into the insulation. Furthermore, high current density and temperature gradients can cause irreversible degradation of the superconducting material reducing the current carrying capability [Iwas 05].</p> <p>The quench behavior of a magnet, <i>i.e.</i> the current decay and the hot-spot temperature, depend on the magnet design, <i>i.e.</i> the inductance, the thermal quench propagation velocity, its susceptibility to induced losses, and the external electric circuit.</p>
Passive protection	<p>Following the overview given in [Iwas 05, Coul 94] quench protection can be sketched as shown in Fig. 7.30. Passive quench protection methods aim at the optimization of the inherent features of the magnet; the choice of materials and the design, such that safe operation can be guaranteed even in case of a quench. Providing a parallel path to the current and strong cooling to the conductors allows the current to by-pass the quench, and the quench to recover. This can be applied on the magnet scale, <i>e.g.</i> for small corrector magnets [Schm 00], or on conductor level: If, under all operating conditions, the cooling of the conductor exceeds the ohmic heating in the event of a quench, the conductor is called cryostable or unconditionally stable [Dres 95, pp. 56]. Cryostability was defined by STEKLY in [Stek 65]. A magnet is called self-protecting if the quench propagation over the magnet is generally fast enough to substantially decrease the current and protect the magnet from over heating [Iwas 94, p. 326].</p>
Cryostability	
Self-protecting	
Active protection	<p>Active magnet protection relies on the timely detection of the quench, followed by a rapid current extraction. Due to the inductance of the magnet circuit, the current cannot be switched off instantaneously. Thus the power supply is shortened by means of a free-wheeling diode. The current decay rate is given by the inductance and resistivity of the remaining circuit, $\tau = L/R$. If the magnet is powered in a chain of magnets the time constant can be</p>

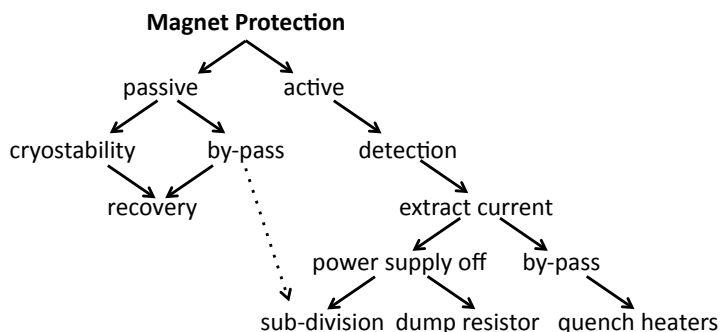


Figure 7.30: Scheme of quench protection methods.

significantly reduced by isolating the quenched magnet from the rest of the chain by means of a by-pass diode or resistor. Triggering additional quenches in the isolated magnet by firing quench heaters and quench back further increases the resistivity and accelerates the current decrease. In the case of the remaining chain, and for individually operated magnets, the time constant can be reduced by switching-in an additional dump resistor. By subdividing a magnet into several inductively coupled loops, the current in the quenched loop decreases faster due to the reduced inductance and, as a positive side-effect, increases the current in the linked loops and consequently drives them resistive. Inductively coupling a secondary circuit with finite resistance allows transfer of some of the stored energy into the secondary circuit. If the resistor of the secondary circuit is in close contact with the primary windings the dissipated energy can be used as a quench heater.

Quench heaters

Dump resistor
Sub-division

Coupled secondary

Two equivalent paradigms can be applied to active quench protection: Extraction and dissipation of the stored magnetic energy, or the reduction of the discharge time. Isolating the quenched magnet and subdividing the circuit reduces the inductance of the considered circuit and, therefore, both the stored magnetic energy as well as the discharge time constant. Any increase in resistivity either extracts energy from the quenched magnet into an external and less critical resistor or helps to evenly dissipate the energy inside the magnet. In doing so, the time constant is further reduced. Nevertheless, both paradigms rely on the rapid disconnection of the magnet from the power supply.

Protection paradigm

The need for quench protection is often motivated by the amount of electromagnetic energy stored in superconducting magnets - in the case of the LHC main bending magnet 7 MJ (at nominal current level). This number sounds impressive if compared to the kinetic energy of a truck (10 t) driving at a speed of 135 km/h, but somewhat underwhelming if we compare it to the energy required to draw a warm bath (100 l of water heated by 18 K). The danger results from the short duration of the energy release and from the high energy density if the stored energy is dissipated only over the initially

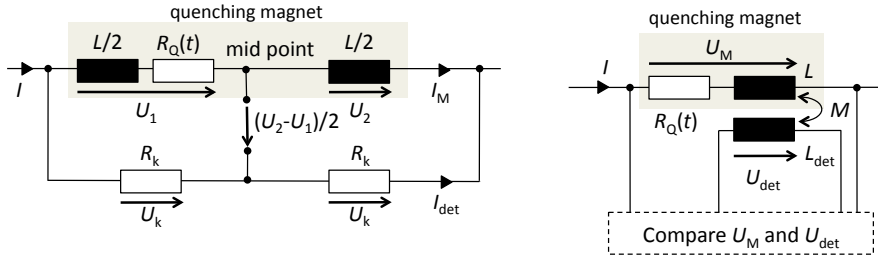


Figure 7.31: Quench detection methods: (left) Floating bridge differential voltage. The inductive voltage is fully compensated by the symmetric voltage taps. (right) Electronic voltage compensation. The inductive voltage is measured by means of a reference system and electronically subtracted.

quenched zone.

7.9.1 Quench Detection

Resistive voltage	A quench in a superconducting magnet can be detected by means of an increasing resistive voltage. The voltage rises due to the propagation of the quench along the cable and to adjacent conductors, as well as the rapid temperature increase within the quenched parts (see temperature dependent resistivity in Sec. A.1.3).
Inductive voltage	The voltage over the magnet (or between two voltage taps within the magnet) also carries the inductive voltage driving the magnet current up or down. Therefore, for the quench detection the resistive voltage signal must be extracted reliably from the measurement.
Compensation methods	Figure 7.31 shows two different detection systems: In the first system the inductive voltage is eliminated by triggering on the differential voltage between two identical parts of the magnet. The induced voltage is fully compensated. This system fails in case of a symmetric quench. For the second method, the induced voltage over the magnet is measured by means of a reference system and electronically compensated. The reference system can be an adjacent magnet, a coil inside the magnet [Wils 83, p. 220] or a co-wound wire within the cable [Borl 04]. Iron-saturation and dynamic effects result in a non-linear or even hysteretic relationship between ramp-rate and induced voltage. If the reference system does not experience an identical flux change, the electronic compensation becomes more demanding.
Quench criteria	The magnet system is considered quenched as soon as the resistive voltage exceeds a given threshold voltage U_{det} for a given duration t_{Dis} . The time discriminator reduces sensitivity to noise and reduces false triggers. For the quench protection of the LHC main bending magnets, the differential voltage between the two apertures is monitored. If this voltage exceeds the threshold of 100 mV for longer than 10.5 ms the magnet is considered as quenched [Denz 06]. The time it takes for the voltage to reach the threshold depends on the physical properties of the superconducting device, the characteristics

of the electrical circuit and the working point of the quenched conductor [Denz 01]. The time between quench start and quench validation constitutes the first part of the quench load - independent of any active quench protection methods (compare MIITs in Sec. 7.2).

The quality of the quench detection system depends on the following three points: How reliably is a quench detected? Under what conditions can a quench remain undetected, *i.e.* be missed? How likely is a false trigger, which would unnecessarily cause the magnet to switch off? [Verg 02] While a delay in the quench detection may cause excessive hot-spot temperatures, false triggers and the successive fast de-excitation may be the major mechanism for aging of the magnets [Evan 09, p. 84].

In the unlikely case [Coul 94], that a quench spreads out symmetrically over the two apertures, the differential voltage remains zero and the quench cannot be detected. The voltage would rise until the switching voltage of the cold diode is reached. The magnet can be protected by comparing the voltage over two adjacent magnets in addition to the voltages over the two apertures [Coul 94]. The small variation of the cable properties due to the high quality requirements further contributes to the symmetry of quenches. Highly symmetric quenches were observed in LHC dipole magnets during commissioning [Verw 08a]. Note that, with an initial voltage rise of approximately $4 - 10 \text{ Vs}^{-1}$ [Verw 08a] and a cold diode switching voltage of $6 - 8 \text{ V}$ (see Sec. 7.9.3), the quench could remain undetected for up to $0.6 - 2 \text{ s}$, and the hot-spot temperature would easily exceed the melting point of copper.

Symmetric
quench

In the case of fast-ramping magnets with large inductive voltages, it is more difficult to electronically detect a resistive voltage on a large background due to the reduced signal-to-noise ratio [Denz 08a]. Higher threshold voltages have to be used, and therefore a quench is detected later. This must be considered during magnet design [Schw 09].

Fast-
ramping
magnets

The quench detection system must also cover all superconducting current leads [Coul 94], *e.g.* bus bars, even if they are designed to be cryostable.

It is also possible to detect a quench by the induced field change in the aperture. If a strand of a Rutherford-type cable quenches, the current through the cable re-distributes over the remaining superconducting strands, thus by passing the normal zone. The resulting field change can be detected by a pick-up coil placed in the magnet aperture [Lero 93]. Sophisticated arrays of pick-up coils covering the full length of the magnet - denoted quench antennas - allow one to localize the quench origin and observe the transverse and longitudinal quench propagation [Siem 95].

Quench
antenna

Example : Detection length of the LHC MB The resistive voltage U_{res} over a quenched conductor depends on several parameters, *e.g.*, the transport current I , the longitudinal expansion of the quench ℓ and the cable properties,

$$U_{\text{res}} = \frac{\ell I}{A_{\text{NC}}} \rho_{\text{E}}^{\text{eff}}(T, B, RRR), \quad (7.87)$$

where $\rho_{\text{E}}^{\text{eff}}$ is the effective field and temperature dependent electrical resistivity

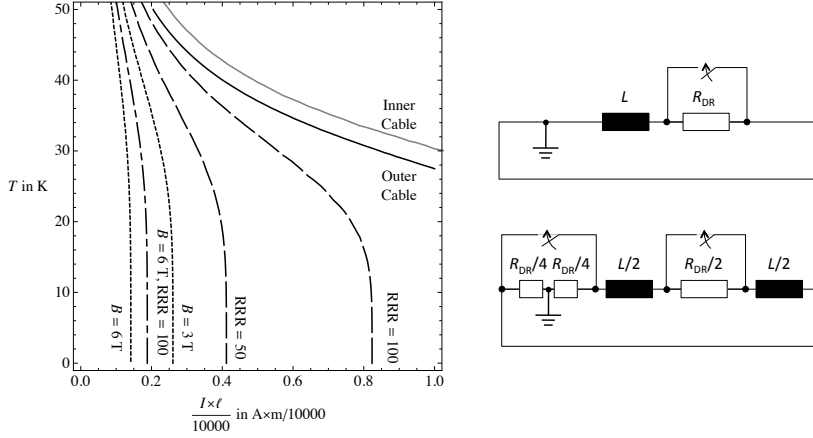


Figure 7.32: (left) Voltage detection conditions for the LHC MB. The black lines refer to the outer layer cable and the grey line to the inner layer cable. The solid lines are for zero applied field and a RRR value of 200. For the dashed lines the RRR has been varied. The dotted lines are for different applied magnetic fields. The dash-dotted line is for a RRR value of 100 and an applied field of 6 T. (right) Reduction of the voltages to ground by splitting the dump resistor and earthing in the middle.

of the normal conducting area A_{NC} . This can be rearranged to calculate the minimum longitudinal expansion of a quench to be detected.

The normal conducting area of the LHC MB inner and outer layer cables are computed in Sec. B.1.3 based on the values given C.1.1 (strand) and C.1.2 (cable). The effective resistivity is given by the resistivity of copper, see Sec. A.1.3.1. Figure 7.32 shows the necessary quench length ℓ to detect a resistive voltage of $U_{det} = 0.1$ V for different configurations.

For a quench in the outer layer cable with an estimated temperature of 20 K and a field of 3 T, the quench needs to propagate over 260 mm per 10 kA transport current to be detected. This translates to a length of 3.4 m at injection current.

7.9.2 Dump Resistor

The use of dump resistors serves two purposes: For a single magnet the dump resistor is used to increase the circuit's resistance, accelerate the current decrease (eventually causing quench back) and thus to reduce the hot-spot temperature in the magnet. In the case of a string of magnets, the quenched magnet is by-passed by a cold diode and discharged over the coil resistance after firing the quench heaters. Here, the dump resistor is used to extract the current from the chain and therefore protect the cold diode and bus bar from overheating.

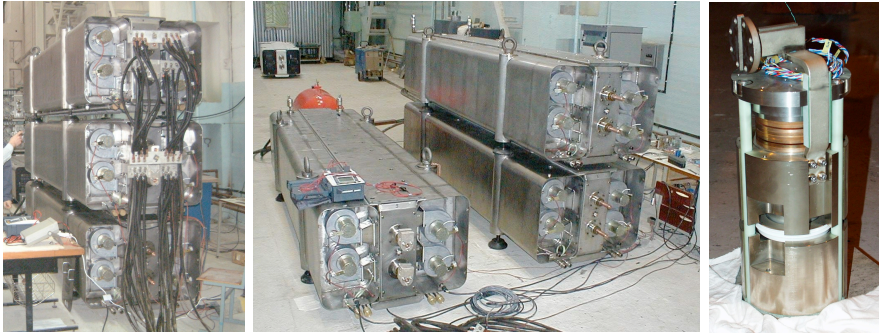


Figure 7.33: (left and center) The $225\text{ m}\Omega$ and 3.5 m long dump resistor used in the LHC main dipole string. Courtesy K. Dahlerup-Petersen CERN TE MPE. (right) Cold diode used in the main dipoles. Courtesy CERN ©

The dimension of the dump resistor for a string of magnets is determined by the maximum allowable time constant of the cold diode and the maximum voltage over each magnet respectively to ground. The time constant of the current decrease is given by the total inductance of the string divided by the dump resistance. The maximum dissipated energy in the diode therefore determines the lower boundary for the resistor. The upper boundary is defined by the maximum voltage to ground and by the maximum di/dt . If the string current decreases too quickly, induced losses may cause further magnets to quench [Coul 94] and eventually damage the cold diodes (see Sec. 7.10.1). The maximum voltage to ground over the dump resistor can be reduced by limiting the number of magnets per string [Dahl 01] and by using multiple dump resistors at adjacent points of the loop [Dahl 00], see Fig. 7.32 (right). For the LHC main bending magnets two sets of three parallel $225\text{ m}\Omega$ -resistors, resulting in a total resistance of $150\text{ m}\Omega$, are installed at adjacent points of each string. One resistor fills 3 m^3 , weighs 1.8 t , and absorbs 230 MJ during a full discharge [Dahl 00]. Figure 7.33 (left) shows the dump resistor used in the main dipole string.

Dimensioning
for a
magnet
string

The current commutation from the switch over the dump resistor into the resistor is not instantaneous. In the case of the LHC MB it takes around 8 ms [Denz 06].

In the unlikely case, that the (redundant) dump resistor switches fail, the current is driven down by firing the quench heaters of further magnets in the string [Denz 01].

For the dump resistor of a single magnet, the maximum size is given by the maximum voltage to ground and the maximum voltage over the magnet terminals (see Sec. 7.10.1). Discharging a magnet over a dump resistor of variable size, allows one to determine the maximum allowable di/t which does not cause a quench by quench back. Furthermore, the amount of extracted energy versus total energy can be optimized.

Dimensioning
for a single
magnet

Generally, the dump resistor can be described by its resistance R_{DR} and the switching delay after quench validation Δt_{DR} (the time for the current commutation is neglected).

7.9.3 Isolating the Magnet

By-pass diode Connecting a diode in parallel to a superconducting magnet provides a parallel path for the current in case of a quench. When the voltage over the quenched fraction of the coil reaches the threshold voltage of the diode, the chain current starts to commute into the diode. The magnet is isolated from the chain and discharges independently over the diode (with a current flowing in reverse direction). The diode threshold can be reached sooner, if quench heaters are fired.

Cold diode In case of the LHC MB cold diodes are used. The diodes are mounted in the same cryostat and initially at bath temperature. Compared to diodes at room temperature, the threshold voltage is significantly larger (6 – 8 V) and decreases to some volts after switching, due to heating of the junction [Verw 08a].

Ramp-rate limitation The maximum ramp-rate on the up-ramp of the magnet is limited by the diode threshold voltage. On the down ramp, the switching of the diode is hampered by the voltage induced across the magnet (see 7.10.1). The used diodes must be able to withstand the radiation level in the environment of the magnet, carry the string current sufficiently long and provide a sufficiently high back-ward voltage in order to hold during a fast-deexcitation [Coul 94]. Figure 7.33 shows the cold diode of the main dipoles.

Alternatively to a diode, a magnet can be by-passed by a resistor. The size of the resistor is determined by the maximum leakage current permitted and thus by resistive losses in the by-pass [Schm 00].

7.9.4 Subdivision and Coupled Secondary

Subdivision The quench process of a magnet can be improved by subdividing the magnet in case of a quench; see Fig. 7.34 (left). Therefore, parts of the coil are by-passed by shunts or diodes. In case of a quench, the by-pass isolates the quenched segment and the current decreases faster due to the reduced inductance. Furthermore, the falling current induces a current increase in the other loops, due to the inductive coupling of the different segments [Wils 83, pp. 226]. This may quench further segments by exceeding the critical current and finally accelerate the current extraction.

Coupled secondary The time constant of the current decrease can also be reduced by coupling in a resistive secondary circuit [Wils 83, pp. 221], see Fig. 7.34 (right). The method can be easily understood by considering it as an ideal transformer with a resistor over the terminals of the secondary winding. If the resistance of the secondary winding is in close contact to the superconducting coil, the dissipated heat can heat up the conductors and cause thermal quench back [Gree 84b] - *e.g.* observed in solenoids wound on an aluminum shell [Eber 77].

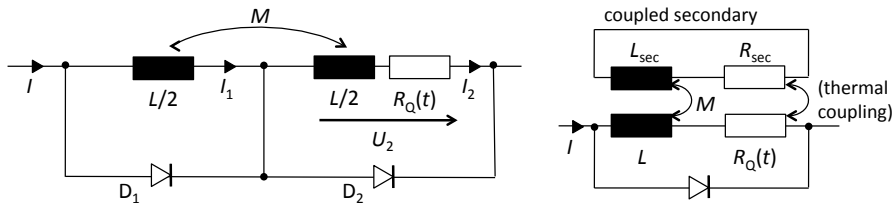


Figure 7.34: (left) Subdivision. The magnet is sub-divided into several segments. In case of a quench, the current in the quenched segment can decrease faster due to the smaller inductance. The current in the residual segments increases due to the induced voltage and may cause further quenches. (right) Coupled secondary. The resistance of the quenched circuit is increased by means of an inductively coupled resistor. If the resistor is in close contact to the superconducting coil thermal quench back accelerate the current extraction.

7.9.5 Quench Heaters

For a magnet which is disconnected from the power supply, the current decrease mainly depends on the resistance built-up. Additional resistance can be created by heating up large fractions of the coil and thus spreading the quench over the entire magnet. This way, the time constant of the discharge is reduced and the stored magnetic energy is dissipated over a larger volume, resulting in lower hot-spot temperatures. In a string of magnets, each by-passed by a diode, the additional resistive voltage contributes to the switching of the diode.

Increase
resistivity

Figure 7.35 (left) shows the electrical circuit of a quench heater consisting of a thin resistive strip, a switch and a capacitor. The parasitic inductance can be neglected for most purposes. The capacitor is discharged over the resistance of the strip. Figure 7.35 (right) shows a sketch of a heater strip with the resistive central element, copper plating and the insulation. Although an electrical insulation hampers the heat transfer from the heater to the coil, the heater strip has to be insulated in order to block turn-to-turn voltages and voltages to ground.

Design

By plating the heater strip with well conducting copper, the resistivity of the strip can be modified and the overall voltage reduced. The spot-like heating is as efficient as full heaters due to quench propagation [Coul 94]. The minimum length of the un-plated zones is given by the cable twist pitch length and the minimum propagating zone. The first guarantees that all strands are covered and the quench can not be by-passed and the latter ensures that the normal zone does not collapse [Rodr 00]. Adapting the resistance of the quench heater strips by plating, allows to use the same power supply for a variety of different magnet types and lengths [Rodr 00].

Copper
plating

The effectiveness of a quench heater, *i.e.* whether the quench heater can provoke a quench in the covered conductors or not, depends on the working point of the covered conductors and the effectively dissipated power. The working point, *i.e.* temperature, current and magnetic induction, defines the

Quench
heater ef-
fectiveness

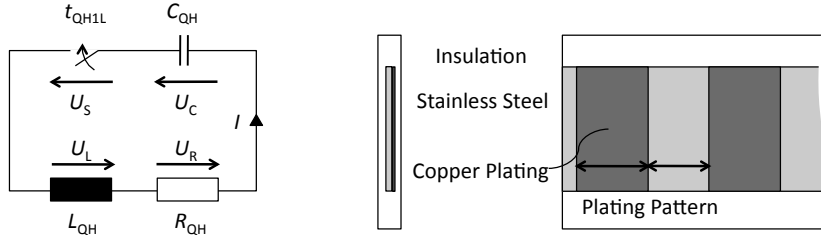


Figure 7.35: (left) Quench heater electrical circuit. (right) Quench heater strip layout with copper plating.

temperature and energy margin (Sec. 7.1.2 and 7.1.4) of the conductors. The effectively dissipated energy depends on the initial power and time constant of the quench heater circuit as well as on the insulation material between coil and heater strip and cooling conditions.

Quench
heater
delay

The time between firing the quench heater circuit and the detection of a quench in one of the covered conductors is denoted quench heater delay, Δt_{QH} . For a given heater circuit, the quench heater delay increases with decreasing current and field on the conductor. Below a certain current level, the quench heaters can be ineffective and thus yield an infinite quench heater delay.

Reliability

The protection with quench heaters is designed such that a maximum redundancy can be provided in case of a heater failure. Heater current leads might accidentally be disconnected, *e.g.* as in the LHC main dipole [Denz 08a], or the electronic system might fail to fire the circuit. Therefore, multiple heater circuits can be used, able to protect the magnet in case of one failing. Furthermore, heater strips can be mounted and connected such that conductors of all poles are covered, *e.g.* instead of covering left and right of one pole, cover only one side of the coil at top and bottom (see Fig. 7.44). For the total loss of a quench heater strip, spare heaters can be foreseen in the magnet. These additional heater strips would need to be mechanically connected, but save the effort of opening the magnet, see *e.g.* low-field heaters of the LHC MB.

Temperature
estimates

For the LHC main dipole, the final heater strip temperature after firing is estimated to 280 K [Rodr 00]. The copper-plating of the heater strips results, at first, in an inhomogeneous temperature distribution along the covered conductor. Nevertheless, the difference reduces to less than 15% within the first 50 ms after firing [Rodr 01] due to longitudinal quench propagation.

Quench Heater Discharge The discharge of a quench heater can be modeled by means of the RLC-series circuit shown in Fig. 7.35 (left). The power supply is represented by the capacitance C_{QH} with an initial voltage $-U_0$. It discharges over the heater strip at $t = 0$. The heater strip has an electrical resistance R_{QH} and forms a current loop with an inductance L_{QH} . The voltage over the capacitance, $U_C(t)$, is described by the ordinary differential equation

of second order,

$$\frac{d^2 U_C}{dt^2} + \frac{R_{QH}}{L_{QH}} \frac{dU_C}{dt} + \frac{1}{L_{QH} C_{QH}} U_C = 0.$$

The general solution is given by

$$U_C(t) = U_1 \exp((- \alpha + j\omega_d)t) + U_2 \exp((- \alpha - j\omega_d)t), \quad (7.88)$$

with

$$\alpha = \frac{1}{2} \frac{R_{QH}}{L_{QH}}, \quad \omega_0 = \frac{1}{\sqrt{L_{QH} C_{QH}}}, \quad \omega_d = \sqrt{\omega_0^2 - \alpha^2}.$$

The damped frequency ω_d takes imaginary values if α exceeds ω_0 , *i.e.* if $R_{QH} > 2\sqrt{L_{QH}/C_{QH}}$. The oscillation of the system is over-damped and Eq. (7.88) can be re-written as

$$U_C(t) = U_1 \exp\left(-\frac{t}{\tau_1}\right) + U_2 \exp\left(-\frac{t}{\tau_2}\right), \quad (7.89)$$

with

$$\tau_1 = \frac{1}{\alpha + \sqrt{\alpha^2 - \omega_0^2}}, \quad \tau_2 = \frac{1}{\alpha - \sqrt{\alpha^2 - \omega_0^2}}, \quad \tau_1 < \tau_2. \quad (7.90)$$

The two constants U_1 and U_2 are determined by the initial values for capacitor voltage and circuit current I ,

$$\begin{aligned} U_C(t=0) &= -U_0 = U_1 + U_2 \\ I(t=0) &= 0 = C_{QH} \left. \frac{dU_C}{dt} \right|_{t=0} = \frac{U_1}{\tau_1} + \frac{U_2}{\tau_2}, \end{aligned}$$

which yields

$$U_1 = U_0 \frac{\tau_1}{\tau_2 - \tau_1}, \quad U_2 = -U_0 \frac{\tau_2}{\tau_2 - \tau_1}, \quad |U_1| < |U_2|. \quad (7.91)$$

The current I rises with the time constant τ_1 followed by a decay with the time constant τ_2 ,

$$I(t) = \frac{U_0 C_{QH}}{\tau_2 - \tau_1} \left[\exp\left(-\frac{t}{\tau_2}\right) - \exp\left(-\frac{t}{\tau_1}\right) \right]. \quad (7.92)$$

Figure 7.36 shows voltage, current and power versus time during rise and decay.

For quench heaters where $\tau_1 \ll \tau_2$, *i.e.* where $2\sqrt{L_{QH}/C_{QH}} \ll R_{QH}$, and the current rise does not need to be taken into account, the system simplifies significantly:

$$U_C(t) = -U_0 \exp\left(-\frac{t}{\tau_2}\right), \quad I(t) = U_0 \frac{C_{QH}}{\tau_2} \exp\left(-\frac{t}{\tau_2}\right).$$

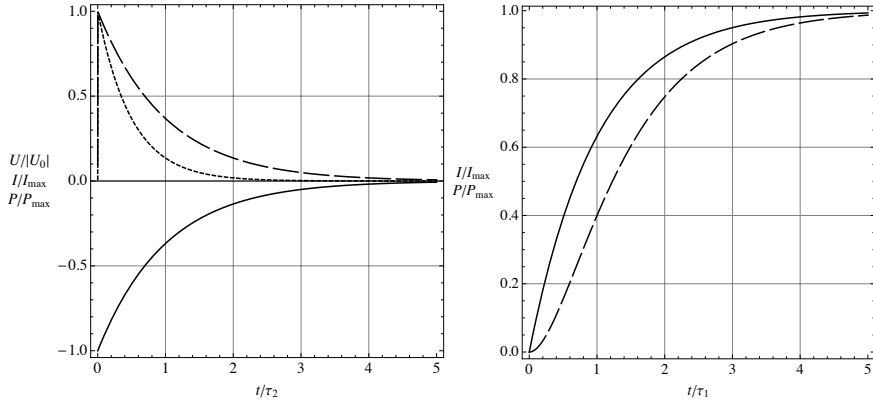


Figure 7.36: (left) Quench heater voltage (full), current (dashed) and power (dotted) versus time. The current rise is shown in more detail on the right. The rise time τ_1 is much smaller than the current decay time constant τ_2 .

The power dissipated in the heater strips decreases with half the time constant of the voltage and current:

$$P(t) = R_{\text{QH}} \left(U_0 \frac{C_{\text{QH}}}{\tau_2} \right)^2 \exp \left(-\frac{t}{\tau_2/2} \right) = P_{\text{max}} \exp \left(-\frac{t}{\tau_2/2} \right). \quad (7.93)$$

Example : Quench heaters of the LHC MB For the quench heaters of the LHC MB the following values are given: $U_0 = -900$ V, $R_{\text{QH}} = 12.5 \Omega$, and $C_{\text{QH}} = 7.05$ mF (see Sec. C.1.5). The inductance of the high-field heater loop is calculated by an approximation to $L_{\text{QH}} = 16.5 \mu\text{H}$, see Sec. 7.10.2.

$$\begin{array}{ll} U_1 = 0.0135 \text{ V} & U_2 = -900.0135 \text{ V} \\ \tau_1 = 1.3 \mu\text{s} & \tau_2 = 88 \text{ ms} \end{array} \quad (7.94)$$

Since the two time constants differ by 4 orders of magnitude, the peak current, the maximum dissipated power, and the total dissipated energy are calculated from the simplified model:

$$I_{\text{max}} = 72 \text{ A} \quad P_{\text{max}} = 65 \text{ kW} \quad E_{\text{tot}} = 5.7 \text{ kJ} \quad (7.95)$$

The energy is dissipated evenly along the length of the two heater strips $\ell_{\text{QH}} = 15$ m. Due to the plating the energy is mostly dissipated on the side facing the conductors. The heater strip is $w_{\text{QH}} = 15$ mm wide and covers 9 conductors for the high-field heaters. The surface power density is then $S_{\text{max}} = P_{\text{max}}/A = 14.4 \text{ W/cm}^2$ and the power per conductor per length 240 W/m .

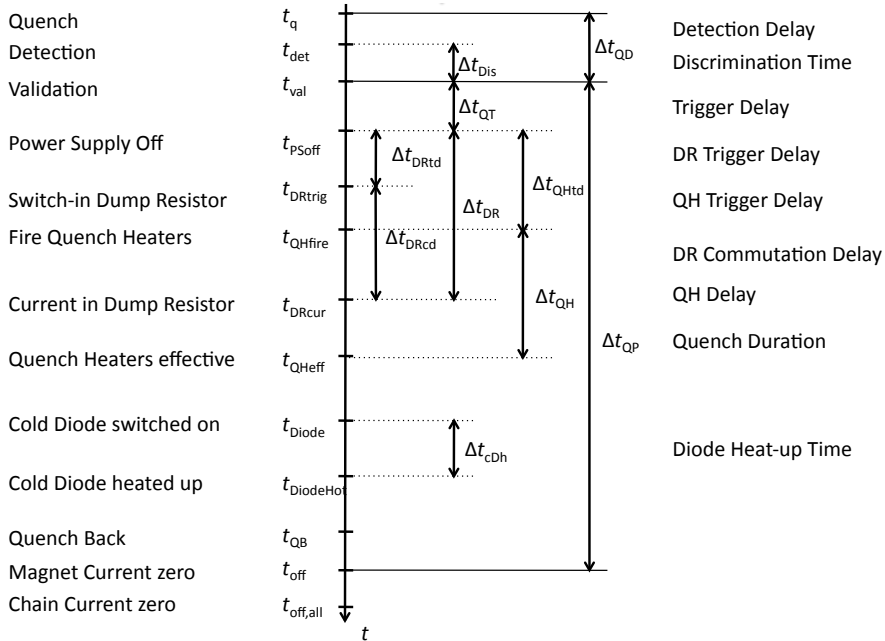


Figure 7.37: Sequence of events during a quench with quench protection. The distances are not up to scale. Trigger delays are in the order of milliseconds while the quench-heater delays are between 30 to 100 ms. The duration of a quench is in the order of several 100 milliseconds.

7.9.6 Quench Protection Sequence of Events

Figure 7.37 shows the sequence of events during a quench and succeeding quench protection actions. This example represents more or less the LHC tunnel configuration, but can be easily adapted to other protection schemes.

After detection and validation, the power supply is switched off and the current commutates into the free-wheeling diode. The beam is aborted, *i.e.* directed into a beam dump. The dump-resistor and the quench-heater power supply of the quenched magnet are triggered. The current commutates into the dump resistor and starts to decrease. After the quench heaters show to be effective, the voltage over the quenched magnet rises and switches the cold diode. The magnet is now decoupled from the chain and discharges over the internal resistance. The diode heats up and the forward voltage decreases. The current decrease induces losses in the magnet windings yielding further quench, *i.e.* quench back. The current of the quenched magnet commutates fully into the cold diode. The magnet chain is switched off.

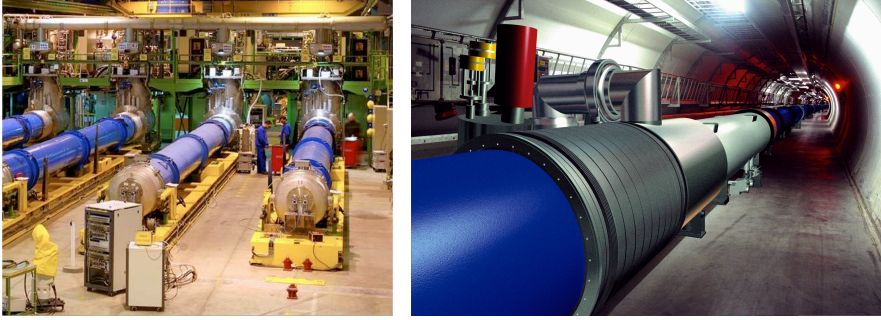


Figure 7.38: (left) LHC magnet test station in SMA 18. (right) LHC main dipole magnets in the tunnel. Pictures courtesy of CERN©

7.10 Voltages Occurring During a Quench

Protection
from
excessive
voltages

In case of a quench, superconducting magnets have to be protected from excessive voltages in order to prevent permanent damage to the coil insulation (see Sec. 7.9). The voltage build-up depends on the used materials, the quench protection system and the working point of the magnet.

Terminal,
coil and
turn-to-
turn
voltages

The voltages are analyzed for a genuine LHC main dipole (MB) as described in Sec. C.1. The differences between operation in the LHC tunnel, where the magnet is connected to a string of identical magnets, and the operation on the test bench are indicated for the magnet terminal voltage (see also Fig. 7.38). By means of the voltages over the four poles, quench heater induced voltages as well as the influence of asymmetric quenching can be shown. From the turn-to-turn voltages, peak electrical fields can be calculated, and limitations for the size of a dump resistor can be derived.

7.10.1 Terminal Voltages

Tunnel
setup

LHC Tunnel: The LHC MB is operated in a chain of $N_{\text{mag}} = 153$ dipole magnets connected to a controlled voltage source. Each magnet is bridged by a cold diode. In case of a quench the power supply is switched off and the current commutates into the free-wheeling diode. A dump-resistor is switched-in in order to extract the energy from the magnet chain (see Sec. 7.9 for the quench protection paradigm and Sec. 7.9.2 for protection method). The electrical circuit is shown in Fig 7.39. The voltage development over the different stages is shown in Fig. 7.40.

Normal
up-ramp

During the up-ramp of the magnet string the voltage of the power supply is evenly distributed over all N_{mag} magnets. The current ramp-rate $\frac{dI}{dt}$ and the magnet terminal voltage U_{Terminal} are given by

$$\frac{dI}{dt} = \frac{U_{\text{PS}}}{N_{\text{mag}} L_d(I)}, \quad U_{\text{Terminal}} = \frac{U_{\text{PS}}}{N_{\text{mag}}} = U_{\text{up-ramp}}, \quad (7.96)$$

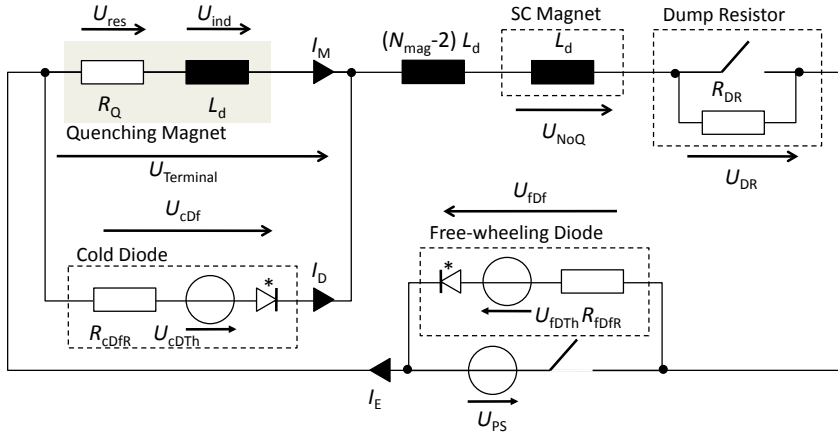


Figure 7.39: Electrical circuit of the LHC tunnel configuration: Quenching magnet in a string with N_{mag} other magnets and a dump resistor. One non-quenched magnet has been exemplarily highlighted. The cold by-pass diode of non-quenched magnets has been omitted. In case of a quench, the power supply is switched off and the current commutates into free-wheeling diode. After the voltage over the quenched magnet has reached the threshold voltage of the cold by-pass diode the magnet starts to discharge over the diode and the internal resistance.

with U_{PS} the voltage of the power supply and L_d the differential inductance of a single dipole (see Sec. 7.4). Note, that in order to follow a given current-curve, the power supply has to be controlled due to the non-linear differential inductance.

If any of the magnets in the chain quenches, a small resistive voltage starts to develop. The quench is detected by monitoring the differential voltage over the two apertures of each magnet (see quench detection in Sec. 7.9.1). The detection is thus independent of the ramping of the magnet. The magnet is considered quenched if the voltage exceeds the detection threshold U_{det} for a given time Δt_{Dis} .

Quench
detection

In case of a quench, the power supply is switched off and the current commutates into the free-wheeling diode. The terminal voltage of the quenched magnet is given by

Power
supply off

$$U_{\text{Terminal}} = -\frac{U_{\text{fDf}} + U_{\text{res}}}{N_{\text{mag}}} + U_{\text{res}}, \quad (7.97)$$

with U_{res} the resistive voltage of the quenched magnet and U_{fDf} the forward voltage over the free-wheeling diode of the power supply. This has to be distinguished from the voltage over each of the residual, non-quenched magnets of the string denoted as U_{NoQ} ,

$$U_{\text{NoQ}} = -\frac{U_{\text{fDf}} + U_{\text{res}}}{N_{\text{mag}}} \approx -\frac{U_{\text{fDf}}}{N_{\text{mag}}}. \quad (7.98)$$

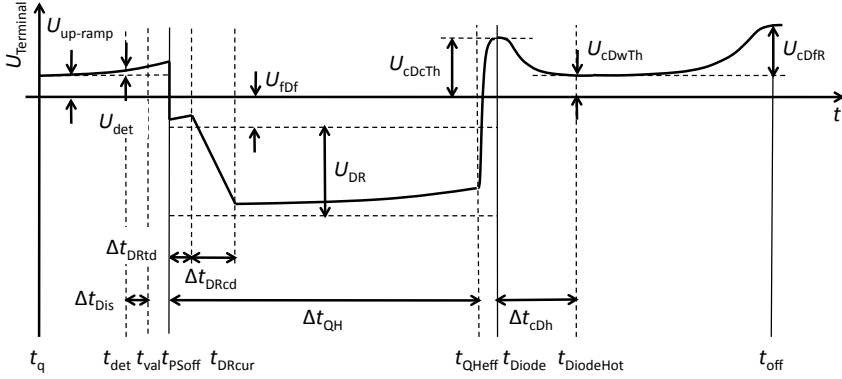


Figure 7.40: Voltage development over the terminals of a quenched magnet in the LHC string. Voltages and time intervals are not to scale.

Dump
resistor

The diode forward voltage consists of the diode threshold voltage U_{fDTh} and the voltage over the differential resistivity R_{fDfR} giving only a few volts in total. The current remains more or less constant due to the large inductance of the chain. By switching-in a dump resistor the current decrease can be significantly accelerated. After switching, the current commutates from the switch into the resistor during Δt_{DRcd} and yields approx. 1800 V (for a quench at nominal current and a dump resistor of 150 m Ω) evenly distributed over all magnets:

$$U_{NoQ} = -\frac{U_{DR} + U_{fDf} + U_{res}}{N_{mag}} \approx -\frac{U_{DR}}{N_{mag}}, \quad (7.99)$$

$$U_{Terminal} = -\frac{U_{DR} + U_{fDf} + U_{res}}{N_{mag}} + U_{res}, \quad (7.100)$$

where $U_{DR} = R_{DR}I_E$ and R_{DR} the resistance of the dump resistor. With the dump resistor, the current of the magnet chain decreases with a time constant of approximately 100 s, see Sec. 7.9.2.

Quench
heaters

Cold diode

The quench heaters of the quenched magnet are fired upon quench detection. After the quench-heater delay Δt_{QH} (see Sec. 7.9.5), the first conductors covered by quench heaters turn resistive, and the resistive voltage over the magnet increases rapidly. As soon as the voltage across the magnet reaches the cold diode forward threshold voltage U_{cDcTh} , the cold diode switches and decouples the magnet from the chain. The magnet terminal voltage is clamped to the diode forward voltage:

$$U_{Terminal} = U_{cDf} = U_{cDcTh} + R_{cDfR}I_D \approx U_{cDcTh}.$$

The string current I_E slowly starts to commutate from the quenched magnet into the diode. The current flow through the diode causes the junction temperature to increase and the forward threshold voltage to drop to U_{cDwTh}

after Δt_{cDh} . With increasing diode current I_{D} the forward voltage over the diode rises and the terminal voltage is given by

$$U_{\text{Terminal}} = U_{\text{cDwTh}} + R_{\text{cDfR}} I_{\text{D}}, \quad (7.101)$$

with R_{cDfR} the differential forward resistance of the cold diode. The voltage over the differential inductance of the quenched magnet, responsible for decreasing the current, thus consists of

$$U_{\text{ind}} = -U_{\text{Terminal}} + U_{\text{res}}. \quad (7.102)$$

The current decay in the remaining string is dominated by the dump resistor and the string inductance is

$$\frac{dI_{\text{E}}}{dt} = -\frac{U_{\text{DR}} + U_{\text{cDf}}}{N_{\text{mag}} - 1}. \quad (7.103)$$

The dump resistor has been chosen to give a time constant of around 100 s in order to protect the cold diode and the busbars from overheating.

If the quench propagates along the string, *e.g.* by a heat wave propagating along the cooling system, the current decrease in the chain accelerates following Eq. (7.103) and more magnets can be quenched by induced losses (quench back). Furthermore, the voltage of the dump resistor drops over the cold diodes of the remaining magnets in reverse direction. If the reverse blocking voltage of the cold diode is exceeded it can be damaged or destroyed. For quenches at high currents, quenching of adjacent magnets after 30 – 300 s has been observed [Verw 08a].

The ramp-rate of the magnet is limited by the forward threshold voltage of the cold diode.

The current in the magnet string changes very slowly compared to the current in the magnet where the quench does not take much more than half a second. Therefore the external circuit could be modeled by means of a constant current source. This simplifies the approach, but neglects the negative terminal voltage in Eq. (7.103). Due to the rapid voltage increase after quench heater firing the error is small.

Test bench: On the test bench the magnet is connected directly to a power supply. In case of a quench, the power supply is switched off and the current commutates into the free-wheeling diode. Eventually a dump resistor can be switched-in. The electrical circuit is shown in Fig 7.41 (left). The voltage development over the different stages is shown in Fig. 7.41 (right).

The quench detection and power supply switch-off happen similarly to the setup in the tunnel. The terminal voltage of the magnet is clamped to the free-wheeling diode forward voltage:

$$U_{\text{Terminal}} = -(U_{\text{fDTh}} + R_{\text{fDfR}} I_{\text{E}}). \quad (7.104)$$

Note, that the cold protection diode parallel to the magnet is prevented from switching since the voltage over the magnet is clamped to the warm diode

String
current
decay

Multiple
quench

Ramp-rate
limitation

Constant
current
source

Test bench
setup

Terminal
voltage,
diode

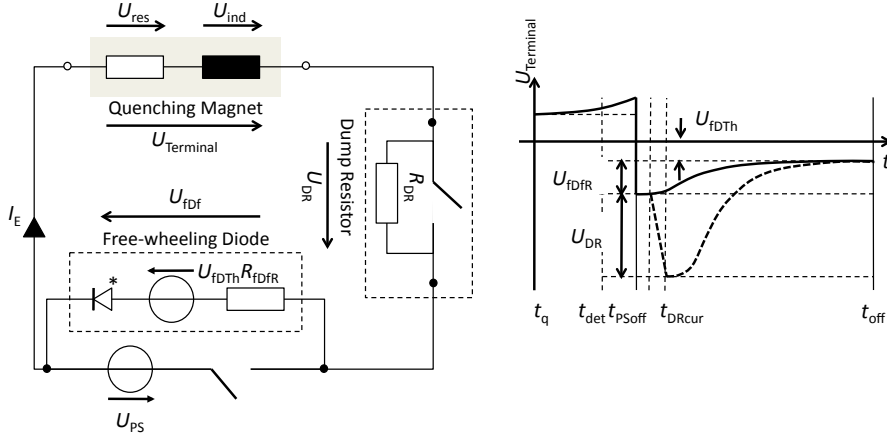


Figure 7.41: (left) Electrical circuit of a magnet on the test bench. (right) Voltage development over the terminals of a quenching magnet on the test bench. In the case when a dump resistor is switched into the circuit, the voltage is given by the dashed line. Voltages and time intervals are not to scale.

forward voltage. It is therefore omitted in Fig. 7.41 (left). The voltage over the differential inductance of the quenched magnet thus consists of

$$U_{ind} = U_{Terminal} - U_{res} = -(U_{fDTh} + R_{fDfR} I_E) - U_{res}. \quad (7.105)$$

Compared to Eq. (7.102) the forward voltage of the diode is of opposite orientation and thus contributes to decrease the current (although only minimally).

If a dump resistor is available, the terminal voltage after switching and commutation is given by

$$U_{Terminal} = -(U_{fDTh} + (R_{DR} + R_{fDfR}) I_E) \approx -R_{DR} I_E, \quad (7.106)$$

with R_{DR} the dump resistor resistivity. The current decrease can be significantly increased. Note that the voltage of the dump resistor drops over the magnet terminals and therefore over the connection turns. The maximum dump resistor size is limited by the highest allowable turn-to-turn voltage (see Sec. 7.10.3).

7.10.2 Coil Voltages

Before installation in the LHC tunnel all magnets are tested for their quench performance, *i.e.* whether they can reach a given current level without quenching. In case of a quench on the test bench, current and voltages over the magnet and the four poles are recorded. Although the terminal voltage is clamped to the diode forward voltage (see above), the four coil voltages show significant variations.

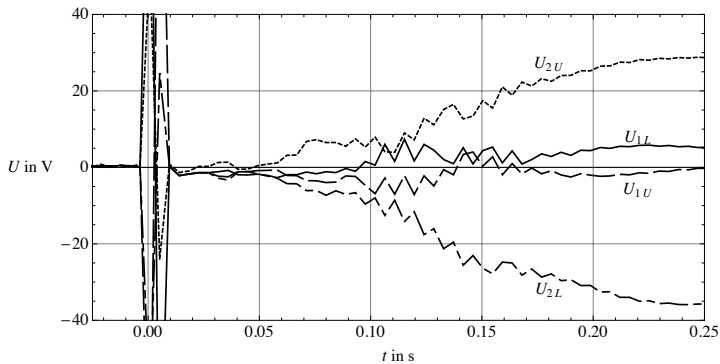


Figure 7.42: Coil voltages recorded during a quench of an LHC main dipole on the test bench.

Quench
heater
signals
scattering

As shown in Sec. 4.1.1, the coil voltages can be successfully reproduced by de-tuning the time when the different quench heaters show to be effective by less than 2 ms. As stated in [Rodr 00] the quench heater trigger signal can already vary by up to 10 ms.

Figure 7.42 shows the coil voltages recorded for an LHC dipole. The plot shows sharp voltage spikes around $t = 0.0$ s not exceeding a duration of much more than 10 ms. Note that the sampling rate of the measurement is only 5 ms. Following the voltage spikes, the four voltages slowly diverge. From approximately $t = 70$ ms to $t = 200$ ms the voltages show a slight modulation, or voltage jumps. The voltage jumps have also been reproduced in the simulations.

Voltage
shows
jumps and
spikes

In this section it is shown that the spikes result from the firing of the quench heaters and the jumps stem from the asynchronous quenching of the four poles.

Quench Heater Induced Voltages At the start of the quench, the total voltage over the magnet is given by the resistive voltage of the quench and the diode of the power supply (after switch-off, see above). The resulting current change is small compared to the total current and the considered time-frame of the spikes and is neglected. The electrical circuit of the magnet and the four quench heaters is shown in Fig. 7.43. The four coils are connected in series and are short-circuited. Each quench heater circuit constitutes an over-damped RLC-circuit (see Sec. 7.9.5) coupled over the mutual inductance $M_{QH,C}$ to the magnet circuit.

Since quench heaters are only modeled as effective heat sources inside the covered conductors, the self and mutual inductances (see Sec. 7.4) have to be estimated: Figure 7.44 (left) shows the coil cross-section of one aperture with four additional conductors functioning as quench heaters. The quench heater loops are mounted perfectly symmetrically on both sides of the two

Approximation

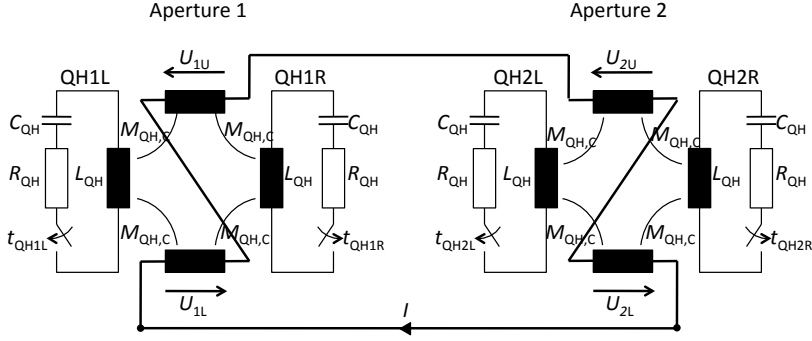


Figure 7.43: Electrical circuit model of the quench heater induced voltage spikes.

apertures. The mutual inductance matrix $[M]/\ell$ is calculated with ROXIE for nominal current,

$$\frac{[M]}{M_0\ell} = \begin{pmatrix} 935.7 & 479.6 & 45.7 & 52.6 & 6.3 & -6.3 & -0.5 & -0.1 \\ 479.6 & 935.7 & 52.6 & 45.7 & -6.3 & 6.3 & 0.5 & 0.1 \\ 45.7 & 52.6 & 935.7 & 479.6 & 0.1 & 0.5 & 6.3 & -6.3 \\ 52.6 & 45.7 & 479.6 & 935.7 & -0.1 & -0.5 & -6.3 & 6.3 \\ 6.3 & -6.3 & 0.1 & -0.1 & 1.1 & 0.1 & 0. & 0. \\ -6.3 & 6.3 & 0.5 & -0.5 & 0.1 & 1.1 & 0.1 & 0. \\ -0.5 & 0.5 & 6.3 & -6.3 & 0. & 0.1 & 1.1 & 0.1 \\ -0.1 & 0.1 & -6.3 & 6.3 & 0. & 0. & 0.1 & 1.1 \end{pmatrix}, \quad (7.107)$$

where $[M] = (M_{i,j})$ and $i, j = \{1L, 1U, 2U, 2L, QH1L, QH1R, QH2L, QH2R\}$ and with $M_0 = 1 \mu\text{Hm}^{-1}$. The numbering can be taken from Fig. 7.43. Due to symmetry, the mutual inductances between a heater and the coil have identical absolute values which shall be denoted $M_{QH,C}$. The mutual inductance between a heater and a coil of the other aperture is neglected. The self inductance of each heater circuit has the same value and is denoted as L_{QH} .

In Sec. 7.9.5 the quench heater discharge is calculated using the self inductance L_{QH} and neglecting any influence of the main circuit or other quench heaters. The derivative of the heater current Eq. (7.92) is then given by

$$\gamma(t) = \frac{dI}{dt} = \begin{cases} \frac{U_0 C_{QH}}{\tau_2 - \tau_1} \left[-\frac{\exp\left(-\frac{t}{\tau_2}\right)}{\tau_2} + \frac{\exp\left(-\frac{t}{\tau_1}\right)}{\tau_1} \right] & t \geq 0 \\ 0 & t < 0 \end{cases}, \quad (7.108)$$

and is denoted γ . As shown in Sec. 7.9.5, the time constants τ_1 and τ_2 differ by more than 4 orders of magnitude. During the regime of τ_1 the current increases rapidly followed by the slow decay over τ_2 .

The four quench heaters follow the trigger signal after $t_{QH1L} = 0.0\text{ ms}$, $t_{QH1R} = 0.8\text{ ms}$, $t_{QH2L} = 1.9\text{ ms}$ and $t_{QH2R} = 0.4\text{ ms}$.

Due to the symmetric mounting, each quench heater induces identical voltages over both coils of one aperture, but with opposite signs. Therefore,

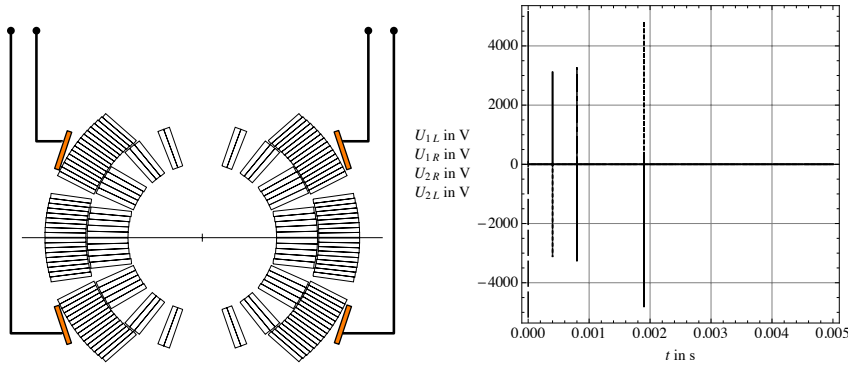


Figure 7.44: (left) ROXIE model for the calculation of the inductance matrix in Eq. (7.107). (right) Simulated voltage spikes.

the total voltage over the magnet remains zero and the magnet current I is constant. The induced voltages over each coil can be calculated from

$$\{U_{\text{ind}}\} = [M] \frac{d}{dt} \{i\}, \quad (7.109)$$

with

$$\frac{d}{dt} \{i\} = (0, 0, 0, 0, \gamma(t - t_{\text{QH1L}}), \gamma(t - t_{\text{QH1R}}), \gamma(t - t_{\text{QH2L}}), \gamma(t - t_{\text{QH2R}}))^T.$$

Figure 7.44 (right) shows the induced voltages over the four coils. The voltage level of the spikes depends on the rise time τ_1 of the heater circuits. Overlapping spikes in the same aperture cancel each other out. The length of non-overlapping spikes only depends on the heater rise time. The current decay after the sharp rise induces only a very small voltage of opposite sign.

Voltages Arising from the Chronology of Quench Events As in the section before, the voltage over the initial quench and the diode of the power supply are neglected. The magnet circuit is shown in Fig. 7.45. Each coil consists of one quarter of the total inductance of the magnet and a time-dependent resistance caused by the quench heaters. Each coil is covered by two different quench heaters, one on each side.

Quench
heater
layout

A quench heater is effective as soon as the first conductor under the quench heater quenches. Nevertheless, the covered conductors do not quench instantaneously due to differences in temperature and energy margin to quench (see Sec. 7.1.2 and 7.1.4). The quench then propagates due to thermal conduction. At a certain point, the entire magnet quenches due to quench back. This is modeled by the function N_{hp} representing the number of conductors quenched by a quench heater as shown in Fig. 7.46 (left). The quench heater

Model

has a delay of t_{QHF} .

$$N_{\text{hp}}(t, t_{\text{QHF}}) = \begin{cases} 0 & t < t_{\text{QHF}} \\ \frac{N_{\text{QHC}}}{t_{\text{HQC}}} (t - t_{\text{QHF}}) & t_{\text{QHF}} < t < t_{\text{QHF}} + t_{\text{HQC}} \\ \frac{dN_{\text{C}}}{dt} (t - t_{\text{QHF}} + t_{\text{HQC}}) & t_{\text{QHF}} + t_{\text{HQC}} < t < t_{\text{QB}} \\ N_{\text{hp}} & t > t_{\text{QB}} \end{cases}, \quad (7.110)$$

with N_{QHC} conductors quenched within the time t_{HQC} after t_{QHF} . The quench propagates with $\frac{dN_{\text{C}}}{dt}$ conductors per second. Quench back sets in independently of t_{QHF} at $t = t_{\text{QB}}$. The used values are given in Tab. 7.1.

For the calculation of the time-dependent resistance of each half pole two different models are applied. As assumed for the quench model, a conductor quenches over the full cross-section nearly instantaneously. Therefore, the function N_{hp} can only have discrete values. In magnets with a much greater number of conductors, *e.g.* superconducting solenoids, the quench propagation is more continuous. Here N_{hp} is applied directly:

$$R_{\text{hp}}^{\text{disc.}}(t) = R_0 \text{round} \left(N_{\text{hp}}(t) \right), \quad R_{\text{hp}}^{\text{cont.}}(t) = R_0 N_{\text{hp}}(t). \quad (7.111)$$

The resistance of one conductor is derived from the electrical resistivity of copper (see Sec. A.1.3.1) at approximately 10 K and 3 T,

$$\rho_0 = \rho_{\text{E}}^{\text{copper}}(T = 10 \text{ K}, B = 3 \text{ T}, RRR = 200) \approx 4.9 \cdot 10^{-10} \Omega\text{m},$$

and $\lambda = 1.95$, $N_{\text{s}} = 36$ and $r_{\text{s}} = 0.4125 \cdot 10^{-3} \text{ m}$ (from Sec. C.1), yielding

$$R_0 = \rho_0 \frac{\ell_{\text{Magnet}}}{\left(\frac{\lambda}{1+\lambda} \right) N_{\text{s}} \pi r_{\text{s}}^2} = 0.58 \cdot 10^{-3} \Omega.$$

Figure 7.46 (right) shows both models.

It is assumed that the quench heater delays follow directly the scattering of the quench heater firing, *i.e.* that the resistance change in the circuits appear with the same delays. A general delay of 20 ms is added. To reflect differences

Table 7.1: Assumptions made regarding the quench heater efficiency and the quench propagation in the magnet

Quantity	Unit	Value
N_{QHC}	-	8
Δt_{HQC}	s	0.006
$\frac{dN_{\text{C}}}{dt}$	1/s	$\frac{1}{0.02}$
t_{QB}	s	0.2
N_{hp}	-	40

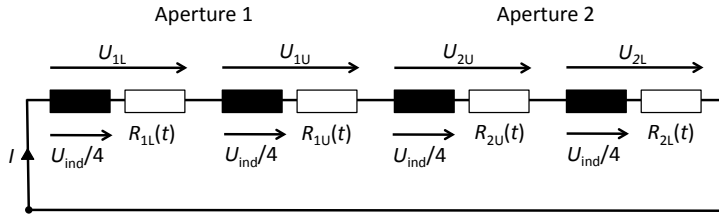


Figure 7.45: Model circuit for the explanation of voltages induced by asynchronous quenching

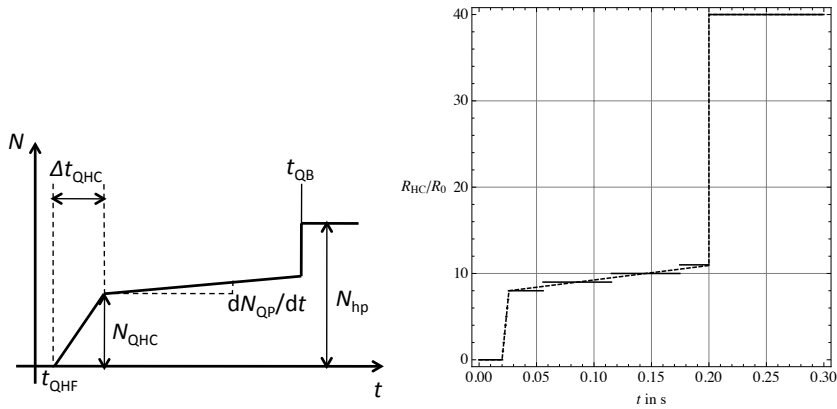


Figure 7.46: Model of the resistance growth in a half coil due to quench heater firing. (left) Explanation of the different model parameters. (right) Comparison between discrete and continuous approach.

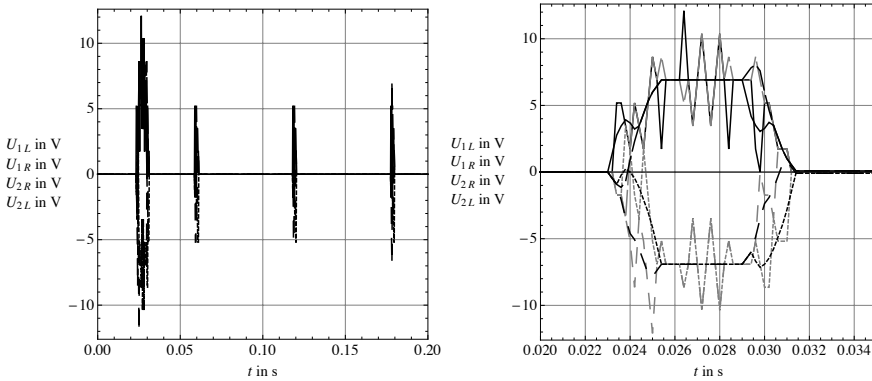


Figure 7.47: Voltage jumps on coil voltages. (left) Voltage jumps due to all asynchronous quench events. No jumps at the instance of simultaneous quench back. (right) Comparison of the continuous and discrete approach. In case of the very drastic voltage change, the continuous model shows similar behavior as the discrete approach.

between upper and lower heater strips, an additional delay of $\Delta t_{\text{lu}} = 0.5 \text{ ms}$ is applied to all upper heater strips. This results in 8 different starting times.

Since the voltage over the magnet is short-circuited, the total resistive voltage has to be matched by the voltage over the inductance. Due to symmetry, the induced voltage is distributed evenly over the four coils. Although this voltage causes the current of the magnet to decrease, the current change is neglected to simplify the model. The voltage over each coil thus consist of the individual resistive voltage plus one quarter of the total inductive voltage, *e.g.*:

$$\begin{aligned} U_{\text{1L}}(t) &= \left(R_{\text{hp}}(t, t_{\text{QH1L}}) + R_{\text{hp}}(t, t_{\text{QH1R}} + \Delta t_{\text{lu}}) \right) I + U_{\text{ind}}/4 \\ &= I \left[\left(R_{\text{hp}}(t, t_{\text{QH1L}}) + R_{\text{hp}}(t, t_{\text{QH1R}} + \Delta t_{\text{lu}}) \right) \right. \\ &\quad \left. - \frac{1}{4} \sum_i \left(R_{\text{hp}}(t, t_i) + R_{\text{hp}}(t, t_i + \Delta t_{\text{lu}}) \right) \right], \end{aligned} \quad (7.112)$$

with $i = \{\text{QH1L}, \text{QH1R}, \text{QH2L}, \text{QH2R}\}$.

Figure 7.47 (left) shows the voltage over the four coils for the discrete approach. Voltage jumps can be found around all asynchronous events, especially throughout the time where the quench heaters show to be effective. The simultaneous quench of all coils due to quench back does not cause any voltage jumps. Figure 7.47 (right) shows the first and most pronounced jump in higher resolution for both models. Although the quench propagates smoothly in the latter model, the first voltage jump remains, and is of similar size. The smaller, later jumps disappear. Without taking into account the up-down asynchronous quenching Δt_{lu} the number of voltage jumps halves.

This model shows that the voltage jumps result from the redistribution of the sudden changes of resistive voltage over the magnet. The “discretization” of the quench events in terms of conductors accentuates the effect. This hypothesis is supported by the observations made in [Verw 08a]: Kinks in the differential voltage of the quench detection system (see Sec. 7.9.1) are identified by the propagation of the quench to adjacent conductors. In [Coul 96] similar voltage redistributions were observed over magnets operated in the LHC string and quenching asynchronously.

7.10.3 Voltages in the Coil Cross-Section

Based on the coil geometry and the winding scheme of the magnet, the lumped quantities U_{res} and U_{ind} (used above) can be mapped over the coil winding. This allows for the computation of peak electric fields and excessive voltages to ground.

Voltage
along
magnet
winding

Figure 7.48 (right) shows a schematic coil cross-section of a $\cos \theta$ -magnet featuring two nested coil layers. The winding scheme is highlighted by the dotted arrows. The magnet is connected to the external circuit at the conductors denoted 1 and 5. The external network consists of a power supply with

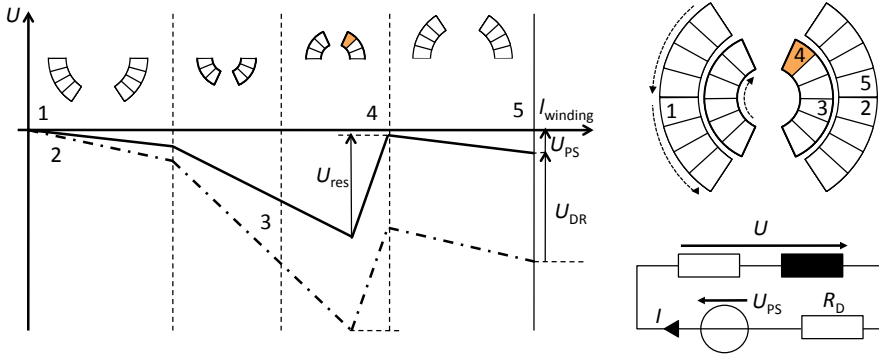


Figure 7.48: (left) Voltage along the magnet winding length ℓ_{winding} . The dash-dotted line represents a magnet protected by a dump resistor. The solid line shows the same magnet connected only to a power supply with a free-wheeling diode. The different slopes for the induced voltage in the inner and outer layer are to represent the differences in inductance within the coil cross-section. (right) Schematic coil cross-section of a $\cos \theta$ -magnet featuring two nested coil layers.

free-wheeling diode and eventually a dump resistor. The terminal denoted 1 is connected to the ground.

In case of a quench (in the conductor indicated with 4), a resistive voltage rises over the magnet. This voltage, and the voltage across the external circuit, are matched by the inductive voltage across the magnet. The resistive voltage can be localized to the quenched conductor and the magnet terminals. The induced voltage is distributed over the entire coil winding. Figure 7.48 (left) shows the voltage along the winding length ℓ_{winding} through the entire magnet. The fact that the induced voltage varies over the coil cross-section is represented by two slopes for the induced voltage (different in inner and outer layer); compare [Wils 83, p. 203].

Two observations can be made. The voltage between subsequent turns increases with the gradient along the winding (the slope of the graph). Even if the turn-to-turn voltage remains below critical values, the voltage between adjacent turns of different layers can be excessive. An example is given by means of the conductors 2 and 3. Although the voltage over the dump resistor is distributed evenly over the winding, it drops over the two adjacent conductors 2 and 5. Therefore, the resistance of the dump resistor needs to be limited.

Consider the schematic coil cross-section shown in Fig. 7.49 (left). The letters A and B indicate two different winding schemes. In scheme A, the conductors are connected row by row; in scheme B, column by column. For the sake of simplicity, the magnet shall be short circuited. Quenched conductors are shaded.

Figure 7.49 (right) shows the voltage distribution over the magnet winding for both schemes. In the case of scheme A, the resistive voltage of the quench

Turn-to-turn voltages

Winding scheme

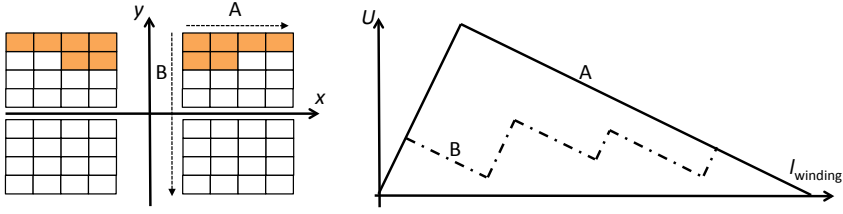


Figure 7.49: Influence of the winding scheme on the voltage to ground. (left) Schematic coil cross-section with two different winding schemes. We consider a double-solenoid with axis along the y -axis. The quenched turns are indicated by shading. In winding scheme A the turns form interconnected radial disks. In scheme B the turns form connected sub-solenoids. (right) Voltage along the magnet for the two different schemes

is concentrated at the start of the winding, resulting in one voltage peak. In the case B, the resistive parts alternate with purely inductive parts of the coil. The maximum voltage to ground is significantly smaller. Hence, the voltage to ground is smaller if the quench propagates orthogonally to the coil winding scheme, *i.e.* the quench spreads over turns which are not directly electrically connected.

Electrical fields are calculated from the potential difference between two conductors divided by the distance (taken from the coil geometry).

Capacitive Effects The approach presented above does not take into account parasitic capacitances in the coil winding. The winding of the coil yields a capacitance to ground as well as a series or winding capacitance. Fig. 7.50 (left) shows a schematic transmission line model of the coil winding with parasitic elements [Brec 73, pp. 332]. Here C_g/ℓ denotes the capacitance to ground per unit length, $C_s\ell$ the series capacitance and $L, M/\ell$ the self and mutual inductance per unit length. The end of the winding is connected to the ground.

Consider a sudden voltage rise U_{dist} due to a quench at an arbitrary position inside the coil. This position is considered as terminal for the simplified model. Following [Blum 19], the initial voltage distribution depends only on the capacitances and the inductance can be neglected. The initial voltage distribution along the winding coordinate z is given by

$$\frac{U}{U_{\text{dist}}} = \begin{cases} 1 - \frac{z}{\ell_{\text{winding}}} & \alpha = 0 \\ \frac{\sinh\left(\alpha\left(1 - \frac{z}{\ell_{\text{winding}}}\right)\right)}{\sinh(\alpha)} & \alpha > 0 \end{cases}, \quad (7.113)$$

with

$$\alpha = \sqrt{\frac{C_g}{C_s}}. \quad (7.114)$$

After all transient effects decay the voltage distribution is given by the line for $\alpha = 0$. This is consistent with the approach presented above. During

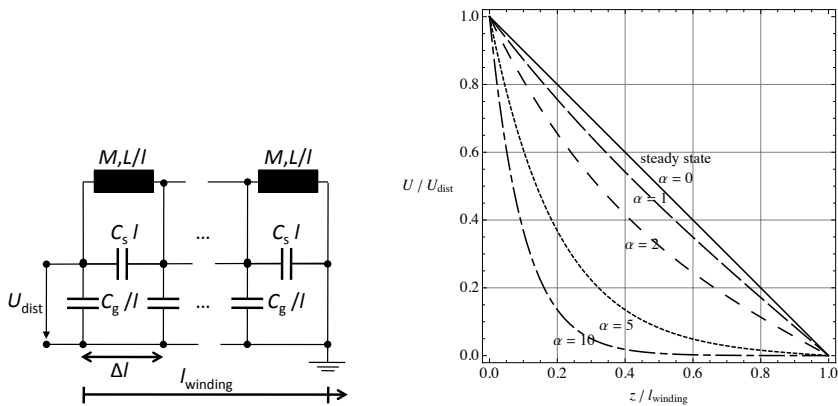


Figure 7.50: (left) Transmission line representation of a the coil winding. (right) Voltage over the coil winding for different values of α .

the transition, the voltage disturbance propagates along the coil winding and may result in voltages greater than the initial disturbance [Brec 73, pp. 332].

Figure 7.50 (right) shows the initial voltage distribution over the magnet winding. For increasing values of α the voltage distribution becomes less uniform and more concentrated at the location of the disturbance. This increases the voltage gradient at the terminal by the factor α . As shown above, turn-to-turn voltages can be estimated from the voltage gradient along the winding, and consequently increase.

For small values of α , turn-to-turn voltages and voltages to ground well below critical limits, the capacitive effects can be neglected. Capacitance measurements for the SSC dipole [Smed 93], *i.e.* a $\cos \theta$ dipole similar to magnets used in the LHC, suggest a value for α of approximately 2. Therefore, capacitive effects do not need to be considered while turn-to-turn voltages remain orders of magnitude below critical values.

7.11 Runge-Kutta Method

The Runge-Kutta method denotes a family of implicit and explicit iteration schemes for the numerical approximation of ordinary differential equations. In this work we use the classic *explicit Runge-Kutta method of 4th order*.

We introduce the scheme following [Seld 73, pp. 210]. Consider the initial value problem of the form

$$y' = f(t, y) \quad \text{with} \quad y(t_0) = y_0 \quad (7.115)$$

where $y' = \frac{dy}{dt}$ and f is continuously differentiable. The basic idea of numerical integration (the classical Euler method) is to approximate the increment

by $\Delta y = h y' = h f(t_n, y_n)$ at a certain point, *e.g.*, the initial value (t_0, y_0) . The step size of the integration is denoted h . A way to improve this method is to calculate the derivative at the point y_{n+1} and average it with the derivative at y_n before the actual integration step is performed (trapezoid method). The Runge-Kutta method of 4th order is further refinement and reads:

$$k_1 := f(t_n, y_n), \quad (7.116)$$

$$k_2 := f\left(t_n + \frac{h}{2}, y_n + \frac{h}{2}k_1\right), \quad (7.117)$$

$$k_3 := f\left(t_n + \frac{h}{2}, y_n + \frac{h}{2}k_2\right), \quad (7.118)$$

$$k_4 := f(t_n + h, y_n + hk_3), \quad (7.119)$$

With $t_{n+1} = t_n + h$ it yields

$$y_{n+1} = y_n + \frac{h}{6}(k_1 + 2k_2 + 2k_3 + k_4). \quad (7.120)$$

As all explicit methods, the Runge-Kutta of 4th order is not unconditionally stable and depends on the chosen time-step width h . The error can be controlled by repeating the calculation with twice the step-size and comparing the results [Seld 73, p. 212].

Adaptive Time-Stepping For systems with varying parameters, the typical time-constants of the system may vary throughout the computation. This way, an initially well adapted time-step width may end up being too short, causing unnecessary high computational effort, or too long, yielding great numerical uncertainty. The Runge-Kutta method of 4th order can be improved by introducing an adaptive time-step width h_n . A quality-factor [Coll 55, p. 68],

$$q = \left| \frac{k_2 - k_3}{k_1 - k_2} \right| \quad (7.121)$$

indicates if the Runge-Kutta time-step has been appropriate or whether it should be shortened and repeated. If possible, the time-step size is increased for the subsequent step:

$0 < q < 0.02$	accept time step and increase the time-step width for the following calculation step
$0.02 \leq q < 0.05$	accept time step
$0.05 < q$	recalculate time step with shorter time-step width

In both cases, the new step-size can be conveniently calculated from the quality factor,

$$h_{\text{new}} = h_{\text{old}} \frac{0.03}{q}. \quad (7.122)$$

A Material Properties

*“Ihr zahmen Täubchen, ihr Turteltäubchen, all ihr
Vöglein unter dem Himmel, kommt und helft mir
lesen, die guten ins Töpfchen, die schlechten ins
Kröpfchen.”*

ASCHENPUTTEL

(Jacob Grimm and Wilhelm Grimm)

Low-temperature superconducting magnets most often consist of similar components and materials: Ferromagnetic low-carbon steel (magnetic iron) is used to guide the magnetic flux, stainless steel or aluminum parts form support structures, and copper components are employed as spacers in the coil cross section. The cables consist of uninsulated superconducting strands, eventually surrounded by a stabilizer made of copper or aluminum, or containing a core of copper or iron. The cables are insulated by wraps of Kapton¹, or impregnated with Epoxy resin or PVA². The superconducting strands consist either of Niobium-Titanium (Nb-Ti) or Niobium-3-Tin (Nb₃Sn) filaments embedded in a copper matrix. Nb₃Sn-strands contain, in addition, fractions of niobium (Nb), tin (Sn) and tantalum (Ta), due to the fabrication process. The magnets are cooled with liquid helium (He).

Materials
used in
accelerator
magnets

The materials can be subdivided into fluid (respectively gaseous) and solid matter. The solid components can be further subdivided into chemical elements (Al, Cu, Nb, Sn, Ti, Ta), alloys³ (MI, SS, Nb-Ti) and compounds (Nb₃Sn, Kapton, Epoxy, G10). Some of the materials exhibit superconductivity at low temperature and low magnetic fields (Al, Nb, Ti, Ta, and especially Nb-Ti, Nb₃Sn). Liquid helium exhibits different phases at low temperature.

Classification
Phases

The simulation of superconducting accelerator magnets requires the following material properties: The relative magnetic permeability μ_r of all components of the magnet for the calculation of static magnetic fields. The critical

Relevant
Properties

¹Kapton is a polyimide film developed by DuPont. The chemical name for Kapton H and HN is poly(4,4'-oxydiphenylene-pyromellitimide).

²As pointed out in [Lin 95] the abbreviation PVA can refer either to polyvinyl acetate or polyvinyl alcohol. In the context of accelerator magnets PVA refers to polyvinyl acetate.

³In the notation of alloys different materials are separated by a hyphen, *e.g.* niobium-titanium: Nb-Ti. "NbTi" would represent a compound!

current density J_c is needed for the calculation of quenching and superconductor magnetization currents. The computation of quench propagation relies on thermal properties, *i.e.*, thermal conductivity κ_T and volumetric specific heat c_p of the coil and the coolant. The electrical resistivity ρ_E of all magnet components is required for the calculation of induced eddy and magnetization currents. For the calculation of internal voltages the relative permittivity ϵ_r of the insulating materials is used. For practical reasons some of the material properties are expressed per unit volume. The mass density ρ_D is required in order to convert to quantities expressed per unit mass.

The material properties may depend on the applied magnetic induction B , the temperature T and the electrical current density J . A dependence on the applied electrical field or on mechanical stress/strain is not taken into account. In both cases, magnetic iron and helium, a dependence on the applied pressure p_m is considered.

Sources

The material properties given in the following sections are taken from a wide range of publications. Some of the used publications are data compilations and refer to original measurements. The work of JENSEN *et al.* [Jens 80], FLOCH [Floc 03] and BRECHNA [Brec 73] is in particular helpful.

As shown by AMATI in [Amat 04], a comparison of the available measurement data shows differences of up to 25% for the resistivity, up to 10% for the specific heat and up to 25% for the heat conductivity. It is not always possible to find adequate measurement data due to the difficulties measuring at very low temperatures and/or very high magnetic fields. Furthermore, the variety of different alloys is too big in order to always find measurements of material properties. Therefore alternative data is given based on similarity or linear combinations. This clearly disregards any metallurgical and microscopical effects.

Structure
of the text

The material properties of the solids in the normal conducting state are given first, followed by their properties in the superconducting state. At the end the properties of liquid helium are presented. The text is organized by the properties and not by the materials in order to facilitate comparisons. When different sources deviate significantly, a comparison is made and the final choice is justified.

A.1 Solids in Normal Conducting State

A.1.1 Temperature Levels

The term *ambient temperature* or *room temperature* is not strictly defined. It can range from 273 K, over 293 K, and 295 K to 300 K [IEV 08]. Therefore, in this text the term ambient temperature is used to refer to a generic temperature accessible without technical aids and of common experience, *i.e.* between 273 and 300 K.

Cryogenic

Cryogenic temperature refers to temperatures only accessible by employing cryogenic cooling, *i.e.* temperatures below 120 K [Rade 02].

Standard
conditions

The *standard temperature* is defined as 293.15 K (or 20 °C). The melting

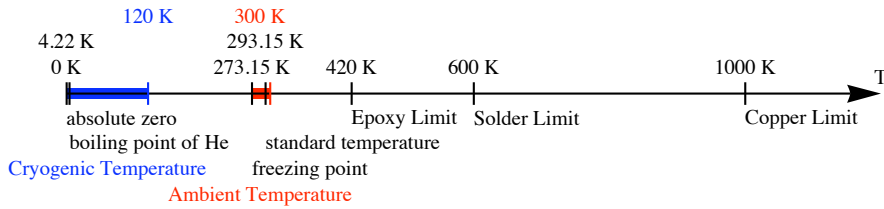


Figure A.1: Temperature levels.

and boiling point of materials are given at *normal pressure* of 101.325 kPa (both from the NIST publication [Wrig 03, p. 22]).

Furthermore, the following three fixed temperatures are referred to: The freezing point of water (at normal pressure) 273.15 K (or 0 °C), the boiling temperature of liquid helium (at normal pressure) 4.22 K, and *absolute zero* 0 K (or −273.15 °C). Figure A.1 shows all temperature levels on one graph.

In order to use the material properties below for the solid state, it is important to know the melting point. Table A.1 shows the melting temperature T_M for materials found in superconducting magnets.

It can be seen from the melting temperatures that two limits of operating a magnet are given. The melting point of copper reduces the maximum plausible temperature to around 1000 K. The melting point of solder, consisting of lead and tin, reduces the maximum operation temperature to below 600 K. The transition temperature of epoxy and epoxy-composites, *i.e.*, where the crystal structure changes, is in the range of 410 – 430 K [Imba 03, p.3-21].

Melting
tempera-
ture

Thermal
limits

A.1.2 Mass Density

Some material properties, *e.g.*, the specific heat are given as quantity per unit mass. In simulation programs the accelerator magnet is usually described by its geometry, and thus by the volume of the different parts. In order to

Table A.1: Melting temperature of the some materials [Lide 06]

Material	Symbol	Melting Temperature T_M in K
Aluminium	Al	933
Copper	Cu	1358
Iron	Fe	1811
Lead	Pb	601
Niobium	Nb	2750
Tantalum	Ta	3290
Tin	Sn	505
Titanium	Ti	1941

convert between the two definitions the mass density ρ_D , *i.e.* the mass per unit volume, is needed ($[\rho_D] = \text{kgm}^{-3}$). Table A.2 shows the mass density of the most common materials at ambient and cryogenic temperature. The change of density with temperature, $\Delta\rho_D/\rho_D = (\rho_D(300\text{ K}) - \rho_D(0\text{ K}))/\rho_D(300\text{ K})$, is less than 2% for most materials and can thus be neglected. For Nb_3Sn the change is in the order of 6%.

A.1.3 Electrical Resistivity

The electrical resistivity ρ_E is given by the relation between the electrical field \mathbf{E} and the electrical current density \mathbf{J} . The electrical conductivity κ_E is the inverse of ρ_E .

$$\mathbf{E} = \rho_E \mathbf{J}, \quad [\rho_E] = \text{VmA}^{-1} = \Omega\text{m}. \quad (\text{A.1})$$

Motivation of electrical resistivity The electrical conductivity of metals depends on the length of the mean free path of the conduction electrons. This path length is limited by collisions of electrons with either imperfections of the crystal or with lattice phonons [Van 86, pp. 25]. The rate of collision is further increased by an applied magnetic field by the Lorentz force acting on the electrons. This is referred to as magneto-resistivity [Brec 73, pp. 430].

Matthiessen's rule The resistivity of a metal at zero magnetic field consist of two additive parts (Matthiessen's rule [Brec 73, p. 423 and p. 428]): The residual resistivity

Table A.2: Mass density ρ_D of the most common materials at different temperatures

Material	Symbol	$\rho_D(0\text{ K})$ in kgm^{-3}	$\rho_D(300\text{ K})$ in kgm^{-3}	$\frac{\Delta\rho_D}{\rho_D}$ -	Remark
Aluminum	Al	$2.74 \cdot 10^3$	$2.70 \cdot 10^3$	-1.5%	[Jens 80]
Copper	Cu	$9.08 \cdot 10^3$	$8.96 \cdot 10^3$	-1.4%	[Jens 80]
Iron	Fe	$7.95 \cdot 10^3$	$7.83 \cdot 10^3$	-1.5%	[Jens 80]
Lead (chemical)	Pb		$\approx 11.3 \cdot 10^3$		[Lide 06, 12-211]
Niobium	Nb	$8.61 \cdot 10^3$	$8.58 \cdot 10^3$	-0.3%	[Jens 80]
Tin	Sn	$7.42 \cdot 10^3$	$7.28 \cdot 10^3$	-1.9%	[Jens 80]
Tantalum	Ta		$16.69 \cdot 10^3$	-4%	1 & 2
Titanium (com.)	Ti		$\approx 4.5 \cdot 10^3$		[Lide 06, 12-211]
Niobium-Titanium	Nb-Ti		$6 \cdot 10^3$	-0.2%	1, 2 & 3
Niobium-3-Tin	Nb_3Sn		$8.4 \cdot 10^3$	-6%	1 & 2
Stainless Steel	SS	$8.00 \cdot 10^3$	$7.89 \cdot 10^3$	-1.4%	[Floc 08]
Polyimide			$1.42 \cdot 10^3$		
Epoxidharz (pure)			$\approx 1.2 \cdot 10^3$		[Schn 73, p. 87]
Polyester (pure)			$\approx 1.1 \cdot 10^3$		[Schn 73, p. 87]

Remark 1: The change of density is calculated from the linear contraction factor $\Delta L/L$ assuming an isotropic contraction of the volume. Therefore the density change is given by $\frac{\Delta\rho_D}{\rho_D(300\text{ K})} = 1 - (1 + \Delta L/L)^3$.

Remark 2: The density is taken at room temperature from [Baue 07].

Remark 3: The sources quoted in [Baue 07, p. 5-2] vary strongly, *i.e.* between 5600 kgm^{-3} and 6500 kgm^{-3} . Therein it is suggested to use 6000 kgm^{-3} .

$\rho_o(RRR)$ and the intrinsic resistivity $\rho_i(T)$,

$$\rho_E(T, RRR) = \rho_o(RRR) + \rho_i(T). \quad (\text{A.2})$$

The residual resistivity represents the temperature independent part of the resistivity resulting from the scattering of the electrons at chemical impurities or physical imperfections of the lattice [Hust 75]. The residual resistivity thus only depends on the purity of the metal. At ambient temperatures the electron-scattering process is dominated by electron-phonon-scattering, and results in an approximately linear temperature dependence. This is denoted as intrinsic resistivity [Hust 75]. In the intermediate temperature range the two regimes are joined smoothly [Van 86, p. 25].

The ratio between the resistivity at ambient temperature and the residual resistivity is called the residual resistivity ratio (RRR). Since the residual resistivity depends only on the number of imperfections in the lattice of the metal the RRR can be used as a measure of purity [Van 86] and freedom from strain [Hust 75]. RRR increases with increasing purity. The exact definition is given below. RRR

The dependence of the electrical resistivity on an applied magnetic field can be added by means of Magneto-resistivity

Kohler's Rule: The following expressions are introduced in order to explain Kohler's rule: The change of resistivity due to a magnetic field $\Delta\rho_E/\rho_E$,

$$\frac{\Delta\rho_E}{\rho_E} = \frac{\rho_E(B, T, RRR) - \rho_E(T, RRR)|_{B=0\text{ T}}}{\rho_E(T, RRR)|_{B=0\text{ T}}}. \quad (\text{A.3})$$

Note that this quantity depends on B , T , and RRR . A normalized magnetic field $B \cdot S(T, RRR)$ is defined by

$$S(T, RRR) := \frac{\rho_E(RRR)|_{T=273\text{ K}}}{\rho_E(T, RRR)} \Big|_{B=0\text{ T}}. \quad (\text{A.4})$$

Due to the minimal influence of the purity at ambient temperature the quantity $\rho_E(RRR)|_{T=273\text{ K}}$ can be considered as constant.

According to Kohler's rule [Brec 73, pp. 430] the change of resistivity depends only on the normalized field $B \cdot S$ and the angle φ between the applied field and the current/wire. The dependence defines a unique function f for every material. Anisotropy

$$\frac{\Delta\rho_E}{\rho_E} = f(B \cdot S(T, RRR), \varphi). \quad (\text{A.5})$$

The double logarithmic representation of the function f is known as the Kohler plot. For most common metals the graph is a straight line [Seeb 98, pp. 1070] or can be expressed by a polynomial in terms of $\log(B \cdot S)$:

$$\log\left(\frac{\Delta\rho_E}{\rho_E}\right) = \sum_n a_n (\log(B \cdot S))^n. \quad (\text{A.6})$$

The electrical resistivity depending on temperature, magnetic field, and purity can be obtained by solving (A.6) for $\rho_E(B, T, RRR)$.

Residual Resistivity Ratio: The electrical resistivity ρ_E of normal conductors changes with temperature. For practical reasons, this can be expressed by the residual resistivity ratio (RRR), *i.e.*, the ratio of the resistivity at a common and easily accessible temperature, *i.e.* ambient temperature, and cryogenic temperature. Unfortunately the precise definition of the two temperature levels varies among most common sources.

Table A.3 shows the definition of lower and upper temperatures according to common sources. The error e_{RRR} denotes by how much the RRR value has to be modified compared to the NIST definition: $e_{RRR} = RRR_{\text{other}}/RRR_{\text{NIST}}$. Note that the error itself grows with increasing RRR . The quoted values are for a RRR of 200.

Two definitions shall be highlighted: In [Voll 02] the two temperatures are defined by phase-transition temperatures of water and helium. The lower temperature by the boiling point of liquid helium at normal pressure and the upper temperature by the freezing point of water. This way the temperature measurement is less difficult. The definition in [Char 06] with a lower temperature of 10 K is a direct consequence of measuring the RRR of Nb-Ti strands: Passing the critical temperature T_c the Nb-Ti filaments become superconducting and hence it is impossible to measure any resistivity. Therefore a temperature above T_c has to be chosen (in line with [Supe 07b, p. 6]). In case of copper this can result in a small error for very high RRR .

In the following the definition of NIST⁴ shall be used [Prop 92]:

$$RRR = \frac{\rho_E(273 \text{ K})}{\rho_E(4 \text{ K})} \Big|_{B=0 \text{ T}}. \quad (\text{A.7})$$

For materials or material combinations which exhibit superconductivity, the lower temperature is chosen right above the transition temperature [Supe 07b,

⁴The National Institute of Standards and Technology (NIST), Agency of the United States Department of Commerce.

Table A.3: Temperatures defining the RRR value according to different sources.

Source	lower temperature in K	upper temperature in K	e_{RRR}
NIST [Hust 75], Floch [Floc 03]	4	273	–
Verweij [Verw 05]	4	290	$\approx 7\%$
Van Sciver [Van 86]	4.2	273	$< 0.1\%$
Brechna [Brec 73]	4.2	293	$\approx 8.5\%$
Rossi [Ross 06]	4.2	295	$\approx 9\%$
Vollinger [Voll 02]	4.22	273.15	$< 0.1\%$
Charifouline [Char 06]	10	293	$> 11\%$

Applied
definition
of RRR

p. 6]. If the RRR is derived from the ratio of the bulk resistivity of a sample, then the thermal contraction of the sample at low temperature has to be taken into account.

A.1.3.1 Copper

For the resistivity of copper two different functions are shown. The first function is based on data from NIST. The second function is more approximative, but favorable in terms of computation speed.

NIST: The electrical resistivity of copper for zero magnetic field $\rho_{\text{E,Cu},0}^{\text{NIST}}$ is taken from [Prop 92, pp. 8-4].

$$\begin{aligned} \rho_{\text{E,Cu},0}^{\text{NIST}}(T, RRR) &= (\rho_o + \rho_i + \rho_{\text{io}}) \Omega\text{m} & (\text{A.8}) \\ \text{with:} & \\ \rho_o(RRR) &= \frac{1.553 \cdot 10^{-8}}{RRR}, \\ \rho_i &= \frac{P_1 \left(\frac{T}{T_0}\right)^{P_2}}{1 + P_1 P_3 \left(\frac{T}{T_0}\right)^{P_2 - P_4} \exp\left(-\left(\frac{P_5}{\left(\frac{T}{T_0}\right)}\right)^{P_6}\right)} + \rho_c, \\ \rho_{\text{io}} &= P_7 \frac{\rho_i \rho_o}{\rho_i + \rho_o}, \\ \rho_c &= 0. \end{aligned}$$

The constants are:

$$\begin{aligned} T_0 &= 1 \text{ K}, & P_1 &= 1.171 \cdot 10^{-17}, & P_2 &= 4.49, & P_3 &= 3.841 \cdot 10^{10}, \\ P_4 &= 1.14, & P_5 &= 50, & P_6 &= 6.428, & P_7 &= 0.4531. \end{aligned}$$

The field dependence is taken into account by means of Kohler's rule and the following polynomial $p(x)$ [Prop 92, pp. 8-23]:

$$x = \frac{B}{B_0} \cdot S(T, RRR) \quad (\text{A.9})$$

$$\begin{aligned} p(x) &= -2.662 + 0.3168 \log_{10}(x) + 0.6229(\log_{10}(x))^2 \\ &\quad - 0.1839(\log_{10}(x))^3 + 0.01827(\log_{10}(x))^4 \end{aligned} \quad (\text{A.10})$$

$$\rho_{\text{E,Cu}}(T, B, RRR) = \rho_{\text{E,Cu},0}(T, RRR) \left(1 + 10^{p(x)}\right), \quad (\text{A.11})$$

with $B_0 = 1 \text{ T}$. It is important to notice that the polynomial $p(x)$ shows a minimum for $x_{\min} \approx -0.23$. For values of $x = B \cdot S(T, RRR)$ smaller than x_{\min} the resistivity would increase with decreasing magnetic induction. This

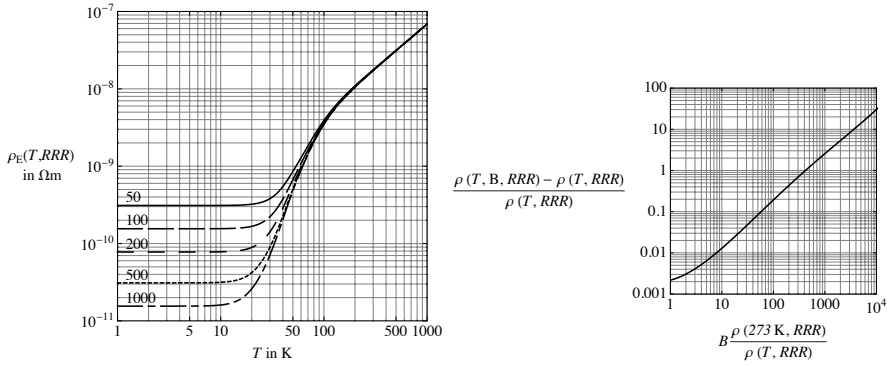


Figure A.2: Electrical resistivity of copper after [Prop 92]. (left) Electrical resistivity $\rho_{E,Cu,0}^{NIST}$ versus temperature for different values of RRR . (right) Kohler plot.

translates directly to a minimum magnetic induction B_{min}^{NIST} for which the approach fails:

$$B_{min}^{NIST} = 10^{x_{min}} \left. \frac{\rho_E(T, RRR)|_{B=0T}}{\rho_E(RRR)} \right|_{T=273K} \quad (A.12)$$

For ambient temperature the minimum field B_{min}^{NIST} is in the order of 1 T! At cryogenic temperatures it is much smaller depending on RRR .

Figure A.2 (left) shows the electrical resistivity $\rho_{E,Cu,0}^{NIST}$ versus temperature for different values of RRR . Figure A.2 (right) shows the polynomial $p(x)$ in the Kohler plot.

The NIST function is computationally very demanding. The accuracy to measurements is estimated by NIST to be 15%.

Alternative function: The second approach is based on the zero field electrical resistivity found in [McAs 88]:

$$\rho_{E,Cu,0}(T, RRR) = \rho_0 \left(\frac{1.545}{RRR} + \frac{1}{\left(\frac{P_1}{T}\right)^5 + \left(\frac{P_2}{T}\right)^3 + \left(\frac{P_3}{T}\right)} \right), \quad (A.13)$$

with $\rho_0 = 1 \cdot 10^{-8} \Omega m$ and

$$P_1 = 74.697 K, \quad P_2 = 98.550 K, \quad P_3 = 162.74 K.$$

In Fig. A.3 (left) the electrical resistivity is plotted versus temperature for different values of RRR and zero field.

The field dependence is taken into account by adding a linear term⁵ depending on RRR and magnetic induction B [Verw 05]:

$$\rho_{E,Cu}(T, RRR, B) = \rho_{E,Cu,0}(T, RRR) + a(b + RRR)B \quad (A.14)$$

⁵see also [Krai 97] and [Floc 03]

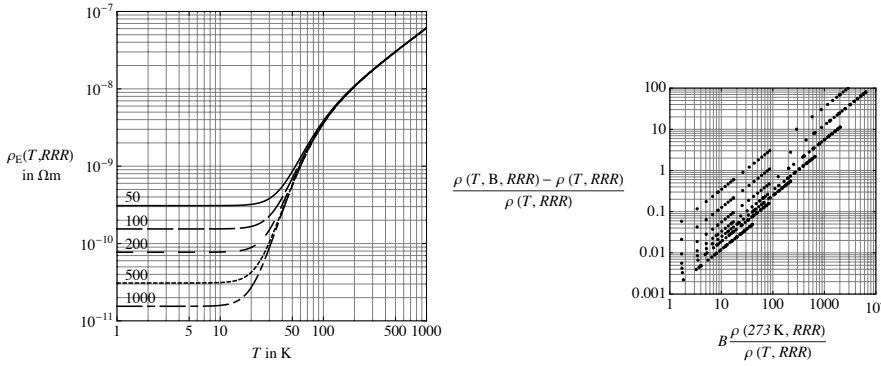


Figure A.3: Electrical resistivity of copper after [McAs 88] and [Verw 05]. (left) Electrical resistivity $\rho_{E,Cu,0}$ versus temperature for different values of RRR . (right) Kohler plot.

with $a = 2 \cdot 10^{-12} \Omega m T^{-1}$ and $b = 74$.

In Fig. A.3 (right) the Kohler plot for the function $\rho_{E,Cu}(T, RRR, B)$ is shown. This approach does not obey Kohler's rule, but nevertheless, the lines are within a relatively small band. The band is fully covered by the range of uncertainty published in [Prop 92, p. 8-27]. The deviation of the zero field resistivity to the NIST function is of less than 10% for a RRR of 200. The advantage is the faster computation, since both parts of the function are relatively simple to evaluate. The anisotropy of the magneto-resistivity is neglected.

A.1.3.2 Niobium-Titanium

The electrical resistivity of Niobium-Titanium (Nb-Ti) in the normal conducting state, $\rho_{E,Nb-Ti}(T)$, is given by [Baue 07, p. 5-8]. Figure A.4 (left) shows the resistivity versus temperature.

$$\rho_{E,Nb-Ti}(T) = (0.0558T + 55.668) \cdot 10^{-8} \Omega m. \quad (A.15)$$

A.1.3.3 Niobium-3-Tin

For the electrical resistivity of Niobium-3-Tin $\rho_{E,Nb3Sn}$ no analytic function is available. In Tab. A.4 measurement data from [Baue 07, p. 4-11] is given for interpolation. Figure A.4 (right) shows the resistivity versus temperature.

A.1.3.4 Insulators (Kapton, PVA, Epoxy)

The electrical resistivity of all insulation materials, *e.g.* Epoxy and polyimide (Kapton), is considered to be infinitely high. For PVA a value of approximately $2 \cdot 10^{13} \Omega m$ has been found [Lin 95]. This is nearly 20 orders of magnitude greater than the resistivity of copper.

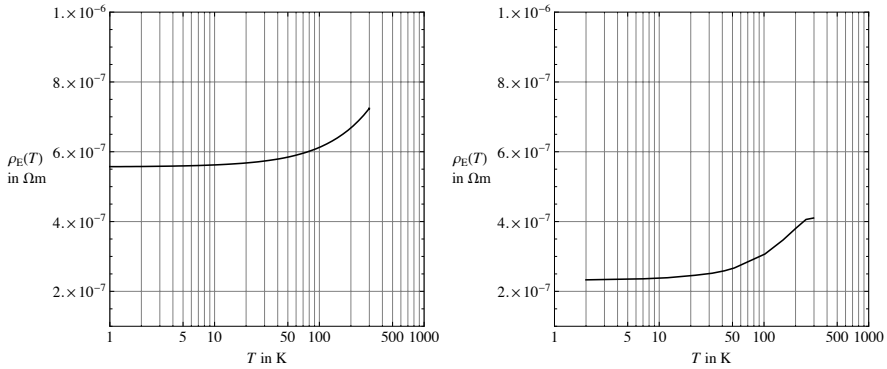


Figure A.4: (left) Electrical resistivity of Nb-Ti in the normal conducting state, $\rho_{E,\text{Nb-Ti}}$ after [Baue 07, p. 5-8]. (right) Electrical resistivity of Nb₃Sn in normal conducting state, $\rho_{E,\text{Nb3Sn}}$ after [Baue 07, p. 4-11].

Nevertheless, the electrical field has to remain under a maximum field level, the breakdown field strength (Sec. A.1.7).

A.1.3.5 Other Materials

The electrical resistivity of other common materials is given in Tab. A.5. For comparison the resistivity of copper is given in the first line.

A.1.4 Thermal Conductivity

The thermal conductivity κ_T is given by the relation of the heat flux density \mathbf{J}_T and the gradient of the temperature distribution T .

$$\mathbf{J}_T = \kappa_T \nabla T, \quad [\kappa_T] = \text{WmK}^{-1}. \quad (\text{A.16})$$

In solids heat is transported in two ways, by electrons and by lattice vibrations. The total thermal conduction κ_T is the sum of electronic κ_e and lattice

Table A.4: Electrical resistivity of Niobium-3-Tin versus temperature from [Baue 07, p. 4-11]

T in K	$\rho_{E,\text{Nb3Sn}}$ in $\text{WK}^{-1}\text{m}^{-1}$	T in K	$\rho_{E,\text{Nb3Sn}}$ in $\text{WK}^{-1}\text{m}^{-1}$
2	$2.33 \cdot 10^{-7}$	52	$2.67 \cdot 10^{-7}$
7	$2.36 \cdot 10^{-7}$	102	$3.07 \cdot 10^{-7}$
12	$2.39 \cdot 10^{-7}$	152	$3.47 \cdot 10^{-7}$
22	$2.46 \cdot 10^{-7}$	202	$3.81 \cdot 10^{-7}$
32	$2.52 \cdot 10^{-7}$	252	$4.06 \cdot 10^{-7}$
42	$2.59 \cdot 10^{-7}$	297	$4.10 \cdot 10^{-7}$

conduction κ_1 :

$$\kappa_T = \kappa_e + \kappa_1 \quad (\text{A.17})$$

In pure metals κ_e is much greater than κ_1 and thermal conductivity and electrical resistivity are intimately related. According to the Wiedemann-Franz law, the thermal conductivity of metals can be calculated from the electrical resistivity by:

Wiedemann-Franz law

$$\kappa_T = \frac{L_0 T}{\rho_E} \quad (\text{A.18})$$

where L_0 is the Lorenz⁶ number ($L_0 = 2.44 \cdot 10^{-8} \text{ W}\Omega\text{K}^{-2}$) and T is the absolute temperature. The Lorenz number is constant when the conduction electrons are scattered elastically. This is only true for very small and very high temperatures [Brec 73, p. 434]. The Lorenz number varies most for high purity (RRR) and is in addition also field dependent [Seeb 98, pp. 1086]. The thermal conductivity of metals thus depends on the same quantities as the electrical resistivity, i.e., temperature T , RRR , and magnetic induction B .

Lorenz number

For insulators with a very high electrical resistivity, the thermal conductivity is dominated by lattice vibrations (phonon transport). Since the transport of phonons is less efficient compared to the electron transport in metals, the thermal conductivity of insulators is several orders of magnitude smaller [Van 86, p. 29].

Thermal conductivity for insulators

A.1.4.1 Copper

For the thermal conductivity of copper at zero magnetic induction, $\kappa_{T,\text{Cu},0}$, an analytic formula is given in [Prop 92, p. 7-16]:

$$\kappa_{T,\text{Cu},0}(T, RRR) = \frac{1}{W_o + W_i + W_{io}} \text{Wm}^{-1}\text{K}^{-1} \quad (\text{A.19})$$

⁶Note that Ludvig Lorenz is spelled without a “t”.

Table A.5: Electrical resistivity ρ_E of some exemplary materials at 273.15 K.

Element/Material	Symbol	$\rho_E(273.15 \text{ K})$ in Ωm	RRR	Comments
Copper	Cu	$1.553 \cdot 10^{-8}$	up to 30000	[Prop 92], [Seeb 98, p. 1076]
Aluminum	Al	$2.50 \cdot 10^{-8}$	25-1000	[Jens 80, sec: X-B-2]
Niobium	Nb	$16.1 \cdot 10^{-8}$	≈ 30	[Jens 80, sec: X-M]
Lead	Pb	$19.2 \cdot 10^{-8}$	1000	[Jens 80, sec: X-I-1]
Tin	Sn	$11.15 \cdot 10^{-8}$	100	[Jens 80, sec: X-Q-1]
Tantalum	Ta	$12.4 \cdot 10^{-8}$	10	[Jens 80, sec: X-P-1]
Titanium	Ti	$39.4 \cdot 10^{-8}$		[Seeb 98, p. 1076]
Iron	Fe	$8.66 \cdot 10^{-8}$	100 to 200	[Jens 80, sec: X-H-1]
Stainless steel	SS 304	$1.02 \cdot 10^{-6}$	2	[Jens 80, sec: X-X]
	SS 304L	$0.704 \cdot 10^{-6}$	1.42	[Verw 07b]

with:

$$\begin{aligned}
 W_o &= \frac{\beta(RRR)}{(T/T_0)}, \\
 W_i &= \frac{P_1 \left(\frac{T}{T_0}\right)^{P_2}}{1 + P_1 P_3 \left(\frac{T}{T_0}\right)^{P_2+P_4} \exp\left(-\left(\frac{P_5}{\left(\frac{T}{T_0}\right)}\right)^{P_6}\right)} + W_c, \\
 W_{io} &= P_7 \frac{W_i W_o}{W_i + W_o}, \\
 W_c &= 0.
 \end{aligned}$$

Here, β is given by

$$\beta(RRR) = \frac{\rho_o(RRR)}{L_0} = \frac{1.553 \cdot 10^{-8} \Omega\text{m}/RRR}{2.443 \cdot 10^{-8} \text{W}\Omega\text{K}^{-2}} = \frac{0.634 \text{mK}^2\text{W}^{-1}}{RRR},$$

and $\rho_o(RRR)$ denotes the above introduced residual resistivity of copper, see Eq. (A.8). The constants are:

$$\begin{aligned}
 T_0 &= 1 \text{ K}, & P_1 &= 1.754 \cdot 10^{-8}, & P_2 &= 2.763, \\
 P_3 &= 1102, & P_4 &= -0.165, & P_5 &= 70, \\
 P_6 &= 1.756, & P_7 &= 0.838/\beta_r^{0.1661}, & \beta_r &= \beta/0.0003.
 \end{aligned}$$

The thermal conductivity of copper versus temperature is shown in Fig. A.5 (left).

For the calculation of magnets, the considerable change of conductivity [Prop 92, 7-20] has to be taken into account and another function has to be used.

Using the Wiedemann-Franz law, it is possible to calculate the thermal conductivity based on the electrical resistivity which itself is field dependent. As mentioned above, the Lorenz number is not constant in the intermediate temperature range, it depends on RRR and magnetic field. Figure A.5 (right) shows the change of the Lorenz number with RRR as computed from the thermal conductivity after [Prop 92, p. 7-16] and the electrical resistivity after [Prop 92, p. 8-4]. A variation of a factor of 2 can be easily noticed (see also [Brec 73, p. 434] and [Van 86, p. 29])! Furthermore in [Aren 82] it was shown that the Lorenz number for copper depends anisotropically on the magnetic induction. The Lorenz number describing the thermal conductivity transversal to the magnetic field, changes by $0.112 \cdot 10^{-8} \text{W}\Omega\text{K}^{-2}$ per tesla, *i.e.* approximately 5%. The longitudinal Lorenz number remains constant. There is no analytic function available describing the Lorenz number as function of temperature, RRR and magnetic induction.

For this work the thermal conductivity is calculated from the electrical resistivity using a constant value for the Lorenz number. The Lorenz number varies by a factor of ≈ 2 over temperature (see Fig. A.5 (right)) and increases by a factor of ≈ 2 if the magnetic flux density is increased to 10 T [Aren 82].

For the same field change the electrical resistivity changes by more than a factor of 10 (see Fig. 2.7 for $RRR = 200$).

A.1.4.2 Niobium-Titanium

The thermal conductivity can be expressed as [Baue 07, p. 5-10]:

$$\kappa_{\text{T,Nb-Ti}}(T) = \kappa_0 (aT^6 + bT^5 + cT^4 + dT^3 + eT^2 + fT + g), \quad (\text{A.20})$$

with $\kappa_0 = 1 \text{ WK}^{-1}\text{m}^{-1}$ and

$$\begin{aligned} a &= -5 \cdot 10^{-14} \text{ K}^{-6}, & b &= 1.5 \cdot 10^{-11} \text{ K}^{-5}, & c &= 6 \cdot 10^{-9} \text{ K}^{-4}, \\ d &= -3 \cdot 10^{-6} \text{ K}^{-3}, & e &= 3 \cdot 10^{-4} \text{ K}^{-2}, & f &= 4.56 \cdot 10^{-2} \text{ K}^{-1}, \\ g &= 6.6 \cdot 10^{-2}. \end{aligned}$$

The thermal conductivity is shown in Fig. A.6 (left).

A.1.4.3 Niobium-3-Tin

For Niobium-3-Tin only measured data for interpolation is available [Baue 07, p. 4-13] as shown in Tab. A.6 and Fig. A.6 (right).

A.1.4.4 Polyimide (Kapton)

The thermal conductivity of Polyimide (Kapton) is given by NIST [Nati 08] to an exponential function of polynomial argument:

$$\begin{aligned} \kappa_{\text{T,Kapton}}^{\text{NIST}}(T) &= \kappa_0 10^{p(x)}, & (\text{A.21}) \\ x &= \frac{T}{T_0}, \\ p(x) &= a + b(\log_{10}(x)) + c(\log_{10}(x))^2 + d(\log_{10}(x))^3 \\ &\quad + e(\log_{10}(x))^4 + f(\log_{10}(x))^5 + g(\log_{10}(x))^6 \\ &\quad + h(\log_{10}(x))^7, \end{aligned}$$

with $\kappa_0 = 1 \text{ WK}^{-1}\text{m}^{-1}$, $T_0 = 1 \text{ K}$ and the following parameters:

$$\begin{aligned} a &= 5.73101, & b &= -39.5199, & c &= 79.9313, & d &= -83.8572, \\ e &= 50.9157, & f &= -17.9835, & g &= 3.42413, & h &= -0.27133. \end{aligned}$$

The function is shown in Fig. A.7.

A.1.4.5 Other Materials

The thermal conductivity⁷ of other common materials is given in Tab. A.7. Since the thermal conductivity of many metals is not a monotonous function, the maximum value between 2 and 500 K is given. For comparison, the

⁷In US publications often the unit BTU / °F FT HR is used. This can be converted to SI units by

$$1 \frac{\text{BTU}}{^\circ\text{F FT HR}} = 1.731 \text{ WK}^{-1}\text{m}^{-1} \quad (\text{A.22})$$

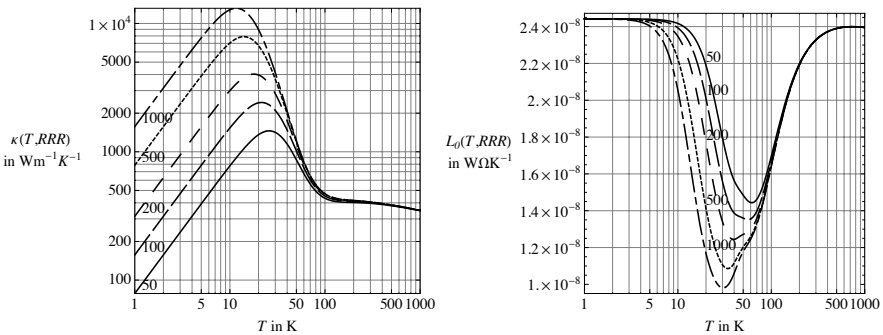


Figure A.5: (left) Thermal conductivity of copper for zero magnetic induction. (right) Variation of the Lorenz number of copper with RRR as calculated from the heat conductivity and electrical resistivity functions published in [Prop 92].

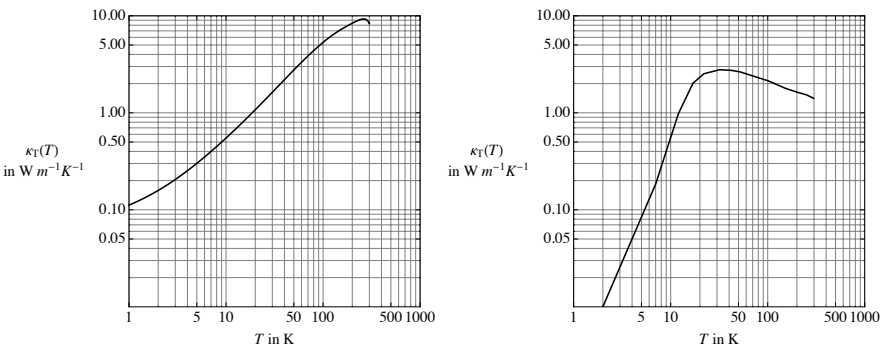


Figure A.6: Thermal conductivity versus temperature. (left) Niobium-Titanium [Baue 07, p. 5-10]. (right) Niobium-3-Tin [Baue 07, p. 4-13].

Table A.6: Thermal conductivity of Niobium-3-Tin versus temperature from [Baue 07, p. 4-13]

T in K	$\kappa_{\text{T,Nb3Sn}}$ in $\text{W K}^{-1} \text{m}^{-1}$	T in K	$\kappa_{\text{T,Nb3Sn}}$ in $\text{W K}^{-1} \text{m}^{-1}$
2	0.01	52	2.64
7	0.184	102	2.13
12	0.98	152	1.79
17	2.02	202	1.63
22	2.53	252	1.53
32	2.78	297	1.41
42	2.74		

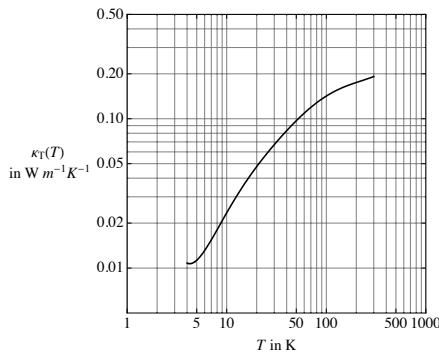


Figure A.7: Thermal conductivity of Polyimide (Kapton), $\kappa_{T,\text{Kapton}}$. Function from [Nati 08].

maximum thermal conductivity of copper ($RRR = 200$) is given in the first line.

A.1.5 Heat Capacity

The heat capacity C_T is defined as the amount of energy needed to raise the temperature of a material by one degree. In terms of thermodynamic quantities the heat capacity can be written as the derivative of the internal energy U_T under either constant pressure, C_p or constant volume, C_v :

$$C_v = \left(\frac{\partial U_T}{\partial T} \right)_{V=\text{const.}}, \quad C_p = \left(\frac{\partial U_T}{\partial T} \right)_{p=\text{const.}}, \quad (\text{A.23})$$

$$[C_v] = [C_p] = \text{Jmol}^{-1}\text{K}^{-1}.$$

Table A.7: Maximum thermal conductivity of most common materials

Material	Symbol	$\max(\kappa_T)$ in $\text{WK}^{-1}\text{m}^{-1}$	Comment
Copper	Cu	4000.0	see above
Aluminum	Al	389.5	Al 1100, [Schw 70, p. 43]
Niobium	Nb	86.4	[Baue 07, p. 6-14]
Tantalum	Ta	69.0	[Baue 07, p. 7-12]
Titanium	Ti	24.0	[Schw 70, p. 611]
Stainless steel	SS	14.7	316 LN, [Baue 07, p. 1-14]
Epoxy (pure)		0.11 – 0.14	at 25 °C [Schn 73]
Polyester (pure)	PE	0.2	at 25 °C [Schn 73]
Polyvinyl acetate	PVA	0.05	[Karp 08b]

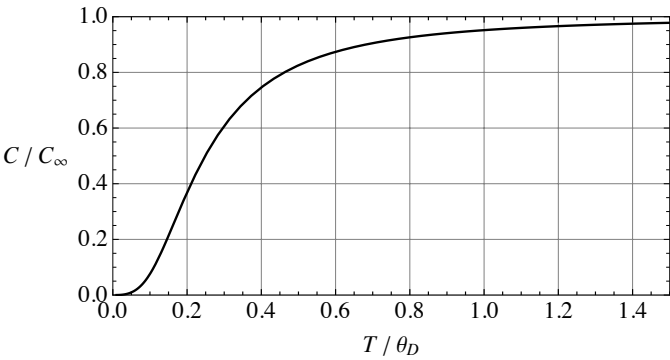


Figure A.8: Normalized specific heat of solids. The value of C_∞ is given to $3R$ (see Eq. A.24). The Debye temperature θ_D is given in Tab. A.8. The figure has been recalculated after [Deby 12].

The internal energy consists of the energy associated with the motion of molecules, the vibration of atoms in molecules and crystals, the electric energy of atoms in molecules and lattices, the energy of all chemical bonds and the energy of the free conduction electrons in metals. In solids the heat capacity is dominated by the vibration of the lattice described in the Debye theory. In metals below a temperature of 1 K the contribution of the free conduction electrons has to be taken into account [Van 86, p. 21], but will not be considered in this work.

Debye
theory

DEBYE derives the heat capacity of solids as a function of temperature from the spectra and associated energy levels of the lattice vibrations [Deby 12]. The heat capacity of all common solids essentially follows the same function of normalized temperature T/θ_D . At low temperatures the function shows a cubic dependence on the absolute temperature. Figure A.8 shows the normalized function. The Debye temperature θ_D is a property of the material. In Tab. A.8 the values of some materials are reported. For very high temperatures, *i.e.* $T > 2\theta_D$ the heat capacity approaches the Dulong-Petit-limit

Dulong-
Petit-limit

Table A.8: Debye temperature of some of the used materials

Material	Symbol	Debye Temperature θ_D in K
Aluminium	Al	428
Copper	Cu	343
Iron	Fe	470
Niobium	Nb	450
Tin	Sn	200
Titanium	Ti	420

C_∞ [Peti 19].

$$C_\infty = 3N_A k_B = 3R_{\text{gas}} = 24.93 \text{ Jmol}^{-1} \text{K}^{-1}. \quad (\text{A.24})$$

Here, N_A denotes the Avogadro number, k_B the Boltzmann constant and $R_{\text{gas}} = 8.31 \text{ Jmol}^{-1} \text{K}^{-1}$ the gas constant.

For solids and fluids it is difficult to measure the heat capacity for constant volume (due to the huge forces of the thermal expansion!). Therefore the heat capacity for constant volume and constant pressure have to be converted. For metals at ambient temperature both capacities differ minimally [Van 86, pp. 18].

$C_V \rightarrow C_P$

The heat capacity per unit mass is called *specific heat* and is denoted with a lower case, dashed c' . $[c'_V] = [c'_p] = \text{Jkg}^{-1} \text{K}^{-1}$. For the computation of accelerator magnets the so-called *volumetric specific heat*, *i.e.* the specific heat per volume, is more practical. It is denoted with a lower case c . Where not available from literature, it is calculated from the specific heat by means of the mass density. For all solids the mass density is considered constant (see Sec. A.1.2).

Specific
heat

$$\begin{aligned} c_V &= \rho_D c'_V, & c_p &= \rho_D c'_p, \\ [c_V] &= [c_p] & &= \text{Jm}^{-3} \text{K}^{-1}. \end{aligned} \quad (\text{A.25})$$

A.1.5.1 Copper

The volumetric specific heat of copper $c_{\text{T,Cu}}$ depends only on temperature and is given by a fit to measurement [Floc 03]:

$$c_{\text{T,Cu}}(T) = c_0(aT^4 + bT^3 + cT^2 + dT + e) \quad (\text{A.26})$$

with $c_0 = 1 \text{ JK}^{-1} \text{m}^{-3}$. The fit parameters can be found in Tab. A.9. Figure A.9 (left) shows the volumetric specific versus temperature.

A.1.5.2 Niobium-Titanium

The volumetric specific heat of Niobium-Titanium in the normal conducting state is given by a fit to measurements [Verw 05]:

$$c_{\text{T,Nb-Ti}}(T) = c_0(aT^4 + bT^3 + cT^2 + dT + e). \quad (\text{A.27})$$

with $c_0 = 1 \text{ JK}^{-1} \text{m}^{-3}$. The fit parameters can be found in Tab. A.10. The function is displayed in Fig. A.10 (left).

A.1.5.3 Niobium-3-Tin

For Niobium-3-Tin only measured data for interpolation is available, as shown in Tab. A.11 and Fig. A.10 (right).

Table A.9: Fit parameters for the volumetric specific heat of copper [Floc 03]

Temperature Range in K	a in K^{-4}	b in K^{-3}	c in K^{-2}	d in K^{-1}	e
$T < 10$	$-3.08 \cdot 10^{-2}$	$7.23 \cdot 10^0$	$-2.13 \cdot 10^0$	$1.02 \cdot 10^2$	$-2.56 \cdot 10^0$
$10 \leq T < 40$	$-3.05 \cdot 10^{-1}$	$2.99 \cdot 10^1$	$-4.56 \cdot 10^2$	$3.47 \cdot 10^3$	$-8.25 \cdot 10^3$
$40 \leq T < 125$	$4.19 \cdot 10^{-2}$	$-1.4 \cdot 10^1$	$1.51 \cdot 10^3$	$-3.16 \cdot 10^4$	$1.78 \cdot 10^5$
$125 \leq T < 300$	$-8.48 \cdot 10^{-4}$	$8.42 \cdot 10^{-1}$	$-3.26 \cdot 10^2$	$6.06 \cdot 10^4$	$-1.29 \cdot 10^6$
$300 \leq T < 500$	$-4.8 \cdot 10^{-5}$	$9.17 \cdot 10^{-2}$	$-6.41 \cdot 10^1$	$2.04 \cdot 10^4$	$1.03 \cdot 10^6$
$500 \leq T < 1000$	—	$1.2 \cdot 10^{-4}$	$-0.215 \cdot 10^0$	$1.00 \cdot 10^3$	$3.18 \cdot 10^6$

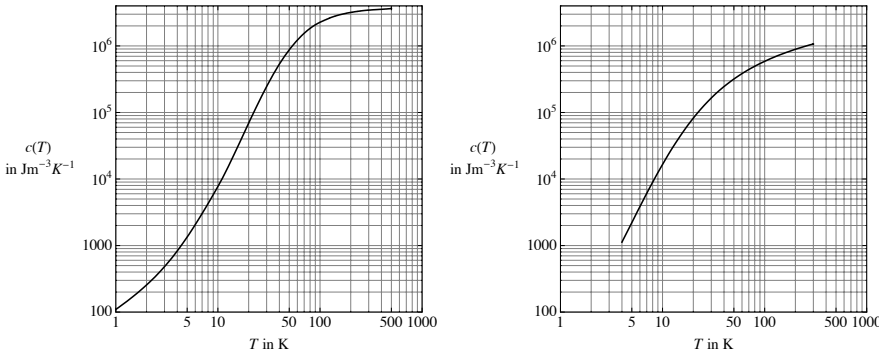


Figure A.9: (left) Volumetric specific heat of copper [Floc 03]. (right) Specific heat of Kapton after [Nati 08] using the mass density as given in Sec. A.1.2.

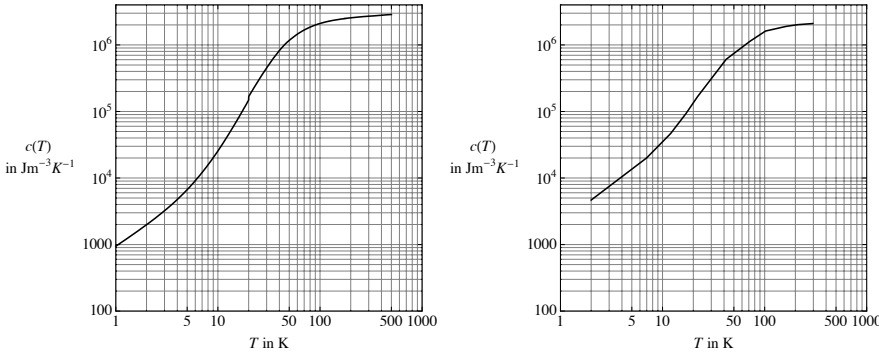


Figure A.10: Volumetric specific heat of (left) Niobium-Titanium [Verw 05] and (right) Niobium-3-Tin [Baue 07, p. 4-13].

A.1.5.4 Polyimide (Kapton)

The volumetric specific heat of Polyimide (Kapton) is given by NIST [Nati 08] to an exponential function of polynomial argument:

$$\begin{aligned} c_{\text{T,Kapton}}^{\text{NIST}}(T) &= c_0 10^{p(x)} \\ x &= \frac{T}{T_0}, \\ p(x) &= a + b(\log_{10}(x)) + c(\log_{10}(x))^2 + d(\log_{10}(x))^3 \\ &\quad + e(\log_{10}(x))^4 + f(\log_{10}(x))^5 + g(\log_{10}(x))^6 \\ &\quad + h(\log_{10}(x))^7 \end{aligned} \quad (\text{A.28})$$

with $c_0 = 1.42 \cdot 10^3 \text{ Jm}^{-3}\text{K}^{-1}$, $T_0 = 1 \text{ K}$ and the following parameters:

$$\begin{aligned} a &= -1.3684, & b &= 0.65892, & c &= 2.8719, & d &= 0.42651, \\ e &= -3.0088, & f &= 1.9558, & g &= -0.51998, & h &= 0.051574. \end{aligned}$$

The function is shown in Fig. A.9 (right). The published data on the specific heat shows variations of around 100% [Floc 08].

A.1.5.5 Other Materials

The volumetric specific heat of other common materials is given in Tab. A.12 for comparison [Jens 80].

A.1.6 Permeability

Materials can be classified into one of three different groups by the force they experience in a gradient magnetic field. Diamagnetic material is weakly repelled, paramagnetic material weakly attracted and ferromagnetic material is strongly attracted [Purc 89, pp. 258].

Classification

The magnetic force acting on a material generally results from the spin and orbit magnetic moments of the electrons. The three classes differ in the way the magnetic momenta compensate or couple.

General
Mechanism

In diamagnetic materials the spin and orbit magnetic moments cancel in the absence of an external magnetic field. An applied field causes the spin moments to slightly exceed the orbit moments, resulting in a small magnetic moment opposing the external field [Russ 07, p. 155].

Diamagnetic

In paramagnetic materials the individual spin magnetic momenta do not interact and take a random distribution. An external magnetic field causes them to align with the field direction, resulting in a small magnetic moment nearly independent of field strength and fully reversible [Russ 07, p. 155].

Paramagnetic

In ferromagnetic materials the spins are coupled and build clusters of identical orientation. The cluster size is given by an energetic minimum depending on applied magnetic field, temperature and impurities. Increasing the magnetic field causes clusters with parallel orientation to grow. A further increase, results in rotation of the orientation of whole clusters parallel to the field.

Ferromagnetic

Table A.10: Fit parameters for the volumetric specific heat of Nb-Ti

Temperature Range in K	a in K^{-4}	b in K^{-3}	c in K^{-2}	d in K^{-1}	e
$T_c < T < 20$	–	$1.624 \cdot 10^1$	–	$9.28 \cdot 10^2$	–
$20 \leq T < 50$	$-2.177 \cdot 10^{-1}$	$1.19838 \cdot 10^1$	$5.5371 \cdot 10^2$	$-7.846 \cdot 10^3$	$4.138 \cdot 10^4$
$50 \leq T < 175$	$-4.82 \cdot 10^{-3}$	$2.976 \cdot 10^0$	$-7.163 \cdot 10^2$	$8.3022 \cdot 10^4$	$-1.53 \cdot 10^6$
$175 \leq T < 500$	$-6.29 \cdot 10^{-5}$	$9.296 \cdot 10^{-2}$	$-5.166 \cdot 10^1$	$1.3706 \cdot 10^4$	$1.24 \cdot 10^6$

If the change of specific heat in superconducting state is not taken into account the critical temperature T_c is set to 0 K.

Table A.11: Volumetric specific heat of Niobium-3-Tin versus temperature from [Baue 07, p. 4-3]

T in K	$c_{T,\text{Nb3Sn}}$ in $\text{JK}^{-1}\text{m}^{-3}$	T in K	$c_{T,\text{Nb3Sn}}$ in $\text{JK}^{-1}\text{m}^{-3}$
2	$4.66 \cdot 10^3$	72	$1.14 \cdot 10^6$
7	$2.01 \cdot 10^4$	102	$1.62 \cdot 10^6$
12	$4.66 \cdot 10^4$	162	$1.90 \cdot 10^6$
17	$9.36 \cdot 10^4$	212	$2.02 \cdot 10^6$
22	$1.67 \cdot 10^5$	262	$2.07 \cdot 10^6$
42	$6.09 \cdot 10^5$	297	$2.10 \cdot 10^6$

Table A.12: Volumetric specific heat of common materials for comparison [Jens 80]. All values are given in $\text{JK}^{-1}\text{m}^{-3}$.

Material	Symbol	$c_p(2\text{ K})$	$c_p(10\text{ K})$	$c_p(100\text{ K})$	$c_p(300\text{ K})$	Comment
Copper	Cu	$0.25 \cdot 10^3$	$7.7 \cdot 10^3$	$2.28 \cdot 10^6$	$3.46 \cdot 10^6$	Sec. A.1.5.1
Aluminum	Al	$0.3 \cdot 10^3$	$3.8 \cdot 10^3$	$1.3 \cdot 10^6$	$2.44 \cdot 10^6$	Remark 1
Niobium	Nb	$1.54 \cdot 10^3$	$19 \cdot 10^3$	$1.73 \cdot 10^6$	$2.3 \cdot 10^6$	
Lead	Pb				$1.47 \cdot 10^6$	
Tin	Sn	$0.34 \cdot 10^3$	$58 \cdot 10^3$	$1.38 \cdot 10^6$	$1.62 \cdot 10^6$	
Tantalum	Ta	$1.13 \cdot 10^3$	$19 \cdot 10^3$	$1.9 \cdot 10^6$	$2.33 \cdot 10^6$	Remark 1
Titanium	Ti				$2.35 \cdot 10^6$	
Iron	Fe				$3.52 \cdot 10^6$	Remark 1
Stainless steel	SS					
Polyvinyl acetate	PVA					
Epoxy					$\approx 2 \cdot 10^6$	[Schn 73]

Remark 1: From [Lide 06, p. 4-127] in combination with Sec. A.2.

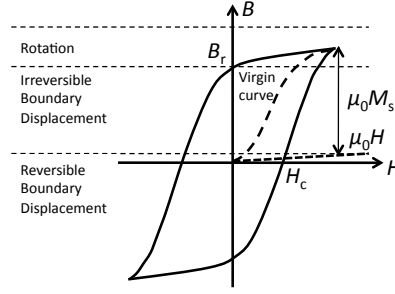


Figure A.11: General BH-curve [Russ 07]. Increasing the magnetic field from zero, the virgin curve passes the reversible, rapid irreversible and finally the saturation stage. Lowering the field to zero, the magnetic induction follows a new curve to the remanence magnetization field. Further decreasing the magnetic field (to negative values) causes the induction to drop to zero at the coercitive field. This behavior is denoted hysteretic and associated with losses. Field sweeps of smaller amplitude result in minor loops.

The magnetization \mathbf{M} is defined as the magnetic moment density,

Magnetization

$$\mathbf{M} = N\bar{\mathbf{p}}_m, \quad (\text{A.29})$$

where $\bar{\mathbf{p}}_m$ denotes the average magnetic moment and N the number of dipoles per volume [Henk 01, p. 152]. This way the magnetic induction is most generally given by,

$$\mathbf{B} = \mu_0 (\mathbf{H} + \mathbf{M}). \quad (\text{A.30})$$

The magnetization of a ferromagnetic material M rises with magnetic field H in three stages: initial reversible magnetization, rapid irreversible magnetization and slow approach of the saturation, related to the reversible shifts of domain walls, irreversible rotation and shift of domain walls, and reversible rotation of domains [Wlod 06]. Figure A.11 shows a schematic plot of the magnetic induction versus magnetic field of a hysteretic, ferromagnetic sample.

BH-curve

The magnetization can be anisotropic resulting from the microscopical crystal orientation or macroscopical lamination of the material.

Anisotropy

In case of non-hysteretic materials, the magnetic permeability μ is defined by the relation between the magnetic induction \mathbf{B} and the magnetic field \mathbf{H} .

Non-hysteretic

$$\mathbf{B} = \mu \mathbf{H}, \quad [\mu] = 1 \text{ VsA}^{-1} \text{m}^{-1}. \quad (\text{A.31})$$

The relative permeability μ_r is given by the ratio of the permeability and the permeability of empty space, *i.e.* $\mu_0 = 4\pi \cdot 10^{-7} \text{ VsA}^{-1} \text{m}^{-1}$:

Relative permeability

$$\mu_r = \frac{\mu}{\mu_0}. \quad (\text{A.32})$$

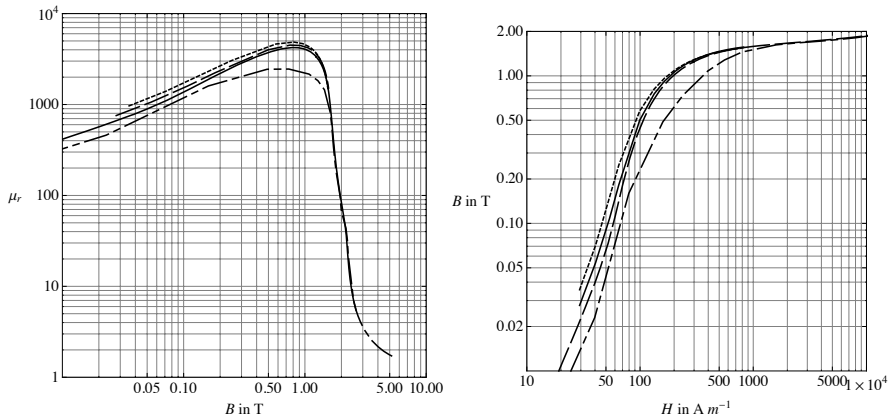


Figure A.12: Relative permeability μ_r as function of magnetic induction (left). Change of magnetic induction with magnetic field (right). The operating conditions are: No pressure at (full) 4.2 K, (dashed) 77 K, (dotted) ambient temperature, and at a pressure of 20 MPa and 4 K (dash-dotted).

A.1.6.1 Magnetic Iron

The iron used for yoke laminations in accelerator magnets needs to meet the following three requirements: Low coercitive force (for high permeability and low hysteresis losses), high resistivity at low temperature (for low induced eddy currents), and high saturation magnetization (reduction of the influence of the iron-nonlinearity) [Shch 04].

Modification For iron, the relative permeability increases with the purity of the material. Values of 7000 to 40,000 can be found while providing a saturation field strength of $B_s = 2.14$ T. Nevertheless impurities, *e.g.* silicium (Si), are introduced in order to increase the electrical resistivity (eddy currents) and narrow the hysteresis loop [Schn 73, p. 92].

LHC The iron used for the LHC lamination also consists of 0.02% nickel (Ni), 0.02% sulfur (S), 0.02% tin (Sn), and 0.01 % phosphorous (P). In [Shch 04] a large number of different magnetic steels have been measured and can be consulted for comparison. Furthermore, the 4-digit steel grade nomenclatura is explained briefly.

Measurements: Figure A.12 shows the BH-curve as well as the relative permeability for different operating conditions and different sources of measurement versus magnetic field respectively magnetic induction. It can be seen that the maximum relative permeability varies with temperature and applied pressure, but the saturation field, *i.e.* where the relative permeability starts to drop significantly, is nearly identical.

Analytical Formula: As shown in [Wlod 06] the magnetization of iron can be approximated analytically by means of the following function:

$$L\left(\frac{H}{a}\right) = \coth\left(\frac{H}{a}\right) - \left(\frac{a}{H}\right) \quad (\text{A.33})$$

$$M(H) = M_a L\left(\frac{H}{a}\right) + M_b \tanh\left(\frac{|H|}{b}\right) L\left(\frac{H}{b}\right) \quad (\text{A.34})$$

The parameters M_a and M_b denote the reversible and irreversible components of the saturation magnetization. The parameters a and b determine the rate of their approach to saturation. The sum of M_a and M_b equals the saturation magnetization M_s .

Figure A.13 shows the fit for a steel made by Cockerill and used at LHC for 4 K and zero applied stress. The fit parameters are:

$$\begin{aligned} M_a &= 3.711 \cdot 10^5 \text{ Am}^{-1}, & a &= 9.338 \cdot 10^4 \text{ Am}^{-1}, \\ M_b &= 1.370 \cdot 10^6 \text{ Am}^{-1}, & b &= 8.943 \cdot 10^1 \text{ Am}^{-1}, \end{aligned}$$

and $\mu_0 M_s = \mu_0 (M_a + M_b) = 2.188 \text{ T}$.

A.1.6.2 Other Materials

Table A.13 shows the magnetic properties of other materials used in accelerator magnets.

A.1.7 Dielectric Strength

Insulation material withstands electrical fields up to the so-called breakdown field strength or dielectric strength E_{bt} ($[E_{bt}] = \text{Vm}^{-1}$).

According to [Schn 73, pp. 82] it is distinguished between a fast, purely electrical breakdown, and a thermal breakdown. The electrical breakdown is caused by an electron avalanche. The thermal breakdown results from a current flowing through the insulation. The resulting temperature and conductivity increase causes a further increase of the insulation current. The thermal breakdown is more important for the design of accelerator magnets.

Electrical
and
thermal
breakdown

The thermal breakdown field decreases with temperature (exponentially) and insulation thickness d ($\propto 1/\sqrt{d}$). The values given in Tab. A.14 are based on the data published in [Schn 73, p. 84]. They shall serve only as a first orientation.

The breakdown strength of the insulation may vary if the magnet is cooled by liquid helium. Therefore the dielectric strength of helium, especially in the gaseous phase, has to be considered (see Sec. A.3.6).

A.1.8 Electrical Permittivity

The electrical permittivity ϵ_E is given by the relation between the dielectric displacement \mathbf{D} and the electrical field \mathbf{E} .

$$\mathbf{D} = \epsilon_E \mathbf{E}, \quad [\epsilon_E] = \text{AsV}^{-1}\text{m}^{-1}. \quad (\text{A.35})$$

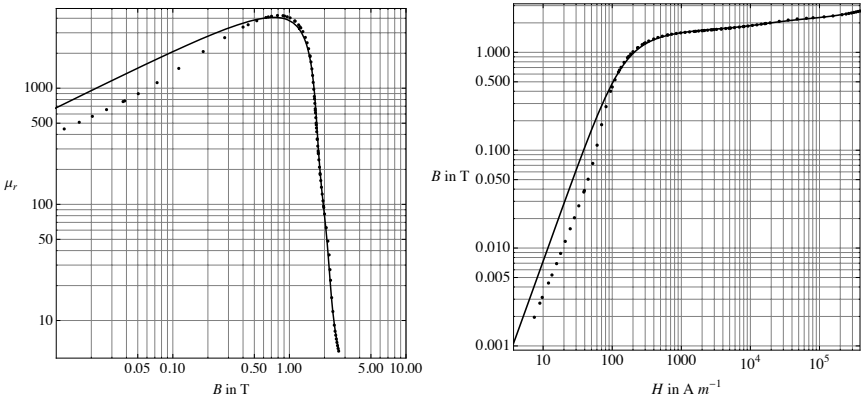


Figure A.13: Analytical μ_r - (left) and BH-curve (right) for the Peiro Steel at 4K with no stress.

Table A.13: Relative permeability of commonly used materials at room temperature and zero magnetic field

Element/Material	Symbol	μ_r	Comments
Iron	Fe	5000	[Henk 01, p. 162], see 1
Stainless steel	-	1.005	[Peir 04], see 2
Aluminum	Al	1.000017	[Henk 01, p. 162]
Copper	Cu	0.999991	[Henk 01, p. 162]

The relative permeability of Niobium, Titanium and Tantalum is in the same order of magnitude as of Aluminium. For Lead and Tin it is similar to Copper [Lide 06].

Remark 1: This value is stated for general, "back of the envelope" calculations not taking into account saturation. For more details see Sec. A.1.6.1.

Remark 2: The relative permeability of stainless steel decreases from 1.05 at nearly zero field to 1.005 at less than 2 T.

Table A.14: Breakdown field strength E_{bt} of common insulation materials [Schn 73, p. 84]

Material	E_{bt} in kVmm^{-1}			
$d =$	3 mm	1 mm	0.25 mm	0.1 mm
Polyimide (Kapton)	30	52	104	165
Epoxy	16-23	27-40	56-81	88-127
Polyester	15	26	53	83
PVC	30-40	52-70	104-140	165-220
Glass	80 at 77K [Seeb 98, p. 1055]			
polyvinyl acetate (PVA)	5-20 at 105 °C [Lin 95]			

The values in the first column ($d = 3 \text{ mm}$) are taken form [Schn 73, p. 84]. The values given for thinner insulation thickness are calculated by scaling by $\sqrt{3/d}$.

The relative permittivity ϵ_r is given by the ratio of the permittivity and the permittivity of empty space, *i.e.* $\epsilon_0 = 8.854 \cdot 10^{-12} \text{ AsV}^{-1}\text{m}^{-1}$;

relative
permittiv-
ity

$$\epsilon_r = \frac{\epsilon_E}{\epsilon_0}. \quad (\text{A.36})$$

A.1.8.1 Insulators

The relative electrical permittivity of Kapton (polyimide) at room temperature is in the order of 3-4 [DuPo 96]. For polyvinyl acetate (PVA) a value of 3.5 is given [Lide 06, p. 13-13].

A.2 Solids in Superconducting State

Below a certain temperature some materials exhibit superconductivity, *i.e.* the total loss of resistivity. The transition between normal and superconducting state is abrupt. The transition temperature is called critical temperature T_c .

Supercon-
ductivity

According to the critical temperature level, superconductors can be classified into low-temperature superconductors (LTS) and high-temperature superconductors (HTS). The distinction can be made by the necessary coolant, *i.e.* liquid helium for LTS and liquid nitrogen for HTS [Voll 02, p. 11]. The boiling temperatures of both gases can be found in Sec. A.3.1. In this text only LTS are considered.

LTS, HTS

Low-temperature superconductors are further distinguished by their behavior in an external magnetic field:

Different
types

Type I superconductors, *e.g.* elements as niobium and mercury, prevent any magnetic flux from penetrating. The interior of the superconductor is perfectly screened from any external field by surface currents. The screening disappears when the field exceeds the critical field level B_c and the superconductor transits to normal conducting state. As shown by MEISSNER and OCHSENFELD the screening does not depend on how the superconductor was exposed to the field, *i.e.* whether it was moved into a field or cooled down to superconducting state in a pre-existing field. Superconductors of type I can be considered perfect diamagnetics with fully reversible magnetization. The magnetization over applied field is shown in schematically in Fig. A.14 (left). Since superconductors of type I expel any magnetic field, they are not capable of carrying volumetric currents and thus cannot be used for superconducting cables and magnets [Voll 02, pp. 14].

Type I

Up to the lower critical field B_{c1} type II superconductors exhibit the same behavior as type I superconductors. Exceeding the lower critical field, flux starts to penetrate the superconductor in flux tubes. Flux tubes consist of a normal conducting center enclosed by supercurrents screening the residual superconductor from the penetrating flux. The flux inside the tube is quantized to

Type II

$$\Phi_0 = \frac{h_p}{2e_m} \approx 2.067 \cdot 10^{-15} \text{ Vs}, \quad (\text{A.37})$$

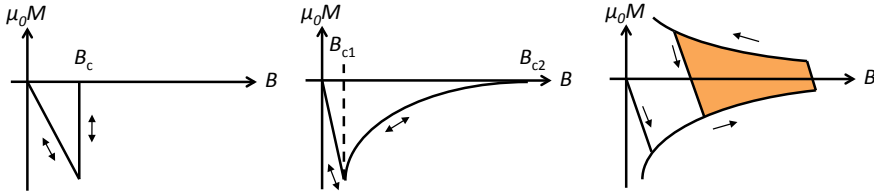


Figure A.14: Superconductor magnetization of type I (left) and type II (center), both fully reversible. Type II superconductor with pinning centers, so-called hard superconductors (right).

where h_p denotes the PLANCK constant and e_m is the elementary electrical charge (see Tab. E.1). As the external field increases, the number of flux tubes through the superconductor consequently rises. A repelling force acts between the flux tubes, moving them across the sample until their position reaches an energetic minimum. This state of partly penetrated magnetic field is called mixed-state. It persists up to the upper critical field B_{c2} ($B_{c1} \ll B_{c2}$) where the superconductor transits to the normal conducting state. The magnetization is fully reversible and field dependent (Fig. A.14 (center)).

Flux
motion

A current density is applied through the superconductor perpendicular to the external field. This results in a force on the flux tubes, perpendicular to both field and current density, and the flux tubes start to move out of the sample. Any motion of flux tubes causes heating in the superconductor and can cause it to quench. Furthermore, the applied current density requires a gradient of magnetic induction over the superconductor and therefore a gradient of flux tubes.

Flux
pinning

The free motion of the flux tubes is hampered by lattice imperfections and grain boundaries inside the microstructure of the superconductor. By introducing pinning centers, a counter-force is introduced and flux tubes can be pinned up to a certain field respectively current density level. If the external field is reduced again, the number of flux tubes would need to be decreased by moving flux tubes out of the sample. Since a large number is trapped in pinning centers, instead flux tubes of inverse orientation start to enter the sample. The magnetization now shows a hysteresis, see Fig. A.14 (right). Such superconductors are also denoted as hard superconductors.

Hard
supercon-
ductors

In this section, the conditions to exhibit superconductivity for different materials are listed. For the technical relevant low-temperature superconductors all material properties are given in the superconducting state.

A.2.1 Transition Temperature / Critical Field

Table A.15 shows the transition temperature T_{c0} at zero applied field and the critical field B_{c0} at zero temperature for some superconducting elements (type I) [Jens 80]. Furthermore, the upper critical field B_{c20} at zero temperature of the two commonly used type II superconductors is given.

It is important to note, that not only the alloy Nb-Ti and compound Nb₃Sn exhibit superconductivity, but also the elements they consist of as well as elements used for stabilization and improvement of the strands. Niobium in particular shows a rather high critical temperature and field.

For further information the common elements aluminum, lead and mercury are provided. Mercury was the first superconducting element discovered by ONNES[Buck 93].

A.2.2 Critical Current

The transition of a superconductor from superconducting to normal conducting state is not a step function, but a continuous transition [Clar 77]. Figure A.15 (left) shows the voltage-current-characteristic of a superconductor (VAC), *i.e.* the plot of the voltage over the superconductor versus applied current for fixed magnetic induction and bath temperature.

Voltage-current-characteristic (VAC)

From a certain current level upwards, the voltage starts to rise significantly and ohmic heating sets in. When the heating exceeds the heat removal by the coolant, the temperature of the strand starts to rise drastically and the sample quenches. This is called thermal run-away. The quench current level is denoted by I_q . It strongly depends on the measurement setup, especially on the cooling conditions, and can therefore not be used as universal characterization value for a superconductor [Clar 77].

For the characterization of superconductors and the definition of the superconducting state, 5 different criteria were suggested in [Bruz 04]. The current level, where

Criteria

- 1. the longitudinal electrical field equals E_c , *e.g.* 10^{-6} Vm^{-1} ,

Table A.15: Transition temperature and critical field of superconducting elements (type I) [Lide 06, p. 12-57] and the two technically applied hard superconductors Nb-Ti [Voll 02, p. 21] and Nb₃Sn [Devr 04, p. 44]

Element	Symbol	Transition temperature at zero field, T_{c0} in K	Critical magnetic induction at zero temperature, B_{c0} respectively B_{c20} in T
Aluminum	Al	1.175	0.0104
Mercury	Hg	4.154	0.0411
Niobium	Nb	9.25	0.2060
Lead	Pb	7.196	0.0803
Tin	Sn	3.722	0.0305
Tantalum	Ta	4.47	0.0829
Titanium	Ti	0.40	0.0056
Niobium-titanium	Nb-Ti	9.2	14.5
Niobium-3-tin (binary) ¹	Nb ₃ Sn	16	24
Niobium-3-tin (ternary) ¹	Nb ₃ Sn	18	28

¹ Binary Nb₃Sn consists only of Nb and Sn, while ternary Nb₃Sn contains one more substance, *e.g.* Ti or Ta for stabilization and performance improvement.

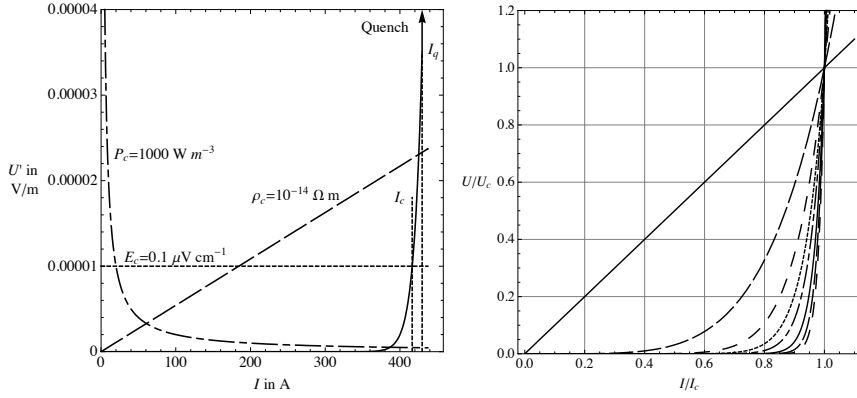


Figure A.15: (left) Voltage-current-curve for a strand of the LHC MB outer layer cable at 1.9 K and 9 T. The first three definitions for the critical current I_c are shown. Furthermore, a thermal run-away is illustrated by means of a vertical arrow. It can be seen that the quench current I_q is greater than the critical current. (right) Variation of the voltage over a superconductor depending on the n -value N_{sc} . The lines are for $N_{sc} = 1, 5, 10, 15, 20, 30, 40$, and 50 . Niobium-Titanium strands have a value of approximately 40, while Niobium-3-Tin strands show values between 10 and 20.

2. the resistivity onset equals ρ_c , *e.g.* $10^{-11} \Omega m$,
3. power per strand volume equals P_c , *e.g.* $10^3 W m^{-3}$,
4. the current equals the quench current (take-off point) I_q , or
5. the current equals linear down extrapolation of the slope before take-off point,

shall be denoted critical current I_c .

The first 3 were investigated earlier by CLARK and EKIN in [Clar 77]. It was demonstrated that even if all 3 criteria intersect at one point for a given temperature and applied magnetic induction, due to the nature of the VAC they differ at most other working points. Therefore, the resulting critical current strongly depends on the applied definition! The 4th criterium was already ruled out in the introduction to this section and the last criterium has been ruled out because not all superconductors reach a linear transition part before take-off [Bruz 04].

In the international standard of the CENELEC⁸ the critical current is defined as the maximum direct current that can be regarded as flowing without resistance [Supe 07a, p. 13]. The standard⁹ allows one to use either the critical electrical field criterion or the resistivity criterium. In the case of

⁸European committee for Electrotechnical Standardization, Brussels, Belgium

⁹The standard applies for Nb-Ti strands with $\lambda > 1$, $d_f > 1 \mu m$, $N_{SC} > 12$, $I_c|_{B=0.7B_{c20}} < 1000 A$, where λ denotes the copper to superconductor area ratio, d_f the filament diameter. For varying strands the standard has to be adapted [Supe 07a, p. 11].

the critical field criterium the current is measured for an electrical field of $E_{c1} = 1 \cdot 10^{-5} \text{ Vm}^{-1}$ and $E_{c2} = 1 \cdot 10^{-4} \text{ Vm}^{-1}$. For the resistivity criterium levels of $\rho_{c1} = 1 \cdot 10^{-14} \Omega\text{m}$ and $\rho_{c2} = 1 \cdot 10^{-13} \Omega\text{m}$ are applied, where the resistivity refers to the resistivity of the total strand cross-section [Supe 07a, pp. 25].

Throughout this work, the electrical field criterion is used for calculations. The critical current I_c is defined as the current level where the longitudinal electrical field over the sample reaches 10^{-5} Vm^{-1} .

Applied
definition

The applied levels for critical electrical field as well as resistivity vary among different sources. Sources and values are given in Tab. A.16 for comparison.

Variety in
Literature

A.2.3 The n-Index

Following WILSON¹⁰ [Walt 74, p. 30], the voltage-current-characteristic (VAC) can be fitted by an exponential function

$$\frac{U}{\ell} = E_c \left(\frac{I}{I_c} \right)^{N_{SC}} \quad (\text{A.38})$$

where U/ℓ denotes the voltage per sample length ℓ , I_c and E_c the above defined values and N_{SC} a fit parameter. Equation (A.38) is shown in Fig. A.15 (right) for different values of N_{SC} . According to the CENELEC standard, the fit is performed close to the critical current or between the two electrical field levels E_{c1} and E_{c2} [Supe 07a, p. 27].

The exponent N_{SC} is usually denoted as the "n-index" or quality index. This is due to the fact that the n-index increases with the quality of production, *i.e.* filament size distribution and filament distortion [Devr 04, p. 43]. The n-index also depends on applied magnetic induction [Warn 86] and temperature [Devr 04, p. 43].

Quality
index

Within this work, for Niobium-Titanium an n-index of $N_{SC, \text{Nb-Ti}} = 40$ and for Niobium-3-Tin of $N_{SC, \text{Nb3Sn}} = 20$ are used [Verw 08b]. Note that the critical current and n-index of a strand can be degraded by mechanical strain,

¹⁰Most authors refer to the informal report of WALTER for the introduction of the n-index.

In the report, WALTER quotes unpublished work of WILSON giving correct reference. Therefore, we cite WALTER's report while rightfully referring to WILSON.

Table A.16: Different limits for the critical current I_c from common literature

Source	E_c in Vm^{-1}	ρ_c in Ωm^{-1}
Bruzzone [Bruz 04]	$1 \cdot 10^{-6}$	10^{-11}
Boutboul [Bout 01]	—	10^{-14}
Clark [Clar 77]	$3 \cdot 10^{-4}$	10^{-13}
Devred [Devr 04, p. 41]	$1 \cdot 10^{-5}$	10^{-14}
CENELEC [Supe 07a]	$1 \cdot 10^{-5}$	10^{-14}
	$1 \cdot 10^{-4}$	10^{-13}

e.g. bending and rolling. Therefore, the n -index of a complete Rutherford-type cable can be significantly smaller (around $\approx 30\%$ in case of LHC MB) than of the strands before cabling [Verw 07a].

Alternative
expression

Alternatively to the fit by WALTER a full field and temperature exponential approach was published by DOROFJEV [Doro 80]:

$$E = J\rho_n \exp\left(\frac{T - T_c}{T_0} + \frac{B}{B_0} + \frac{J}{J_0}\right). \quad (\text{A.39})$$

A.2.4 Critical Current Density

As previously mentioned, the critical current I_c depends on the applied magnetic induction B and temperature T . In the space of these three quantities, the limit between normal conducting state and superconducting state constitutes a surface. Instead of the critical current, most commonly the critical current density J_c is used. The critical surface is thus given by $J_c(B, T)$.

Critical
surface

The critical current density can be obtained in two different ways: Either from the critical current or from the magnetization measurement. In the first case the critical current is converted into the critical current density under certain assumptions on the current distribution and influence of the conductor self-field¹¹ [Bout 06]. In the second case, the measured magnetic moment is first converted into a magnetization density, and then into a current density based on the assumption of a local current density distribution [Wils 83, pp. 243]. It should be noted that this approach strongly relies on the underlying model assumption for the superconductor magnetization (Sec. D.3).

Limitations

Both approaches suffer from some inherent and external limitations. For the critical current measurement, the influence of the self-field on the measurement increases with current. The temperature can be stabilized very accurately up to the boiling point of liquid helium. Beyond that point the sample needs to be thermally stabilized by a heated and thermally controlled sample holder [Wils 83, p. 249]. A lower temperature limit is given by the increasing effort in refrigeration power. For the LHC, the maximum magnetic induction is limited to 1.5 T in the magnetization measurement station [Le N 01] and to 11 T in the critical current measurements station [Bout 01]. For the critical current measurement, the maximum current is limited to 1000 A [Bout 01]. Figure A.16 shows the limitations to either measurement method. The critical current density is only accessible in two disconnected patches!

Parameter-
ization

In order to overcome this limitation, GREEN presented in [Gree 88] a method to predict the critical current density based only on the critical field, temperature, and one measured value for J_c . With a mathematical function representing all underlying physical effects limiting the current density in a superconductor, the critical current density could be parametrized by means

¹¹ The CENELEC standard strongly encourages not to apply any self-field compensation to the measurement results in order to allow an inter-laboratory comparison. In case it is nevertheless necessary, a very simple approach with the field of a straight line current is recommended [Supe 07a, Appendix B].

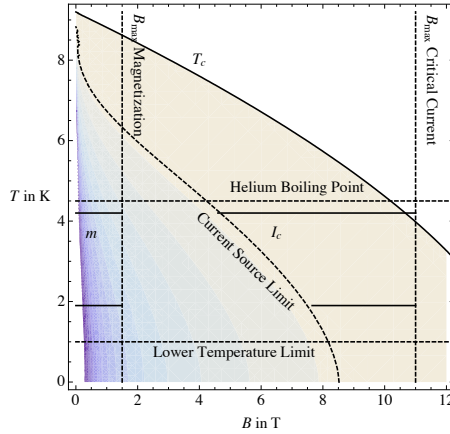


Figure A.16: Critical current density measurement limitations. All limits are plotted with dashed lines, leaving two disconnected patches where measurements can be performed. The full lines highlight where extensive measurement took place for the LHC. Remark: The current source limit is given by the intersection of the critical surface (shading) with the maximum current density and therefore curved line.

of a few fitting parameters¹². This function is called the critical surface parameterization.

A.2.5 Critical Surface Parameterization

A.2.5.1 Niobium-Titanium

In [Bott 00] BOTTURA published a parameterization for the critical current density as a function of the applied magnetic induction B , local temperature T and reference current density, J_{ref} . The function relies on the four fit parameters α , β , γ and C_0 :

$$J_c(B, T) = J_{\text{ref}} \frac{C_0}{B} \left(\frac{B}{B_{c2}(T)} \right)^\alpha \left(1 - \frac{B}{B_{c2}(T)} \right)^\beta \left(1 - \left(\frac{T}{T_{c0}} \right)^n \right)^\gamma \quad (\text{A.40})$$

where T_{c0} denotes the upper critical temperature for zero field. $B_{c2}(T)$ is given by:

$$B_{c2}(T) = B_{c20} \left(1 - \left(\frac{T}{T_{c0}} \right)^n \right) \quad (\text{A.41})$$

Here B_{c20} denotes the upper critical field at zero temperature. The parameter range was given to α between 0.5 and 0.8, β around 1, and γ in the range of 2.

¹² This approach can be illustrated by the following example. Basic NEWTON's physics teaches: The trajectory of a falling object with a horizontal velocity greater than zero, follows a parabola. Knowing the shape of the trajectory, the position of the object can be predicted based on the position of the apex and any second point.

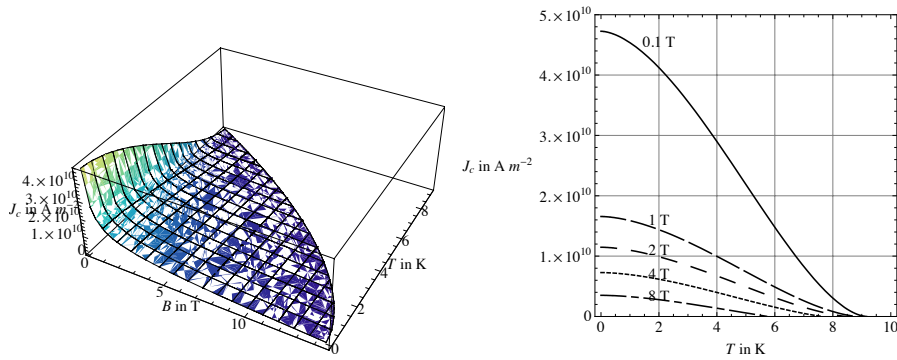


Figure A.17: Critical current density of Niobium-Titanium after [Bott 00] and [Voll 02]. (left) Critical surface of Nb-Ti. (right) Critical current density versus temperature for different values of magnetic induction.

For high fields, the critical current density is mainly influenced by the value for the parameter β . As pointed out in [Schw 06], the nature of the function changes from parabolic to root-like according to β greater or smaller than 1.

As shown in [Ekin 81], the strain dependence of Nb-Ti is very small and is thus neglected.

The parameters are taken from [Voll 02] and can be found in Tab. A.17. The critical surface of Nb-Ti is shown in Fig. A.17.

A.2.5.2 Niobium-3-Tin

The parameterization presented by SUMMERS in [Summ 91] allows the prediction of the critical current density of Nb_3Sn as a function of field, temperature, strain and radiation damage, and relies on one fit parameter only: C_0 .

Table A.17: Fit parameters for the critical current density

Parameter	Value	Unit
B_{c20}	14.5	T
T_{c0}	9.2	K
J_{ref}	$3 \cdot 10^9$	A m^{-2}
C_0	27.04	T
α	0.57	—
β	0.9	—
γ	2.32	—
n	1.7	—

The critical current density J_c is given by

$$J_c(B, T, \varepsilon) = \frac{C_{\text{Nb}_3\text{Sn}}(\varepsilon)}{\sqrt{B}} \left(1 - \frac{B}{B_{c2}(T, \varepsilon)}\right)^2 \left(1 - \left(\frac{T}{T_{c0}(\varepsilon)}\right)^2\right)^2 \quad (\text{A.42})$$

where B denotes the applied magnetic induction, T denotes the temperature and ε denotes the compression of the superconductor.

The constant $C_{\text{Nb}_3\text{Sn}}(\varepsilon)$ consists of the free fit parameter C_0 and a strain depending term.

$$C_{\text{Nb}_3\text{Sn}}(\varepsilon) = C_0 \left(1 - \alpha |\varepsilon|^{1.7}\right)^{0.5}.$$

The constant α is given by Summers to 900 for compressive ($\varepsilon < 0$) and to 1250 for tensile ($\varepsilon > 0$) stress.

The upper critical field B_{c2} is given by

$$\frac{B_{c2}(T, \varepsilon)}{B_{c20}(\varepsilon)} = \left(1 - \left(\frac{T}{T_{c0}(\varepsilon)}\right)^2\right) \left[1 - 0.31 \left(\frac{T}{T_{c0}(\varepsilon)}\right)^2 \left(1 - 1.77 \ln \left(\frac{T}{T_{c0}(\varepsilon)}\right)\right)\right]$$

where the upper critical field due to strain $B_{c20}(\varepsilon)$ is given to

$$B_{c20}(\varepsilon) = B_{c20m} \left(1 - \alpha |\varepsilon|^{1.7}\right),$$

and B_{c20m} denotes the upper critical field at zero temperature and strain.

The upper critical temperature T_{c0} for zero intrinsic strain is given by

$$T_{c0}(\varepsilon) = T_{c0m} \left(1 - \alpha |\varepsilon|^{1.7}\right)^{1/3} \quad (\text{A.43})$$

where T_{c0m} denotes the upper critical temperature at zero field and zero stress.

The constants B_{c20m} and T_{c0m} depend on the number of materials in the alloy, *i.e.* whether only Nb and Sn are used or Ta respectively Ti are added for stabilization. The constants are given in [Devr 04, p. 44] to 24 K and 16 K for binary and 28 T and 18 K for ternary compounds.

For the powder-in-tube (PIT) strand developed at the university of Twente [Oude 01] for the Next-European-Dipole (NED) project [Devr 06] the critical current density has been fitted in [Schw 05b, Appendix] using the above function. With ε given to -0.0025 [Devr 04] and

$$\begin{aligned} B_{c20}(-0.0025) &= 23.97 \text{ T}, \\ T_{c20}(-0.0025) &= 17.79 \text{ K}, \end{aligned}$$

the fit is performed by means of the Mathematica function `NonlinearFit` and yields the constant

$$C_0 = 52.05 \cdot 10^3 \text{ T}^{1/2} \text{ Am}^{-2}.$$

The deviation from the measured magnetization is in the order of 25%.

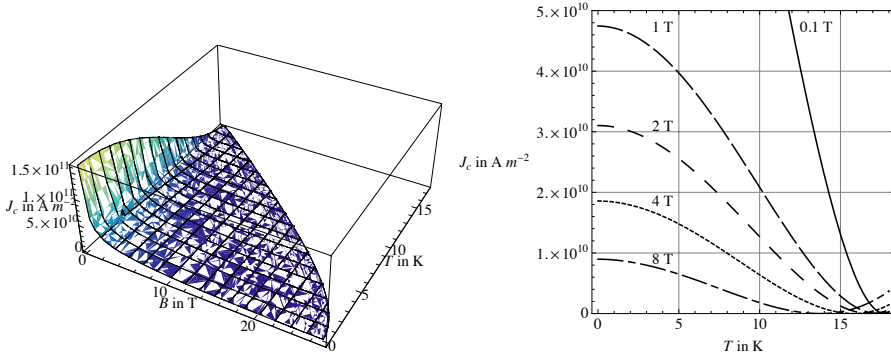


Figure A.18: Critical current density of Niobium-3-Tin after [Summ 91] and [Schw 05b]. (left) Critical surface. (right) Critical current density versus temperature for different values of magnetic induction.

A.2.6 Electrical Resistivity

As seen in Sec. A.2.2 the electrical field rises sharply across a superconductor when the current density approaches the critical current density. Equation (A.38) can be transformed to express the resistivity of the superconductor, ρ_{SC} , during the transition

$$\rho_{SC}(B, J, T) = E_c \frac{J^{N_{SC}-1}}{J_c(B, T)^{N_{SC}}}. \quad (\text{A.44})$$

Figure A.19 shows the resistivity of Nb-Ti and Nb₃Sn versus temperature and magnetic induction for different transport current densities.

A.2.7 Thermal Conductivity

Data on the thermal conductivity of superconducting materials is very scarce. In [Kim 00] KIM suggests an extrapolation of data from the normal conducting state to the superconducting state. Even though electrical superconducting, thermally the heat conduction remains limited.

A.2.8 Heat Capacity

The volumetric specific heat for type II superconductors is given in [Dres 95, p. 22] to

$$c_{SC}(T, B) = \begin{cases} \left(\beta + 3 \frac{\gamma}{T_{c0}^2} \right) T^3 + T \frac{B}{B_{c20}} & T < T_{\text{phonon}} \\ c_{NC}(T) + 3 \frac{\gamma T^3}{T_{c0}^2} - \gamma T + \gamma + T \frac{B}{B_{c20}} & T > T_{\text{phonon}} \end{cases}. \quad (\text{A.45})$$

Here, c_{NC} denotes the specific heat in the normal conducting state, and β and γ are fit constants. The temperature T_{phonon} denotes the limit up to which the specific heat is proportional to T^3 .

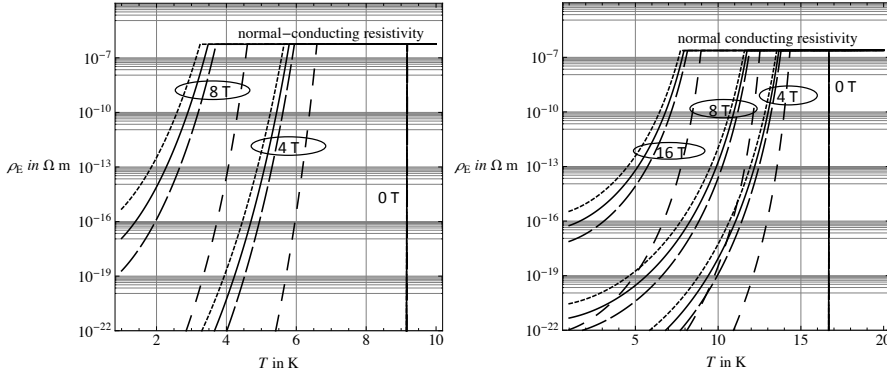


Figure A.19: Resistivity of Nb-Ti (left) and Nb₃Sn (right) in superconducting state versus temperature for different field levels. The current density is varied between 0.5 and 1.1 of the design critical current density. The design critical current density for Nb-Ti is $J_c(8.4 \text{ T}, 1.9 \text{ K}) = 2.6 \cdot 10^9 \text{ Am}^{-2}$ and for Nb₃Sn $J_c(15 \text{ T}, 4.2 \text{ K}) = 1.4 \cdot 10^9 \text{ Am}^{-2}$: (dotted) $J = 1.1 J_c$, (full) $J = 1.0 J_c$, (densely dashed) $J = 0.9 J_c$, and (dashed) $J = 0.5 J_c$.

It can be seen from the formula, that the specific heat in the superconducting state increases with applied magnetic induction. For $T > T_{\text{phonon}}$ it is greater than in the normal conducting state. Below that limit it can be smaller.

When exceeding the critical temperature for an applied magnetic induction, $T_c(B)$, the specific heat drops down to the specific heat in the normal conducting state. This drop is typical for phase transitions without latent heat [Dres 95, p. 22].

A.2.8.1 Niobium-Titanium

In the superconducting state, the volumetric specific heat $c_{\text{th,Nb-Ti}}$ of Nb-Ti depends on the temperature and on the applied magnetic induction. In the normal conducting state the heat capacity depends only on the temperature [Verw 05]. Therefore, two separate fits to measurement are given: One for temperatures above the critical temperature $T_c(J, B)$ shown in Eq. (A.27), and one for below in thus superconducting state:

$$c_{\text{T,Nb-Ti}}(T, B) = c_0(aT^3 + cTB), \quad (\text{A.46})$$

with $c_0 = \text{JK}^{-1}\text{m}^{-3}$, $a = 49.1 \text{ K}^{-3}$ and $c = 64 \text{ K}^{-1}\text{T}^{-1}$. The critical temperature depends on the applied field and the current density in the superconductor. The specific heat is shown in Fig. A.20 (left).

A.2.8.2 Niobium-3-Tin

In [Kim 00, p. 5] the volumetric specific heat of Nb₃Sn is given to

$$c_{\text{T,Nb}_3\text{Sn}}(T) = aT^3 + b, \quad (\text{A.47})$$

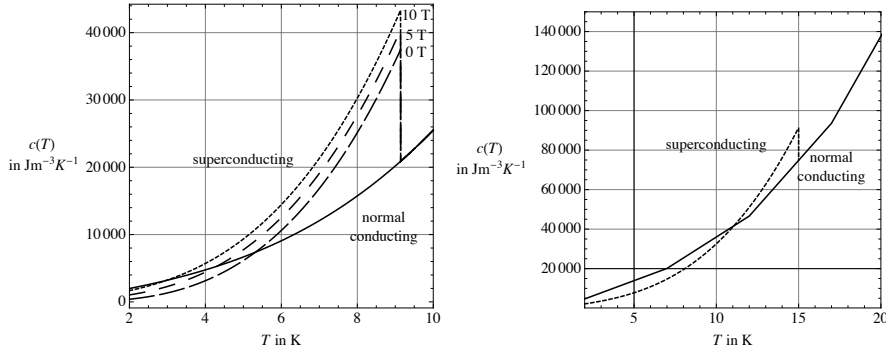


Figure A.20: Volumetric specific heat in superconducting state. The transition is discontinuous when the critical temperature is reached. (left) Nb-Ti [Verw 05]. The specific heat is plotted for different applied magnetic induction. The transition is shown exemplarily for the maximum temperature $T = 9.14$ K, but would happen in the same way for any lower temperature. (right) Nb₃Sn after [Kim 00] in superconducting state and after [Baue 07, p. 4-13] in normal conducting state.

with the constants $a = 22.68 \text{ Jm}^{-3}\text{K}^{-4}$ and $b = 988.2 \text{ Jm}^{-3}\text{K}^{-1}$. Contrary to the general formula (A.45) this function does not show any dependence on magnetic induction.

A.2.9 Permeability

Type I superconductors expel any external magnetic induction up to the critical field B_{c1} . Therefore they can be considered as perfect diamagnetics.

In type II superconductors the interior is partially screened from the external field while it also penetrates in form of flux tubes. The flux tubes are trapped by so-called pinning centers preventing free movement. Therefore type II superconductors show a hysteretic diamagnetic magnetization.

The magnetization is not expressed by means of a relative permeability constant (as for magnetic iron), but by macroscopical models as in [Voll 02] for type II superconductors.

A.3 Fluid/Gaseous Matter - Helium Properties

Helium
⁴He

For the application of low temperature superconducting magnets the only available coolant is liquid helium¹³. Here, it is referred to helium-4 (⁴He), *i.e.* helium atoms with 2 neutrons, in comparison to the much rarer helium-3.

Apart from the coolant, all other materials are solid. Therefore this section addresses only properties of helium. Other gases or liquids are quoted

¹³Hydrogen is in liquid state between 14.01 K (melting point) and 20.28 K (boiling point). Within that temperature range it could be used as a coolant, but comes with certain general disadvantages as, *e.g.*, being highly explosive.

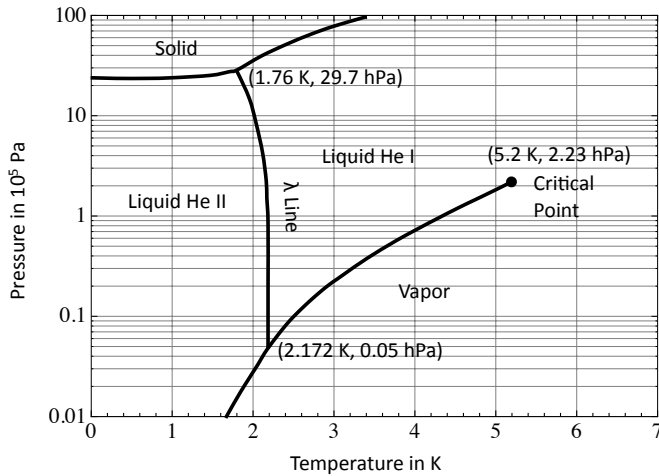


Figure A.21: Phase diagram of helium (^4He) following [Van 86, p. 55].

occasionally to give a comparison.

A.3.1 Temperature Levels / Phases

Figure A.21 shows the phase diagram of helium-4. Helium features a gaseous, a solid and two liquid phases. The liquid phases separate the gaseous and the solid state in the phase diagram. The two liquid phases are denoted normal liquid helium or helium I (He I) and superfluid helium or helium II (He II). They are separated by the vertical λ -line, *i.e.* the temperature of the lambda-transition $T_\lambda(p)$ as a function of pressure p . The λ -line spans from the lower triple-point (gaseous) at (2.172 K, $5 \cdot 10^3 \text{ Pa}$) to the upper triple-point (solid) at (1.76 K, $2.97 \cdot 10^6 \text{ Pa}$). The critical point of the transition between He I and the supercritical helium is at (5.2 K, $2.23 \cdot 10^5 \text{ Pa}$).

Phases

The transport properties of He II are very different to those of normal liquids featuring very low viscosity and extremely high heat conductivity [Van 86, p. 90].

He II

Table A.18 shows the boiling points of different gases for comparison.

A.3.2 Density

The density of helium is a function of temperature and pressure. For increasing temperature the density starts to decrease and drops by nearly an order of magnitude at evaporation. The evaporation temperature increases with increasing pressure. For a confined volume of liquid helium, the pressure and temperature rise simultaneously when subjected to heating.

Saving the effort of modeling the helium liquid/gas transition and a full model of the pressure distribution inside a magnet, certain assumption can be

Simplified model

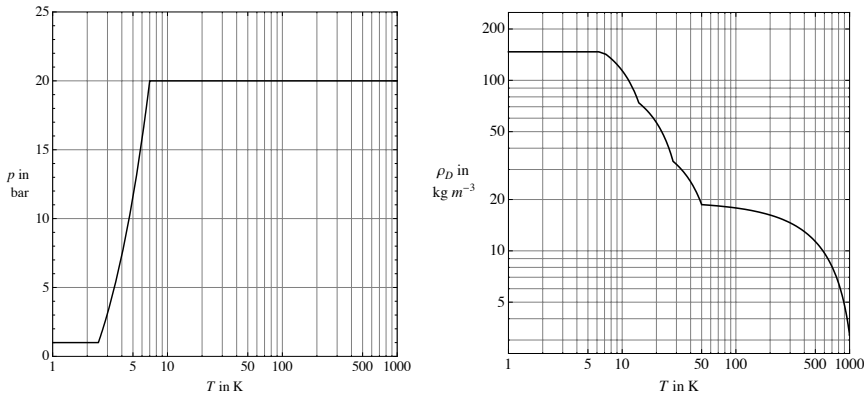


Figure A.22: (left) Assumption of the pressure rise over temperature. (right) Resulting piece-wise linear approximation of the density of helium versus temperature.

made. After passing the λ -point, the pressure rises linearly with temperature from the operating pressure to the maximum pressure in the magnet vessel given by the pressure release valve (*e.g.* 20 bar). From approximately 6 K onwards, the pressure stays constant for the rest of the quench process. The assumed pressure rise is shown in Fig. A.22 (left). This approach is in good agreement with the experiences gained at the LHC prototype magnet string [Chor 98].

Combining the helium property tables for constant pressure in [Van 86, Appendix 2] results in an approximated helium mass density versus temperature as shown in Fig. A.22 (right).

A.3.3 Latent Heat

The latent heat denotes the amount of energy released or absorbed by a substance during the change of state or phase. The transition from helium I to gaseous helium requires around $2 \cdot 10^4 \text{ J kg}^{-1}$ up to a temperature of 4.5 K, and then drops to zero at around 5 K [Van 86, p. 65]. In [Iwas 94, p. 112] 2.6 J cm^{-3} are given. Table A.19 shows the latent heat or enthalpy of

Table A.18: Boiling point of different gases (at room temperature) at normal pressure [Rade 02]

Material	Symbol	Boiling point in K
Oxygen	O ₂	90.2
Nitrogen	N ₂	77.4
Hydrogen	H ₂	20.3
Helium	He	4.22

vaporization of other common gases and liquids.

The phase transition of He II to He I is considered of second order and has no heat of transformation [Van 86, p. 91].

A.3.4 Heat Conductivity

The thermal conductivity of helium II is orders of magnitude greater than of other liquids and even of highly conducting metals as copper [Van 86, pp. 94]. In [Iwas 94, p. 116] a value of approximately $100 \text{ kWm}^{-1}\text{K}^{-1}$ is given. This is 10 to 100 times more than the heat conductivity of copper (see Sec. A.1.4.1) and 100,000 times more than of water under standard conditions.

The thermal conductivity of helium II is considered as perfect, *i.e.* without any temperature gradient, but limited to a maximum heat flux. Exceeding the lambda point or the critical flux He II transits to He I with very low heat conductivity - this can be compared to the quenching of superconducting material [Iwas 94, p. 117]. The heat conductivity of helium I is only $0.02 \text{ Wm}^{-1}\text{K}^{-1}$ [Iwas 94, p. 116].

A.3.5 Volumetric Specific Heat

Based on the pressure assumption in Sec. A.3.2 the specific heat (for constant volume) can be taken from [Van 86, Appendix 2] as shown in Fig. A.23 (left). The specific heat shows a peak at the λ -point, drops after transition and rises to an approximately constant value after evaporation.

Combining the mass density of Sec. A.3.2 with the specific heat yields the volumetric specific heat. Figure A.23 (right) shows the decrease of specific heat due to the drop of density.

A.3.6 Dielectric Strength

Considering an electrical field over a gas filled void, free electrons are accelerated. Collisions with neutral atoms or molecules ionize the gas and create further free electrons. At a certain field level, the electrons gain enough energy between two successive collisions to cause further ionization: TOWNSEND avalanche breakdown [Cobi 41, p. 145].

Breakdown
in gases

The number of ionizing collisions depends on the free path length of the electrons and their kinetic energy. Thus the electrical breakdown field depends

Paschen's
law

Table A.19: Heat or Enthalpy of Vaporization [Lide 06, pp. 6-94]

Material	Symbol	H_v in Jkg^{-1}
Helium	He	$2.1 \cdot 10^4$
Hydrogen	H_2	$4.55 \cdot 10^5$
Nitrogen	N_2	$2 \cdot 10^5$
Water	H_2O	$2.26 \cdot 10^6$

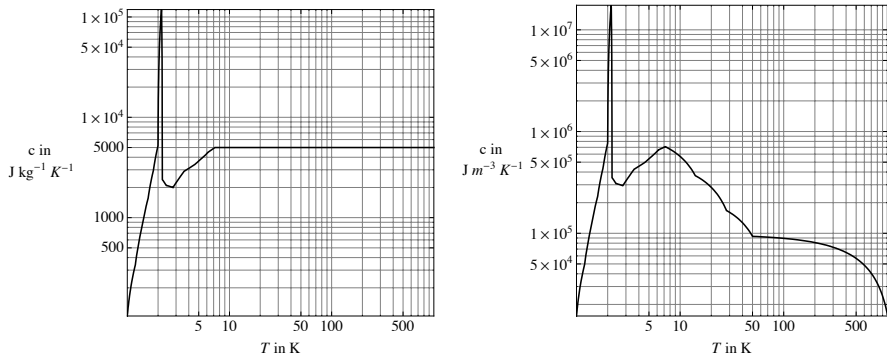


Figure A.23: Approximation of the thermal properties of helium with varying pressure. (left) Specific heat of helium. (right) Volumetric specific heat.

on the distance between the two electrodes, as well as the density of the gas (or the pressure). Plotted over the product of pressure and distance the electrical breakdown voltage shows a minimum for each gas at characteristic value: PASCHEN's law [Cobi 41, pp. 162].

Helium For helium at ambient temperature the minimum break down voltage is 156 V at a pressure distance product of 5.33 Pa m. In the field of superconducting magnets with distances of approximately 0.2 mm between two conductors and 1 mm between two layers, the pressure with minimum breakdown voltage is given to 0.25 bar and 50 mbar, respectively. Operating the device with pressurised helium II reduces the risk of an electric breakdown [Lebr 97].

Air For comparison the values for air are 327 V and 0.76 Pa m [Cobi 41, p. 165].

B Parameters

The Devil is in the details, but so is salvation.

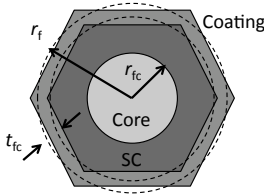
HYMAN G. RICKOVER
(1900-1986)

B.1 Geometrical Quantities

B.1.1 Filament

Most basically, a filament of a superconductor consists of the superconducting material and is of circular cross-section. For the stacking process of the superconducting strands hexagonal filaments are used as well. The cross-sectional area is approximated by a circle.

While this basic model holds well for common Nb-Ti filaments, Nb₃Sn filaments feature more details. Here, the superconducting fraction is produced by a thermal diffusion process of niobium and tin resulting in unreacted fractions of these materials, as well as diffusion barriers to protect the surrounding matrix material from pollution. Therefore, the filament cross-section $A_{\text{fil,tot}}$ consists of at least 3 fractions, *i.e.* the core $A_{\text{fil,core}}$, the superconducting tube $A_{\text{fil,sc}}$ and a coating $A_{\text{fil,coat}}$.



$$A_{\text{fil,tot}} = \pi r_f^2 \quad (\text{B.1})$$

$$A_{\text{fil,core}} = \pi r_{\text{fc}}^2 \quad (\text{B.2})$$

$$A_{\text{fil,coat}} = \pi (2r_f t_{\text{fc}} + t_{\text{fc}}^2) \approx 2\pi r_f t_{\text{fc}} \quad (\text{B.3})$$

$$\begin{aligned} A_{\text{fil,sc}} &= A_{\text{fil,tot}} - A_{\text{fil,coat}} - A_{\text{fil,core}} \\ &= \pi (r_f^2 - (2r_f t_{\text{fc}} + t_{\text{fc}}^2) - r_{\text{fc}}^2) \end{aligned} \quad (\text{B.4})$$

For even more complex filaments or different reaction processes, more shells would need to be considered.

B.1.2 Strand

The superconducting filaments are embedded in a matrix of normal conducting material, *e.g.* copper or aluminum. During extrusion the strand is twisted

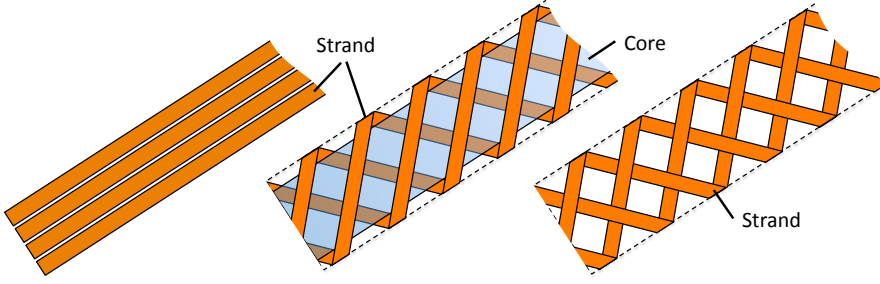
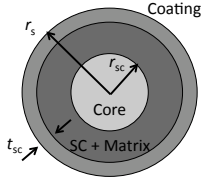


Figure B.1: Different cable types. (left) Ribbon-type cable with glued strands. (center) Rutherford-type cable with metal core. (right) Braided strands.

along its axis, to minimize the loop surface area spanned by the filaments inside. Most often no filament is placed in the strand center, since it would not be twisted, leaving a normal conducting core. For insulation purposes between neighboring strands, the strands may be coated.

Apart from the filaments described above, the strand cross-section features a core $A_{\text{str,core}}$, a matrix $A_{\text{str,mat}}$ and a coating $A_{\text{str,coat}}$ (maybe even more than one layer).



$$A_{\text{str,tot}} = \pi r_s^2 \quad (\text{B.5})$$

$$A_{\text{str,core}} = \pi r_{\text{sc}}^2 \quad (\text{B.6})$$

$$A_{\text{str,coat}} = \pi (2r_s t_{\text{fc}} + t_{\text{sc}}^2) \approx 2\pi r_s t_{\text{sc}} \quad (\text{B.7})$$

$$\begin{aligned} A_{\text{str,inner}} &= A_{\text{str,tot}} - A_{\text{str,coat}} - A_{\text{str,core}} \\ &= \pi (r_s^2 - (2r_s t_{\text{sc}} + t_{\text{sc}}^2) - r_{\text{sc}}^2) \end{aligned} \quad (\text{B.8})$$

$$A_{\text{str,fil}} = N_f A_{\text{fil,tot}} \quad (\text{B.9})$$

$$A_{\text{str,mat}} = A_{\text{str,inner}} - A_{\text{str,fil}} \quad (\text{B.10})$$

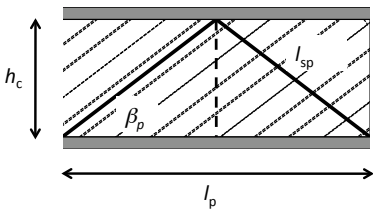
If the materials used for core, matrix and coating are identical and the filaments only consist of the superconducting material, the area fractions by material can be easily calculated by the copper to superconductor area ratio (see Sec. B.2.1).

B.1.3 Cable

Three different kinds of cables can be distinguished: Rutherford-type cables, ribbon-type cables and braided cables, see Fig. B.1.

Rutherford-type cables consist of a number of strands, twisted along the axis of the cable and rolled in a rectangular or trapezoidal form. The center of the cable may contain a core in order to increase the electrical resistance between crossing strands. The cable is insulated by multiple wraps of insulation tape, and/or may further be potted with a resin.

The transposition of the strands along the cable axis has the following implications: The current follows a zig-zag path along the cable, resulting in a small longitudinal field component (see Sec. 7.8) and a higher resistivity per length [Imba 03, p. 3-22], *i.e.* $\ell_{sp} > \ell_p/2$. In the cross-section of the cable, the cross-section of the strands is of elliptical shape. The volume covered by the strands can be calculated by means of the formulas given in Sec. D.2.



Cable Top View

$$\ell_{sp} = \sqrt{\left(\frac{\ell_p}{2}\right)^2 + h_c^2} \quad (B.11)$$

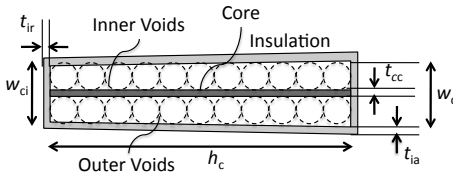
$$\beta_p = \arccos\left(\frac{\ell_p/2}{\ell_{sp}}\right)$$

$$= \arctan\left(\frac{h_c}{\ell_p/2}\right) \quad (B.12)$$

$$A_{str,ell} = \frac{A_{str,tot} \ell_{sp}}{\ell_p/2} = \frac{A_{str,tot}}{\cos(\beta_p)} \quad (B.13)$$

Between the strands, as well as between strands and the insulation, voids remain. The confined volume in between four circles with radius a can be easily derived to $(4 - \pi)a^2$. Depending on the compression and the key-stoning of the cable the voids might be smaller than estimated above, and especially not evenly distributed over the cable width. The first disadvantage is overcome by introducing two dimensionless tuning coefficients, $k_{cab,void,inner}$ and $k_{cab,void,outer}$. For a thermal model with homogeneous temperature distribution over the cable cross-section (see Sec. 3.6), the local distribution of the voids can be neglected, if the total void volume is modeled correctly.

The effective cable cross-sectional area A_{cab}^{eff} consists of a core $A_{cab,core}$, the elliptically cut strands $A_{cab,str}$, the inner and outer voids, $A_{void,inner}$ and $A_{void,outer}$, as well as the insulation A_{ins} .



$$A_{cab,xs} = \frac{w_{ci} + w_{co}}{2} h_c \quad (B.14)$$

$$A_{cab,str} = N_s A_{str,ell}$$

$$= \frac{N_s A_{str,tot}}{\cos(\beta_p)} \quad (B.15)$$

$$A_{cab,core} = h_c t_{cc} \quad (B.16)$$

$$A_{void,inner} = k_{cab,void,inner} \frac{(4 - \pi) (N_s/2 - 1)}{\cos(\beta_p)} \quad (B.17)$$

$$A_{\text{void,outer}} = k_{\text{cab,void,outer}} \left(A_{\text{cab,xs}} - A_{\text{cab,str}} - A_{\text{cab,core}} - A_{\text{void,inner}} \right) \quad (\text{B.18})$$

$$A_{\text{ins}} \approx (w_{\text{ci}} + w_{\text{co}})t_{\text{ia}} + 2h_{\text{c}}t_{\text{ir}} + 4t_{\text{ia}}t_{\text{ir}} \quad (\text{B.19})$$

$$A_{\text{cab}}^{\text{eff}} = A_{\text{cab,str}} + A_{\text{cab,core}} + A_{\text{void,inner}} + A_{\text{void,outer}} + A_{\text{ins}} \quad (\text{B.20})$$

This approach neglects the length of the strand changing between two layers in the cable edges. Note that neglecting the twist pitch results in an error of $1/\cos(\beta_{\text{p}})$ for the calculated longitudinal lengths and cross-sectional areas.

The superconducting as well as the normal conducting surface area perpendicular to the current are given by (using the geometrical ratios λ and η from Sec. B.2.1),

$$A_{\text{cab,SC}} = N_{\text{s}}N_{\text{f}}A_{\text{fil,SC}} = N_{\text{s}}\pi r_{\text{s}}^2\eta_{\text{SC}}^A = N_{\text{s}}\pi r_{\text{s}}^2\frac{1}{1+\lambda} \quad (\text{B.21})$$

$$\begin{aligned} A_{\text{cab,NC}} &= N_{\text{s}} \left(A_{\text{str,tot}} - N_{\text{f}}A_{\text{fil,SC}} \right) \\ &= N_{\text{s}}\pi r_{\text{s}}^2\eta_{\text{NC}}^A = N_{\text{s}}\pi r_{\text{s}}^2\frac{\lambda}{1+\lambda} \end{aligned} \quad (\text{B.22})$$

Due to the keystoneing, the long edge of the cable is longer than h_{c} and given by

$$\ell_{\text{long-edge}} = \sqrt{\left(\frac{w_{\text{co}} - w_{\text{ci}}}{2} \right)^2 + h_{\text{c}}^2}. \quad (\text{B.23})$$

Ribbon-type cables are most conveniently modeled by means of cables only consisting of a single strand and an insulation layer. Braided cables are not addressed in this work.

Example : Normal and superconducting area for the LHC MB

The LHC main dipole features two different cables used in the inner and outer layer of the coil: The normal and superconducting surface areas are calculated based on the values given in Sec. C.1.1 (strand) and Sec. C.1.2 (cable).

For the inner layer cable, with a strand radius of $r_{\text{s}} = 0.5325$ mm, a copper-to-superconductor ratio of $\lambda = 1.65$, and $N_{\text{s}} = 28$ strands, this results in:

$$A_{\text{SC}}^{\text{LHCinner}} = 9.41 \text{ mm}^2, \quad A_{\text{NC}}^{\text{LHCinner}} = 15.53 \text{ mm}^2 \quad (\text{B.24})$$

For the outer layer cable, with a strand radius of $r_{\text{s}} = 0.4125$ mm, a copper-to-superconductor ratio of $\lambda = 1.95$, and $N_{\text{s}} = 36$ strands, this yields

$$A_{\text{SC}}^{\text{LHCouter}} = 6.52 \text{ mm}^2, \quad A_{\text{NC}}^{\text{LHCouter}} = 12.72 \text{ mm}^2 \quad (\text{B.25})$$

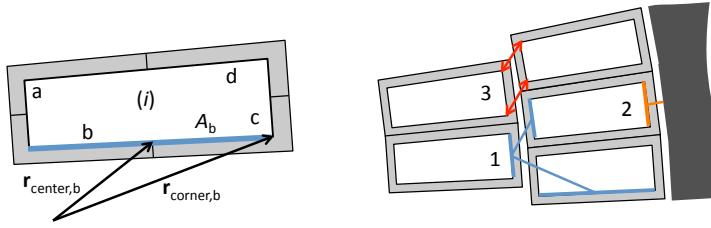


Figure B.2: Contact coefficients: (left) Conductor cross-section with named surfaces and position vectors. (right) Different thermal contact coefficients for transversal heat conduction and cooling (1) and (2). Minimum distance for the electrical field calculation (3).

B.1.4 Cable Twist-pitch in a 2D Approach

Regarding the magnet as a 2D problem where 3D features are included by extruding longitudinally, it is convenient to relate everything to properties of the 2D cross-section. Therefore, only the cross-sectional areas of Eq. (B.14) to (B.20) are used.

The cross-sectional areas perpendicular to the current in the strands, *e.g.* in Eqs. (B.24) and (B.25), can be derived by applying the factor $\cos(\beta_p)$.

For the calculation of the longitudinal resistivity of a cable, the overestimated cross-sectional area as well as the underestimated path length have to be compensated by a factor $1/(\cos(\beta_p))^2$. For longitudinal conductivity the inverse is applied.

B.1.5 Coil Cross-Section

The coil cross-section of a superconducting magnet consists of N_{cond} arbitrarily distributed conductors. For the calculation of heat transfer between adjacent conductors, it is necessary to define a measure of proximity. The calculation of electrical fields within the cross-section relies on the minimum distance between two conductors.

Figure B.2 (left) shows the cross-section of the conductor i . The four faces are denoted by $\alpha \in \{a, b, c, d\}$. Each face is characterized by the surface area, A_{α}^i , the vector to the center of the face, $\mathbf{r}_{\text{center},\alpha}^i$, and the vector to the corner, $\mathbf{r}_{\text{corner},\alpha}^i$.

Thermal Contact Coefficients Assuming homogeneous and especially constant thermal properties, the heat flux along a cylinder depends on the ratio of cross-sectional area and height - further on denoted as the transversal thermal contact coefficient K . In case of the arbitrarily shaped volumes in between two conductors, *i.e.* right tetragonal prisms, the approach is adapted by considering mean areas and the distance of the surface centers.

The distance between the center of two faces α and β of the conductors i and n is given by

$$d_{\alpha,\beta}^{i,n} = \left| \mathbf{r}_{\text{center},\alpha}^i - \mathbf{r}_{\text{center},\beta}^n \right|. \quad (\text{B.26})$$

The area A_{α}^i is calculated from the longitudinal discretization length times the conductor inner width w_{ci} ($\alpha = \text{a}$), the conductor outer width w_{co} ($\alpha = \text{c}$) or the long-edge $l_{\text{long-edge}}$ ($\alpha = \text{b}$ or c).

The contact coefficient $\tilde{K}_{\alpha,\beta}^{i,n}$ is calculated for any two faces of the coil cross-section.

$$\tilde{K}_{\alpha,\beta}^{i,n} = \frac{\frac{A_{\alpha}^i + A_{\beta}^n}{2}}{d_{\alpha,\beta}^{i,n}}. \quad (\text{B.27})$$

Multiple connections between two conductors are eliminated by considering only the strongest of the 16 links. Connections between two conductors passing through a third conductor are eliminated by a maximum distance criterium: Only links over a distance smaller than a user-supplied maximum distance d_{max} (smaller than the conductor thickness) are taken into account. In order to adjust the heat transfer between two conductors, *e.g.* for the implementation of quench stopper, the contact coefficient can be modified by assigning a real constant $k_{\text{T,trans}}^i$ to each conductor.

$$\tilde{K}^{i,n} = \begin{cases} \frac{k_{\text{T,trans}}^i + k_{\text{T,trans}}^n}{2} \max \left\{ \tilde{K}_{\alpha,\beta}^{i,n} \right\} & \left(d_{\alpha,\beta}^{i,n} < d_{\text{max}} \right) \\ 0 & \text{else} \end{cases}, \quad (\text{B.28})$$

with $i \neq n$ and $\alpha, \beta \in \{\text{a}, \text{b}, \text{c}, \text{d}\}$. The number of links can be further reduced by dropping all connections where the contact coefficient $\tilde{K}^{i,n}$ is smaller than a user supplied ratio $k_{\text{max,trans}}$ of the maximum link, yielding

$$K_{\text{trans}}^{i,n} = \begin{cases} \tilde{K}^{i,n} & \tilde{K}^{i,n} > k_{\text{max,trans}} \max \left\{ \tilde{K}^{i,n} \right\}_{i,n=1 \dots N_{\text{cond}}} \\ 0 & \text{else} \end{cases}. \quad (\text{B.29})$$

The contact coefficient for cooling is calculated in a similar way. Here, the user supplies a distance $d_{\text{cool},\alpha}^i$ between a specified face and the cold surface. The cooling coefficient is then given to

$$K_{\text{cool},\alpha}^i = \frac{A_{\alpha}^i}{d_{\text{cool},\alpha}^i}. \quad (\text{B.30})$$

Here multiple connections are possible. Where no distance is specified, cooling is not taken into account.

By means of the aforementioned approach it is possible to generate a transversal thermal network for an arbitrary coil cross-section. The grade of inter-linkage as well as certain variations to the thermal contact between elements can be easily applied. For a common coil cross-section built of conductor blocks, the turn-to-turn contact coefficients are reliably detected.

Because of the strong simplification of the heat transfer process and the possibility of intersecting “heat conduction prisms”, the approach is not valid for strongly non-linear heat conductivity.

Minimum Distance between Conductors For the calculation of electrical fields between adjacent conductors, the minimum distance is needed:

$$d_E^{i,n} = \min \left\{ \left| \mathbf{r}_{\text{corner},\alpha}^i - \mathbf{r}_{\text{corner},\beta}^n \right| \right\}_{\alpha,\beta \in \{a, b, c, d\}} \quad (\text{B.31})$$

The vector $\mathbf{r}_{\text{corner}}$, and the faces a, b, c and d are defined in Fig. B.2.

B.1.6 Magnet

For a superconducting magnet five different geometrical lengths shall be distinguished: The overall length ℓ_{total} , the magnetic length ℓ_{mag} , the inductance length ℓ_{ind} , the average winding length ℓ_w , and the coil length ℓ_c .

The magnetic length ℓ_{mag} is defined as [Brun 04, p. 165]

$$\ell_{\text{mag}}(I) = \frac{\int_{s=-\infty}^{+\infty} B_0(I, s) \, ds}{B_{\text{av}}(I)}, \quad (\text{B.32})$$

where I denotes the excitation current, B_{av} the average field in the straight part of the magnet and B_0 is the main component integrated along the orbit. Approaching the coil end, the magnetic induction starts to change depending on the design of the coil and the iron yoke. Outside the magnet, the magnetic field decreases quickly to zero. Due to the difference of the iron saturation in the coil ends compared to the magnet center, the current dependence in Eq. (B.32) does not cancel out. The variation over excitation current depends thus on the iron yoke design and the overall length of the magnet - for longer magnets it is smaller. If not stated otherwise, the magnetic length is given at operating temperature and nominal current [Brun 04, p. 164]. Notice that for higher order multipole magnets the field in the center is zero, and therefore B_{av} has to be replaced by the maximum field on the reference radius.

The inductance length is similarly defined as

$$\ell_{\text{ind}} = \frac{U_{\text{ind}}}{\frac{di}{dt} L'_d}, \quad (\text{B.33})$$

where U_{ind} is the measured voltage induced over the whole magnet for a current ramp rate $\frac{di}{dt}$. L'_d denotes the differential inductance per unit length of an infinitely long magnet with identical cross-section (see Sec. 7.4). The inductance length depends on the level of excitation and thus represents 3-D saturation effects. The inductance length is used to map the induced voltage onto the coil windings. It can be motivated that $\ell_{\text{mag}} \approx \ell_{\text{ind}}$, by extending the expression for the magnetic length by an effective coil width and differentiating by time.

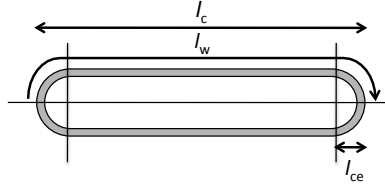


Figure B.3: Definition of coil end and coil end length.

The winding length is defined as the average length along one half-turn including the coil heads as shown in Fig. B.3. The winding length is used for the calculation of resistive voltages as well as for the longitudinal discretization.

The coil end length is the distance from the coil end to the part of the coil where the magnetic field problem can be assumed 2-D.

B.2 Filling Factors

B.2.1 Length, Area and Volume Ratios

Given an area A_{tot} segmented into n subareas A_n , then the area ratio η_n^A is defined as

$$\eta_n^A = \frac{A_n}{A_{\text{tot}}}. \quad (\text{B.34})$$

The length ratio η_n^ℓ and volume ratio η_n^V are defined accordingly:

$$\eta_n^\ell = \frac{\ell_n}{\ell_{\text{tot}}}, \quad \eta_n^V = \frac{V_n}{V_{\text{tot}}}. \quad (\text{B.35})$$

For identical lengths $\eta_n^V = \eta_n^A$ and for identical cross sectional areas $\eta_n^V = \eta_n^\ell$.

For superconductors only consisting of a superconducting material and a copper matrix, the copper to superconductor area ratio λ is widely used. It is defined as the ratio of the superconducting, A_{SC} , and the copper, A_{Cu} , cross-sectional area:

$$\lambda = \frac{A_{\text{Cu}}}{A_{\text{SC}}}. \quad (\text{B.36})$$

The copper to superconductor ratio can be transformed into η_{SC}^A and η_{Cu}^A by means of

$$\eta_{\text{SC}}^A = \frac{1}{1 + \lambda}, \quad \eta_{\text{Cu}}^A = \frac{\lambda}{1 + \lambda}. \quad (\text{B.37})$$

For strands consisting of more than 2 materials, *e.g.* most of the Nb_3Sn superconductors, an additional ratio can be used. The copper to non-copper area ratio $\lambda_{\text{non-Cu}}$,

$$\lambda_{\text{non-Cu}} = \frac{A_{\text{Cu}}}{A_{\text{non-Cu}}}. \quad (\text{B.38})$$

Note that the cross-sectional area is now divided into 3 parts, and thus the copper and superconducting parts do not add up to the strand cross-sectional area:

$$\eta_{\text{Cu}}^A = \frac{\lambda_{\text{non-Cu}}}{1 + \lambda_{\text{non-Cu}}}, \quad \eta_{\text{SC}}^A = \frac{\frac{\lambda_{\text{non-Cu}}}{\lambda}}{1 + \frac{\lambda_{\text{non-Cu}}}{\lambda}}, \quad \eta_{\text{non-Cu}}^A = \frac{1 + \frac{\lambda_{\text{non-Cu}}}{\lambda}}{1 + \lambda_{\text{non-Cu}}}. \quad (\text{B.39})$$

B.2.2 Material Fractions

By means of the following scheme materials are assigned to the different parts of the filament, strand and cable cross-section:

			Area	Cu	Nb-Ti	Kapton	He	...
			$A_{\text{fil,core}}$					
			$A_{\text{fil,SC}}$					
			$A_{\text{fil,coat}}$					
$N_s \times$	$N_f \times$	\sum	$A_{\text{fil,tot}}$					1
			$A_{\text{str,core}}$					
			$A_{\text{str,matrix}}$					
			$A_{\text{str,coat}}$					
$N_s \times$	\sum		$A_{\text{str,tot}}$					2
			$A_{\text{cab,core}}$					
			$A_{\text{void,inner}}$					
			$A_{\text{void,outer}}$					
			A_{ins}					
\sum			$A_{\text{cab,eff}}$					3

Combining areas of identical material filling and dividing by the total area of the filament, strand or cable yields the respective material area ratios, *e.g.* $\eta_{\text{str,Cu}}^A$. Due to the identical longitudinal length, the volume ratios are equal to the area ratios.

B.2.3 Effective Electrical Resistivity, Thermal Conductivity and Specific Heat

Consider a cuboid of length ℓ and cross-sectional area A . It is transversally segmented into N sub-volumes of length ℓ and resistivity ρ_{En} (see Fig. B.4 (left)). The effective longitudinal resistivity of the cuboid is given by

$$\rho_E^{\text{eff}, [=]} = \frac{1}{\sum_{n=1}^N \eta_n^A \frac{1}{\rho_{En}}}. \quad (\text{B.40})$$

For a cuboid segmented longitudinally in N cuboids of length ℓ_n and identical cross-sectional areas (see Fig. B.4 (center)), the effective longitudinal resistivity of the cuboid is given by

$$\rho_E^{\text{eff}, [|||]} = \sum_{n=1}^N \eta_n^\ell \rho_{En}. \quad (\text{B.41})$$

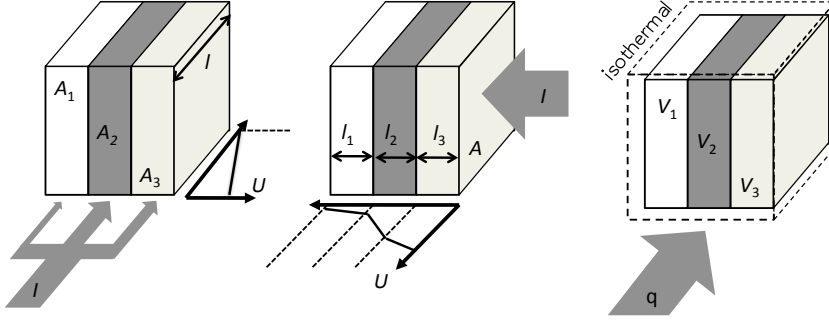


Figure B.4: Effective thermal and electrical properties. Electrical resistivity and thermal conductivity for parallel sub-domains (left) and sub-domains in series (center). Effective specific heat (right).

The effective thermal conductivity is then given by:

$$\kappa_T^{\text{eff}, [=]} = \sum_{n=1}^N \eta_n^A \kappa_{Tn}, \quad \kappa_T^{\text{eff}, [|||]} = \frac{1}{\sum_{n=1}^N \eta_n^l \frac{1}{\kappa_{Tn}}}. \quad (\text{B.42})$$

A volume of homogeneous temperature, consisting of N sub-volumes V_n with specific heat c_T (see Fig. B.4 (right)) shows an effective specific heat of

$$c_T^{\text{eff}} = \sum_{n=1}^N \eta_n^V c_{Tn}. \quad (\text{B.43})$$

This approach is only valid if the material properties are homogeneous within each sub-domain. It can be adapted for materials depending on an external quantity and thus varying within the sub-domains. These domains are sub-divided such that constant quantities can be assumed.

C Cases

On two occasions I have been asked,-"Pray, Mr. Babbage, if you put into the machine wrong figures, will the right answers come out?" [...] I am not able rightly to apprehend the kind of confusion of ideas that could provoke such a question.

CHARLES BABPAGE
(1791-1871)

This chapter serves as a collection of all parameters used for the simulations presented in the main part of the thesis. The description of the LHC main bending magnet is exemplary for all cases.

C.1 LHC Main Bending Magnet

The LHC main dipole features two apertures in a common iron yoke. The coils in each aperture are subdivided in an upper and a lower pole. Each pole consists of 6 conductor-blocks per quadrant, arranged in two layers. Both, strands and cables, are different for the outer and inner layer resulting in a grading of current density.

C.1.1 Strand

The parameters of the Nb-Ti filaments and the copper-stabilized strands for the inner and outer layer cables are given in Tab. C.1 and C.2, respectively. Figure 2.3 (left) shows a photography of the strand cross-section.

The critical current density J_c in the strands is given by a parameterization (Sec. A.2.5.1). Identical fit parameters are used for the inner and outer layer strands (see Tab. A.17). The residual resistivity ratio (RRR) of the copper matrix in the strands is in the range of 150 to 250 [Char 06].

C.1.2 Cable

The LHC MB coil is wound from key-stoned Rutherford type cables. The cable parameters for the inner and outer layer cables are given in Tab. C.3.

Table C.1: LHC Main Bending Magnet (MB) Filament

Quantity	Symbol	Unit	Inner Layer	Outer Layer	Ref.
Materials					
Superconductor			Nb-Ti	Nb-Ti	Sec. A.2.5.1, Sec A.1.5.2
Core			–	–	
Coating			–	–	
Geometry					
Radius	r_f	μm	3.5	3	[Brun 04, p. 157]
Core radius	r_{fc}	μm	–	–	
Coating thickness	t_{fc}	μm	–	–	

Table C.2: LHC Main Bending Magnet (MB) Strand

Quantity	Symbol	Unit	Inner Layer	Outer Layer	Ref.
Materials					
Matrix			Copper	Copper	Sec. A.1.3.1, Sec A.1.4.1, & Sec. A.1.5.1
Core			–	–	
Coating			Sn5wt%Ag	Sn5wt%Ag	[Brun 04, p. 157]
Geometry					
No. of filaments	N_f	–	8900	6500	[Brun 04, p. 157]
Radius	r_s	mm	0.5325	0.4125	[Brun 04, p. 157]
Core radius	r_{sc}	mm	–	–	
Coating thickness	t_{sc}	mm	–	–	
Twist pitch	p_s	mm	18 ± 1.5	15 ± 1.5	[Brun 04, p. 157]
Model parameters - Electrical / Inter-filament coupling losses					
Copper/Supercond. ratio	λ	–	1.65 ± 0.05	1.95 ± 0.05	[Brun 04, p. 157]
Copper RRR	RRR	–	150 – 250	150 – 250	[Char 06]
Copper matrix resistivity	ρ_{IFCC}	Ωm	$1.24 \cdot 10^{-10}$	$1.24 \cdot 10^{-10}$	
Copper matrix resistivity B dependence	$\frac{d\rho_{IFCC}}{dB}$	$\frac{\Omega m}{T}$	$9 \cdot 10^{-11}$	$9 \cdot 10^{-11}$	
Filling factor	η_s	–	0.5	0.5	
Specification					
Critical current at 10 T, 1.9 K	I_c	A	≥ 515		[Brun 04, p. 157]
at 9 T, 1.9 K				≥ 380	[Brun 04, p. 157]

Figure 2.3 (right) shows a photography of the cable. The filaments of one strand have been extracted by etching.

C.1.3 Magnet Data

The magnet features a two-in-one design, i.e. two apertures in one common iron yoke. To each aperture belong a lower and a upper coil, each built in two-layers. The inner layer consist of 4 coil blocks and the outer layer of two. Figure C.1 shows the magnet cross-section with cryostat, iron yoke and superconducting coils. The winding scheme is shown in Fig. C.2. The block and conductor numbering scheme used in ROXIE is shown in Fig. C.3. All parameters are given in Tab. C.4.

At a ramp rate of $7.5 \text{ mT} \cdot \text{s}^{-1}$, AC losses of 180 mW per meter can be expected in the magnet [Brun 04]. During a quench, these losses increase by many orders of magnitude, and cause quench-back [Rodr 01]. For a full ramp-cycle from injection to nominal current level and down to injection, hysteresis losses of 280 – 400 J per meter were calculated [Voll 02, p. 135] and [Verw 95, p. 153].

C.1.4 External Electrical Circuit

For quench simulation two different electrical situations have to be distinguished: The operation in the LHC tunnel and the setup on the test bench. All parameters are given in Tab. C.5.

Tunnel Setup For the LHC the main bending dipoles are operated in strings of 153 magnets. Each magnet is bridged by a diode mounted inside the cryostat. The forward voltage of the diode is assumed to be constant at 8 V. In case of a quench, the power supply is switched off and by passed by thyristors [Dahl 01]. Two dump resistors are switched into the circuit. The discharge time constant of the string is $\tau = 104 \text{ s}$ resulting in a maximum $di/dt = 125 \text{ As}^{-1}$ [Dahl 00]. The electrical network is shown in Fig. C.4

Test Stand On the test bench the magnet is only connected to a power supply with by-pass thyristor. The cold diode is prevented from switching by the power supply bypass diode and can thus be omitted in this configuration.

C.1.5 Magnet Protection

The quench protection consists of a quench detection system, a cold by-pass diode and quench heaters placed on the outer layer of the coil as indicated in Fig. C.2. The resistive voltage over the magnet is detected by a double floating bridge detector as shown in Fig. C.5. The threshold voltage of the detection system is 0.1 V [Denz 06]. Quench heaters are fired after a delay of 10.5 ms for signal validation [Denz 06]. The timing of the different heaters may vary by up to 10 ms [Sonn 01a].

Table C.3: LHC Main Bending Magnet (MB) Cable

Quantity	Symbol	Unit	Inner Layer	Outer Layer	Ref.
Materials					
Insulation			kapton	kapton	Sec. A.1.4.4, & Sec. A.1.5.4
Cable Core			–	–	
Inner void filling			helium	helium	Sec. A.3
Outer void filling			–	–	
Geometry					
No. of strands	N_s	–	28	36	[Brun 04, p. 157]
Insulation Thickness					
radial	t_{ir}	mm	0.15	0.15	[Gran 08]
azimuthal	t_{ia}	mm	0.12	0.13	[Gran 08]
Cable					
Height	h_c	mm	15.1	15.1	[Brun 04, p. 157]
Width, inner	w_{ci}	mm	1.736	1.362	[Brun 04, p. 157]
Width, outer	w_{co}	mm	2.064	1.598	[Brun 04, p. 157]
Core thickness	t_{cc}	mm	–	–	
Keystone angle	ϕ_{key}	$^\circ$	1.25 ± 0.05	0.9 ± 0.05	[Brun 04, p. 157]
Aspect ratio			7.95	10.2	[Brun 04, p. 157]
Twist pitch	ℓ_p	mm	115 ± 5	100 ± 5	[Brun 04, p. 157]
Cabling angle	β_p	$^\circ$			
Model parameters - Thermal / Inter-strand coupling losses					
Helium in voids	–	%	10	10	Study
Cross-over resistance	R_c	$\mu\Omega$	30	60	[Verw 07b]
Adjacent resistance	R_a	Ω	100	100	[Verw 07b]
Specification					
Critical current	I_c	A			
at 10 T and 1.9 K			> 13750		[Brun 04, p. 157]
at 9 T and 1.9 K				> 12960	[Brun 04, p. 157]
Linearization	$\frac{dI_c}{dB}$	AT^{-1}	> 4800	> 3650	[Brun 04, p. 157]
MIITs		MA^2s			
at 300 K, 8 T			45		[Brun 04, p. 157]
at 300 K, 6 T				30	[Brun 04, p. 157]

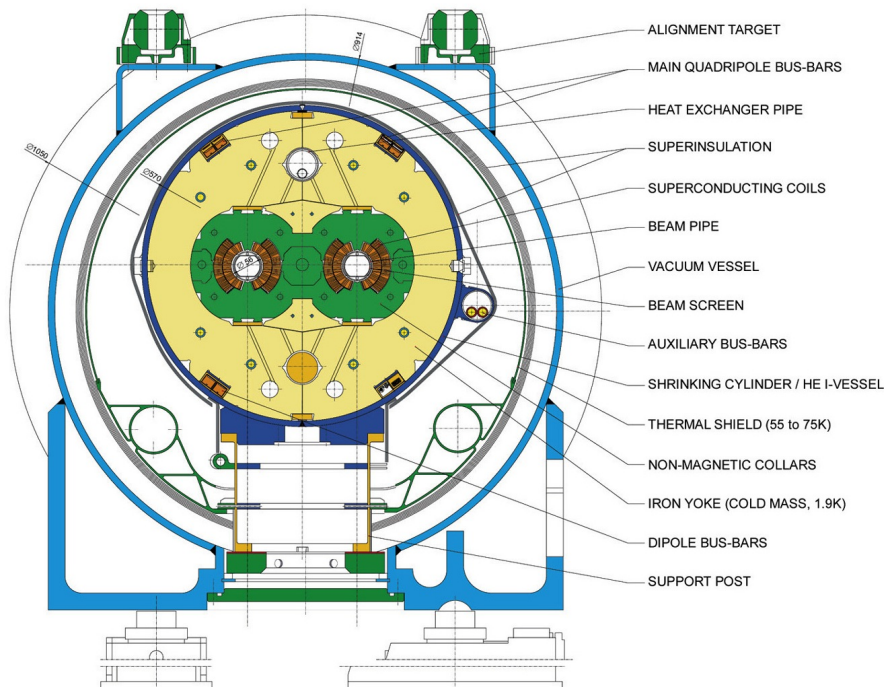


Figure C.1: LHC Main Bending Magnet (MB) dipole cross-section. Courtesy of CERN ©.

Table C.4: LHC Main Bending Magnet (MB) Magnet Data

Quantity	Symbol	Unit	Value	Ref.
Material				
Wedge material:	copper			
Quench stopper:	none			
Cooling surfaces:	cooling to cold bore tube (distance around 1 mm) and collar (distance around 0.5 mm)			
Iron yoke:	magnetic iron			Sec A.1.6.1
Number of apertures	–	–	2	
Number of poles	–	–	2	
Number of blocks per pole	–	–	6	
Num. of conductors per pole	N_{cp}	–	40	
Coil length	ℓ_c	m	15	
Average winding length	ℓ_w	m	14.57	
Magnetic length	ℓ_{mag}	m	14.31	[Brun 04, p. 164]
End part of coil	ℓ_{ce}	m	–	

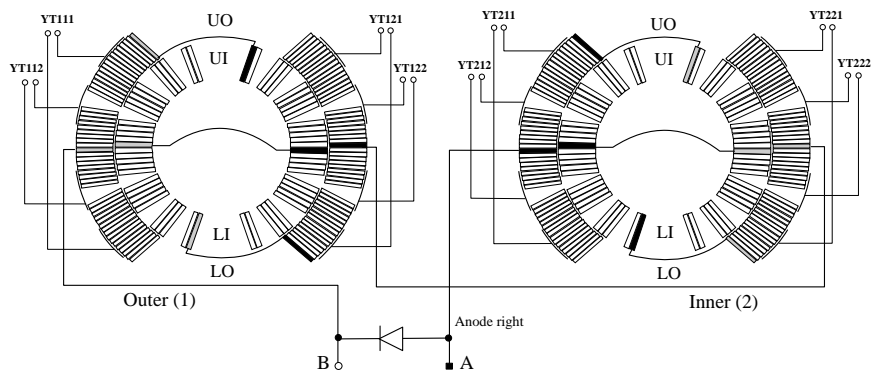


Figure C.2: LHC Main Bending Magnet (MB) winding scheme and quench heater layout [Brun 03].

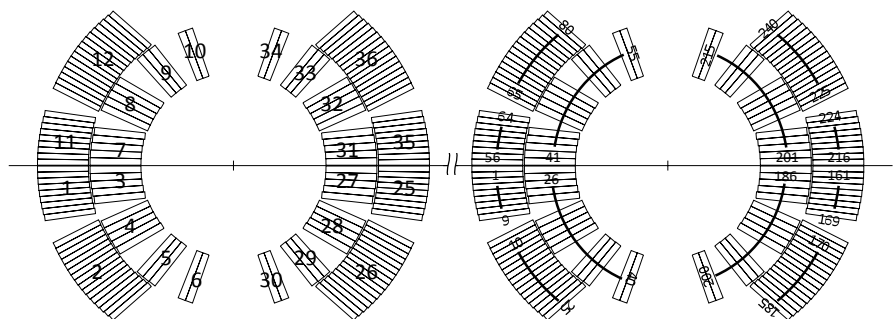


Figure C.3: LHC Main Bending Magnet (MB) Numbering schemes for the right aperture. (left) Block numbers. (right) Conductor numbers. The skipped numbers are located in the left aperture.

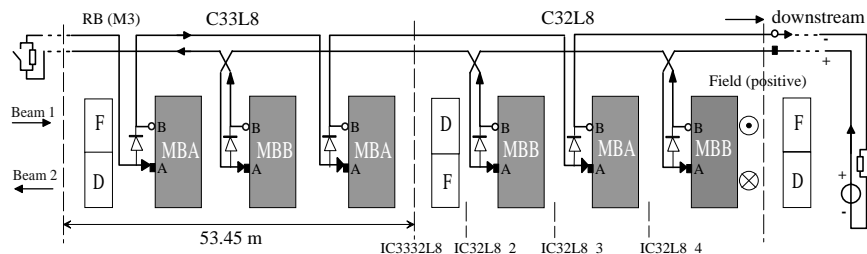


Figure C.4: LHC Main Bending Magnet (MB) connection scheme in the tunnel.

The quench heater strips consists of 15.0×0.025 mm stainless steel with copper plating insulated with 0.175 mm polyimide insulation and epoxy glue. Two heaters covering 13 cables, 15 m long and 9 mm apart. Sufficient to heat spot-wise due to quench propagation velocities of 15 to 20 ms^{-1} . The optimized pattern of 400 mm covered followed by 120 mm non-covered strip results in a heater resistance of $0.35 \Omega \text{ m}^{-1}$ [Rodr 00].

A capacitor is discharged over the resistance of the heater strip, resulting in an exponential voltage decay [Rodr 01]. The time constant for the dissipated power is about 37.5 ms [Sonn 01a]. Measurements indicate that a heater-provoked quench at 1.5 kA occurs around 80 ms after the heaters are fired. At nominal current the delay reduces to 35 ms [Pugn 07].

In case of a quench in the LHC tunnel, the diodes and busbars are protected from overheating by extracting the current by means of a dump resistor (Sec. C.1.4).

All parameters of the quench protection are given in Tab. C.6.

C.1.6 Operating Conditions / Critical Values

The operation conditions and current levels of the LHC MB are given in Tab. C.7. For orientation some critical values are given, too.

Table C.5: LHC Main Bending Magnet (MB) Electrical Circuit

Quantity	Symbol	Unit	Value	Ref.
Power supply				
Switch off delay	Δt_{QT}	ms	0	
Crowbar forward resistance	R_{fDR}	Ω	0	
Crowbar forward voltage	U_{fDTh}	V	1	
Cold diode				
Switching voltage	U_{cDcTh}	V	6	[Verw 08a]
Forward voltage	U_{cDwTh}	V	1-2	[Verw 08a]
Forward resistance / resistance	R_{cCfR}	Ω	–	
Delay from switching voltage to forward voltage	Δt_{cDh}	ms	–	
Serial elements - Tunnel				
Inductance	L_s	H	$153 \times L_d$	
Resistance	R_s	Ω	–	
Serial elements - Test stand				
Inductance	L_s	H	0	
Resistance	R_s	Ω	0	

Table C.6: LHC Main Bending Magnet (MB) Protection

Quantity	Symbol	Unit	Value	Ref.
Quench detection				
Detection voltage	U_{det}	V	± 0.1	[Denz 06]
Discrimination delay	Δt_{Dis}	ms	10.5	[Denz 06]
Quench heater				
Material	stainless steel, copper plating			[Rodr 00]
Width	w_{QH}	mm	15.0	[Rodr 00]
Height	h_{QH}	mm	0.025	[Rodr 00]
Insulation thickness	d_{QH}	mm	0.175	[Rodr 00]
Length	ℓ_{QH}	m	15	[Rodr 00]
Nominal resistance (at cold)	R_{QH}	Ωm^{-1}	0.35	[Rodr 00]
Capacity	C_{QH}	mF	7.05	[Rodr 00]
Time constant (power)	τ_{QH}	ms	37.5	[Rodr 00], Sec. 7.9.5
Initial voltage	U_{QH}	V	900	[Rodr 00]
Switching delay	Δt_{QHtd}	ms	4	[Denz 06]
Quench-heater delay (at nom. current)				
high field heaters	Δt_{QH}	ms	25	[Rodr 00]
low field heaters		ms	35	[Rodr 00]
Scattering of switching delay	Δt_{QHs}	ms	< 10	[Rodr 00]
Quench Heater Model				
Initial power density per conductor	P_{QH0}	Wm^{-1}	20	
Heat transfer delay	Δt_{QH0}	ms	22-25	
Dump resistor - Tunnel				
Resistance	R_{DR}	$m\Omega$	75	[Dahl 00]
Switching/commutation delay	Δt_{DR}	ms	11.5	[Denz 06]
Decay time constant	τ_{DR}	s	104	[Dahl 00]

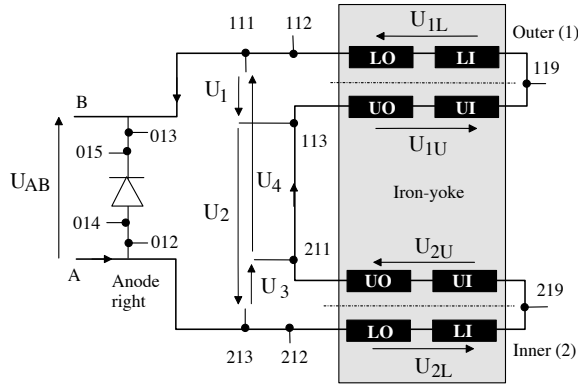


Figure C.5: LHC Main Bending Magnet (MB) Quench detection. The resistive voltage over the LHC MB is measured redundantly. The two floating bridges with voltages $U_1 - U_4$ and $U_2 - U_3$ overlap, such that the interconnection between the two apertures is covered twice.

Table C.7: LHC Main Bending Magnet (MB) Operating Conditions and Critical Values

Quantity	Symbol	Unit	Value	Ref.
Operation temperature	T_b	K	1.9	[Siem 05]
Injection,				
current	I_{inj}	A	763	[Brun 04, p. 164]
peak field		T	0.54	[Brun 04, p. 164]
energy		TeV	0.45	[Brun 04, p. 164]
Nominal,				
current	I_{nom}	A	11850	[Brun 04, p. 164]
peak field		T	8.33	[Brun 04, p. 164]
energy		TeV	7	[Brun 04, p. 164]
Ultimate,				
current	I_{ult}	A	12840	[Brun 04, p. 164]
peak field		T	9.0	[Brun 04, p. 164]
Maximum temperature	T_{max}	K	600	Sec. A.1.1
Maximum ramp rate	$\max\{di/dt\}$	A/s	-125	[Dahl 00]
Maximum turn to turn voltage	$U_{max,tt}$	V	75	[Brun 04, p. 159]
Maximum voltage to ground	$U_{max,ground}$	V	488	[Dahl 01]
Max. voltage between apertures		V	150	[Verw 08a]

C.2 LHC Inner Triplet Nested Dipole - MCBX

The MCBX consists of two nested independently powered dipoles. We consider the outer dipole only. The quench simulation is carried out for a magnet of the pre-series, *i.e.* the MCBXT horizontal dipole [Karp 08a].

C.2.1 Strand and Cable

The magnet is wound from a 7-strand ribbon-type conductor using a strand of the LHC MB inner layer cable (see Sec. C.1.1) rolled into a rectangular form (no change of properties is assumed). Each strand with cross-section 1.53×0.85 mm is insulated by a layer of 0.06 mm PVA. The strands are glued on the short edge to the cable [Karp 08a].

C.2.2 Magnet Data

The strands are connected in one coil end such that each radial layer of strands is connected in series. Figure C.6 shows the coil cross-section and the winding scheme of the magnet [Karp 08a]. All magnet parameters are given in Tab. C.8.

The connection of the strands allows for radial and azimuthal quench propagation within a coil block and for longitudinal propagation within each radial layer of strands. The coil is fully impregnated so that no cooling needs to be considered. The magnet is operated at 1.9 K [Brun 04, p. 245].

The MCBX consists of two nested dipole coil layers surrounded by an aluminum shrinking cylinder, a laminated iron yoke, a stainless-steel outer shell and an end plate, which supports the electrical connection [Brun 04, p. 244]. The magnet cross-section is shown in Fig. C.7. The inner radius of the yoke is 90.2 mm and the outer radius 164.6 mm [Karp 08a].

For the present simulations, the magnet is neither protected by quench heaters nor a dump resistor. The voltage across the power supply is neglected.

Table C.8: LHC MCBX Magnet Data

Quantity	Symbol	Unit	Value	Ref.
Material				
Wedge material:	copper with thick layer of G10 as insulation			Sec A.1.6.1
Quench stopper:	each layer is connected to the next one on the outside. The connection is covered by a copper plate and immersed to liquid helium			
Cooling surfaces:	cooling to cold bore tube (distance around 1mm)			
Iron yoke:	magnetic iron			
Number of apertures	–	–	1	[Karp 08a] [Karp 08a] [Karp 08a] [Karp 08a]
Number of poles	–	–	2	
Number of blocks per pole	–	–	(3)	
Number of conductors per pole	N_{cp}	–	406	
Coil length	ℓ_c	m	0.5	
Average winding length	ℓ_w	m	0.5	
Magnetic length	–	m	0.38	
End part of coil	ℓ_{ce}	m	–	

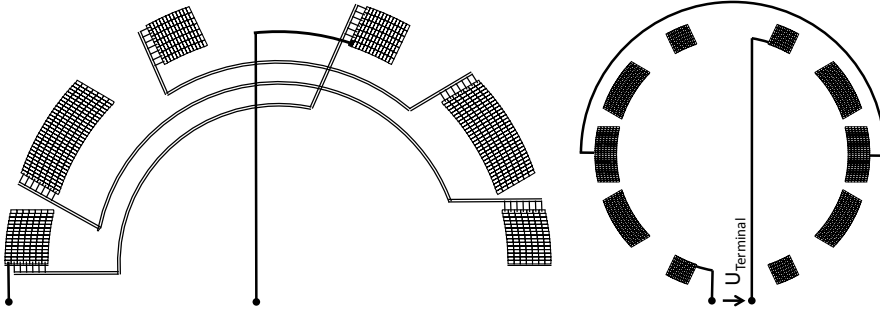


Figure C.6: LHC MCBX corrector magnet coil cross-section and winding scheme. (left) winding scheme for one coil. The current enters the coil at the top in the inner layer. From there the coil is wound down to the mid-plane in a radial layer. The next layer is connected from the mid-plane to the coil top. This connection is done outside the magnet and functions as quench stopper. (right) The second coil is identically wound and connected on the mid-plane.

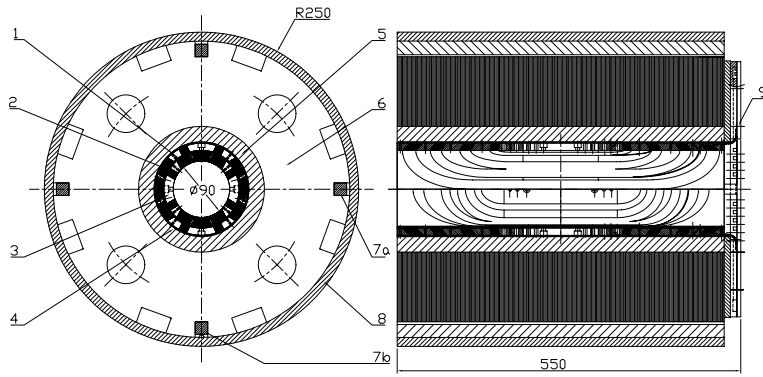


Figure C.7: LHC MCBX magnet cross-section (old design) [Karp 99]. 1. Inner Coil, 2. Outer Coil, 3. Coil spacer, 4. Fiber-glass insulation, 5. Shrink ring, 6. Iron yoke laminations, 7a. Vertical, and 7b. Horizontal blocking keys, 8. Outer shell, 9. End plate for series connections. Courtesy of M. Karppinen TE MCS.

C.3 LHC Inner Triplet Upgrade Quadrupole - MQXC

C.3.1 Strand and Cable

For the Inner Triplet Upgrade Quadrupole the same cables as for the LHC MB will be used. The parameters are given in Sec C.1.1 and C.1.2, respectively.

By sorting and picking the best performing cables, the critical current is expected to be larger than for the LHC MB. Therefore, the fit parameters of the critical current density parameterization (see Tab. A.17) are modified. The critical current as well as the updated fit parameters are given in Tab. C.9.

C.3.2 Magnet Data

The MQXC features a 120 mm aperture. The magnet coil consists of 4 poles, each built in two-layers. The inner layer consist of two coil blocks as well as the outer layer (where one block is made from one conductor only). The coil cross-section and winding scheme are shown in Fig. C.8. All parameters are given in Tab. C.10.

For the first study a round iron yoke with inner radius of 129 mm and outer radius of 275 mm is considered. The differential inductance varies less than 5% over excitation due to iron saturation.

C.3.3 Electrical Circuit

The magnet is connected to a power supply and a dump resistor. In case of a quench, the power supply is switched of and bridged by a diode. All parameters are given in Tab. C.11.

C.3.4 Magnet Protection

The quench protection consists of a quench detection system, a dump resistor and quench heaters placed on the outer layer of the coil as indicated in Fig. C.8. The threshold voltage of the detection system is 0.1 V. Quench heaters are fired after a delay of 10 ms for signal validation. The dump resistor is switched in the same instance. All parameters of the magnet protection system can be found in Tab. C.12.

C.3.5 Operating Conditions / Critical Values

The operation conditions and current levels of the MQXC are given in Tab. C.13. For orientation some critical values are given, too.

Table C.9: MQXC Cable Parameters. All other parameters are identical with the LHC MB.

Quantity	Symbol	Unit	Inner Layer	Outer Layer	Ref.
Critical current	I_c	A	14800		[Osto 08]
at 10 T, 1.9 K				14650	[Osto 08]
at 9 T, 1.9 K				4050	[Osto 08]
Linearization	dI_c/dB	AT^{-1}	5040		[Osto 08]
Fit parameters,					
C_0	–	T	29.47	30.94	
β	–	–	1.044	1.044	

Table C.10: Inner Triplet Upgrade MQXC Magnet Data

Quantity	Symbol	Unit	Value	Ref.
Wedge material:	copper			
Quench stopper:	none			
Cooling surfaces:	not considered			
Iron yoke:	magnetic iron			Sec A.1.6.1
Number of poles	–	–	4	[Borg 08]
Number of blocks per pole	–	–	4	[Borg 08]
Number of conductors per pole	N_c	–	36	[Borg 08]
Coil length	l_c	m	10.3	[Fess 08]
Average winding length	l_w	m	10.3	[Fess 08]
Magnetic length	–	m	10.0	[Fess 08]
End part of coil	I_{ce}	m	0.3	[Fess 08]

Table C.11: Inner Triplet Upgrade MQXC Electrical Circuit

Quantity	Symbol	Unit	Value	Ref.
Power supply				
Switch off delay	Δt_{QT}	ms	0	[MQXC 08b]
Crowbar forward resistance	R_{fDR}	Ω	0	[MQXC 08b]
Crowbar forward voltage	U_{fDTh}	V	1	[MQXC 08b]

Table C.12: Inner Triplet Upgrade MQXC Magnet Protection

Quantity	Symbol	Unit	Value	Ref.
Quench detection				
Detection voltage	U_{det}	V	± 0.1	[MQXC 08a]
Discrimination delay	Δt_{Dis}	ms	10	[MQXC 08a]
Quench Heater Model				
Initial power density/conductor	P_{QH0}	Wm^{-1}	30	
Heat transfer delay	Δt_{QH0}	ms	20	
Time constant (power)	τ_{QH}	ms	37.5	[Osto 08]
Quench-heater delay		see LHC MB		[MQXC 08a], Sec. C.1.5
Dump resistor				
Resistance	R_{DR}	$m\Omega$	40	[MQXC 08a]
Switching/commutation delay	Δt_{DR}	ms	0	[MQXC 08a]

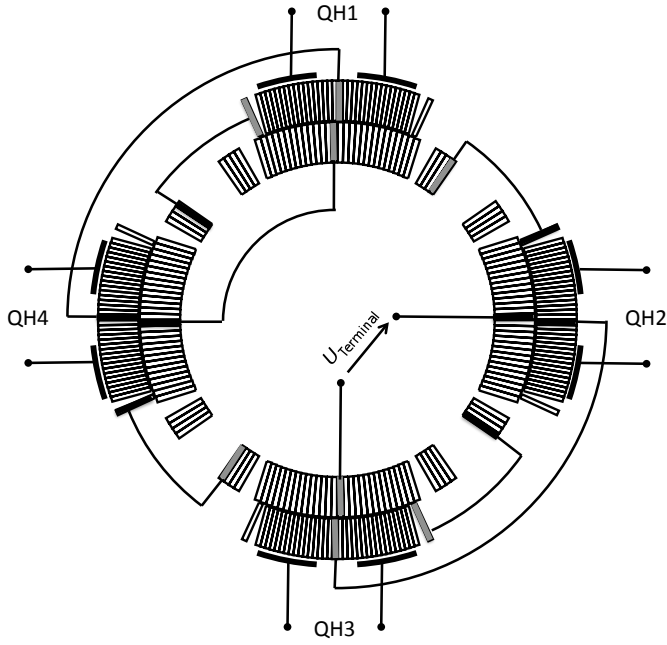


Figure C.8: MQXC coil cross section [Borg 08], winding scheme and quench heater layout [Fess 08].

Table C.13: Inner Triplet Upgrade MQXC Operating Conditions and Critical Values

Quantity	Symbol	Unit	Value	Ref.
Operation temperature	T_b	K	1.9	[Siem 05]
Nominal current	I_{nom}	A	12580	[Fess 08]
Ultimate current	I_{ult}	A	15720	[Fess 08]
Maximum temperature	T_{max}	K	600	[MQXC 08a], Sec. A.1.1
Maximum turn to turn voltage	$U_{\text{max,tt}}$	V	75	LHC MB Sec. C.1.6
Maximum voltage to ground	$U_{\text{max,ground}}$	V	250	[MQXC 08a]

C.4 Fast Ramping Dipole Magnet

C.4.1 Strand and Cable

The strand consists of a Nb-Ti filament of $3.5\mu\text{m}$ embedded in a copper matrix. The strand parameters can be found in Tab. C.14.

The parameters of the Rutherford-type cable with stainless steel core are given in Tab. C.15. The geometry of the cable is identical to the LHC MB outer layer cable (Sec. C.1.2).

C.4.2 Magnet Data

The fast ramping dipole coil consists of two poles, each built in two-layers. The inner layer consist of 4 coil blocks and the outer layer of two. The coil cross-section and winding scheme are shown in Fig. C.10. All parameters are given in Tab. C.16.

C.4.3 Electrical Circuit

The magnet is only connected to a power supply with by-pass thyristor and a dump resistor. In case of a quench, the power supply can be inverted in order to drive down the current.

C.4.4 Magnet Protection

The quench protection consists of a quench detection system, a dump resistor and quench heaters placed on the outer layer of the coil as indicated in Fig. C.10. The threshold voltage of the detection system is varied from 0.1 to 1.0 V. Quench heaters are fired after a delay of 10 ms for signal validation. The dump resistor is switched in 50 ms after quench validation. All parameters of the magnet protection system can be found in Tab. C.17.

C.4.5 Operating Conditions / Critical Values

The magnet is operated at 4.7 K. The ramp cycle is given in [Kozu 06] as an up-ramp from 1.6 T to 6 T in 4.4 s, followed by a plateau at 6 T of 11 s, and a down ramp to 1.6 T in 4.4 s. Critical values, *e.g.*, maximum temperatures, are taken from the LHC MB in Sec. C.1.6.

Table C.14: Fast Ramping Dipole Strand

Quantity	Symbol	Unit	Value	Ref.
Materials				
Matrix	Copper			Sec. A.1.3.1, Sec. A.1.4.1, Sec. A.1.5.1
Coating	Stabrite			
Geometry				
Number of filaments	N_f	–	–	
Radius	r_s	mm	0.4125	[Kozu 06, p. 5]
Core radius	r_{sc}	mm	–	
Coating thickness	t_{sc}	μm	0.5	[Kozu 06, p. 5]
Twist pitch	p_s	mm	5	[Kozu 06, p. 5]
Model parameters - Electrical / Inter-filament coupling losses				
Copper/Super-conductor ratio	λ	–	1.4	[Kozu 06, p. 5]
Copper RRR	RRR	–	278	
Copper matrix resistivity	ρ_{IFCC}	Ωm	$4 \cdot 10^{-10}$	[Kozu 06, p. 5]
Copper matrix resistivity B dependence	$\frac{d\rho_{\text{IFCC}}}{dB}$	$\Omega\text{m/T}$	$9 \cdot 10^{-11}$	[Kozu 06, p. 5]
Filling factor	η_s	–	0.5	

Table C.15: Fast Ramping Dipole Cable

Quantity	Symbol	Unit	Value	Ref.
Materials				
Insulation	kapton			Sec. A.1.4.4, Sec. A.1.5.4
Cable Core	stainless steel			
Inner void filling	helium			Sec. A.3
Outer void filling	–			
Geometry				
Number of strands	N_s	–	36	[Kozu 06, p. 5]
Insulation Thickness				
radial	t_{ir}	mm	–	
azimuthal	t_{ia}	mm	–	
Cable				
Geometry			see LHC MB outer layer	Sec. C.1.2
Core thickness	t_{cc}	μm	25	[Kozu 06, p. 5]
Keystone angle	ϕ_{key}	$^\circ$	–	
Twist pitch	ℓ_p	mm	100	[Kozu 06, p. 5]
Cabling angle	β_p	$^\circ$		
Model parameters - Thermal / Inter-strand coupling losses				
Helium in voids	–	%	10	
Cross-over resistance	R_c	$\text{m}\Omega$	20	[Kozu 06, p. 5]
Adjacent resistance	R_a	$\mu\Omega$	200	[Kozu 06, p. 5]

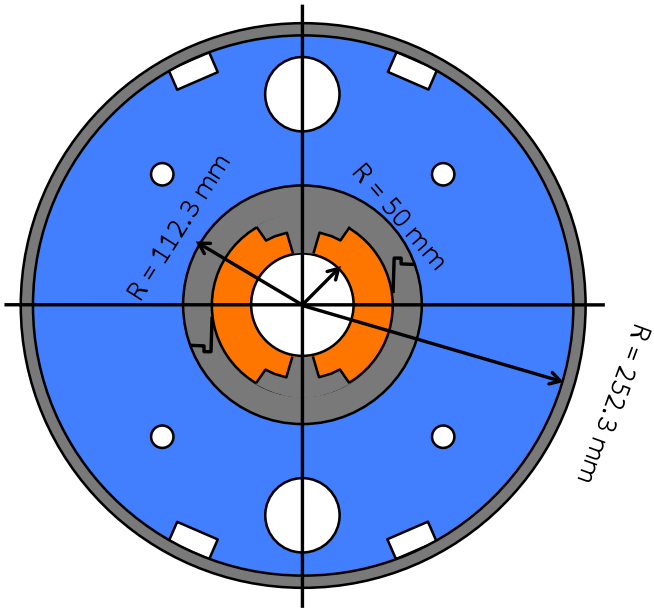


Figure C.9: Fast ramping dipole iron yoke and magnet cross-section after [Kozu 06, p. 10].

Table C.16: Fast Ramping Dipole Magnet Data

Quantity	Symbol	Unit	Value	Ref.
Material				
Wedge material:	copper			
Quench stopper:	none			
Cooling surfaces:	cooling to cold bore tube and collar (distance around 1mm)			
Iron yoke:	magnetic iron			Sec A.1.6.1
Number of apertures	–	–	1	
Number of poles	–	–	2	
Number of blocks per pole	–	–	6	
Number of conductors per pole	N_{cp}	–	71	
Coil length	ℓ_c	m	1	
Average winding length	ℓ_w	m	1	
Magnetic length	–	m	0.75	
End part of coil	ℓ_{ce}	m	–	

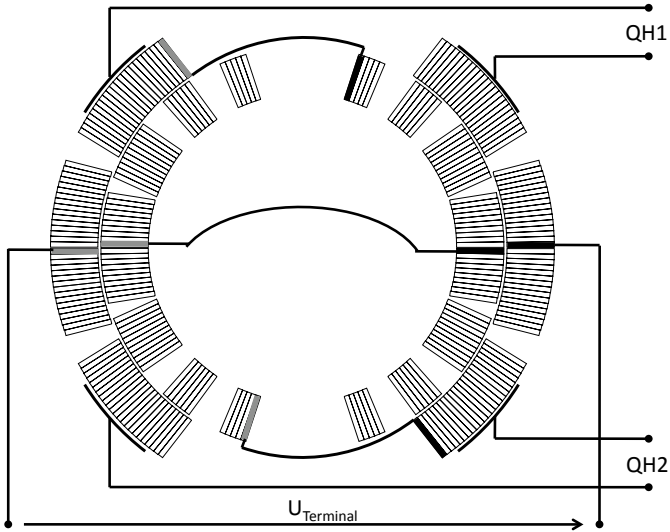


Figure C.10: Fast Ramping Dipole coil cross section, winding scheme and quench heater layout.

Table C.17: Fast Ramping Dipole Magnet Protection

Quantity	Symbol	Unit	Value	Ref.
Quench detection				
Detection voltage	U_{det}	V	0.1 – 1.0	Study
Discrimination delay	Δt_{Dis}	ms	10	
Quench Heater Model				
Initial power density per conductor	P_{QH0}	Wm^{-1}	200	
Heat transfer delay	Δt_{QH0}	ms	60	
Time constant (power)	τ_{QH}	ms	37.5	
Quench-heater delay (at nominal current)	Δt_{QH}	ms	around 90	
Dump resistor				
Resistance	R_{DR}	$\text{m}\Omega$	200	
Switching/commutation delay	Δt_{DR}	ms	50	

D Digressions

Hier stehe ich, ich kann nicht anders

MARTIN LUTHER
(1483-1546)

D.1 Surface-Charge of a Discontinuity of Resistivity

Given is a homogeneous current density \mathbf{J} flowing perpendicularly through the interface of two half-spaces of different electrical resistivity ρ_{E1} and ρ_{E2} . The entire space is of homogeneous electric permittivity ϵ_0 and magnetic permeability μ_0 (see Fig. D.1).

For a continuous current density \mathbf{J} , the electrical field \mathbf{E} as well as the electric displacement field \mathbf{D} show a discontinuity at the interface, due to:

$$\mathbf{E}_1 = \rho_{E1}\mathbf{J}, \quad \mathbf{D}_1 = \epsilon_0\rho_{E1}\mathbf{J}, \quad (\text{D.1})$$

$$\mathbf{E}_2 = \rho_{E2}\mathbf{J}, \quad \mathbf{D}_2 = \epsilon_0\rho_{E2}\mathbf{J}. \quad (\text{D.2})$$

From MAXWELL's equation,

$$\oint_{\partial V} \mathbf{D} \cdot d\mathbf{a} = \int_V q_V dV = Q, \quad (\text{D.3})$$

this gives rise to a surface charge density q_F ,

$$q_F = J\epsilon_0(\rho_{E1} - \rho_{E2}). \quad (\text{D.4})$$

Normalizing Eq. (D.4) to J , gives the charge per current, Q/I , independent of the surface area and only depending on the material properties ϵ_0 , ρ_{E1} and ρ_{E2} ,

$$\frac{Q}{I} = \epsilon_0(\rho_{E1} - \rho_{E2}). \quad (\text{D.5})$$

Considering the interface between an ideal superconductor with zero resistivity and copper (at ambient temperature, $\rho_{E,Cu} = 1.553 \cdot 10^{-8} \Omega\text{m}$), the charge per current yields only $Q/I = 1.375 \cdot 10^{-19} \text{CA}^{-1}$. Compared to the elementary electrical charge, *i.e.* $e_m = 1.602 \cdot 10^{-19} \text{C}$, this is less than one electron!

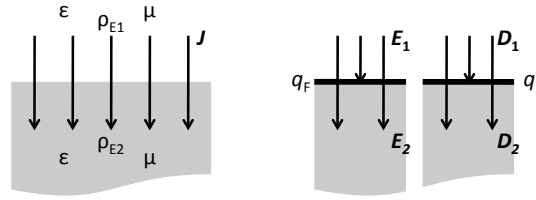


Figure D.1: Surface charge density due to a discontinuity of the electrical resistivity: (left) homogeneous current density, (right) discontinuous electrical field and field of electrical displacement.

Conclusion: Taking into account the discrete nature of the electric charge, this example clearly exceeds assumptions of continuous, homogenized matter in MAXWELL's theory! Nevertheless, the result shows that the surface charge can be totally neglected for any material with a resistivity well below $1 \Omega\text{m}$.

D.2 An Arbitrarily Cut Cylinder

A circular cylinder of radius a is cut by a plane under an arbitrary angle β . The geometry is shown in Fig. D.2 (left) and (center). In a cartesian co-ordinate system parallel to the cylinder axis, the equation of the two intersecting objects read:

$$1 = \left(\frac{x}{a}\right)^2 + \left(\frac{y}{a}\right)^2, \quad (\text{D.6})$$

$$\frac{z}{x} = \tan(\beta). \quad (\text{D.7})$$

The line of intersection is given by

$$\begin{aligned} \mathbf{x}(\varphi) &= a \cos(\varphi) (\mathbf{e}_x + \tan(\beta) \mathbf{e}_z) + a \sin(\varphi) \mathbf{e}_y \\ &= ak \cos(\varphi) \mathbf{e}_k + a \sin(\varphi) \mathbf{e}_y, \end{aligned} \quad (\text{D.8})$$

with \mathbf{e}_k parallel to the plain of intersection and orthogonal to \mathbf{e}_y . Equation (D.8) can be identified as the coordinates of an ellipses. The major half-axis is given by b ,

$$b = ak = a \sqrt{1 + \tan(\beta)^2} = \frac{a}{\cos(\beta)}, \quad (\text{D.9})$$

and the minor half-axis by a . The surface area of the ellipse is given by

$$A_{\text{ellipses}} = \pi ab = \pi \frac{a^2}{\cos(\beta)}. \quad (\text{D.10})$$

The volume of a cylinder terminated by two parallel cuts, is either given by the length of the axis ℓ_{axis} times the surface area of the circular cross-section or by its height ℓ_{height} times the surface area of its elliptical base [Bron 00, p. 160]. Note that $\ell_{\text{height}} = \ell_{\text{axis}} / \cos(\beta)$. See Fig. D.2 (right).

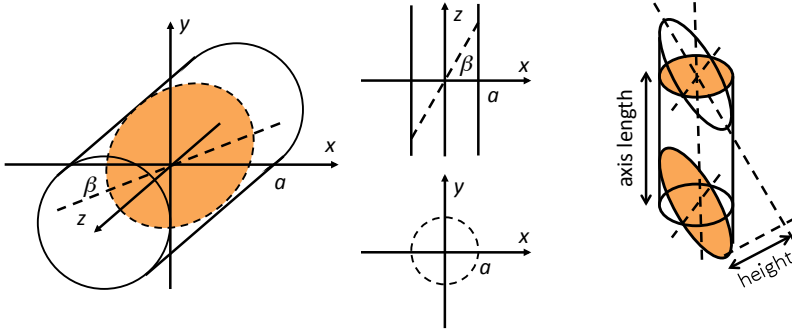


Figure D.2: Arbitrarily cut circular cylinder. (left) elliptical cut shape. (right) volume of a cylinder cut by two parallel planes.

D.3 Critical Current Density Relies on the Model of the Superconductor

The critical current density J_c is not a unique property of the superconducting material but a parameter of the model used to describe the superconductor.

In general, current density as such evades direct measurement. By measuring the current flowing through special cross-sections it is possible to conclude on the local current distribution. In case of superconducting filaments, the small diameter of only some micro meters does not allow to perform such studies. Hence the only quantities which can be measured are the critical current and the superconductor magnetization.

As explained in Sec. A.2.4, the measurement of both quantities is difficult and suffers from technical limitations. Typically only parts of the field and temperature range can be accessed.

Under the assumption of a local current distribution the global quantity critical current as well as the secondary quantity magnetic moment can be converted to the critical current density, see Fig. D.3 (left). The current distribution is a property of the used model of the superconductor. Therefore, this conversion must be performed differently for every model and consequently the same set of measurement data yields different results for the critical current density!

Disregarding this fact, most often analytical formulae are used for the conversion. Before showing a general method of conversion the analytical formulae shall be derived and discussed.

For the critical current measurement a homogeneous distribution of current over the conductor cross-section is assumed. This allows to calculate the critical current density to

$$J_c = \frac{I_c}{A_{SC}}, \quad (\text{D.11})$$

with A_{SC} the superconducting cross-sectional area. Calculating the self-field

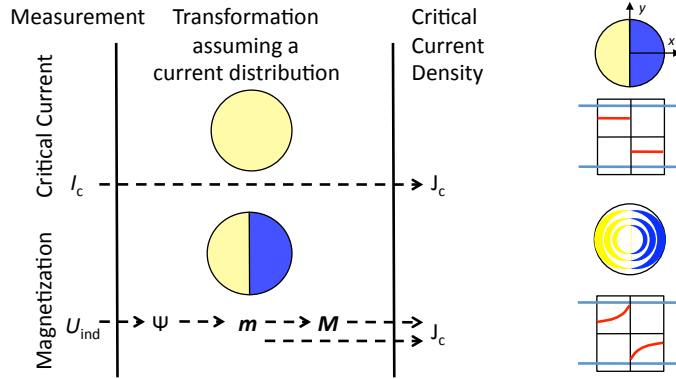


Figure D.3: (left) Transformation of the measured critical current and superconductor magnetization to the critical current density. The conversion relies on an assumed current distribution. (right) Current distribution in a superconducting strand exposed to an external magnetic field for two different models: (top) Wilson model [Wils 83, pp. 165], (bottom) intersecting-ellipses model [Voll 02].

of the applied current, the influence on the field dependence can be corrected [Bout 06]. This approach neglects the influence of screening currents.

According to the Bean model [Bean 62, Bean 64] of superconductor magnetization, the superconductor is screened from an external field by a layer of screening currents. The current density of the screening currents always equals the critical current density. The layer thickness varies with the applied external field. When reaching a certain field level the screening currents cover the full sample. This state is denoted as fully penetrated.

The Wilson model [Wils 83, pp. 165] applies this approach to a circular filament assuming screening currents with an elliptical inner boundary. With increasing field the minor axis of the ellipses decreases and equals zero in fully penetrated state. At this point the current distribution is given by two half-circles of homogeneous current density. The magnetic moment per unit length, m' , of this geometry depends only on the radius a and the current density. Re-arranging yields the critical current density to

$$J_c = m' \frac{3}{4} \frac{1}{a^3}, \quad (\text{D.12})$$

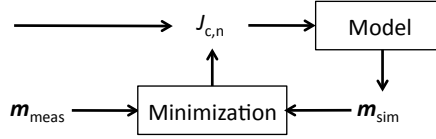
see [Le N 99] and [Voll 02, p. 35]

If the model of superconductor magnetization does not rely on a homogeneous current density as shown in Fig. D.3 (right), the magnetic moment has to be computed from the integral of the local current density J_{mag} ,

$$\mathbf{m} = \int_{V_{sample}} \mathbf{M}(\mathbf{r}') dV' = \int_{V_{sample}} \mathbf{r}' \times \mathbf{J}_{mag}(\mathbf{r}') dV', \quad (\text{D.13})$$

and the conversion can not be performed analytically. Here \mathbf{M} denotes the

local magnetization¹, V_{sample} the sample volume, \mathbf{r}' a position within the sample cross-section, and dV' a differential volume element. This poses an inverse problem and the critical current density can only be determined iteratively:



The function of critical current density would then be defined as the function which minimizes the differences between measured and simulated magnetic moment. The same applies for the critical current transformation.

The intersecting-ellipses model is based on the assumption of screening currents varying over the strand cross-section with local magnetic induction. Regarding a fully penetrated sample this variation is nevertheless small. The error caused by a critical current density assuming homogeneous current densities should be small. For lower fields that approach is inconsistent and might result in undesired limitations of the model!

¹Note: Magnetization \mathbf{M} is also a local quantity and evades direct measurements.

E Formulary and Constants

E.1 Formulary

E.1.1 Inductance of a Ring Conductor

A conductor of radius b is bent to a circle of radius a thus forming a single turn. With a and b both in cm, the geometrical inductance in μH is given by [Gro04, p. 143 (119b)]:

$$L = 0.004\pi a \left[\ln \left(\frac{8a}{b} \right) - 1.75 \right], \quad [L] = \mu\text{H}. \quad (\text{E.1})$$

E.1.2 Field of a Long Solenoid

The field along the axis of an iron-free, long solenoid can be estimated by means of AMPERE's law:

$$B = \mu_0 \frac{N}{h} I, \quad [B] = \text{T}, \quad (\text{E.2})$$

where N denotes the number of windings over the solenoid height h in meter and I the winding current in ampere.

E.2 Constants

Table E.1: Constants used throughout this work

Constant	Symbol	Value	Unit
Critical electrical field	E_c	10^{-5}	Vm^{-1}
Permittivity of empty space	ϵ_0	$8.8541 \cdot 10^{-12}$	$\text{AsV}^{-1}\text{m}^{-1}$
Permeability of empty space	μ_0	$4\pi \cdot 10^{-7}$	$\text{VsA}^{-1}\text{m}^{-1}$
Speed of light in empty space	c_0	$\frac{1}{\sqrt{\mu_0 \epsilon_0}} = 2.9979 \cdot 10^8$	ms^{-1}
Elementary electrical charge	e_m	$1.602 \cdot 10^{-19}$	As
Planck's constant	h_p	$0.626 \cdot 10^{-34}$	Js
Flux quantum	Φ_0	$\frac{h_p}{2e_m} = 2.067 \cdot 10^{-15}$	Vs
Boltzmann constant	k_B	$1.38065 \cdot 10^{-23}$	JK^{-1}
Gas constant	R_{gas}	8.31	$\text{J mol}^{-1}\text{K}^{-1}$
Avogadro number	N_A	$6.022 \cdot 10^{23}$	mol^{-1}

Bibliography

- [Aird 06] G. J. C. Aird, J. Simkin, S. C. Taylor, C. W. Trowbridge, and E. Xu. “Coupled Transient Thermal and Electromagnetic Finite Element Simulation of Quench in Superconducting Magnets”. In: *Proceedings of the ICAP 06*, pp. 69–72, Chamonix, France, October 2006. submitted for publication.
- [Amat 04] M. Amati, M. Sorbi, and G. Volpini. “Material Properties - A Comparison of Sources”. June 2004. EDMS no. 555753.
- [Appl 69] A. D. Appleton. “Superconducting Machines”. *Science Journal*, Vol. 5, No. 4, pp. 41–46, May 1969.
- [Aren 82] R. W. Arenz, C. F. Clark, and W. N. Lawless. “Thermal conductivity and electrical resistivity of copper in intense magnetic fields at low temperatures”. *Physical Review B*, Vol. 26, No. 6, pp. 2727–2732, September 1982.
- [Auch 08] B. Auchmann, R. de Maria, and S. Russenschuck. “Calculation of Time-transient Effects with the CERN Field Computation Program ROXIE”. *IEEE Trans. Appl. Supercond.*, Vol. 18, No. 2, pp. 1569–1572, June 2008.
- [Bagl 08] V. Baglin, A. Ballarino, F. Cerutti, R. Denz, P. Fessia, K. Foraz, M. Fuerstner, W. Herr, M. Karppinen, N. Kos, H. Mainaud-Durand, A. Mereghetti, Y. Muttoni, D. Nisbet, R. Ostojic, H. Prin, J.-P. Tock, R. van Weelderen, E. Wildner, and L. Williams. “Conceptual Design of the LHC Interaction Region Upgrade – Phase-I”. LHC Project Report 1163, November 2008.
- [Baue 07] P. Bauer, H. Rajainmaki, and E. Salpietro. “EFDA Material Data Compilation for Superconductor Simulation”. EFDA CSU, Garching, 04/18/07, April 2007.
- [Bean 62] C. P. Bean. “Magnetization of Hard Superconductors”. *Physical Review Letters*, Vol. 8, pp. 250–253, 1962.
- [Bean 64] C. P. Bean. “Magnetization of High Field Superconductors”. *Review of Modern Physics*, Vol. 36, pp. 31–39, 1964.
- [Bert 06] Bertotti and I. D. Mayergoyz, Eds. *The Science of Hysteresis*. Vol. 1, Academic Press (Elsevier), Amsterdam, Netherlands, first Ed., 2006.

- [Bett 06] S. Bettoni. *Design and integration of superconducting undulators for the LHC beam diagnostics*. PhD thesis, Università degli studi di Milano, Milano, Italy, 2006. Presented on 19 Dec 2006.
- [Blum 19] L. F. Blume and A. Boyajian. “Abnormal Voltages Within Transformers”. *Proceedings of the American Institute of Electrical Engineers*, Vol. 38, pp. 211–248, February 1919.
- [Boci 06] D. Bocian, M. Calvi, and A. Siemko. “Enthalpy Limit Calculations for transient perturbations in LHC magnets”. AT-MTM-IN-2006-021, EDMS 750204, June 2006.
- [Borg 08] F. Borgnolutti. “MQXC Coil Cross-Section 120 mm V3”. Private Communication, June 2008.
- [Borl 04] M. Borlein. *Optimierung eines Quenchedetektierungssystems für supraleitende Magnetspulen*. Master’s thesis, Fachhochschule Würzburg-Schweinfurt, 2004.
- [Bott 00] L. Bottura. “A Practical Fit for the Critical Surface of NbTi”. *IEEE Transactions on Applied Superconductivity*, Vol. 10, No. 1, pp. 1054–1057, March 2000.
- [Bout 01] T. Boutboul, Z. Charifoulline, C. H. Denarié, L. R. Oberli, and D. Richter. “Critical Current Test Facilities for LHC Superconducting NbTi Cable Strands”. Tech. Rep. LHC-Project-Report-520. CERN-LHC-Project-Report-520, CERN, Geneva, Nov 2001.
- [Bout 06] T. Boutboul, S. Le Naour, D. Leroy, L. Oberli, and V. Previtali. “Critical Current Density in Superconducting Nb-Ti Strands in the 100 mT to 11 T Applied Field Range”. *IEEE Transactions on Applied Superconductivity*, Vol. 16, No. 2, pp. 1184–1187, June 2006.
- [Bozo 93] M. Bozorth. *Ferromagnetism*. IEEE Press, 1993.
- [Brec 73] H. Brechna. *Superconducting Magnet Systems*. Springer, Berlin, Germany, first Ed., 1973.
- [Bron 00] I. N. Bronstein, K. A. Semendajew, G. Musiol, and H. Mühlig. *Taschenbuch der Mathematik*. Harri Deutsch, Thun und Frankfurt am Main, Germany, fifth Ed., 2000.
- [Brow 03] K. S. Brown and J. P. Sethna. “Statistical mechanical approaches to models with many poorly known parameters”. *PHYSICAL REVIEW E*, Vol. 68, August 2003.

- [Brun 03] G. Brun. “Series MBA-MBB Cold Mass Instrumentation”. LHC-Project-Document LHC-MB-IP-0001 rev. 1.0, CERN, Geneva, Switzerland, January 2003.
- [Brun 04] O. Brüning, P. Collier, P. Lebrun, S. Myers, R. Ostojic, J. Poole, and P. Proudlock, Eds. *LHC design report - The LHC main ring*. Vol. 1, CERN, Geneva, Switzerland, 2004.
- [Bruz 04] P. Bruzzone. “The index n of the voltage-current curve, in the characterization and specification of technical superconductors”. *Physica C: Superconductivity*, Vol. 401, No. 1-4, pp. 7–14, 2004.
- [Buck 93] W. Buckel. *Supraleitung*. VCH Verlagsgesellschaft mbH, Weinheim, Germany, fifth Ed., 1993.
- [Calv 00] M. Calvi. *Quench Propagation in the LHC Superconducting Busbars*. Master’s thesis, Politecnico Di Torino, 2000.
- [Camp 07] A. M. Campbell. “A new method of determining the critical state in superconductors”. *Superconductor Science and Technology*, Vol. 20, pp. 292–295, February 2007.
- [Cana 93] M. Canali and L. Rossi. “Dynque : a computer code for quench simulation in adiabatic multicoil superconducting solenoids”. INFN-TC-93-06, June 1993.
- [Casp 03] S. Caspi, L. Chiesa, P. Ferracin, S. A. Gourlay, R. Hafalia, R. Hinkins, A. F. Lietzke, and S. Prestemon. “Calculating Quench Propagation With ANSYS”. In: *IEEE Transactions On Applied Superconductivity*, pp. 1714–1717, IEEE, June 2003.
- [CERN 91] “CERN - Ort internationaler wissenschaftlicher Zusammenarbeit”. CERN-Veröffentlichungen (Europäisches Laboratorium für Teilchenphysik), April 1991.
- [Char 06] Z. Charifouline. “Residual Resistivity Ratio (RRR) Measurements of LHC Superconducting NbTi Cable Strands”. *IEEE Transactions on Applied Superconductivity*, Vol. 16, No. 2, pp. 1188–1191, 2006.
- [Choh 07] V. Chohan and E. Veyrunes. “Measurement data from the training quench of magnet MB2381 at 12.82 kA”. Private Communication, July 2007.
- [Chor 98] M. Chorowski, P. Lebrun, L. Serio, and R. van Weelderren. “Thermohydraulics of quenches and helium recovery in the LHC prototype magnet strings”. *Cryogenics*, Vol. 38, No. 5, pp. 533–543, 1998.

- [Clar 77] A. F. Clark and J. W. Ekin. “Defining Critical Current”. *IEEE Transactions on Magnetics*, Vol. MAG-13, No. 1, pp. 38–40, January 1977.
- [Cobi 41] J. D. Cobine. *Gaseous Conductors*. McGraw-Hill Book Company, Inc., New York, USA, first Ed., 1941.
- [Coll 55] L. Collatz. *Numerische Behandlung von Differentialgleichungen*. Springer, Berlin, Germany, 1955.
- [Coul 94] L. Coull, D. Hagedorn, V. Remondino, and F. Rodriguez-Mateos. “LHC Magnet Quench Protection System”. *IEEE Transactions on Magnetics*, Vol. 30, No. 4, pp. 1742–1745, July 1994.
- [Coul 96] L. Coull, D. Hagedorn, G. Krainz, F. Rodriguez-Mateos, and R. Schmidt. “Electrodynamic Behaviour of the LHC Superconducting Magnet String during a Discharge”. In: *5th European Particle Accelerator Conference EPAC '96*, pp. 2240–2242, CERN, Barcelona, Spain, June 1996.
- [Dahl 00] K. Dahlerup-Petersen, B. Kazmine, V. Popov, L. Sytchev, L. Vassiliev, and V. Zubko. “Energy Extraction Resistors for the Main Dipole and Quadrupole Circuits of the LHC”. LHC Project Report 421, September 2000.
- [Dahl 01] K. Dahlerup-Petersen, A. Medvedko, A. Erokhin, B. Kazmin, V. Sytchev, and L. Vassiliev. “Energy extraction in the CERN Large Hadron Collider: a project overview”. *Pulsed Power Plasma Science, 2001. PPPS-2001. Digest of Technical Papers*, Vol. 2, pp. 1473–1476, 2001.
- [Deby 12] P. Debye. “Zur Theorie der spezifischen Wärme”. *Annalen der Physik*, Vol. 39(4), pp. 789–839, 1912.
- [Deme 99] N. A. Demerdash and T. W. Nehl. “Electrical Machinery Parameters and Torques by Current and Energy Perturbations from Field Computations - Part I: Theory and Formulation”. *IEEE Transactions on Energy Conversion*, Vol. 14, No. 4, pp. 1507–1513, December 1999.
- [Denz 01] R. Denz and F. Rodriguez-Mateos. “Detection of Resistive Transitions in LHC Superconducting Components”. LHC Project Report 482, June 2001.
- [Denz 06] R. Denz. “Electronic Systems for the Protection of Superconducting Elements in the LHC”. *IEEE Transactions on Applied Superconductivity*, Vol. 16, No. 2, pp. 1725–1728, 2006.

- [Denz 08a] R. Denz, K. Dahlerup-Petersen, and K. H. Mess. “Electronic Systems for the Protection of Superconducting Devices in the LHC”. Tech. Rep. LHC-PROJECT-Report-1142, CERN, Geneva, Aug 2008.
- [Denz 08b] R. Denz. “Current measurements of the recovering MQY in Q6”. Private Communication, July 2008.
- [Devr 04] A. Devred. “Practical Low-Temperature Superconductors For Electromagnets”. Tech. Rep. CERN-2004-006, CERN, Geneva, Switzerland, 2004.
- [Devr 06] A. Devred, B. Baudouy, D. E. Baynham, T. Boutboul, S. Canfer, M. Chorowski, P. Fabbriatore, S. Farinon, H. Félice, P. Fessia, J. Fydrych, V. Granata, M. Greco, J. Greenhalgh, D. Leroy, P. Loverige, M. Matkowski, G. Michalski, F. Michel, L. R. Oberli, A. den Ouden, D. Pedrini, S. Pietrowicz, J. Polinski, V. Previtali, L. Quettier, D. Richter, J. M. Rifflet, J. Rochford, F. Rondeaux, S. Sanz, C. Scheuerlein, N. Schwerg, S. Sgobba, M. Sorbi, F. Toral-Fernandez, R. van Weelderen, P. Védrine, and G. Volpini. “Overview and status of the Next European Dipole (NED) joint research activity”. In: *Superconductor Science and Technology*, pp. 67–83, CERN, Geneva, Switzerland, March 2006.
- [Devr 89] A. Devred. “General Formulas for the Adiabatic Propagation Velocity of the Normal Zone”. *IEEE Transactions on Magnetics*, Vol. 25, No. 2, pp. 1698–1705, March 1989.
- [Devr 95] A. Devred and T. Ogitsu. “Influence of eddy currents in superconducting particle accelerator magnets using Rutherford-type cables”. In: *CAS - CERN Accelerator School : Superconductivity in Particle Accelerators*, pp. 93–122, CERN, Geneva, Switzerland, May 1995.
- [Doro 80] G. L. Dorofeyev, A. B. Imenitov, and E. Y. Klimenko. “Voltage current characteristics of type III superconductors”. *Cryogenics*, Vol. 20, No. 6, pp. 307–312, 1980.
- [Dres 95] L. Dresner. *Stability of Superconductors*. Plenum Press, New York, USA, 1995.
- [DuPo 96] DuPont. “Kapton (C) polyimide film”. Technical Information, June 1996.
- [Eber 77] P. H. Eberhard, M. A. Green, W. B. Michael, J. D. Taylor, and W. A. Wenzel. “Tests on large diameter superconducting solenoids designed for colliding beam accelerators”. *IEEE Transactions on Magnetics*, Vol. MAG-13, No. 1, pp. 78–81, 1977.

- [Ekin 81] J. W. Ekin. “Strain Scaling Law For Flux Pinning in NbTi, Nb₃Sn, Nb-Hf/Cu-Sn-Ga, V₃Ga and Nb₃Ge”. In: *IEEE Transactions on Magnetics*, pp. 658–661, IEEE, 1981.
- [Elsch 92] H. Elschner and A. Möschwitzer. *Einführung in die Elektrotechnik-Elektronik*. Verlag Technik Berlin, Berlin, Germany, third Ed., 1992.
- [Evan 09] L. Evans, Ed. *The Large Hadron Collider: a Marvel of Technology*. EPFL Press, Lausanne, Switzerland, first Ed., 2009.
- [Fess 08] P. Fessia. “MQXC Parameters (Heater Layout, Geometry, Winding Schemes ...)”. Private Communication, June 2008.
- [Flei 99] D. Fleischmann. *Basiswissen Elektrotechnik*. Vogel Buchverlag, Würzburg, Germany, first Ed., 1999.
- [Floc 03] E. Floch. “Specific Heat, Thermal Conductivity and Resistivity of Cu and NbTi - A Bibliography”. AT-MTM, Aug. 2003.
- [Floc 08] E. Floch. “Preliminary quench study for 43 SIS300 quadrupoles in series”. MT Internal Note: MT-INT-ErF-2008-0?? (draft), May 2008.
- [Gilo 08] C. Giloux. “Current and voltage measurements of the LHC MCBX”. Private Communication, May 2008.
- [Gran 08] P. P. Granieri, M. Calvi, P. Xydi, B. Baudouy, D. Bocian, L. Bottura, M. Breschi, and A. Siemko. “Stability Analysis of the LHC cables for Transient Heat Depositions”. *IEEE Trans. Appl. Supercond.*, Vol. 18, No. 2, pp. 1257–1262, June 2008.
- [Gree 84a] M. A. Green. “Quench back in thin superconducting solenoid magnets”. *Cryogenics*, Vol. 24, No. 1, pp. 3–10, 1984.
- [Gree 84b] M. A. Green. “The role of quench back in quench protection of a superconducting solenoid”. *Cryogenics*, Vol. 24, No. 12, pp. 659–668, 1984.
- [Gree 88] M. A. Green. “Generation of the J_c, H_c, T_c Surface for Commercial Superconductor Using Reduced-State Parameters”. Lawrence Berkeley Laboratory, SSC-N-502, April 1988.
- [Grov 04] F. W. Grover. *Inductance Calculations*. Dover Phoenix Editions, Mineola, New York, USA, 2004.
- [Hein 07] H. Heinrich. “Auf der Suche nach Gottes Urknall”. *Playboy*, March 2007.
- [Henk 01] H. Henke. *Elektromagnetische Felder*. Springer, Heidelberg, Germany, first Ed., 2001.

- [Henn 04] W. Henning. “FAIR - an international accelerator facility for research with ions and antiprotons”. In: *Proceedings of EPAC 2004*, pp. 50–53, Nov. 2004.
- [Hila 03] A. Hilaire and C. Vollinger. “Quench simulations for the LHC Undulator”. LHC Project Note 328, Oct. 2003.
- [Hust 75] J. G. Hust and P. J. Giarratano. “Thermal Conductivity and Electrical Resistivity Standard Reference Materials: Electrolytic Iron, SRM’s 734 and 797 from 4 to 1000 K”. NBS Special Publication 260-50, U.S. Department of Commerce / National Bureau of Standards, Boulder, Colorado, USA, June 1975.
- [IEV 08] “IEV 815-04-64”. November 2008. <http://www.electropedia.org/iev/iev.nsf/display?openform&ievref=815-04-64>.
- [Imba 03] L. Imbasciati. *Studies of Quench Protection in Nb₃Sn Superconducting Magnets for Future Particle Accelerators*. PhD thesis, Technische Universität Wien, Wien, Austria, 2003.
- [Iwas 05] Y. Iwasa. “Stability and Protection of Superconducting Magnets—A Discussion”. *IEEE Transactions on Applied Superconductivity*, Vol. 15, No. 2, pp. 1615–1620, June 2005.
- [Iwas 94] Y. Iwasa. *Case Studies in Superconducting Magnets*. Plenum, New York, USA, 1994.
- [Jean 96] J. B. Jeanneret, D. Leroy, L. R. Oberli, and T. Trenkler. “Quench levels and transient beam losses in LHC magnets”. Tech. Rep. CERN-LHC-Project-Report-44, CERN, Geneva, May 1996.
- [Jens 80] J. E. Jensen, W. A. Tuttle, R. B. Stewart, H. Brechna, and A. Prodel, Eds. *Selected Cryogenic Data Book*. Vol. 1, Brookhaven National Laboratory, 1980.
- [Kanb 87] K. Kanbara. “Hysteresis loss of a round superconductor carrying a DC transport current in an alternating transverse field”. *Cryogenics*, Vol. 27, pp. 621–630, November 1987.
- [Karp 08a] M. Karppinen. “Parameters for the MCBX”. Private Communication, April 2008.
- [Karp 08b] M. Karppinen. “Polyvinyl acetate (PVA) Thermal Conductivity”. Private Communication, May 2008.
- [Karp 08c] M. Karppinen. “Quench propagation velocity LHC MCBX”. Private Communication, June 2008.

- [Karp 99] M. Karppinen, A. Ijspeert, N. Hauge, and B. R. Nielsen. "The Development of the Inner Triplet Dipole Corrector (MCBX) for LHC". CERN-LHC-Project-Report-265, February 1999.
- [Kim 00] S.-W. Kim. "Material Properties for Quench Simulation (Cu, NbTi and Nb₃Sn)". TD-00-041, 2000.
- [Kim 01] S.-W. Kim. "Quench Simulation Program for Superconducting Accelerator Magnets". In: *IEEE Particle Accelerator Conference PAC '01*, pp. 3457–3459, FNAL, IEEE, Batavia, USA, June 2001.
- [Kirb 07] G. A. Kirby, A. P. Verweij, L. Bottura, B. Auchmann, and N. Catalan Lasheras. "Fast Ramping Superconducting Magnet Design Issues for Future Injector Upgrades at CERN". sent in for publication to IEEE Transactions on Applied Superconductivity, August 2007.
- [Kozu 06] S. Kozub, I. Bogdanov, A. Seletsky, P. Shcherbakov, V. Sytnik, L. Tkachenko, and V. Zubko. "Final Report on the Research and Development Contract "Technical Design of the SIS-300 Dipole Model"". Tech. Rep., IHEP, Protvino, July 2006.
- [Krai 97] G. Krainz. *Quench Protection and Powering in a String of Superconducting Magnets for the Large Hadron Collider*. PhD thesis, Technische Universität Graz, Graz, Austria, Feb. 1997.
- [Kurz 04] S. Kurz. "Some Remarks about Flux Linkage and Inductance". *Advances in Radio Science*, No. 2, pp. 39–44, 2004.
- [Lapp 91] R. Lappe, H. Conrad, and M. Kronberg. *Leistungselektronik*. Verlag Technik Berlin, Ostberlin, German Democratic Republic, second Ed., 1991.
- [Laty 97] D. Latypov, P. McIntyre, and W. Shen. "Quench Simulation for 16 T Dipole Built at Texas A&M University". In: *17th Particle Accelerator Conference*, pp. 3446–3448, Texas A&M University, Vancouver, Canada, May 1997.
- [Le N 01] S. Le Naour, R. Wolf, J. Billan, and J. Genest. "Test station for magnetization measurements on large quantities of superconducting strands". *IEEE Transactions on Applied Superconductivity*, Vol. 11, No. 1, pp. 3086–3089, 2001.
- [Le N 99] S. Le Naour, L. Oberli, R. Wolf, R. Pusniak, A. Szewczyk, A. Wiesniewski, H. Fikis, M. Foitl, and H. Kirchmayr. "Magnetization Measurement on LHC Superconducting Strands". *IEEE Transactions on Applied Superconductivity*, Vol. 9, No. 2, pp. 1763–1766, June 1999.

- [Lebr 97] P. Lebrun. “Superfluid Helium as a Technical Coolant”. LHC Project Report 125, June 1997.
- [Lefe 95] P. Lefèvre and T. Pettersson, Eds. *The Large Hadron Collider - Conceptual Design*. CERN, Geneva, Switzerland, 1995.
- [Lero 06] D. Leroy. “Review of the R&D and Supply of the LHC Superconducting Cables”. *IEEE Transactions on Applied Superconductivity*, Vol. 16, No. 2, pp. 1152–1159, 2006.
- [Lero 93] D. Leroy, J. Krzywinski, V. Remondino, L. Walckiers, and R. Wolf. “Quench observation in LHC superconducting one meter long dipole models by field perturbation measurements”. *Applied Superconductivity, IEEE Transactions on*, Vol. 3, No. 1, pp. 781–784, Mar 1993.
- [Lewi 96] R. W. Lewis, K. Morgan, H. R. Thomas, and K. Seetharamu. *The Finite Element Method in Heat Transfer Analysis*. Wiley & Sons, July 1996.
- [Lide 06] D. R. Lide, Ed. *CRC Handbook of Chemistry and Physics*. Taylor and Francis, Boca Raton, Florida, USA, 86th Ed., 2006. Internet Version 2006, <<http://www.hbcpnetbase.com>>.
- [Lin 95] Z. Lin. “Evaluation on Two PVA Adhesives for Gluing Transformer Insulating Components”. In: *Electrical Electronics Insulation Conference, 1995, and Electrical & Coil Winding Conference. Proceedings*, pp. 119–121, 1995.
- [Mari 04] R. de Maria. *Time Transient Effects in Superconducting Magnets*. Master’s thesis, Università degli Studi di Roma “La Sapienza”, Rome, Italy, 2004.
- [Mass 07] P. J. Masson, V. R. Rouault, G. Hoffmann, and C. A. Lungo. “Development of Quench Propagation Models for Coated Conductors”. sent in for publication to *IEEE Transactions on Applied Superconductivity*, August 2007.
- [McAs 88] M. S. McAshan. “MIITs Integrals for Copper and for Nb -46.5 wt% Ti”. SSC Laboratory Report, SSC-N-468, February 1988.
- [Mess 96] K.-H. Mess, P. Schmüser, and S. Wolff. *Superconducting Accelerator Magnets*. World Scientific Publishing Co., New Jersey, USA., 1996.
- [MQXC 08a] “MQXC Parameters - Agreed on Meeting”. Private Communication, June 2008.
- [MQXC 08b] “MQXC Parameters - Agreed on Meeting”. Private Communication, July 2008.

- [Nati 08] National Institute of Standards and Technology (NIST). “Material Properties: Polyimide (Kapton)”. October 2008. <http://cryogenics.nist.gov/MPropsMAY/Polyimidehtm>.
- [Naun 02] D. Naunin. “Einführung in die Netzwerktheorie”. Vorlesungsskript, 2002.
- [Okam 36] T. Okamura. “Change of thermal energy due to magnetisation in Ferromagnetic substances.”. *Science Reports of the Tohoku Imperial University*, Vol. 24, pp. 745–807, February 1936.
- [Osto 08] R. Ostojic. “MQXC Parameters (Critical Current, Heater Circuits, ...)”. Private Communication, June 2008.
- [Oude 01] A. den Ouden, W. A. J. Wessel, G. A. Kirby, T. Taylor, N. Siegel, and H. H. ten Kate. “Progress in the Development of an 88-mm Bore 10 T Nb3Sn Dipole Magnet”. In: *IEEE Transactions On Applied Superconductivity*, pp. 2268–2271, March 2001.
- [Peir 04] G. Peiro. “Steel Measurement Report”. CERN Report no. 2004-10-08, 2004. EDMS no. 496251.
- [Peti 19] A.-T. Petit and P.-L. Dulong. “Recherches sur quelques points importants de la Théorie de la Chaleur”. *Annales de Chimie et de Physique*, Vol. 10, pp. 395–413, 1819.
- [Prop 92] *Properties of Copper and Copper Alloys at Cryogenic Temperature*. National Institute of Standards, 1992.
- [Pugn 07] P. Pognat. “Measurement of quench heater delays”. Private Communication, July 2007.
- [Purc 89] E. M. Purcell. *Elektrizität und Magnetismus*. Vol. 2 of *Berkeley Physik Kurs*, Vieweg, Braunschweig, Germany, fourth Ed., 1989.
- [Rade 02] R. Radebaugh. “Cryogenics”. *The MacMillan Encyclopedia Of Chemistry*, 2002.
- [Rodr 00] F. Rodríguez-Mateos, P. Pognat, S. Sanfilippo, R. Schmidt, A. Siemko, and F. Sonnemann. “Quench Heater Experiments on the LHC Main Superconducting Magnets”. LHC Project Report 418, September 2000.
- [Rodr 01] F. Rodríguez-Mateos and F. Sonnemann. “Quench Heater Studies for the LHC Magnets”. LHC Project Report 485, August 2001.

- [Rodr 96] F. Rodríguez-Mateos, G. Gerin, and A. Marquis. “Quench protection test results and comparative simulations on the first 10 metre prototype dipoles for the Large Hadron Collider”. *IEEE Transactions on Magnetics*, Vol. 32, No. 4, pp. 2109–2112, July 1996.
- [Rodr 97] F. Rodriguez-Mateos, F. Calmon, A. Marquis, and R. Schmidt. “Quaber 4.0 User Guide”. LHC-PROJECT-NOTE, Apr. 1997. Draft.
- [Roeb 15] L. Roebel. “Electrical Conductor”. Patent, 1915. No. 1,144,252.
- [Ross 04] L. Rossi and M. Sorbi. “QLASA: A Computer Code for Quench Simulation in Adiabatic Multicoil Superconducting Windings”. INFN-TC-04-13, July 2004.
- [Ross 06] L. Rossi and M. Sorbi. “MATPRO: A Computer Library of Material Property at Cryogenic Temperature”. CARE-Note-2005-018-HHH, INFN-TC-06/02, January 2006.
- [Russ 07] S. Russenschuck. *Electromagnetic Design and Mathematical Optimization Methods in Magnet Technology*. CERN, Geneva, Switzerland, fifth Ed., 2007. ISBN: 92-9083-242-8.
- [Russ 98] S. Russenschuck, Ed. *ROXIE: Routine for the optimization of magnet X-sections, inverse field calculation and coil end design, Proceedings of the First international ROXIE Users Meeting and Workshop*, CERN, Geneva, Switzerland, March 1998.
- [Schm 00] R. Schmidt, C. Giloux, A. Hilaire, A. Ijspeert, F. Rodríguez-Mateos, and F. Sonnemann. “Protection of the Superconducting Corrector Magnets for the LHC”. LHC Project Report 419, September 2000.
- [Schn 73] G. Schnell. *Magnete*. Verlag Karl Thieme, München, Germany, 1973.
- [Schw 05a] N. Schwerg. *Electromagnetic Design Study for a Large Bore 15T Superconducting Dipole Magnet*. Master’s thesis, Technische Universität Berlin, Berlin, Germany, Nov. 2005.
- [Schw 05b] N. Schwerg, A. Devred, and C. Vollinger. “Estimation of the Critical Current Density for the Strand Used for NED”. Technical Note 2005-07, EDMS 638344, Sep. 2005.
- [Schw 06] N. Schwerg and C. Vollinger. “Development of a Current Fit Function for NbTi to be Used for Calculation of Persistent Current Induced Field Errors in the LHC Main Dipoles”. *IEEE Transactions On Applied Superconductivity*, Vol. 16, No. 2, pp. 1828–1831, June 2006.

- [Schw 09] N. Schwerg, B. Auchmann, , K.-H. Mess, and S. Russenschuck. “Numerical Study of Quench Protection for Fast-Ramping Accelerator Magnets”. *IEEE Trans. Appl. Supercond.*, Vol. 19, No. 3, June 2009. submitted for publication.
- [Schw 70] F. R. Schwartzberg, Ed. *Cryogenic Material Data Handbook*. Vol. 1, National Technical Information Service (NTIS), Springfield Va. 22151, USA, 1970.
- [Seeb 98] B. Seeber, Ed. *Handbook of Applied Superconductivity*. Vol. 1, Institut of Physics Publishing, Bristol (UK), 1 Ed., 1998.
- [Seld 73] H. Selder. *Einführung in die Numerische Mathematik für Ingenieure*. Carl Hanser Verlag, München, Germany, first Ed., 1973.
- [Shch 04] P. Shcherbakov, I. Bogdanov, S. Kozub, L. Tkachenko, E. Fischer, F. Klos, G. Moritz, and C. Muehle. “Magnetic properties of Silicon electrical steel and its application in fast cycling superconducting magnets at low temperatures”. In: *Proceedings of RuPAC XIX, Dubna 2004*, 2004.
- [Siem 03] A. Siemko. “Cold tests: magnet powering aspects”. LHC Project Workshop - Chamonix XII, March 2003.
- [Siem 05] A. Siemko and M. Calvi. “Beam Loss Induced Quench Levels”. In: *LHC Project Workshop - Chamonix XIV*, pp. 296–298, CERN, Geneva, Switzerland, 2005.
- [Siem 95] A. Siemko, J. Billan, G. Gerin, D. Leroy, L. Walckiers, and R. Wolf. “Quench localization in the superconducting model magnets for the LHC by means of pick-up coils”. *IEEE Trans. Appl. Supercond.*, Vol. 5, No. 2, pp. 1028–1031, June 1995.
- [Smed 93] K. M. Smedley and R. E. Shafer. “Measurement of AC Electrical Characteristics of SSC Superconducting Dipole Magnets”. In: J. Rossbach, Ed., *XVth International Conference on High Energy Accelerators HEACC’92*, pp. 629–631, World Scientific, Singapore, Singapore, 1993.
- [Sonn 01a] F. Sonnemann. *Resistive Transition and Protection of LHC Superconducting Cables and Magnets*. PhD thesis, Rheinisch-Westfälische Technische Hochschule Aachen, Aachen, Germany, May 2001.
- [Sonn 01b] F. Sonnemann and M. Calvi. “Quench simulation studies: Program documentation of SPQR Simulation Program for Quench Research”. LHC Project Note 265, July 2001.

- [Stek 65] Z. J. J. Stekly and J. L. Zar. “Stable Superconducting Coils”. *IEEE Transactions on Nuclear Science*, Vol. 12, pp. 367–372, 1965.
- [Stoe 05] Stoer. *Numerische Mathematik 1*. Springer, Berlin, Germany, ninth Ed., 2005.
- [Summ 91] L. T. Summers, M. W. Guinan, J. R. Miller, and P. A. Hahn. “A Model for the Prediction of Nb₃Sn Critical Current as a Function of Field, Temperature, Strain and Radiation Damage”. In: *IEEE Transactions On Magnetics*, pp. 2041–2044, March 1991.
- [Supe 07a] “Superconductivity – Part 1: Critical current measurements - DC critical current of Nb-Ti composite superconductors”. International Standard IEC 61788-1:2006, June 2007.
- [Supe 07b] “Superconductivity – Part 4: Residual resistance ratio measurement – Residual resistance ratio of Nb-Ti composite superconductors”. International Standard IEC 61788-4, April 2007.
- [Town 35] A. Townsend. “The Change in Thermal Energy Which Accompanies a Change in Magnetization of Nickel”. *Phys. Rev.*, Vol. 47, No. 4, pp. 306–310, Feb 1935.
- [Van 86] S. W. Van Sciver. *Helium Cryogenics*. Plenum Press, New York, USA, first Ed., 1986.
- [Verg 02] A. Vergara Fernandez, R. Denz, and F. Rodriguez-Mateos. “Reliability analysis for the quench detection in the LHC machine”. LHC Project Report 596, July 2002.
- [Verw 05] A. Verweij. “CUDI: Users Manual”. Tech. Rep., CERN, September 2005.
- [Verw 06] A. Verweij. “CUDI : A Model for Calculation of Electrodynamic and Thermal Behaviour of Superconducting Rutherford Cables”. Departmental Report, Aug. 2006. CERN-AT-2006-005.
- [Verw 07a] A. P. Verweij and A. K. Ghosh. “Critical Current Measurements of the Main LHC Superconducting Cables”. *IEEE Trans. Nucl. Sci.*, Vol. 17, pp. 1454–1460, February 2007.
- [Verw 07b] A. Verweij. “Values for time-transient/losses calculation of LHC MB magnets”. Private Communication, July 2007.
- [Verw 08a] A. P. Verweij, V. Baggiolini, A. Ballarino, B. Bellesia, F. Bordry, A. Cantone, M. Casas Lino, A. Castaneda Serra, C. Castillo Trello, N. Catalan-Lasheras, Z. Charifoulline,

- G. Coelingh, K. Dahlerup-Petersen, G. D'Angelo, R. Denz, S. Fehér, R. Flora, M. Gruwé, V. Kain, B. Khomenko, G. Kirby, A. MacPherson, A. Marqueta Barbero, K.-H. Mess, M. Modena, R. Mompò, V. Montabonnet, S. le Naour, D. Nisbet, V. Parma, M. Pojer, L. Ponce, A. Raimondo, S. Redaelli, H. Reymond, D. Richter, G. de Rijk, A. Rijlart, I. Romera Ramirez, R. Saban, S. Sanfilippo, R. Schmidt, A. Siemko, M. Solfaroli Camillocci, Y. Thurel, H. Thiessen, W. Venturini-Delsolaro, A. Vergara Fernandez, R. Wolf, and M. Zerlauth. "Performance of the Main Dipole Magnet Circuits of the LHC during Commissioning". Tech. Rep. LHC-PROJECT-Report-1140, CERN, Geneva, August 2008.
- [Verw 08b] A. Verweij. "The n-value of superconducting cables". Private Communication, October 2008.
- [Verw 95] A. Verweij. *Electrodynamics of Superconducting Cables in Accelerator Magnets*. PhD thesis, Universiteit Twente, Enschede, Netherlands, 1995.
- [Voll 02] C. Vollinger. *Superconductor Magnetization Modeling for the Numerical Calculation of Field Errors in Accelerator Magnets*. PhD thesis, Technische Universität Berlin, CERN, Switzerland, Oct. 2002.
- [Walc 04] L. Walckiers. "Cold Tests of the MB Cold Masses in SM18*". In: *LHC Project Workshop - Chamonix XIII*, 2004.
- [Walt 74] C. R. Walters. "Design of multistrand conductors for superconducting magnet windings". Brookhaven National Laboratory Informal Report - BNL 18928 (AADD 74-2) 30-1, 1974.
- [Warn 86] W. H. Warnes and D. C. Larbalestier. "Critical current distributions in superconducting composites". *Cryogenics*, Vol. 26, No. 12, pp. 643–653, 1986.
- [Will 00] K. Wille. *The Physics of Particle Accelerators - an introduction*. Oxford University Press, Oxford, UK, first Ed., 2000.
- [Will 08a] G. P. Willering, A. P. Verweij, J. Kaugerts, and H. H. J. ten Kate. "Stability of Nb-Ti Rutherford Cables Exhibiting Different Contact Resistances. oai:cds.cern.ch:1116078". Tech. Rep. CERN-AT-2008-009, CERN, Geneva, Jul 2008.
- [Will 08b] G. P. Willering, A. P. Verweij, C. Scheuerlein, A. Den Ouden, and H. H. J. ten Kate. "Difference in Stability Between Edge and Center in a Rutherford Cable". *IEEE Transactions on Applied Superconductivity*, Vol. 18, No. 2, pp. 1253–1256, June 2008.

- [Wils 68] M. N. Wilson. “Computer Simulation of the Quenching of a Superconducting Magnet”. Rutherford High Energy Laboratory, Internal Report, RHEL/M 151, 1968.
- [Wils 72] M. N. Wilson. “Rate Dependent Magnetization in Flat Twisted Superconducting Cables”. RHEL/M/A26, September 1972.
- [Wils 83] M. N. Wilson. *Superconducting Magnets*. Monographs on Cryogenics, Oxford University Press, New York, USA, 1983.
- [Wlod 06] Z. Wlodarski. “Analytical description of magnetization curves”. *Physica B*, Vol. 373, pp. 323–327, 2006.
- [Wrig 03] J. D. Wright, A. N. Johnson, and M. R. Moldover. “Design and Uncertainty Analysis for a PVTt Gas Flow Standard”. *Journal of Research of the National Institute of Standards and Technology*, Vol. 108, No. 1, pp. 21–47, 2003.

List of Figures

1.1	Destroyed coil windings of the LHC main bending magnet MB3004 after an inter-turn short.	2
2.1	CAD image of the superconducting LHC main bending magnet.	8
2.2	CAD image of a double aperture coil configuration. Quadrant of one aperture of the coil cross-section of the LHC MB.	9
2.3	LHC MB strand and cable.	10
2.4	Photo of the coil cross-section of the LHC MQY.	11
2.5	Sketch of other superconducting magnet configurations.	14
2.6	Different phenomena in superconducting magnets which may cause a quench.	15
2.7	Comparison of the electrical resistivity of the different materials.	16
3.1	Different models interacting in a quench simulation.	22
3.2	Numbering schemes.	23
3.3	Current sharing.	25
3.4	Magnetic field computation: Domain subdivision and field re-composition.	26
3.5	Calculation of the field of a conductor.	27
3.6	Generic electrical network model.	31
3.7	Diode model.	32
3.8	Longitudinal cut through the discretized coil winding with lumped electrical elements.	35
3.9	Finite volumes and linear/constant approximations for the thermal network model.	37
3.10	Lumped thermal network model in comparison to the the coil/-conductor geometry.	37
3.11	Comparison of the thermal conductivity and volumetric specific heat of all relevant materials.	39
3.12	Influence of liquid helium in the coil windings on the thermal model.	41
3.13	Quench heater model.	42
3.14	Block diagram of the quench simulation algorithm.	45
4.1	LHC MB. Schematic coil cross-section and iron yoke. Outer iron diameter 570 mm.	47
4.2	LHC MB coil layout and electrical circuit.	48
4.3	LHC MB average cable losses and quench heater delays.	49
4.4	LHC MB reproduction of current measurements.	50

4.5	LHC MB reproduction of measured pole voltages.	51
4.6	LHC MB temperature margin for quench in the tunnel.	53
4.7	LHC MB 3D temperature plot for a quench in the tunnel.	53
4.8	LHC MCBX. Schematic coil cross-section and iron yoke. Outer iron diameter 330 mm.	54
4.9	LHC MCBX Magnet.	54
4.10	LHC MCBX temperature margin.	55
4.11	LHC MCBX current decrease and temperature distribution.	56
4.12	MCBX quench propagation over outer coil.	56
4.13	LHC MCBX potential to ground during a quench.	57
4.14	LHC MCBX voltage along the coil winding and reason to quench.	57
4.15	LHC MQY. Schematic coil cross-section and iron yoke. Outer iron diameter around 495 mm.	58
4.16	LHC MQY magnet.	58
4.17	LHC MQY current decrease and temperature margin to quench.	59
5.1	Inner Triplet Upgrade MQXC schematic coil cross-section and iron yoke. Outer iron diameter 550 mm.	61
5.2	Inner Triplet Upgrade MQXC conductor numbering and cur- rent and temperature change for an unprotected quench.	63
5.3	Inner Triplet Upgrade MQXC temperature margin over con- ductors versus time for an unprotected quench.	64
5.4	Inner Triplet Upgrade MQXC temperature over the coil cross- section for an unprotected quench.	64
5.5	Inner Triplet Upgrade MQXC quench heater layouts and per- formance.	65
5.6	Inner Triplet Upgrade MQXC hot-spot temperature for differ- ent heater setups.	67
5.7	Inner Triplet Upgrade MQXC temperature margin over con- ductors versus time for different heater setups	67
5.8	Inner Triplet Upgrade MQXC dump resistor study in case of a quench and no pre-existing quench.	68
5.9	Inner Triplet Upgrade MQXC dump resistor study in case of quench for various dump resistors.	69
5.10	Inner Triplet Upgrade MQXC energy extraction with dump resistor.	69
5.11	Inner Triplet Upgrade MQXC comparison of the three different protection methods.	70
5.12	Fast-Ramping Dipole. Schematic coil cross-section and iron yoke. Outer iron diameter 504.6 mm.	71
5.13	Fast-Ramping Dipole standard and modified coil cross-section.	72
5.14	Fast-Ramping Dipole temperature variation during ramp-cycle. Current and peak temperature in a magnet during an up-ramp to the quench	73
5.15	Fast-Ramping Dipole temperature margin to quench versus time for an up-ramp.	74

5.16	Fast-Ramping Dipole current decay and peak-temperature for quenches during the up-ramp phase.	75
5.17	Current- and peak-temperature evolution for quenches during the down-ramp	75
5.18	Fast-Ramping Dipole peak-temperature and current evolution during quenches.	76
7.1	Margins to quench.	82
7.2	Temperature margin to quench.	83
7.3	Critical temperature as a function of applied current density and local magnetic induction. Margin on the load-line.	84
7.4	Energy reserve density as function of temperature and excitation.	85
7.5	Energy margin to quench for the LHC MB.	86
7.6	MIITs computation.	88
7.7	Energy exchange between different physical systems and different volumes.	90
7.8	Self inductance geometry.	94
7.9	Inductance of a bulk or Rutherford-type conductor.	97
7.10	ROXIE simulation of the differential inductance of the LHC main bending magnet considering field dependent and hysteretic materials.	98
7.11	Differential inductance of a magnet with time-transient effects	99
7.12	Differential inductance by means of hysteresis.	99
7.13	Simplified electrical networks containing superconducting and normal conducting elements.	101
7.14	Current-sharing	103
7.15	Model problem circuit and solution of the initial value problem.	104
7.16	Currents induced in a superconducting current loop with resistive joint. Geometry and model of the superconductor.	106
7.17	Superconductor with resistive joint.	107
7.18	Graphical solution for current sharing.	108
7.19	Inter-filament coupling currents.	111
7.20	Model for inter-strand coupling currents.	112
7.21	Critical state model geometry and excitation current.	116
7.22	Hysteresis losses: Screening current density and inner magnetic field.	118
7.23	Hysteresis losses: Magnetic induction and flux.	119
7.24	Hysteresis losses: Time derivative of the magnetic induction and electrical field.	119
7.25	Hysteresis loop.	119
7.26	Hysteresis losses: Energy and power versus time.	121
7.27	Rutherford-type cable.	123
7.28	Current distribution over a Rutherford-type cable.	124
7.29	Field and temperature over a twisted cable and field decomposition.	125
7.30	Scheme of quench protection methods.	127

7.31	Quench detection methods	128
7.32	Voltage detection conditions for the LHC MB	130
7.33	LHC MB dump resistor and cold diode.	131
7.34	Quench protection by subdivision or coupled secondary	133
7.35	Quench heater electrical circuit. Quench heater strip layout with copper plating.	134
7.37	Sequence of events during a quench with quench protection.	137
7.38	LHC magnet test station and main dipoles in the LHC tunnel.	138
7.39	Electrical circuit of the LHC tunnel configuration	139
7.40	Voltage development over the terminals of a quenched magnet in the LHC string. Voltages and time intervals are not to scale.	140
7.41	Electrical circuit and terminal voltage of a magnet on the test bench	142
7.42	Coil voltages recorded during a quench of an LHC main dipole on the test bench.	143
7.43	Electrical circuit model of the quench heater induced voltage spikes.	144
7.44	ROXIE model for the calculation of the inductance matrix. Simulated voltage spikes.	145
7.45	Model circuit for the explanation of voltages induced by asyn- chronous quenching	147
7.46	Model of the resistance growth in a half coil due to quench heater firing	147
7.47	Voltage jumps on coil voltages	147
7.48	Voltage along the magnet winding.	149
7.49	Influence of the winding scheme on the voltage to ground.	150
7.50	Capacitive effects on the voltage distribution over the coil wind- ing.	151
A.1	Temperature levels.	155
A.2	Electrical resistivity of copper	160
A.3	Electrical resistivity of copper	161
A.4	Electrical resistivity of Nb-Ti and Nb ₃ Sn in the normal con- ducting state	162
A.5	Thermal conductivity and Lorenz number of copper.	166
A.6	Thermal conductivity of Niobium-Titanium and Niobium-3-Tin.	166
A.7	Thermal conductivity of Polyimide (Kapton).	167
A.8	Normalized specific heat of solids after Debye.	168
A.9	Volumetric specific heat of copper. Specific heat of Kapton	170
A.10	Volumetric specific heat of Niobium-Titanium and Niobium-3- Tin.	170
A.11	General BH-curve.	173
A.12	Relative permeability as a function of magnetic induction	174
A.13	Analytical μ_r - and BH-curve.	176
A.14	Superconductor magnetization of type I, type II and hard su- perconductor.	178

A.15 Voltage-current-curve for a strand of the LHC MB outer layer cable and variation of the voltage over a superconductor depending on the n -value.	180
A.16 Critical current density measurement limitations.	183
A.17 Critical current density of Niobium-Titanium.	184
A.18 Critical current density of Niobium-3-Tin.	186
A.19 Resistivity of Nb-Ti and Nb ₃ Sn in superconducting state.	187
A.20 Volumetric specific heat of Nb-Ti and Nb ₃ Sn in superconducting state.	188
A.21 Phase diagram of helium.	189
A.22 Assumption of the pressure rise over temperature and resulting approximated density of helium.	190
A.23 Approximation of the thermal properties of helium with varying pressure.	192
 B.1 Different cable types.	 194
B.2 Contact coefficients	197
B.3 Definition of coil end and coil end length.	200
B.4 Effective thermal and electrical properties.	202
 C.1 LHC MB dipole cross-section.	 207
C.2 LHC MB winding scheme and quench heater layout.	208
C.3 LHC MB numbering schemes.	208
C.4 LHC MB scheme in the tunnel.	208
C.5 LHC MB quench detection.	211
C.6 LHC MCBX corrector magnet coil cross-section and winding scheme.	213
C.7 LHC MCBX magnet cross-section.	214
C.8 Inner Triplet Upgrade MQXC coil cross section, winding scheme and quench heater layout.	217
C.9 Fast Ramping Dipole iron yoke and magnet cross-section.	220
C.10 Fast Ramping Dipole coil cross section, winding scheme and quench heater layout.	221
 D.1 Surface charge density due to a discontinuity of the electrical resistivity.	 224
D.2 Arbitrarily cut circular cylinder.	225
D.3 Transformation of the measured critical current and superconductor magnetization to the critical current density.	226

List of Tables

7.1	Assumptions made regarding the quench heater efficiency and the quench propagation in the magnet	146
A.1	Melting temperature of the some materials	155
A.2	Mass density of the most common materials	156
A.3	Temperatures defining the RRR value according to different sources.	158
A.4	Electrical resistivity of Niobium-3-Tin versus temperature . . .	162
A.5	Electrical resistivity of some exemplary materials at the ice-point of water	163
A.6	Thermal conductivity of Niobium-3-Tin	166
A.7	Maximum thermal conductivity of most common materials . .	167
A.8	Debye temperature of some of the used materials	168
A.9	Fit parameters for the volumetric specific heat of copper . . .	170
A.10	Fit parameters for the volumetric specific heat of Nb-Ti . . .	172
A.11	Volumetric specific heat of Niobium-3-Tin	172
A.12	Volumetric specific heat of common materials for comparison .	172
A.13	Relative permeability of commonly used materials	176
A.14	Breakdown field strength of common insulation materials . . .	176
A.15	Transition temperature and critical field of superconducting elements	179
A.16	Different limits for the critical current from common literature	181
A.17	Fit parameters for the critical current density	184
A.18	Boiling point of different gases	190
A.19	Enthalpy of vaporization.	191
C.1	LHC MB Filament	204
C.2	LHC MB Strand	204
C.3	LHC MB Cable	206
C.4	LHC MB Magnet Data	207
C.5	LHC MB Electrical Circuit	210
C.6	LHC MB Protection	210
C.7	LHC MB Operating Conditions and Critical Values	211
C.8	LHC MCBX Magnet Data	213
C.9	Inner Triplet Upgrade MQXC Cable Parameters	216
C.10	Inner Triplet Upgrade MQXC Magnet Data	216
C.11	Inner Triplet Upgrade MQXC Electrical Circuit	216
C.12	Inner Triplet Upgrade MQXC Magnet Protection	216

C.13 Inner Triplet Upgrade MQXC Operating Conditions and Critical Values	217
C.14 Fast Ramping Dipole Strand	219
C.15 Fast Ramping Dipole Cable	219
C.16 Fast Ramping Dipole Magnet Data	220
C.17 Fast Ramping Dipole Magnet Protection	221
E.1 Constants used throughout this work	229

Notation and List of Symbols

Roman Letters

		$A_{\text{str,fil}}$	cross-sectional area of the strand covered by filaments
A	(generic) area		
$A_{\text{cab,core}}$	cross-sectional area of the cable core	$A_{\text{str,fil}}$	cross-sectional area of the strand covered by matrix material
$A_{\text{cab,NC}}$	normal conducting part of the cable cross-sectional area	$A_{\text{str,tot}}$	total strand cross-sectional area
$A_{\text{cab,SC}}$	superconducting part of the cable cross-sectional area	$A_{\text{void,inner}}$	cross-sectional area of the inner voids of a insulated cable
$A_{\text{cab,str}}$	cross-sectional area occupied by the strands of the cable	$A_{\text{void,outer}}$	cross-sectional area of the outer voids of a insulated cable
$A_{\text{cab,xs}}$	cross-sectional area of the bare cable	A	(generic) magnetic vector potential
$A_{\text{cab}}^{\text{eff}}$	effective cable cross-sectional area	B	(generic) magnetic induction
$A_{\text{fil,coat}}$	cross-sectional area of the filament coating	B_{c}	critical field type I SC
$A_{\text{fil,core}}$	cross-sectional area of the filament core	B_{c1}	lower critical field type II SC
$A_{\text{fil,SC}}$	superconducting cross-sectional area of the filament	B_{c2}	upper critical field type II SC
$A_{\text{fil,tot}}$	total filament cross-sectional area	B_{peak}	peak field on the conductor
$A_{\text{fil,coat}}$	cross-sectional area of the strand coating	c_0	speed of light in empty space
$A_{\text{str,core}}$	cross-sectional area of the strand	$c_{\text{V}}^{\text{eff}}$	effective volumetric specific heat
$A_{\text{str,ell}}$	elliptical cross-sectional area of the strand core	c_{T}	volumetric specific heat
		$c_{\text{T}}^{\text{eff}}$	effective volumetric specific heat
		C_{QH}	QH power supply capacitance

C_w	kleines Weh am grossen Zeh	I_E	current in the string of magnets
$d_E^{i,n}$	minimum distance in 2D between the conductors i and n .	I_M	current in the quenching magnet
d_{QH}	quench heater insulation thickness	I_q	quench current
D	dielectric displacement	$I_{SC,max}$	maximum induced inter-strand coupling current
e_m	elementary electrical charge	j	numbering of the slices in longitudinal direction of the coil
E	(generic) electrical field	J	(generic) current density
E_c	critical electrical field	J_c	critical current density
E_{bt}	electrical break-down field	J_F	surface current density
h	time step-size of the Runge-Kutta method	J_T	thermal flux density
h_c	cable height	ΔJ_c	current density margin
h_p	Planck's constant	k	coupling factor between two inductances
h_{QH}	quench heater height	k_B	Boltzmann constant
Δh_c	energy density reserve / enthalpy density margin	k_i	coefficient of the Runge-Kutta method
H	(generic) Magnetic field	$k_{cab,void,inner}$	factor of the inner void of a Rutherford-type cable filled with helium
ΔH	energy reserve		
i	(generic) current	$k_{cab,void,outer}$	factor of the outer void of a Rutherford-type cable filled with helium
i	numbering of the conductors in the coil cross-section		
I	(generic) current	$K_{trans}^{i,n}$	Geometrical transversal contact coefficient between conductor i and n considering the surface area of adjacent faces and the distance.
I_c	critical current		
I_c^{lin}	linear approximation of the critical current		
$\frac{dI_c}{dB}$	linearized critical current change with field		
I_D	current in the by-pass diode		

$K_{\text{cool},\alpha}^i$	Geometrical transversal contact coefficient between conductor i and a cold surface on face α considering the surface area the distance.	N_{A} N_{cp} N_{e} N_{f}	Avogadro number number of winding turns per pole number of elements in the thermal model number of filaments in a strand
ℓ	(generic) length	N_{mag}	number of magnets in a string
ℓ_{c}	coil length		
ℓ_{ce}	end part of the length	N_{s}	number of strands in a cable
ℓ_{mag}	magnetic length		
ℓ_{p}	Rutherford-type cable twist-pitch length	N_{SC} N_{z}	n-index number of longitudinal discretization steps
ℓ_{QH}	quench heater length		
ℓ_{w}	average winding length	p_{IFCC}	inter-filament coupling loss density
ℓ_{sp}	length of a strand in a twisted Rutherford-type cable	p_{ISCC}	inter-strand coupling loss density
L_{d}	differential inductance	p_{s}	strand twist pitch length
L_{QH}	QH parasitic inductance	P	(generic) power
L_{s}	inductance in series to the quenching magnet	P_{QH0}	quench heater initial power
L_{W}	energy inductance	r	(generic) distance, radius
L_{Ψ}	apparent inductance		
M	(generic) mutual inductance	r_{f} r_{fc}	filament outer radius filament inner/core radius
M	(generic) magnetization density	t_{fc}	filament coating thickness
M_{d}	differential mutual inductance	r_{s}	strand outer radius
\mathbf{M}_{IFCC}	inter-filament coupling current magnetization	r_{sc}	strand inner/core radius
\mathbf{M}_{ISCC}	inter-strand coupling current magnetization	r	(generic) position/locus
M_{Ψ}	apparent mutual inductance	r_{f} r_{fc} r_{s} r_{sc}	filament radius filament core radius strand radius strand core radius

R	(generic) resistance	t_{ia}	azimuthal cable insulation thickness
R_{a}	Rutherford-type cable adjacent resistance	t_{ir}	radial cable insulation thickness
R_{c}	Rutherford-type cable cross-over resistance	t_{PSoff}	time of power supply off
R_{cDfR}	forward differential resistance of the by-pass diode	t_{q}	time when quench starts
R_{DR}	value of the DR	t_{QB}	time of quench back in the magnet
R_{fDfR}	forward differential resistance of the free-wheeling diode	t_{QHeff}	time when quench heater shows to be effective
R_{gas}	gas constant		
R_{Q}	resistance of the quenched part of the magnet	t_{QHfire}	time when QH fire
		t_{off}	time when current in the quenched magnet decayed to zero
R_{QH}	quench heater strip resistance (at cold)	$t_{\text{off,all}}$	time when current in the string of magnets decayed to zero
L_{s}	resistance in series to the quenching magnet		
q	quality factor of the Runge-Kutta method	t_{sc}	strand coating thickness
q_{V}	electrical charge density	t_{val}	time of quench validation
\mathbf{S}	poynting vector	Δt_{cDh}	time for the cold diode to heat up
t	(generic) time		
t_{cc}	cable core thickness	Δt_{Dis}	discrimination duration for quench detection
t_{det}	time of quench detection		
t_{Diode}	time when diode switches	Δt_{DR}	time between DR trigger and end of current commutation
t_{DiodeHot}	time when diode warmed up	Δt_{DRcd}	DR commutation duration
t_{DRcur}	time when current commutation to DR ends	Δt_{DRtd}	DR trigger delay
		Δt_{QD}	time between quench start and quench validation
t_{DRtrig}	time of switch-in dump resistor		
t_{fc}	filament coating thickness	Δt_{QH}	QH delay, <i>i.e.</i> The time between Pring the quench heater circuit and the detection of a heater quench in one of the covered conductors

Δt_{QH0}	quench heater initial delay	U_{ind}	induced voltage
Δt_{QHs}	QH trigger scattering	$U_{\text{max,ground}}$	maximum allowable voltage to ground
Δt_{QHtd}	QH trigger delay	$U_{\text{max,tt}}$	maximum allowable turn-to-turn voltage
Δt_{QP}	duration of quench process	U_{PS}	voltage over the power supply
Δt_{QT}	trigger delay	U_{QH}	initial voltage over quench heater power supply
T	(generic) temperature	U_{NoQ}	voltage over the non-quenched magnets in the string
T_{b}	bath temperature	U_{res}	resistive voltage
T_{c}	critical or transition temperature	U_{SC}	voltage over a superconductor
T_{cs}	current sharing temperature	U_{Terminal}	voltage over the magnet terminals
$T_{\text{hot-spot}}$	hot-spot temperature	V	volume
T_{max}	maximum allowable temperature in case of quench	w_{ci}	inner width of a key-stoned cable
T_{op}	operating temperature	w_{co}	outer width of a key-stoned cable
ΔT_{c}	temperature margin	w_{QH}	quench heater width
ΔT_{cs}	current sharing temperature range	W_{mag}^V	magnetic energy in the volume V
U	(generic) voltage	W_{hyst}^V	hysteresis energy loss over a full cycle in the volume V
U_{cDf}	forward voltage over the by-pass diode	W_{source}	energy provided by the source
U_{cDcTh}	threshold voltage of the by-pass diode in cold state		
U_{cDwTh}	threshold voltage of the by-pass diode in warm state		
U_{det}	voltage threshold for quench detection		
U_{DR}	voltage over the DR		
U_{fDf}	forward voltage over the free-wheeling diode		
U_{fDTh}	threshold voltage of the free-wheeling diode		

Greek Letters

α	face of conductor: with $\alpha = \{a, b, c, d\}$.
β_{p}	cabling angle in a Rutherford-type cable path
γ	field dependence
Γ	on current, current derivation and current history

δ_{Ξ}^i	longitudinal orientation of the element with index i	Ξ	mapping function between the topological numbering ξ and the numbering scheme using ij
ϵ_E	electrical permittivity		
ϵ_0	electrical permittivity of empty space	ρ_D	mass density
ϵ_r	relative electrical permittivity	ρ_E	electrical resistivity
η	length, area, or volume ratio	ρ_E^{eff}	effective electrical resistivity
η^ℓ	length ratio	$\rho_E^{\text{eff},[=]}$	parallel effective electrical resistivity of stacked materials
η^A	area ratio		
η_{Cu}^A	area ratio of the copper material to the total cross-section	$\rho_E^{\text{eff},[]}$	serial effective electrical resistivity of stacked materials
η_{SC}^A	area ratio of the superconducting material to the total cross-section	ρ_{IFCC}	constant approximation of the electrical resistivity for IFCC
η^d	strand filling factor	$\frac{d\rho_{\text{IFCC}}}{dB}$	linear approximation of the electrical resistivity for IFCC
η^V	volume ratio		
κ_T	thermal conductivity	ρ_{sc}	electrical resistivity in SC state
$\kappa_T^{\text{eff},[=]}$	serial effective thermal conductivity of stacked materials	τ	(generic) time/time constant
$\kappa_T^{\text{eff},[]}$	parallel effective thermal conductivity of stacked materials	τ_{DR}	decay time constant of a string of magnets
λ	copper to superconductor ratio	τ_{QH}	Quench heater power time constant
$\lambda_{\text{non-Cu}}$	copper to non-copper area ratio	v	function relating MITs to the hot-spot temperature $T_{\text{hot-spot}}$
μ	magnetic permeability		
μ_0	magnetic permeability of empty space	φ	angle and polar coordinate
μ_r	relative magnetic permeability	ϕ	electrical potential
ξ	index of the topological numbering of all elements in the coil	ϕ_{key}	cable keystone angle
		Φ_0	flux quantum
		Ψ_{mag}	(generic) magnetic flux

Mathematical Notation

x	variable / cartesian coordinate
\mathbf{e}_i	unit vector in direction of the coordinate i
\mathbf{A}	vector field / vector function (bold upright print)
f	scalar field / scalar function
$f(a)$	value of the function f evaluated for a
$\frac{df}{dx}$	total differential of scalar function f after x
$\left. \frac{df}{dx} \right _{x=a}$	value of the total differential of the scalar function f after x at $x = a$
$\frac{\partial f}{\partial x}$	partial differential of scalar function f after x not considering variations in y, z, \dots
$\nabla \Phi$	gradient of scalar field Φ
$\nabla \times \mathbf{A}$	curl of vector field \mathbf{A}
$\nabla \cdot \mathbf{A}$	divergence of vector field \mathbf{A}
$\{x\}$	algebraic vector
$[A]$	algebraic matrix
\parallel	parallel
\perp	perpendicular
∂	boundary operator
$[...]$	operator returning the unit of measurement of the argument, <i>e.g.</i> $[\mathbf{B}] = \text{T}$

ds	differential path element
da	differential surface element
dV	differential volume element
\oint	closed surface / path integral

Abbreviations

Al	aluminum
ATLAS	A Toroidal LHC Apparatus
CAD	computer-aided design
CENELEC	European committee for Electrotechnical Standardization, Brussels, Belgium
CERN	European Organization for Nuclear Research, Geneva, Switzerland
CMS	Compact Muon Solenoid experiment
Cu	copper
DR	dump resistor
FAIR	Facility for Antiproton and Ion Research at GSI
Fe	iron
GSI	Gesellschaft für Schwerionenforschung, Darmstadt, Germany
H	hydrogen
He	helium
Hg	mercury
H ₂ O	water
HTS	high temperature superconductor

IEC	International Elec- trotechnical Commis- sion	Nb ₃ Sn NIST	niobium-3-tin National Institute of Standards and Tech- nology, Boulder, USA
IFCC	inter-filament cou- pling currents	O	oxygen
ISCC	inter-strand coupling currents	Pb PE	lead polyester
ITER	the way to new en- ergy. International fu- sion program	Ph.D.	<i>philosophiae doctor</i> , lat. doctor of philosophy
LARP	LHC Accelerator Re- search Program	PVA QH	polyvinyl acetate quench heater
LHC	Large Hadron Collider	RAL	Rutherford Appleton Laboratory
LTS	low temperature su- perconductor	ROXIE	Routine for the Opti- mization of magnet X- sections, Inverse field calculation and coil End design
MB	LHC main bending magnet (guiding beam on circular trajectory)	RRR	residual resistivity ra- tio
MCBX	LHC inner triplet dipole	SC	superconductor, superconducting
MITs	mega current square time integral	sLHC	LHC luminosity up- grade
MQE	minimum quench en- ergy	Sn SS SSC	tin stainless steel Superconducting Su- per Collider
MQX	LHC inner triplet quadrupole with wide aperture (focussing the beam for the experiments)	Ta Ti	tantalum titanium
MQXC	sLHC inner triplet up- grade quadrupole	TQ	LARP technology quadrupole
MQY	LHC wide aperture quadrupole	TU-Berlin	Technische Univer- sität Berlin
MRI	magnetic resonance imaging	VAC	voltage-current- characteristic
NC	normal conductor, normal conducting		
N	nitrogen		
Nb	niobium		
Nb-Ti	niobium-titanium		

Translations of Quotes and Background Explanations

Nullus est liber tam malus, ut non aliqua parte prosit!

There is no book so bad that it is not profitable on some part.

Widerstand zwecklos

Resistance is futile - also a catch phrase used by the Borg of the Star Trek fictional universe.

Dicebat Bernardus Carnotensis nos esse quasi nanos, gigantium humeris insidentes, ut possimus plura eis et remotiora videre, non utique proprii visus acumine, aut eminentia corporis, sed quia in altum subvenimur et extollimur magnitudine gigantea.

Bernard of Chartres used to say that we are like dwarfs on the shoulders of giants, so that we can see more than they, and things at a greater distance, not by virtue of any sharpness of sight on our part, or any physical distinction, but because we are carried high and raised up by their giant size.

Rerum cognoscere causas

To know the causes of things - Head note of "Der Tagesspiegel" (Berlin).

Ihr zahmen Täubchen, ihr Turteltäubchen, all ihr Vöglein unter dem Himmel, kommt und helft mir lesen, die guten ins Töpfchen, die schlechten ins Kröpfchen.

O gentle doves, O turtle-doves, And all the birds that be, The lentils that in ashes lie Come and pick up for me! The good must be put in the dish, The bad you may eat if you wish.

Hier stehe ich, ich kann nicht anders

Here I stand. I can do no other.

Milk production at a dairy farm was low so the farmer wrote to the local university, asking help from academia. A multidisciplinary team of professors was assembled, headed by a theoretical physicist, and two weeks of intensive on-site investigation took place. The scholars then returned to the university, notebooks crammed with data, where the task of writing the report was left to the team leader. Shortly thereafter the farmer received the write-up, and opened it to read on the first line: **"Consider a spherical cow... ."**

Curriculum Vitae

Nikolai Schwerg was born 1980 in Berlin. After finishing high-school in 1999, he fulfilled his community service in a nursing home. From October 2000 to April 2006 he studied electrical engineering at the Technical University in Berlin. During his studies he specialized on field theory, radio-frequency engineering and power electronics. Nikolai worked for two years as teaching assistant at the chair of theoretical electrical engineering. He spent more than a year at the European Organization for Nuclear Research (CERN) writing his student minor and diploma thesis. After graduating he began working as doctoral student at CERN in April 2006.



Publications: Parts of the dissertation have been published in the following scientific papers:

1. N. Schwerg, B. Auchmann, and S. Russenschuck. Quench simulation in an integrated design environment for superconducting magnets. *IEEE Trans. Magn.*, 44(6):934-937, June 2008.
2. N. Schwerg, B. Auchmann, and S. Russenschuck. Validation of a coupled thermal-electromagnetic quench model for accelerator magnets. *IEEE Transactions on Applied Superconductivity*, 18(2):1565-1568, June 2008.
3. B. Auchmann, N. Schwerg, and S. Russenschuck. Computational challenges for future projects (from a ROXIE developer's perspective). *Proceedings of the WAMSDO 2008*, June 2008.
4. N. Schwerg, B. Auchmann, and S. Russenschuck. Challenges in the thermal modeling of quenches with ROXIE. *IEEE Trans. Appl. Supercond.*, 19(3):1270-1273, June 2009.
5. N. Schwerg, B. Auchmann, K.-H. Mess, and S. Russenschuck. Numerical study of quench protection for fast-ramping accelerator magnets. *IEEE Trans. Appl. Supercond.*, 19(3):2428-2431, June 2009.